LUND UNIVERSITY

Imaging diffusional variance by MRI [public]

The role of tensor-valued diffusion encoding and tissue heterogeneity

Szczepankiewicz, Filip

2016

Document Version:
Publisher's PDF, also known as Version of record

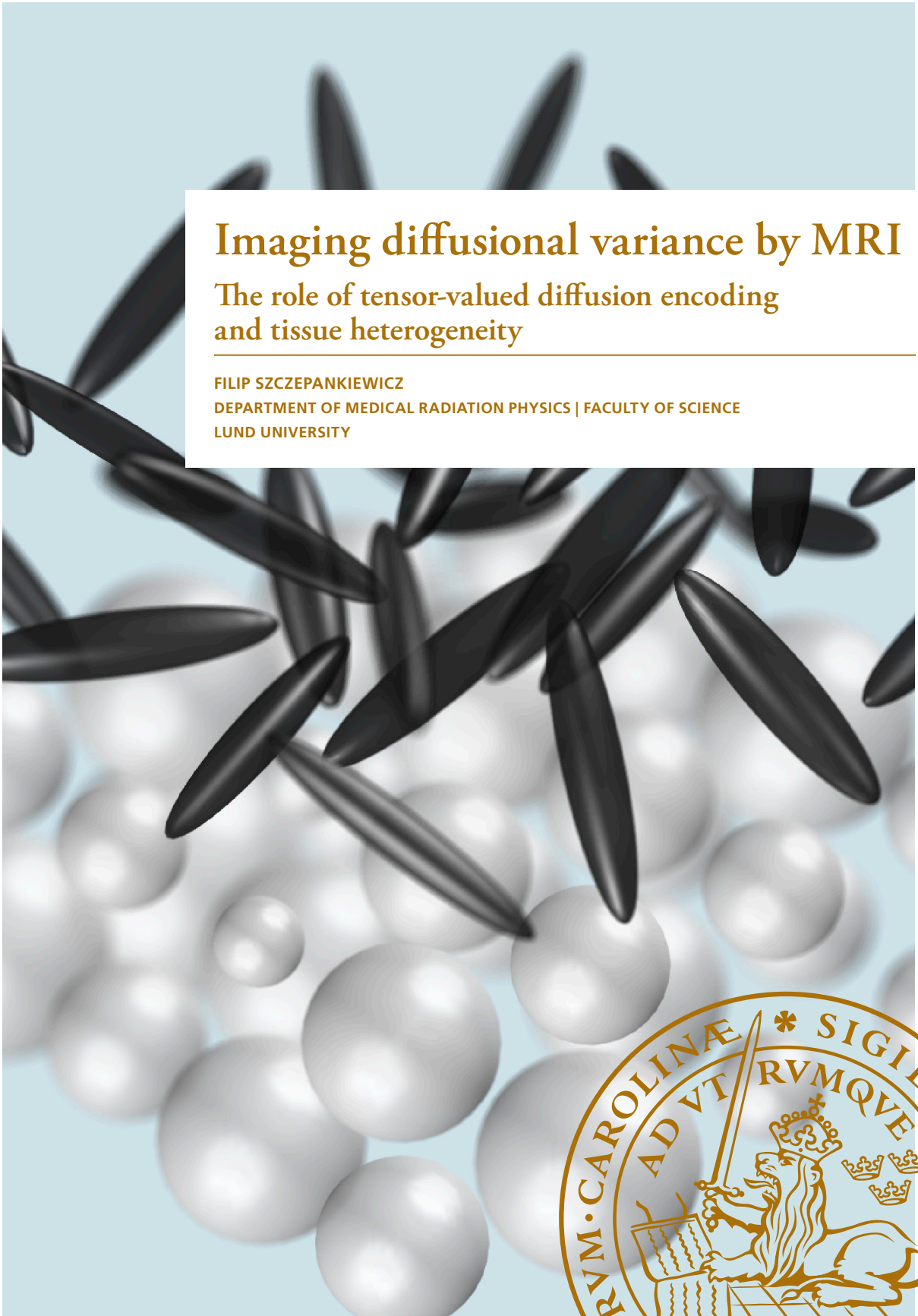

Imaging diffusional variance by MRI

The role of tensor-valued diffusion encoding and tissue heterogeneity

FILIP SZCZEPANKIEWICZ
DEPARTMENT OF MEDICAL RADIATION PHYSICS | FACULTY OF SCIENCE
LUND UNIVERSITY

Imaging diffusional variance by MRI:
The role of tensor-valued diffusion encoding and tissue heterogeneity

Imaging diffusional variance by MRI: The role of tensor-valued diffusion encoding and tissue heterogeneity

Filip Szczepankiewicz

LUND
UNIVERSITY

DOCTORAL DISSERTATION

by due permission of the Faculty of Science, Lund University, Sweden.
To be defended at Skåne University Hospital in Lund, lecture hall 3, on Friday, December 2, 2016 at 9:00.

Faculty opponent

Professor Derek K. Jones, Cardiff University, Cardiff, UK

Organization	Document name
LUND UNIVERSITY Department of Medical Radiation Physics Skåne University Hospital, Lund SE-22185 LUND, Sweden	DOCTORAL DISSERTATION Date of disputation 2016-12-02
Author(s) Filip Szczepankiewicz	Sponsoring organization

Title and subtitle

Imaging diffusional variance by MRI: The role of tensor-valued diffusion encoding and tissue heterogeneity

Abstract

Diffusion MRI provides a non-invasive probe of tissue microstructure. We recently proposed a novel method for diffusion-weighted imaging, so-called q-space trajectory encoding, that facilitates tensor-valued diffusion encoding. This method grants access to b-tensors with multiple shapes and enables us to probe previously unexplored aspects of the tissue microstructure. Specifically, we can disentangle diffusional heterogeneity that originates from isotropic and anisotropic tissue structures; we call this diffusional variance decomposition (DIVIDE).

In Paper I, we investigated the statistical uncertainty of the total diffusional variance in the healthy brain. We found that the statistical power was heterogeneous between brain regions which needs to be taken into account when interpreting results.

In Paper II, we showed how spherical tensor encoding can be used to separate the total diffusional variance into its isotropic and anisotropic components. We also performed initial validation of the parameters in phantoms, and demonstrated that the imaging sequence could be implemented on a high-performance clinical MRI system.

In Paper III and V, we explored DIVIDE parameters in healthy brain tissue and tumor tissue. In healthy tissue, we found that diffusion anisotropy can be probed on the microscopic scale, and that metrics of anisotropy on the voxel scale are confounded by the orientation coherence of the microscopic structures. In meningioma and glioma tumors, we found a strong association between anisotropic variance and cell eccentricity, and between isotropic variance and variable cell density.

In Paper IV, we developed a method to optimize waveforms for tensor-valued diffusion encoding, and in Paper VI we demonstrated that whole-brain DIVIDE is technically feasible at most MRI systems in clinically feasible scan times.

Key words		
Classification system and/or index terms (if any)		
Supplementary bibliographical information		Language English
ISSN and key title		ISBN 978-91-7753-034-3 (print) 978-91-7753-035-0 (pdf)
Recipient's notes	Number of pages	Price
	Security classification	

Signature  Date 2016-10-25

Imaging diffusional variance by MRI: The role of tensor-valued diffusion encoding and tissue heterogeneity

Filip Szczepankiewicz

LUND
UNIVERSITY

Faculty of Science
Department of Medical Radiation Physics

978-91-7753-034-3 (print)
978-91-7753-035-0 (pdf)

Printed in Sweden by Media-Tryck, Lund University
Lund 2016

... the answer is: Don't think about it!

- RICK SANCHEZ - RICK AND MORTY

Table of contents

Summary

Diffusion MRI provides a non-invasive probe of tissue microstructure. We recently proposed a novel method for diffusion-weighted imaging, so-called q-space trajectory encoding, that facilitates tensor-valued diffusion encoding. This method grants access to b-tensors with multiple shapes and enables us to probe previously unexplored aspects of the tissue microstructure. Specifically, we can disentangle diffusional heterogeneity that originates from isotropic and anisotropic tissue structures; we call this diffusional variance decomposition (DIVIDE).

In Paper I, we investigated the statistical uncertainty of the total diffusional variance in the healthy brain. We found that the statistical power was heterogeneous between brain regions which needs to be taken into account when interpreting results.

In Paper II, we showed how spherical tensor encoding can be used to separate the total diffusional variance into its isotropic and anisotropic components. We also performed initial validation of the parameters in phantoms, and demonstrated that the imaging sequence could be implemented on a high-performance clinical MRI system.

In Paper III and V, we explored DIVIDE parameters in healthy brain tissue and tumor tissue. In healthy tissue, we found that diffusion anisotropy can be probed on the microscopic scale, and that metrics of anisotropy on the voxel scale are confounded by the orientation coherence of the microscopic structures. In meningioma and glioma tumors, we found a strong association between anisotropic variance and cell eccentricity, and between isotropic variance and variable cell density.

In Paper IV, we developed a method to optimize waveforms for tensor-valued diffusion encoding, and in Paper VI we demonstrated that whole-brain DIVIDE is technically feasible at most MRI systems in clinically feasible scan times.

Populärvetenskaplig sammanfattning

Diffusion är den slumpmässiga rörelse hos partiklar som drivs av deras kinetiska energi. Den är oftast osynlig för blotta ögat, men den utgör en viktig funktion för vår överlevnad. Diffusionen står bland annat för transporten av näringsämnen över cellmembran, och det är diffusionen som gör att ämnen i kroppen blandas så att livsviktiga kemiska reaktioner kan ske.

Man kan undersöka diffusionsprocessen i det vatten som finns i kroppen med hjälp av magnetresonanstomografi (MRT, eng. MRI). Diffusionsprocessen i biologisk vävnad är dock mycket komplex. Komplexiteten härstammar från vattnets interaktion med vävnad, eftersom diffusionen påverkas av omgivningen där den äger rum. I områden med tätt packade celler blir diffusionen långsam i alla riktningar, medan i cellstrukturer som är extremt avlånga, exempelvis nervfibrer, kan diffusionshastigheten skilja sig mellan olika riktningar. Med en så kallad magnetkamera kan man avbilda diffusionshastigheten och därmed uttala sig om vävnadens struktur på mikroskopisk skala, helt utan invasiva ingrepp. Sådan information kan sedan användas för att undersöka friska vävnader, för diagnostik av sjuka vävnader eller för uppföljning av behandlingar.

Om vävnaden uppvisar olika snabb diffusion inom ett litet område blir diffusionshastigheten heterogen. Denna typ av heterogenitet kan tänkas härröra från områden där friska celler blandas med celler som angripits av en sjukdom och ersatts med lös nekrotisk vävnad. Heterogeniteten kan också återspegla förekomst av avlånga cell-strukturer där vävnadens olika riktningar uppenbarar sig som heterogen diffusion. Denna avhandling beskriver en ny metodik för att mäta heterogenitet i diffusionsprocessen, och tolkar heterogeniteten med stöd av mikroskopi av vävnaden. Vi har utvecklat metoder för att särskilja dessa egenskaper, och visat att dessa kan bidra med ny information i både frisk hjärnvävnad och i tumörer.

Original papers

This thesis is based on five publications and one manuscript, which are referred to in the thesis by their Roman numerals:

I. **Szczepankiewicz F**, Lätt J, Wirestam R, Leemans A, Sundgren P, van Westen D, Ståhlberg F, Nilsson M. Variability in diffusion kurtosis imaging: Impact on study design, statistical power and interpretation. 2013, *NeuroImage* 76, 145-154.

II. Lasič S, **Szczepankiewicz F**, Eriksson S, Nilsson M, Topgaard D. Microanisotropy imaging: quantification of microscopic diffusion anisotropy and orientational order parameter by diffusion MRI with magic-angle spinning of the q-vector. 2014, *Frontiers in Physics* 2 (11). DOI: 10.3389/fphy.2014.00011.

III. **Szczepankiewicz F**, Lasič S, van Westen D, Sundgren P, Englund E, Westin C-F, Ståhlberg F, Lätt J, Topgaard D, Nilsson M. Quantification of microscopic diffusion anisotropy disentangles effects of orientation dispersion from microstructure: Applications in healthy volunteers and in brain tumors. 2014, *NeuroImage* 104, 241-252.

IV. Sjölund J, **Szczepankiewicz F**, Nilsson M, Topgaard D, Westin C-F, Knutsson H. Constrained optimization of gradient waveforms for generalized diffusion encoding. 2015, *Journal of Magnetic Resonance* 261, 157-168.

V. **Szczepankiewicz F**, van Westen D, Englund E, Westin C-F, Ståhlberg F, Lätt J, Sundgren P, Nilsson M. The link between diffusion MRI and tumor heterogeneity: Mapping cell eccentricity and density by diffusional variance decomposition (DIVIDE). 2016, *NeuroImage*, In press. DOI: 10.1016/j.neuroimage.2016. 07.038.

VI. **Szczepankiewicz F**, Sjölund J, Ståhlberg F, Lätt J, Nilsson M. Whole-brain diffusional variance decomposition (DIVIDE): Demonstration of technical feasibility at clinical MRI systems. *Manuscript.*

List of contributions

The following is a brief summary of my contributions to each published paper and manuscript:

I. I participated in the design of the study with the co-authors. I contributed to writing the analysis code, and carried out the image post-processing and statistical analysis. I was the main author of the paper.

II. I wrote the sequence code for the clinical system. I constructed the biological phantom, acquired data, and performed the analysis on the clinical system. I contributed to writing of the paper.

III. I conceived and designed the study with the co-authors. I wrote the sequence code and designed the experiments. I performed the simulations, data acquisition, post-processing, and analysis. I performed the microscopy and quantitative image analysis. I was the main author of the paper.

IV. I wrote the sequence code and designed the in vivo experiments. I acquired the in vivo data and performed the post-processing and analysis of data. I contributed to writing of the paper.

V. I was responsible for the design of the study. I wrote the sequence code and designed the experiments. I carried out the data acquisition, post-processing, and statistical analysis. I was responsible for the histology image analysis, and developed the theoretical link between dMRI and histology features. I was the main author of the paper.

VI. I was responsible for the design of the study. I wrote the sequence code, designed the experiments, and acquired the data. I performed the post-processing and analysis. I was the main author of the manuscript.

Papers not included in this thesis

- Lampinen B, **Szczepankiewicz F**, Mårtensson J, van Westen D, Sundgren P C, and Nilsson M. Neurite density imaging versus imaging of microscopic anisotropy in diffusion MRI: A model comparison using spherical tensor encoding. 2016, *NeuroImage*. Being revised.
- Westin C-F, Knutsson H, Pasternak O, **Szczepankiewicz F**, Özarslan E, van Westen D, Mattisson C, Bogren M, O'Donnell L, Kubicki M, Topgaard D, and Nilsson M. Q-space trajectory imaging for multidimensional diffusion MRI of the human brain. 2016, *NeuroImage* 135, 345-362.
- Lampinen B, **Szczepankiewicz F**, van Westen D, Englund E, Sundgren P, Lätt J, Ståhlberg F, Nilsson M. Optimal experimental design for filter exchange imaging: apparent exchange rate measurements in the healthy brain and in intracranial tumors. 2016, *Magnetic Resonance in Medicine*, E-pub ahead of print.
- Nilsson M, **Szczepankiewicz F**, van Westen D, Hansson O. Extrapolation-based references improve motion correction of high b-value DWI data: Application in Parkinson's disease dementia. 2015, *PLoS One* 10 (11).
- Surova Y, **Szczepankiewicz F**, Lätt J, Nilsson M, Eriksson B, Leemans A, Hansson O, van Westen D, Nilsson C. Assessment of global and regional diffusion changes along white matter tracts in parkinsonian disorders by MR tractography. 2013, *PLoS One* 8 (6).

Abbreviations

ADC	Apparent diffusion coefficient
DIVIDE	Diffusional variance decomposition
DKI	Diffusional kurtosis imaging
dMRI	Diffusion magnetic resonance imaging
DTD	Diffusion tensor distribution
DTI	Diffusion tensor imaging
DWI	Diffusion-weighted imaging
SDE	Single diffusion encoding
DDE	Double diffusion encoding
QTE	q-Space trajectory encoding
LTE	Linear tensor encoding
PTE	Planar tensor encoding
STE	Spherical tensor encoding
ILT	Inverse Laplace transform

Mathematical symbols

$\mathbf{D}$	Distribution of diffusion tensors (DTD)
$\langle\mathbf{D}\rangle$	Diffusion tensor
$\mathbf{B}$	Diffusion encoding tensor, or b-tensor
$\mathbf{N}$	Normalized diffusion encoding tensor
$\mathbf{R}$	Rotation matrix
λ	Diffusion tensor eigenvalue
b	Diffusion encoding strength, or b-value
b_Δ	Encoding tensor anisotropy
D	Distribution of apparent diffusion coefficients
$\langle D\rangle$	Apparent diffusion coefficient (ADC)
D_I	Distribution of apparent isotropic diffusion coefficients
$\langle D_\mathrm{I}\rangle$	Apparent isotropic diffusion coefficient (MD)
$V_{\mathrm{A/I/T}}$	Anisotropic, isotropic and total diffusional variance
V_D	Variance of the distribution of diffusion coefficients

MD	Mean diffusivity
FA	Fractional anisotropy
μFA	Microscopic fractional anisotropy
OP	Order parameter
MK	Mean kurtosis (DKI)
$\mathrm{MK}_{\mathrm{A/I/T}}$	Normalized isotropic, anisotropic, and total variance (DIVIDE)

Mathematical operators

$\langle\cdot\rangle$	Ensemble average of tensors or scalars
$(\cdot)\colon(\cdot)$	Double inner product of two tensors
$\mathbf{E}_{\lambda}[\cdot]$	Mean of tensor eigenvalues
$\mathbf{V}_{\lambda}[\cdot]$	Variance of tensor eigenvalues

1 Introduction

Diffusion magnetic resonance imaging (dMRI) is widely used for examination of biological tissues, and related methods have applications that range from investigation of porous rocks to chemical compounds. The most unique feature of dMRI is arguably its ability to non-invasively probe the microstructure of living tissue. In dMRI, spatial magnetic field gradients are used to sensitize the magnetic resonance (MR) signal to the translational motion of hydrogen atoms bound in water molecules. The effects of the gradients on the signal can be related to the rate of diffusion, which in turn can be used to indirectly infer features of the tissue microstructure. Even though the diffusion process takes place on the microscopic scale, the geometry of the tissue has a significant effect on the diffusion process, and therefore also on the signal measured (Beaulieu, 2002). An early discovery that propelled dMRI as a clinical tool was presented by Moseley et al. (1990a), who showed that diffusion-weighted imaging (DWI) was sensitive tissue disruption in cerebral ischemia in an earlier phase than other imaging techniques (Moseley et al., 1990a, Moseley et al., 1990b).

Currently, one of the most popular dMRI methods in clinical research and neuroscience is diffusion tensor imaging (DTI) (Basser et al., 1994). The diffusion tensor is a mathematical object that describes the diffusion process in terms of the apparent diffusion coefficient (ADC) along any given direction, and can also provide derived parameters such as the average diffusivity and diffusion anisotropy (Figure 1) (Stejskal, 1965, Kingsley, 2006a).

DTI is most frequently applied to the central nervous system. In the brain, it has been used to study, for example, anatomy (Assaf and Pasternak, 2008), maturation (Lebel et al., 2008, Löbel et al., 2009), ageing (Moseley, 2002, Sullivan and Pfefferbaum, 2006) and plasticity (Scholz et al., 2009, Zatorre et al., 2012). It has also been a powerful tool in the investigation of conditions such as ischemia (Sotak, 2002), trauma (Huisman, 2003), and neurodegeneration (Horsfield and Jones, 2002), and in oncology to study tumor differentiation (Jiang et al., 2014), delineation, staging, treatment response (Tropine et al., 2004, Maier et al., 2010), and pre-surgical planning (Potgieser et al., 2014). Although dMRI outside of the brain is more challenging – due in part to elevated subject motion (Taouli et al., 2016) – it

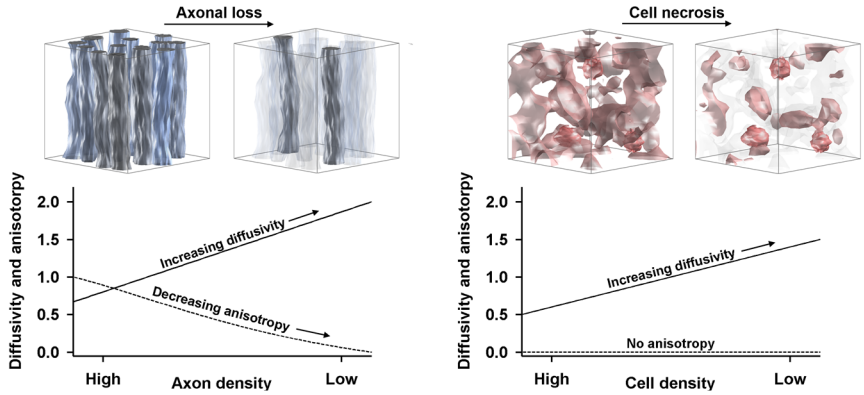

Figure 1 | Schematic examples of axonal loss (left) and cell necrosis (right). The plots exemplify how diffusivity and anisotropy may depend on changes in the tissue microstructure. It appeals to the intuition that the diffusion inside a thin tube would exhibit a preferred direction of movement, since it is restricted along the short axis and free along the long axis of the tube. When axons are removed, or made more permeable, the diffusivity increases and the anisotropy decreases. Similarly, the rate of diffusion appears to be faster in a loosely assembled tissue compared to that in a tightly packed cell matrix. This is because the movement of water molecules is restricted, or hindered, by the obstacles in the tissue.

has been used to study, for example, breast tissue (Partridge et al., 2010), prostate tissue (Li et al., 2015), skeletal muscle (Damon et al., 2016), and even the heart (Mekkaoui et al., 2015). In addition to characterizing tissue on a voxel-by-voxel basis, DTI has been seminal in the evolution of tractography (Mori et al., 1999), which can be used for segmentation of white matter pathways (Catani and Thiebaut de Schotten, 2008) and investigations of brain connectivity (Hagmann et al., 2010, Lazar, 2010).

DTI is a powerful tool because it provides several parameters with seemingly intuitive interpretations. For example, during brain maturation, reduced diffusivity and increased anisotropy in the white matter is interpreted as axon myelination (Lebel et al., 2008), and the anisotropy serves as a marker of healthy development. In white matter afflicted by neurodegenerative disease, elevated diffusivity perpendicular to the nerves may indicate demyelination (Song et al., 2002), whereas reduced diffusivity along the nerves reflects axonal damage (Sun et al., 2006). In both cases, the anisotropy decreases, and may therefore be interpreted as a marker of tissue degeneration. In tumors, changes to the average diffusivity are commonly interpreted as changes in tissue density (Chen et al., 2013) or in the volume fraction of water that is inside or outside cells (Chenevert et al., 2000).

DTI also has several well-known limitations (Alexander et al., 2001, Alexander et al., 2007, Jones and Cercignani, 2010, Jones et al., 2012). For the purposes of this thesis, two major limitations are relevant. First, DTI is ill-suited to capture microscopic diffusion heterogeneity, i.e. the presence of multiple rates of diffusion

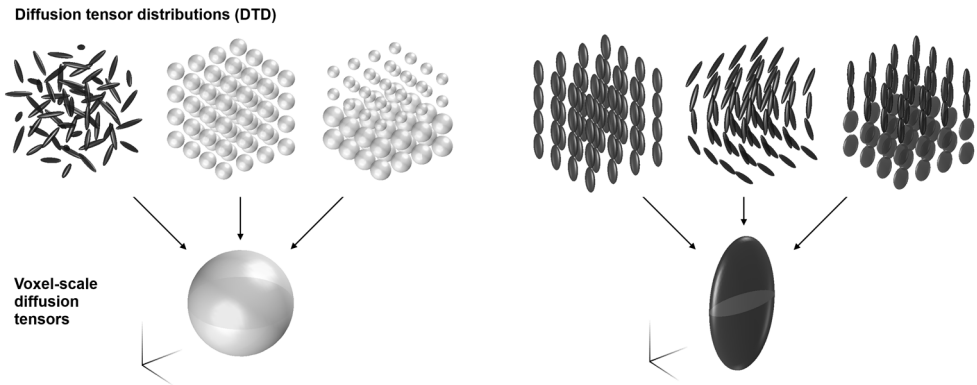

Figure 2 | Multiple intra-voxel diffusion tensor distributions (top row) map onto the same voxel-scale diffusion tensor (bottom row). In the first example (left), the same voxel-scale tensor is observed for randomly oriented anisotropic tensors, homogeneous isotropic tensors, and a mixture of isotropic tensors that exhibit fast and slow diffusion. In the second example (right), the voxel-scale tensor cannot distinguish between ordered tensors with moderate anisotropy, bending tensors with high anisotropy, or a mixture of oblate and prolate tensors. This demonstrates that some tisse characteristics cannot be distinguished by DTI.

within a single voxel, because it only retains information about an average across the whole voxel. This limitation prevents accurate quantification of tissue heterogeneity. The presence of heterogeneous diffusion favors a description of the diffusion process as an intra-voxel distribution of apparent diffusion coefficients (DDC) rather than an average value (Callaghan and Pinder, 1983). Secondly, DTI conflates the effects of diffusion anisotropy and orientation coherence (Pierpaoli et al., 1996). An elegant example of this was demonstrated by Douaud et al. (2011) who showed that partial axonal degeneration in a region with crossing white matter pathways could cause the anisotropy to *increase*, which contradicts the simplistic interpretation. This is one of many examples that contradict the simple – but ultimately flawed – interpretation of voxel-scale anisotropy as a marker of white matter "integrity" (Jones et al., 2012). Thus, measures of voxel-scale anisotropy are most reliable in homogeneous tissues with high orientation coherence (Alexander et al., 2001), but such tissues have been estimated to make up only 10% of the brain volume (Jeurissen et al., 2013). Figure 2 shows six tissue models where anisotropy, orientation coherence, and heterogeneity cannot be accurately distinguished by DTI.

Many alternative approaches have been proposed to overcome the shortcomings of DTI (Shemesh et al., 2010, Yablonskiy and Sukstanskii, 2010, Tournier et al., 2011). The scope of this thesis is limited to diffusional kurtosis imaging as a probe of tissue heterogeneity, and methods based on double diffusion encoding as probes of microscopic anisotropy.

Diffusional kurtosis imaging (DKI) is an extension of DTI that can quantify the heterogeneity of diffusivities within a voxel in terms of the so-called diffusional kurtosis (Jensen et al., 2005, Jensen and Helpern, 2010). Similar parameters have also been derived from q-space analysis (Lätt et al., 2003) and statistical models (Yablonskiy et al., 2003). Traditionally, "diffusional kurtosis" refers to a feature of the so-called "diffusion propagator". In this thesis, we will instead refer to this feature as "diffusional variance" and relate it to the distribution of apparent diffusion coefficients. For example, a mixture of dense and loose tissue contributes both low and high values to the DDC, which is observed as a high diffusional variance. Diffusional variance may therefore reflect tissue heterogeneity. Tissue heterogeneity has been studied in tumors by DKI, where parameters that reflect the diffusional variance tend to outperform DTI metrics for differentiation of tumor grades (Raab et al., 2010, Van Cauter et al., 2012), probably due to an association between tissue heterogeneity and malignancy (Hempel et al., 2016).

A fundamental limitation of DKI is that it entangles the diffusional variance that is caused by anisotropic structures, and variable isotropic diffusivity, on the sub-voxel scale. We refer to these tissue features as "microscopic anisotropy" and "isotropic heterogeneity". For example, if a voxel exhibits a high diffusional variance and no voxel-scale anisotropy, we know that the DDC comprises multiple diffusivities, but we cannot say whether this is due to anisotropic structures that are randomly oriented (microscopic anisotropy) or isotropic structures with variable diffusivity (isotropic heterogeneity), or a mixture of both (Mitra, 1995). This lack of specificity may contribute to the limited interpretability of DKI parameters in terms of relevant structural features (Jensen and Helpern, 2010, Jespersen et al., 2010, Maier et al., 2010, Chuhutin et al., 2015, Tietze et al., 2015). This is not a limitation of the model, but rather an inherent limitation of any method that relies solely on single diffusion encoding (SDE, or sPFG) (Mitra, 1995).

Microscopic anisotropy, orientation coherence, and isotropic heterogeneity can be disentangled (Cheng and Cory, 1999), but it requires diffusion encoding that goes beyond the canonical SDE sequence proposed by Stejskal and Tanner (1965). A prominent example of the evolution of diffusion encoding is the double diffusion encoding sequence (DDE, or dPFG) (Cory et al., 1990). DDE uses two gradient pairs, compared to one pair in SDE, and is capable of encoding the diffusion in two independent directions during a single acquisition of the signal (Shemesh et al., 2010). By doing so, it is possible to access information on the microscopic diffusion anisotropy even if the tissue appears isotropic on the voxel scale (Callaghan and Komlosh, 2002, Ozarslan and Basser, 2008, Lawrenz et al., 2010, Shemesh et al., 2010, Jespersen et al., 2013, Jensen et al., 2014, Shemesh et al., 2016). The main

limitation of imaging techniques based on DDE is the low efficiency of the encoding and the prolonged acquisition time incurred by the extended sampling schemes (Jespersen et al., 2013, Hui and Jensen, 2015). Furthermore, even though DDE is theoretically capable of separating out the isotropic heterogeneity, we know of no studies that have attempted to do this. Consequently, the components of diffusional variance and their relation to the underlying tissue microstructure are largely unexplored.

In summary, DKI provides a probe for tissue heterogeneity but it is unspecific and is fundamentally incapable of resolving the isotropic and anisotropic variance due to its reliance on SDE. More specific features of the tissue microstructure can be accessed by using non-conventional diffusion encoding. To date, however, non-conventional encoding has not been systematically employed to explore the components of diffusional variance.

In this thesis, we investigated two gaps in our current knowledge. First, we sought alternatives to the DDE technique that could facilitate improved imaging of diffusional variance in a clinical setting. Secondly, we investigated the link between dMRI parameters such as the diffusional variance and features of the tissue microstructure.

Our approach was to develop and implement a custom diffusion encoding sequence capable of executing arbitrary gradient waveforms, or so-called q-space trajectory encoding (QTE), in order to yield tensor-valued diffusion encoding. The tissue was modeled by a diffusion tensor distribution (DTD), which allows a straight forward characterization of the tissue without relying on strong assumptions, making it applicable to a wide variety of healthy and diseased tissues. Based on QTE and the DTD framework, we proposed diffusional variance decomposition (DIVIDE) as a means of disentangling the diffusional variance into its isotropic and anisotropic components. Finally, we investigated the validity and interpretation of the DIVIDE parameters by correlating them to features of the tissue microstructure derived from quantitative microscopy.

2 Aims

The work presented in this thesis describes how diffusion in heterogeneous tissue can be modeled by a distribution of diffusion tensors, and how tensor-valued diffusion encoding can be used to explore new aspects of diffusional variance and microscopic diffusion anisotropy. It also describes the theoretical background, practical implementation, and implications of such methods when applied to healthy brain tissue and tumors.

The aims of this thesis were:

- To develop techniques for diffusion weighting with tensor-valued encoding (Paper II), and to investigate the feasibility of diffusional variance decomposition in a clinical setting (Paper III).
- To investigate the experimental design in terms of the encoding waveform (Paper IV), the imaging protocol (Paper VI), and the study design (Paper I) in order to optimize the quality of imaging studies aimed at quantification of diffusional variance.
- Explore the metrics of diffusional variance and anisotropy in healthy tissue and tumor tissue (Paper III and V), and to validate their interpretation by investigating their association with structural features in tumors (Paper V).

3 Diffusion tensor distribution as a model of heterogeneous tissue

Biological tissue comprises many different types of cells and tissues arranged in more or less coherent cell matrices. In neural tissue, structures range from axons, in which the water diffusion is extremely anisotropic, to approximately spherical cells that cause negligible diffusion anisotropy. Approximately 20% of the water is also located in the extracellular space, where the diffusion characteristics are defined by the surrounding tissue (Sykova and Nicholson, 2008, Novikov and Kiselev, 2010). Moreover, the voxel volume is of the order of 1–30 mm^3 and may therefore contain many tissue types, cell types, and orientations of structures. Diffusion in biological tissue may therefore be considered to be quite complex.

A potentially interesting feature of complex tissue is its heterogeneity. In this thesis, we consider "tissue heterogeneity" to be any structural feature that causes multiple rates of diffusion in a single voxel (Paper V). Two types of heterogeneity were identified, namely "microscopic anisotropy" and "isotropic heterogeneity", which correspond to anisotropic and isotropic diffusional variance (Paper II and V).

This chapter describes how a diffusion tensor distribution (de Swiet and Mitra, 1996, Jian et al., 2007, Scherrer et al., 2015, Westin et al., 2016a) can be used to model heterogeneous tissue, and how macroscopic features of the distribution reflect the underlying heterogeneity.

3.1 The diffusion tensor

The rate of diffusion is defined from the relation between the average displacement of particles and the time during which they diffuse. In a medium with no restrictions, the mean-square displacement along the direction x is simply $\langle x^2 \rangle = 2 \cdot D_0 \cdot t_D$, where D_0 and t_D are the diffusion coefficient and diffusion time (Einstein, 1905). The diffusivity of freely diffusing water at body temperature is approximately

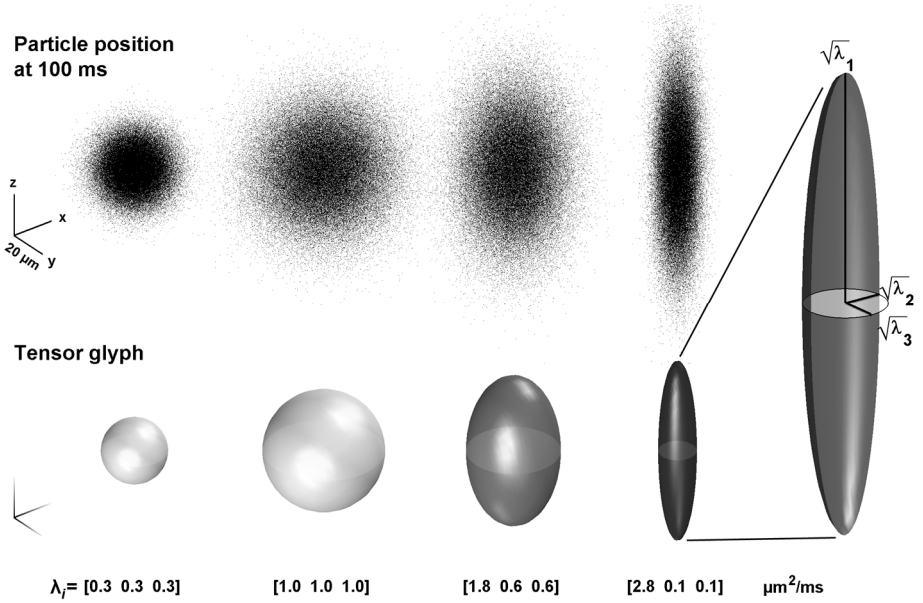

Figure 3 | Particle displacement (top row) and corresponding diffusion tensor glyphs (bottom row). Each tensor glyph reflects the mean-square displacement of the diffusion particles. The square root of the three eigenvalues determines the shape of the ellipsoid. Apart from the leftmost case, all tensors have the same mean diffusivity.

$D_0 = 3.0$ µm^2/ms $= 3.0 \cdot 10^{-9}$ m^2/s (Mills, 1973, Holz et al., 2000). For this diffusivity, the mean-square displacement along x is approximately 25 µm after $t_D =$ 100 ms. This level of displacement is comparable to the size of individual cells, considering that the diameters of axons and cell bodies are roughly 1 and 10 µm (Yablonskiy and Sukstanskii, 2010, Caminiti et al., 2013). Whenever diffusing particles interact with obstacles, e.g. water in biological tissue, the movement of the diffusing particles may be unbounded but slowed down by obstacles (hindered diffusion) or confined to a finite compartment (restricted diffusion). In both situations, the intrinsic diffusivity may be unchanged, but the average displacement for a given diffusion time is reduced. In dMRI, this corresponds to a reduction in the observed diffusivity, and the diffusion coefficient derived from such systems is therefore called the *apparent* diffusion coefficient. Furthermore, the ADC may depend on the direction along which the diffusion is measured, which is referred to as anisotropic diffusion.

The diffusion process can be described in three dimensions in terms of a diffusion tensor (Stejskal, 1965, Basser et al., 1994). The conventional, voxel-scale, diffusion tensor ($\langle \mathbf{D} \rangle$) is written as a matrix with nine elements,

$$\langle \mathbf{D} \rangle = \begin{pmatrix} D_{xx} & D_{xy} & D_{xz} \\ D_{yx} & D_{yy} & D_{yz} \\ D_{zx} & D_{zy} & D_{zz} \end{pmatrix}, \qquad \text{Eq. 1}$$

which has six degrees of freedom due to diagonal symmetry ($D_{ij} = D_{ji}$). In the principal axis system (PAS), the off-diagonal elements are zero and the diagonal elements are its three eigenvalues ($\lambda_i = [\lambda_1\ \lambda_2\ \lambda_3]$), which describe the diffusivity along three orthogonal eigenvectors ($\epsilon_1, \epsilon_2, \epsilon_3$). Figure 3 shows examples of particle displacements and the corresponding diffusion tensor glyphs in isotropic and anisotropic cases.

Throughout this thesis, boldface capital letters denote tensors or tensor distributions. Tensors are visualized as ellipsoids where the length of each axis reflects the square root of the tensor eigenvalues (Basser et al., 1994, Kindlmann, 2004), and the color of the tensor glyph will indicate its fractional anisotropy (white to black indicates low to high anisotropy).

3.2 Diffusion tensor distribution model

Tissue heterogeneity can be captured by describing the diffusion in each segment of coherent tissue with a diffusion tensor. Because the tissue is normally only coherent on short length scales, coherent segments are referred to as "microenvironments" (Westin et al., 2016a). The collection of microenvironments within a voxel can be described by an ensemble of diffusion tensors, where each tensor in the ensemble represents a microenvironment. Since it is not feasible to resolve the individuals of the ensemble, we will consider its macroscopic observables, using an approach similar to statistical mechanics.

We refer to the ensemble of tensors as a diffusion tensor distribution (Westin et al., 2016a), denoted **D**. If the assumptions of the model hold (see section 3.4), the DTD provides a comprehensive and accurate description of the diffusion process within the tissue. From the DTD, it is then possible to derive invariant metrics that are observable on the voxel scale pertaining to the diffusivity and diffusional variance, as well as the diffusion anisotropy on the voxel and microscopic scales.

3.3 Parameterization of the DTD

3.3.1 Tensor operators

The voxel-scale diffusion tensor, $\langle \mathbf{D} \rangle$, is the average over all individuals in the distribution of diffusion tensors. Assuming that the DTD is a continuous probability density function ($P(\mathbf{D})$), the average tensor is

$$\langle \mathbf{D} \rangle = \int \mathbf{D} \cdot P(\mathbf{D}) \, \mathrm{d}\mathbf{D} \ . \qquad \text{Eq. 2}$$

Throughout the thesis, diffusion tensors within averaging brackets represent the voxel-scale diffusion tensor, whereas the same symbol without brackets refers to the diffusion tensor distribution. The placeholder tensor ($\mathbf{T}$) is used to describe three useful operators. The average across tensor eigenvalues ($\mathrm{E}_\lambda[\cdot]$) is defined as

$$\mathrm{E}_\lambda[\mathbf{T}] = \frac{1}{3} \sum_{i=1}^{3} \lambda_i \ , \qquad \text{Eq. 3}$$

where λ_i are the eigenvalues of $\mathbf{T}$. The sum across eigenvalues is equal to the trace of the tensor ($\mathrm{E}_\lambda[\mathbf{T}] = \mathrm{Tr}(\mathbf{T})/3$), which can be calculated without knowing the eigenvalues. The population variance of tensor eigenvalues ($\mathrm{V}_\lambda[\cdot]$) is defined as

$$\mathrm{V}_\lambda[\mathbf{T}] = \frac{1}{3} \sum_{i=1}^{3} (\lambda_i - \mathrm{E}_\lambda[\mathbf{T}])^2 \ . \qquad \text{Eq. 4}$$

Note that Eq. 4 describes the entire population of eigenvalues, rather than a sample, yielding a variance that is normalized by a factor of 1/3 instead of 1/2. The variance can also be calculated without knowing the eigenvalues (Basser and Pierpaoli, 1996, Westin et al., 2016a). Finally, the double inner product (:) of two tensors ($\mathbf{T}$ and $\mathbf{T}'$) is a scalar defined as the sum over all element-wise products, according to

$$\mathbf{T}' : \mathbf{T} = \sum_{i=1}^{3} \sum_{j=1}^{3} \mathbf{T}'_i \ \cdot \mathbf{T}_i \ \ . \qquad \text{Eq. 5}$$

Note that the operations in Eqs. 3 to 5 can also be applied to distributions of tensors, i.e. $\mathbf{T}$ can be exchanged for both $\langle \mathbf{D} \rangle$ and $\mathbf{D}$. If an operation is applied to a distribution of tensors, the result is a distribution of scalars.

3.3.2 Mean and variance of the DTD

The distribution of diffusion tensors can be parameterized in terms of the mean diffusivity and the variance of diffusivities using the operators from section 3.3.1. The voxel-scale average is called the mean diffusivity (MD), defined as

$$\mathrm{MD} = \mathrm{E}_\lambda[\langle \mathbf{D} \rangle] \ . \qquad \text{Eq. 6}$$

The same operation applied to $\mathbf{D}$ yields a distribution of isotropic diffusivities (D_I), according to

$$D_\mathrm{I} = \mathrm{E}_\lambda[\mathbf{D}] \ . \qquad \text{Eq. 7}$$

Thus, MD and D_I represent the isotropic diffusivity on the voxel and microscopic scales. From Eq. 6 and Eq. 7, we can see that MD is also the average across D_I, according to $\mathrm{MD} = \langle D_\mathrm{I} \rangle$.

The DTD also contains information on two types of diffusional variance, namely the isotropic and anisotropic variance (V_I and V_A). The isotropic variance reflects the difference in isotropic diffusivities across microenvironments, according to

$$V_\mathrm{I} = \langle \mathrm{E}_\lambda[\mathbf{D}]^2 \rangle - \mathrm{E}_\lambda[\langle \mathbf{D} \rangle]^2, \qquad \text{Eq. 8}$$

which is equal to the variance of the isotropic diffusivities, according to $V_\mathrm{I} = \mathrm{V}[D_\mathrm{I}]$, where $\mathrm{V}[\cdot]$ is the variance operator. Note that V_I is zero for any DTD where all microenvironments have identical isotropic diffusivity, i.e. if there is no isotropic heterogeneity.

The anisotropic variance reflects the average variance of diffusion tensor eigenvalues, given by (VanderHart and Gutowsky, 1968)

$$V_\mathrm{A} = \frac{2}{5} \langle \mathrm{V}_\lambda[\mathbf{D}] \rangle \ . \qquad \text{Eq. 9}$$

Note that V_A is independent of the orientation of each tensor in the distribution, and that it is only zero if all microenvironments exhibit isotropic diffusion.

The sum of the two types of variance is the total diffusional variance (V_T), according to $V_\mathrm{T} = V_\mathrm{I} + V_\mathrm{A}$ (Paper II and III). The total variance is the variance probed by SDE-based methods, such as DKI (Jensen et al., 2005). To comply with the nomenclature suggested by Jensen et al. (2005), the diffusional variance is normalized and scaled according to

$$\mathrm{MK}_\mathrm{x} = 3 \cdot \frac{V_\mathrm{x}}{\mathrm{MD}^2} \ , \qquad \text{Eq. 10}$$

where the subscript "x" indicates which component of variance is intended. We will refer to both V_x and MK_x as the diffusional variance, and keep the abbreviation "MK" to retain its connection to the mean diffusional kurtosis. Figure 4 depicts DTDs that render variable levels of isotropic and anisotropic variance.

3.3.3 Fractional anisotropy

The fractional anisotropy (FA), conventionally used in DTI, is derived from the voxel-scale diffusion tensor eigenvalues, in terms of their variance and expected value according to (Basser et al., 1994, Westin et al., 2016a)

$$FA^2 = \frac{3}{2} \cdot \frac{V_\lambda[\langle \mathbf{D} \rangle]}{E_\lambda[\langle \mathbf{D} \rangle]^2 + V_\lambda[\langle \mathbf{D} \rangle]} \,. \qquad \text{Eq. 11}$$

The FA in is not commonly expressed in terms of eigenvalue expectancy and variance (Eq. 11), but this formulation is mathematically equal to the definition first introduced by Basser et al. (1994); see Kingsley (2006b) for a comprehensive description of tensor parameterization. It is apparent from Eq. 11 that $V_\lambda[\langle \mathbf{D} \rangle]$ must be non-zero to yield a non-zero FA. This occurs under two conditions. First, microenvironments that exhibit anisotropic diffusion must be present in the voxel. Secondly, these microenvironments must be oriented so that some anisotropy is retained at the voxel scale. As seen in Figure 4 (bottom right), if the anisotropic structures are randomly oriented within the voxel, the voxel-scale tensor will be isotropic, resulting in FA = 0.

The fact that the FA is strongly modulated by orientation coherence is well understood and is widely considered to be a major limitation of DTI (Alexander et al., 2001, Jones et al., 2012). It is therefore beneficial to construct a parameter that probes the *microscopic* diffusion anisotropy, independently of the orientation coherence. Such a parameter can be derived from the DTD (Paper II, Westin et al., 2014, Westin et al., 2016a). This parameter is called the microscopic fractional anisotropy (μFA), and it is defined according to (Paper V, Jespersen et al., 2013, Westin et al., 2016a)

$$\mu FA^2 = \frac{3}{2} \cdot \frac{\langle V_\lambda[\mathbf{D}] \rangle}{\langle E_\lambda[\mathbf{D}]^2 \rangle + \langle V_\lambda[\mathbf{D}] \rangle} \,. \qquad \text{Eq. 12}$$

The difference between FA and μFA is that FA is calculated from the diffusion anisotropy that is observed on the voxel-scale whereas the μFA is calculated from the anisotropic diffusional variance. Mathematically, the difference is determined by the stage at which the ensemble average is performed (Eqs. 11 and 12) (Paper V).

The μFA may be interpreted as the FA that would be observed in a sample if all microenvironments were perfectly ordered. However, the μFA is not mathematically equal to the average FA of all microenvironment tensors unless the microenvironments differ only with respect to their orientation.

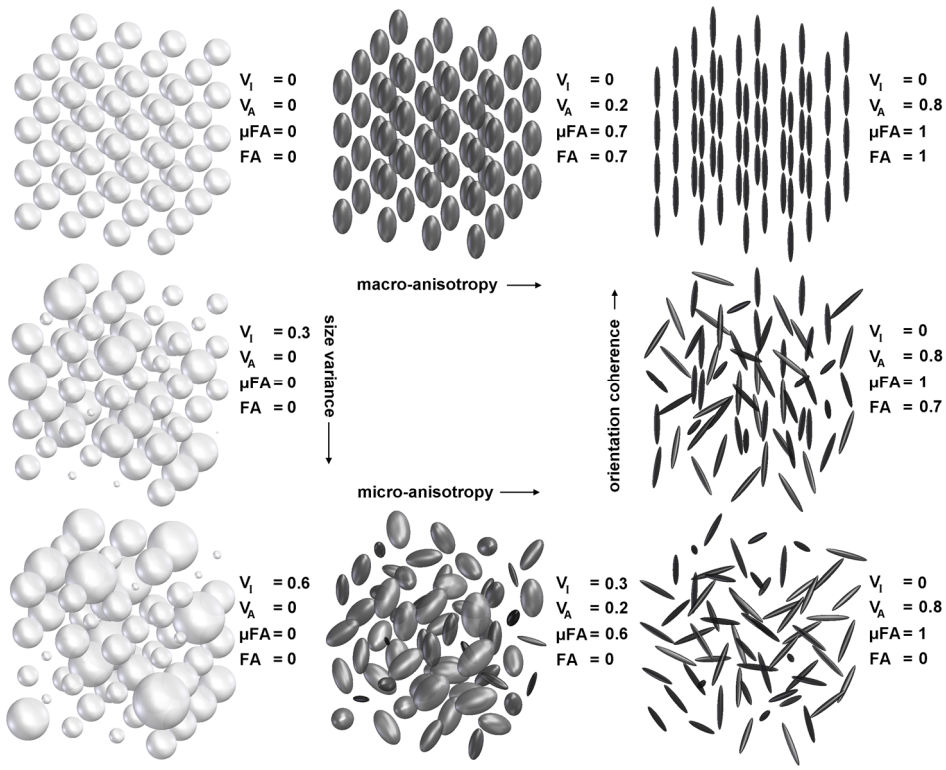

Figure 4 | Schematic representation of DIVIDE parameters in eight different diffusion tensor distributions. The parameters show the isotropic and anisotropic diffusional variance (V_I and V_A), and the fractional anisotropy on the microscopic and voxel scale (μFA and FA). For example, in a perfectly homogeneous tissue, all four parameters are zero (top left), and for randomly oriented anisotropic structures the μFA is high whereas the FA is zero (bottom right).

3.3.4 Order parameter

The discrepancy between FA and μFA is caused by the orientation dispersion, and the difference between the two can be used to quantify the order of the underlying structures. We quantify the orientation coherence in terms of the order parameter (OP), which is a well-established parameter in the field of liquid crystal NMR, according to (Paper II and III)

$$\mathrm{OP}^2 = \frac{\mathrm{V}_\lambda[\langle \mathbf{D} \rangle]}{\langle \mathrm{V}_\lambda[\mathbf{D}] \rangle} \,. \qquad \text{Eq. 13}$$

The numerator and denominator in Eq. 13 are proportional to the FA and μFA, respectively. When FA = μFA, the orientations of the underlying tissue are perfectly coherent, yielding OP = 1, i.e. the "full" microscopic anisotropy is retained on the voxel scale with no reduction due to orientation dispersion. Any level of orientation dispersion yields OP < 1 (Paper II). It is also possible to quantify asymmetric orientation distributions of anisotropic domains in terms of a "Saupe order tensor" (Topgaard, 2016b), but this was outside the scope of this thesis.

3.4 Assumptions of the DTD model

The DTD model is based on two main assumptions under which it accurately describes the diffusion in tissue. These assumptions are that:

- the diffusion in each microenvironment is approximately Gaussian
- the diffusing particles do not exchange between microenvironments during the encoding.

The next two sections briefly describe the ramifications of these assumptions and how they may affect the interpretation of the model parameters.

3.4.1 Non-Gaussian diffusion

The diffusion is only Gaussian in a homogeneous medium that interacts only with itself, such as in an infinite body of pure water. Consequently, the diffusion is non-Gaussian in biological tissue where heterogeneity and obstacles are ubiquitous (de Swiet and Mitra, 1996). This fact contradicts the first assumption of the DTD model

(Beaulieu, 2002), and we will therefore briefly discuss how the first assumption interacts with three aspects of non-Gaussian diffusion, namely the presence of multiple Gaussian components, non-Gaussian phase dispersion, and time-dependent diffusion.

The presence of multiple components with Gaussian diffusion is permitted by the DTD model since it models each component in terms of a diffusion tensor (de Swiet and Mitra, 1996, Yablonskiy et al., 2003). As long as the diffusion in each microenvironment is approximately Gaussian, the first assumption holds.

A non-Gaussian phase distribution may occur, for example, where there is restricted diffusion (Callaghan et al., 1991), which in turn invalidates the simple exponential relation between the signal and the diffusivity assumed by the DTD model. However, the effects of a non-Gaussian phase distribution are small for moderate attenuation, i.e. if the signal is not attenuated below 10% (Topgaard and Söderman, 2003). This aspect of non-Gaussian diffusion should therefore be negligible in biological tissue at moderate encoding strengths (Nilsson et al., 2010).

Time-dependent diffusivity is caused by an interaction between the geometry of the object and the time during which the diffusion is observed (Stejskal, 1965, Gore et al., 2010). For restricted diffusion, the ADC may therefore depend on the size of the restriction (d) and the diffusion time (t_{D}). In the regime where $t_{\mathrm{D}} \ll d^2/D_0$, the diffusing particles do not have time to experience the restriction, and the ADC approaches the intrinsic diffusivity (D_0) (Woessner, 1963). By contrast, when $t_{\mathrm{D}} \gg d^2/D_0$, the restrictions have been probed by most particles and the ADC approaches zero. For these two regimes, the approximation of Gaussian diffusion in each microenvironment holds. However, in the intermediate regime the ADC will be a function of t_{D} and d, and the diffusion must instead be described by a time-dependent diffusion tensor. A similar dependency exists for hindered diffusion, where the apparent diffusivity transitions from D_0 to a lower diffusivity defined by the tortuosity of the environment (Beck and Schultz, 1970). Several studies have demonstrated time-dependent diffusion in neural tissues (Stanisz et al., 1997, Assaf et al., 2000, Does et al., 2003, Assaf et al., 2008, Lundell et al., 2014, Burcaw et al., 2015), but the effect is probably small for the diffusion times commonly used in conventional experiments in vivo (Clark et al., 2001, Ronen et al., 2006, Nilsson et al., 2009, De Santis et al., 2016). Note that an in-depth investigation of the time dependency is outside the scope of this thesis; however, preliminary investigations indicate that the effect is small, at least in healthy tissue (Nilsson et al., 2016). We therefore assume that the DTD model is sufficiently accurate to capture the essentials of the diffusion characteristics in tissue, and acknowledge that this assumption must be validated in future studies.

3.4.2 Exchange

Diffusing particles may visit multiple microenvironments during the diffusion time by passing through permeable boundaries that separate the environments. Although exchange is always present to some degree, effects of exchange can be disregarded under three regimes. These are if the residence time (t_r) is much longer, or much shorter, than the diffusion time, $t_\mathrm{r} \ll t_\mathrm{D}$ or $t_\mathrm{r} \gg t_\mathrm{D}$, i.e. if very few particles have time to exchange or if the time spent in a specific environment is very short (Quirk et al., 2003); or if the diffusion characteristics of the two environments are approximately equal, in which case both environments are accurately described by a single diffusion tensor.

Effects of exchange have been investigated in the context of dMRI (Nilsson et al., 2013b), and several studies have indicated that the exchange in healthy brain tissue has a negligible effect on the diffusion-weighted signal for conventional diffusion times (Nilsson et al., 2013a, Lampinen et al., 2016). However, such assumptions may not hold in diseased tissue, where effects of exchange have been demonstrated (Lätt et al., 2009). In a preliminary study of the exchange rate in tumors, we observed relatively long residence times in the tissue (Lampinen et al., 2016). We therefore assume that exchange has a negligible effect in both healthy tissue and tumor tissue when using the experiments presented in this thesis.

4 Tensor-valued diffusion encoding and the forward signal model

In this chapter, we assume that the diffusion tensor distribution is known, and that it perfectly describes the diffusion within a sample. Based on this, the MR signal can be predicted for a given set of experimental parameters. This constitutes the "forward signal model" and we will use it to explain how tensor-valued diffusion encoding modulates the observed signal and how the diffusion tensor distribution can be interpreted in terms of its distribution of apparent diffusion coefficients.

4.1 Tensor-valued diffusion encoding

Conventional diffusion encoding gradients are applied along a single direction described by a vector ($\mathbf{n} = [n_\mathrm{x}\ n_\mathrm{y}\ n_\mathrm{z}]^\mathrm{T}$, $|\mathbf{n}| = 1$) and yield a specified encoding strength (b) along that direction. In such experiments, the diffusion encoding tensor, or b-tensor ($\mathbf{B}$), is given by $\mathbf{B} = b \cdot \mathbf{n}\mathbf{n}^\mathrm{T}$, where $\mathbf{B}$ is a tensor with one non-zero eigenvalue (order-two tensor of rank one). Diffusion encoding may also be applied in multiple directions within the same acquisition, between the excitation and readout, and can therefore render b-tensors with arbitrary configurations of positive eigenvalues, up to rank three. We refer to such encoding as "tensor-valued" to distinguish it from encoding that can be described with a vector. To distinguish the most common b-tensors, we refer to encoding with one non-zero eigenvalue as linear tensor encoding (LTE); two equal and non-zero eigenvalues as planar tensor encoding (PTE); and three equal eigenvalues as spherical tensor encoding (STE) (Westin et al., 2016a). STE is also known as isotropic encoding, and trace-weighted encoding (Mori and van Zijl, 1995, Wong et al., 1995, Eriksson et al., 2013).

The b-tensor can be derived for a time-dependent gradient waveform, $\mathbf{g}(t) = [g_{\mathrm{x}}(t)\ g_{\mathrm{y}}(t)\ g_{\mathrm{z}}(t)]^{\mathrm{T}}$, by first considering the spin dephasing q-vector ($\mathbf{q}$), defined as

$$\mathbf{q}(t) = \gamma \int_0^{\mathrm{TE}} \mathbf{g}(t')\ \mathrm{d}t' \ , \qquad \text{Eq. 14}$$

where γ is the gyromagnetic ratio and TE is the echo time. The b-tensor is then calculated from the q-trajectory according to

$$\mathbf{B} = \int_0^{\mathrm{TE}} \mathbf{q}(t)\mathbf{q}^{\mathrm{T}}(t)\,\mathrm{d}t \ . \qquad \text{Eq. 15}$$

To simplify the analysis, only axisymmetric b-tensors are considered in this thesis. Axisymmetric tensors are defined by two eigenvalues and can be expressed in terms of the axial ($b_{\parallel}$) and radial ($b_{\perp}$) eigenvalues in the principal axis system, according to

$$\mathbf{B}_{\mathrm{PAS}} = \begin{pmatrix} b_{\parallel} & 0 & 0 \\ 0 & b_{\perp} & 0 \\ 0 & 0 & b_{\perp} \end{pmatrix} . \qquad \text{Eq. 16}$$

Three specific features of the b-tensor can now be defined, namely its orientation, size, and anisotropy. The orientation of the b-tensor is used to describe rotations of $\mathbf{B}_{\mathrm{PAS}}$ along arbitrary directions, so that the applied b-tensor is given by

$$\mathbf{B} = \mathbf{R}\ \mathbf{B}_{\mathrm{PAS}}\ \mathbf{R}^{\mathrm{T}} \ , \qquad \text{Eq. 17}$$

where $\mathbf{R}$ is a rotation matrix (Kingsley, 2006b). The size of the b-tensor describes the diffusion encoding strength, often referred to as the b-value, and is defined as the trace of $\mathbf{B}$, according to

$$b = \mathrm{Tr}(\mathbf{B}) \ . \qquad \text{Eq. 18}$$

The anisotropy of the b-tensor (b_{Δ}) is described by a scalar value, according to (Eriksson et al., 2015)

$$b_{\Delta} = \frac{b_{\parallel} - b_{\perp}}{b_{\parallel} + 2 \cdot b_{\perp}} \ . \qquad \text{Eq. 19}$$

The b-tensor anisotropy can take on values between –0.5 and 1. For planar, spherical, and linear tensor encoding it is –0.5, 0, and 1, respectively. Examples of encoding tensors with variable anisotropy, along with corresponding $\mathbf{g}(t)$ and $\mathbf{q}(t)$, are depicted in Paper IV.

Previously, the b-tensor has also been used to, for example, account for cross terms between diffusion encoding and imaging gradients (Mattiello et al., 1997) and for rotating the encoding direction to match the image space (Leemans and Jones, 2009). It was first used to describe tensor-valued diffusion encoding with a user-defined shape by Westin et al. (2014).

It is sometimes useful to consider the encoding tensor independently of its size. Thus, we construct the normalized encoding tensor ($\mathbf{N}$), which only carries information on its orientation and anisotropy, according to

$$\mathbf{N} = \frac{\mathbf{B}}{\mathrm{Tr}(\mathbf{B})} \, . \qquad \text{Eq. 20}$$

In conclusion, the temporal profile of the applied gradient renders a q-vector trajectory, which in turn determines the b-tensor. Several different waveform can yield the same b-tensor, but some waveforms are more experimentally tractable, as discussed in section 6.1.

4.2 Distribution of apparent diffusion coefficients

For a single diffusion tensor, the apparent diffusion coefficient ($\langle D \rangle$) along a direction specified by $\mathbf{N}$ is given by $\langle D \rangle = \mathbf{N} : \langle \mathbf{D} \rangle$. Likewise, each tensor in a DTD contributes a specific diffusivity to the one-dimensional distribution of apparent diffusion coefficients (D), according to

$$D = \mathbf{N} : \mathbf{D} \, . \qquad \text{Eq. 21}$$

Similar to the DTD in Eq. 2, the DDC can be represented by a continuous probability density function ($P(D)$) such that the probability (p) of finding a diffusivity in the interval $[a, b]$ is

$$p(a \leq D \leq b) = \int_a^b P(D|b_\Delta, \mathbf{R}) \, \mathrm{d}D \, , \qquad \text{Eq. 22}$$

where $P(D|b_\Delta, \mathbf{R})$ reads as the observed DDC given a b-tensor anisotropy b_Δ, and orientation $\mathbf{R}$. In the general case, the DDC depends on the rotation of the b-tensor, as indicated by $\mathbf{R}$ in Eq. 22. Rotationally invariant parameters can be derived from the so-called "powder sample". Powder samples are used in X-ray diffraction and solid-state NMR, and are created by crushing the sample into a powder in order to

remove any orientation coherence in the material investigated (Edén, 2003, Topgaard, 2016a). The DDC in a powder sample ($\bar{P}(D)$) is defined as

$$\bar{P}(D|b_\Delta) = \frac{1}{4\pi}\int_{S^2} P(D|b_\Delta, \mathbf{R}(\Omega))\,\mathrm{d}\Omega\ , \qquad \text{Eq. 23}$$

where the integration is over the surface of the unit sphere (Edén and Levitt, 1998). Note that $\bar{P}(D|b_\Delta)$ is rotationally invariant, i.e. independent of $\mathbf{R}$, but that it retains its dependency on the b-tensor anisotropy, b_Δ. From this point on, we will assume that we have a powder sample in order to abbreviate the theory. Of course, in vivo experiments cannot assume a true powder sample. Instead, a powder sample can be approximated by performing so-called "powder averaging" (Paper II, III, and V), where rotation invariance is achieved by averaging the diffusion-weighted signal over a finite number of encoding directions, as described in section 5.3.1.

4.3 Forward signal model

Assuming that the distribution of apparent diffusion coefficients in a powder sample is known, the powder signal ($\bar{S}$) is given by

$$\bar{S}(b, b_\Delta) = S_0 \int_{-\infty}^{\infty} \bar{P}(D|b_\Delta)\exp(-b\cdot D)\,\mathrm{d}D\ , \qquad \text{Eq. 24}$$

where the signal depends on the encoding strength and anisotropy, i.e. b and b_Δ, but is independent of the orientation of the object and the b-tensor. Importantly, the normalized signal $\bar{S}(b, b_\Delta)/S_0$ is the Laplace transform of $\bar{P}(D|b_\Delta)$, which is central to the parameter estimation described in Chapter 5. By analogy with Eq. 24, the signal can also be derived directly from the distribution of diffusion tensors, according to

$$S(\mathbf{B}) = S_0 \int P(\mathbf{D})\exp(-\mathbf{B}\colon\mathbf{D})\,\mathrm{d}\mathbf{D}\ , \qquad \text{Eq. 25}$$

but we will use the formalism in Eq. 24 to simplify the theory.

4.4 Effect of b-tensor anisotropy

A central concept of this work is that the observed DDC depends on the anisotropy of the b-tensor. For a powder sample, the variance of the observed DDC (V_D) will be the sum of isotropic and anisotropic contributions, according to

$$V_D = V_{\mathrm{I}} + b_{\Delta}^2 \cdot V_{\mathrm{A}} \ , \qquad \text{Eq. 26}$$

where b_{Δ} is the anisotropy of the b-tensor (Eq. 19) (Paper II and III, Eriksson et al., 2015, Topgaard, 2016a). When using a combination of STE and LTE, V_D is equal to V_{I} and V_{T}, respectively (see section 3.3.2) (Paper II, III, and V). Notably, for methods that use only LTE, such as conventional DKI, $V_D = V_{\mathrm{T}}$, so that the two components are entangled. Therefore, the mean kurtosis from DKI is equivalent to $\mathrm{MK_T}$.

To understand why the DDC depends on the b-tensor anisotropy, we will briefly explore the interaction between the diffusion tensor distribution, the properties of the b-tensor, and the measured signal (Figure 5). Consider a large ensemble of randomly oriented anisotropic diffusion tensors that differ only with respect to orientation. For diffusion encoding along a single direction (LTE), each diffusion tensor will contribute a diffusivity to the DDC depending on its orientation relative to the b-tensor. Thus, the observed DDC contains diffusivities between the largest and smallest diffusion tensor eigenvalues. Since the DDC exhibits a substantial variance, the signal vs. b curve will be non-monoexponential. By contrast, for isotropic encoding (STE), all diffusion tensors contribute the same isotropic diffusivity to the DDC, and the DDC becomes a narrow peak centered on the mean diffusivity. The DDC now exhibits a vanishing variance and the signal is mono-exponential.

A DTD that contains only isotropic tensors with variable diffusivities, will also exhibit a DDC with high variance, and therefore a non-monoexponential signal vs b curve. However, each tensor in the distribution is isotropic, and therefore contributes a diffusivity to the DDC that is independent of the orientation and anisotropy of the b-tensor. Thus, the DDC and the signal will be unaffected by the b-tensor anisotropy. The hallmark of isotropic diffusional variance is that it is independent of the b-tensor shape.

Given that we use only one b-tensor anisotropy – be it conventional LTE or otherwise – the DDC from isotropic diffusion tensors may exactly match the DDC from anisotropic tensors. Therefore, it is theoretically impossible to distinguish the sources of diffusional variance if only one b-tensor anisotropy is used (Mitra, 1995).

This is also communicated by Eq. 26, where it is obvious that two observations of V_D with different b_Δ^2 are required to resolve V_I and V_A.

In summary, the hallmarks of anisotropic and isotropic diffusional variance are that the former renders signal that depends on the b-tensor anisotropy, whereas the latter does not. The two can therefore be separated by observing the signal at variable b-tensor anisotropy.

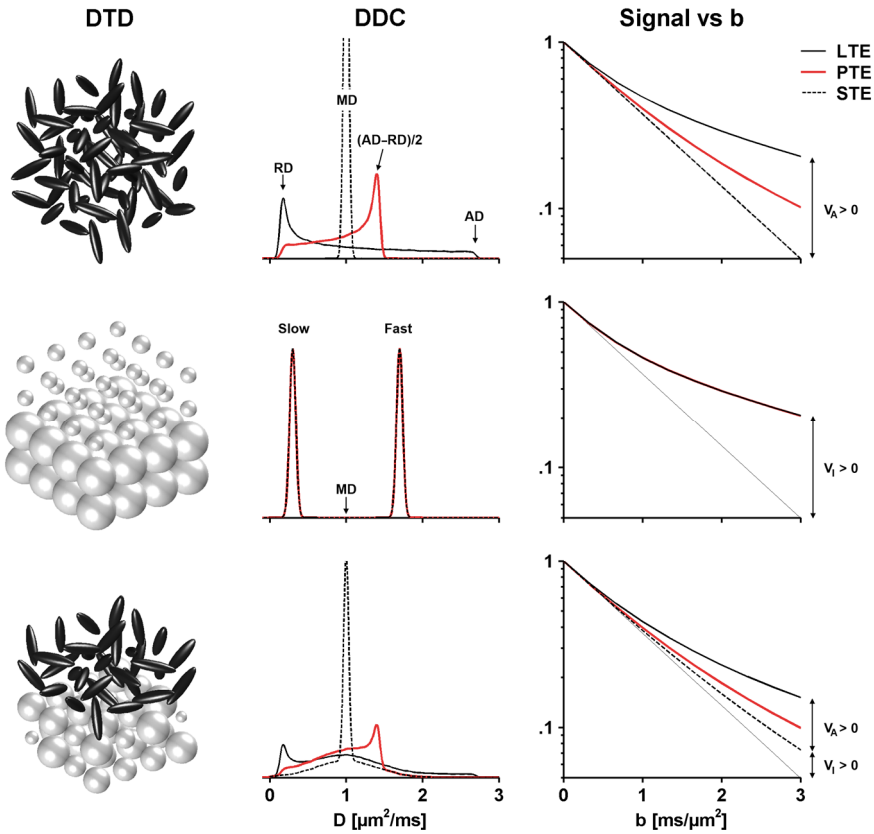

Figure 5 | The relation between the diffusion tensor distributions (DTD), distribution of apparent diffusion coefficients (DDC), and the diffusion-weighted signal vs b. The three systems represent randomly oriented anisotropic diffusion tensors (top); a mixture of isotropic tensors with slow and fast diffusivity (middle); and a mixture of randomly oriented anisotropic tensors and isotropic tensors with heterogeneous diffusivity (bottom). The central column depicts the DDC (y-axis is the probability density) when using linear, planar, and spherical tensor encoding (LTE, PTE, and STE). The peaks in the first DDC are marked out in terms of corresponding axial and radial tensor components (2.8 and 0.1 μm^2/ms). In the second DDC, the peaks are denoted slow and fast (0.3 and 1.7 μm^2/ms). The right-hand column shows the signal observed in each case. The LTE signal is the same in the first two systems. When using PTE or STE in the first system, the signal exhibits less curvature, which indicates diffusion anisotropy. By contrast, the b-tensor anisotropy has no effect on the signal in the second system with purely isotropic diffusion tensors. In the third system, both types of diffusional variance are present.

5 Parameter estimation and the inverse problem

At this point we have established that diffusion in tissue can be described by a distribution of diffusion tensors, which allows us to predict the MR signal for any b-tensor. However, the distribution of diffusion tensors is usually unknown. Instead, we must solve the "inverse problem", i.e. work backwards from the observed signal to infer relevant characteristics of the diffusion tensor distribution and the tissue. This is achieved by modeling the relationship between the observed signal and the underlying diffusion process. The specifics of the model may be motivated by practical, empirical, biophysical, or statistical considerations. Regardless of this, the model is unlikely to capture all details of the tissue, and limited sampling of noisy MR signal may not retain information on subtle features of tissue (Novikov and Kiselev, 2010). This limitation is not unique to any specific approach or model, but is rather a ubiquitous fact in dMRI. This chapter describes the limitations inherent in the inverse problem – and how these pertain to the estimation of diffusional variance.

5.1 Inverse Laplace transform

Apart from the b-tensor, the diffusion-weighted MR signal depends on the DDC, according to Eq. 24. In fact, the normalized signal ($\bar{S}(b)/S_0$) is the Laplace transform of the underlying distribution $\bar{P}(D|b_\Delta)$. Thus, the inverse Laplace transform (ILT) would in theory recover the DDC directly from the signal without any prior assumptions (Whittall and Mackay, 1989). However, numerical ILT methods are mathematically ill-conditioned and sensitive to noise (Håkansson et al., 2000, Epstein and Schotland, 2008). Furthermore, the numerical ILT approach probably requires the signal to be densely sampled in a wide range of b-values (Ronen et al.,

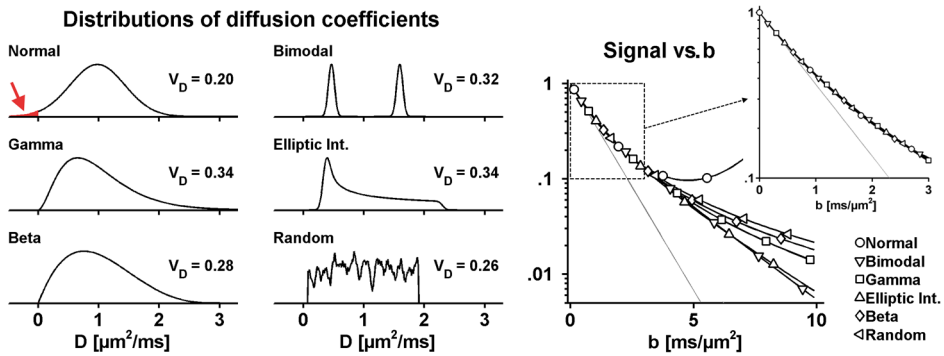

Figure 6 | Six DDCs that yield similar diffusion-weighted signal. The signal was calculated from Eq. 24 using MD = 1.0 μm²/ms and V_D between 0.20 and 0.34 μm⁴/ms². All DDCs render similar signal curves for moderate diffusion encoding strengths (b < 3 ms/μm²). At strong diffusion encoding (up to b = 10 ms/μm²), the signal curves diverge—especially the normal distribution since it contains negative diffusivity values (red arrow). Note that the maximal signal difference for the remaining distributions is approximately 2% at b = 10 ms/μm². The DDC denoted "elliptic integral" is the distribution observed for randomly oriented diffusion tensors with λ_i = [2.3 0.35 0.35] μm²/ms (VanderHart and Gutowsky, 1968). The straight gray line shows monoexponential signal decay for visual reference.

2006), or prior information that can be used to constrain the inversion (de Almeida Martins and Topgaard, 2016).

The problematic nature of the ILT can be understood by considering that there exist many DDCs that render virtually identical diffusion-weighted signals for a given interval of b-values (Figure 6) (Provencher, 1982). We therefore conclude that the DDC cannot be accurately recovered from a finite number of noisy signal samples unless prior knowledge about the underlying tissue can be used to constrain the inversion. Naturally, we must consider what constraints are reasonable, and we explore two alternatives below.

5.2 Truncated cumulant expansion

The diffusion-weighted signal in Eq. 24 can be described by an expansion of the normalized signal in powers of b. This expansion expresses the signal as a sum of cumulants (c) and is equivalent to the Taylor expansion of the logarithm of the signal, according to

$$\ln\left(\bar{S}(b)/S_0\right) = \sum_{n=1}^{\infty} \frac{(-b)^n}{n!} \cdot c_n \ , \qquad \text{Eq. 27}$$

where c_n is the n^{th} cumulant of $\bar{P}(D|b_\Delta)$ according to

$$
\begin{aligned}
c_1 &= \langle D \rangle \\
c_2 &= \langle D^2 \rangle - \langle D \rangle^2 \\
c_3 &= 2\langle D^3 \rangle - 3\langle D \rangle \langle D^2 \rangle + \langle D \rangle^3 \\
c_4 &= -6\langle D^4 \rangle + 12\langle D^2 \rangle \langle D \rangle^2 - 3\langle D^2 \rangle^2 - 4\langle D \rangle \langle D^3 \rangle + \langle D \rangle^4 \\
&\vdots \\
c_n &= \cdots
\end{aligned}
\qquad \text{Eq. 28}
$$

where $\langle D^n \rangle$ is the n^{th} raw moment of $\bar{P}(D|b_\Delta)$, according to

$$
\langle D^n \rangle = \int_{-\infty}^{\infty} D^n \cdot \bar{P}(D|b_\Delta)\, \mathrm{d}D \; . \qquad \text{Eq. 29}
$$

The first four cumulants of $\bar{P}(D|b_\Delta)$ are its expected value, variance, skewness, and kurtosis. Although it is possible to truncate the series in Eq. 27 at an arbitrary cumulant and fit it to the signal, the accuracy of the parameter estimation will decrease rapidly as the number of cumulants increases (Kiselev, 2011), and for data in a limited b-interval the fit will be degenerate, meaning that multiple sets of parameters will yield equally good fits (Kiselev and Il'yasov, 2007). Thus, the expansion is commonly truncated at one or two cumulants to capture the main features of the signal for moderate encoding strengths, where the most prominent features of $\ln\big(\bar{S}(b)/S_0\big)$ are its initial slope and curvature.

Although the cumulant expansion is usually considered to be "model-free", it features implicit assumptions due to the truncation. For example, when Eq. 27 is truncated at the first cumulant, $\bar{P}(D|b_\Delta)$ is implicitly assumed to be a delta function described only by its expected value ($c_n = 0$ for $n \geq 2$). The normalized signal model has a single degree of freedom and becomes an exponential function, $\bar{S}(b)/S_0 \approx \exp(-b\langle D \rangle)$. This is the basis for the signal model used in DWI and DTI, and it holds in homogeneous tissues (Kiselev and Il'yasov, 2007) and at low b-values (Jensen, 2014). If the second cumulant is also included, $\bar{P}(D|b_\Delta)$ is implicitly assumed to be a normal distribution defined by its expected value and variance ($c_n = 0$ for $n \geq 3$). In this case, the normalized signal model has two degrees of freedom and is given by $\bar{S}(b)/S_0 \approx \exp(-b\langle D \rangle + 1/2b^2 V_D)$, which is, in essence, the signal model used in DKI (Jensen et al., 2005).

The fact that a truncation at the second cumulant assumes a Gaussian DDC has several implications. First, the logarithm of the signal becomes a positive quadratic polynomial, and is therefore not monotonically decreasing, which yields non-physical signal behavior where the signal increases as a function of b-value for $b > \langle D \rangle / V_D$ (Figure 6) (Jensen and Helpern, 2010). Secondly, the interpretation of the cumulants as the mean and variance of $\bar{P}(D|b_\Delta)$ are only accurate if the contribution from

higher-order cumulants is negligible. It can be shown, however, that several realistic distributions have relatively large higher-order cumulants. For example, in anisotropic tissue described by randomly oriented tensors with $\lambda_i \approx [2.3\ 0.3\ 0.3]$ $\mu m^2/ms$, the first four cumulants are 1.0, 0.34, 0.12, and –0.11 in units of $(\mu m^2/ms)^n$ (see the DDC from the elliptic integral function in Figure 6). Although the signal in a moderate b-interval can be fitted with a second-order cumulant expansion, the estimated variance may be strongly biased. For example, the normal and elliptic integral DDCs have variances of 0.20 and 0.34 $\mu m^4/ms^2$, but yield virtually indistinguishable signal-versus-b curves for $b < 3$ $ms/\mu m^2$ (Figure 6).

In summary, the cumulant expansion is equivalent to a constrained ILT where the functional form of the underlying DDC is implicitly determined by the number of cumulants included in the model. In the next section, we consider an explicit selection of the DDC.

5.3 Gamma distribution model

The inverse Laplace transform can be constrained by assuming a specific functional form of $\bar{P}(D|b_\Delta)$. We may select any probability density function that has appropriate features to represent the DDC. A reasonable DDC should avoid negative probabilities (Kiselev, 2011), negative diffusivities (Figure 6), and promote physically feasible functions that are defined by few shape parameters (Yablonskiy and Sukstanskii, 2010).

A strong candidate that fulfills these requirements is the gamma distribution function. This distribution was mentioned as a plausible model for the DDC by Jensen and Helpern (2010), and Röding et al. (2012) showed that it was superior to signal models based on the log-normal distribution and the stretched exponential. The gamma distribution function renders a probability density function (P_Γ) that is defined by two shape parameters, which can be interpreted in terms of its expected value and variance, given by

$$P_\Gamma(D) = k \cdot D^{\left(\frac{\langle D\rangle^2}{V_D}-1\right)} \cdot \exp\left(-D \cdot \frac{\langle D\rangle}{V_D}\right), \qquad \text{Eq. 30}$$

where $P_\Gamma(D<0) = 0$, $\langle D\rangle > 0$, $V_D > 0$, and k scales the function so that $\int P_\Gamma(D)\,\mathrm{d}D = 1$. The Laplace transform of $P_\Gamma(D)$ defines the signal model, where the baseline signal, expected value, and variance are the free parameters, according to (Paper II, Jensen and Helpern, 2010)

$$S(b) = S_0 \cdot \left(1 + b \cdot \frac{V_D}{\langle D \rangle}\right)^{-\frac{\langle D \rangle^2}{V_D}} . \qquad \text{Eq. 31}$$

The most apparent benefit of using the gamma distribution, rather than the normal distribution derived from the cumulant expansion, is that $P_\Gamma(D)$ is zero for negative diffusivities, so that it does not predict increasing signal for high b-values (Figure 6). Furthermore, it can represent a wide range of plausible DDCs with only two degrees of freedom (Paper II, Röding et al., 2012, Röding et al., 2015). Of course, it is possible to select from many other plausible distributions (Yablonskiy and Sukstanskii, 2010), but investigation of their qualities was outside the scope of this thesis.

5.3.1 Invariant parameters from the powder averaged signal

As described in section 4.1, the shape of the DDC depends on the orientation and anisotropy of the b-tensor ($\mathbf{R}$ and b_Δ). To achieve a rotationally invariant parameterization of the signal, we mimic the characteristics of a powder sample by performing so-called powder averaging (Bak and Nielsen, 1997, Edén, 2003). The signal from a powder sample can be approximated by the powder-averaged signal ($\bar{S}$) across multiple diffusion encoding directions (Edén, 2003)

$$\bar{S}(b, b_\Delta) = \frac{1}{n_{\text{dir}}} \sum_{i=1}^{n_{\text{dir}}} S\left(b, b_\Delta, \mathbf{R}_i\right) , \qquad \text{Eq. 32}$$

where $\mathbf{R}_i$ indicates the i^{th} rotation of the b-tensor and n_{dir} is the total number of diffusion encoding directions. The powder-averaged signal has been employed in the quantification of diffusion anisotropy in several studies (Jespersen et al., 2013, Lawrenz and Finsterbusch, 2013) and it is also referred to as the "orientational average" (Edén and Levitt, 1998), the "spherical mean" (Kaden et al., 2015), and the "directional mean". The required directional resolution to render a rotationally invariant signal is discussed in more detail in section 6.2.1.

Fitting of Eq. 31 to the powder signal at varying b-tensor anisotropy yields

$$\bar{S}(b, b_\Delta) = S_0 \cdot \left(1 + b \cdot \frac{V_{\text{I}} + b_\Delta^2 \cdot V_{\text{A}}}{\text{MD}}\right)^{-\frac{\text{MD}^2}{V_{\text{I}} + b_\Delta^2 \cdot V_{\text{A}}}} , \qquad \text{Eq. 33}$$

where $\langle D \rangle = \text{MD}$ for a powder sample. The unknown variables $(S_0, \text{MD}, V_{\text{I}}, V_{\text{A}})$ in Eq. 33 can be estimated in a joint non-linear fitting of data if two or more b-tensor anisotropies are used.

We refer to the disentanglement of isotropic and anisotropic diffusional variance by multiple b-tensors as diffusional variance decomposition, or DIVIDE. Note that this expression is used to refer to a set of concepts concerning the decomposition of variance, rather than a specific set of methods.

5.3.2 Examples of parameter maps in phantoms and in vivo

In Paper II, we performed initial parameter validation by quantifying the diffusional characteristics in a phantom where the structure was known. The phantom was composed of two coaxial tubes where the inner tube contained a lamellar liquid crystal (LC), in which the water movement is restricted between sheet-like bilayers (Callaghan and Soderman, 1983). The outer tube contained a yeast suspension, where the water was either restricted to the inside of near spherical cells or hindered in the extracellular space (Tanner and Stejskal, 1968). Figure 7 shows that the lamellar crystal exhibited a homogeneous microscopic anisotropy (MK_A). The voxel-scale anisotropy (FA) was high in regions where the crystals were ordered (Le et al., 2001) and low where it was disordered. The yeast suspension showed negligible anisotropy on the voxel and microscopic scales. On the other hand, it showed a high isotropic diffusional variance (MK_I) due to the mixture of restricted and hindered compartments.

Parameter maps of a healthy brain were first reported in Paper III, and representative examples based on the protocols suggested in Paper VI are shown in Figure 8. In the white matter, the MK_A predominates, which can also be seen as a high μFA. MK_I is non-zero across the brain, and is especially high at the interface between brain matter and corticospinal fluid. The FA and μFA are markedly different in that the μFA is relatively homogeneous and high in the white matter whereas the FA is high only in regions that are known to contain large and well-ordered white matter pathways. The DIVIDE parameters in brain tissue are discussed further in Chapter 7.

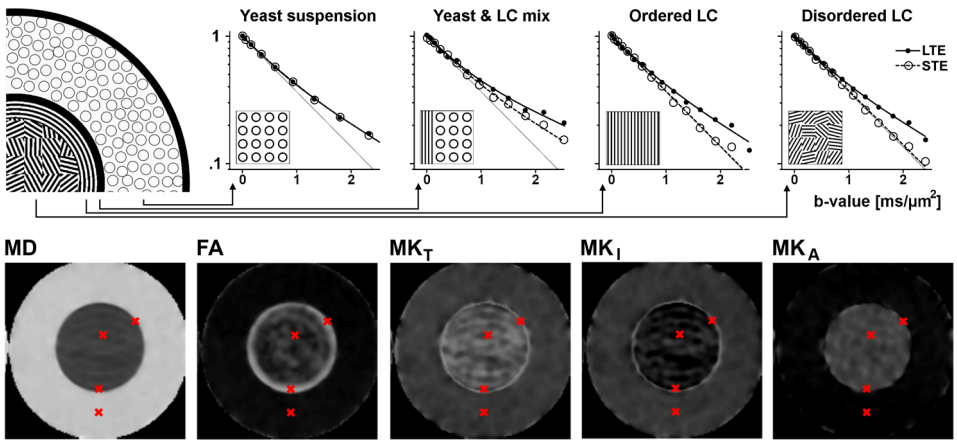

Figure 7 | Parameterization of diffusion characteristics in a phantom at an NMR system. The top row shows the powder averaged signal and the gamma model fit from four locations in the phantom (red crosses). The yeast suspension shows a high diffusivity and no anisotropy. Furthermore, it shows a high degree of diffusional variance, caused exclusively by isotropic diffusional variance (MK_T and MK_I are high, and MK_A is low). The liquid crystals exhibit a homogeneous MD and variable FA, where the FA is high close to the inner tube wall where the crystal bilayers are aligned with the surface of the glass tube (Le et al., 2001). Although the FA is low in the central parts of the crystal, the MK_A shows that the microscopic anisotropy is homogeneous across the LC, and independent of orientation coherence. The figure was adapted, with permission, from Paper II by Lasič et al. (2014), published by Frontiers.

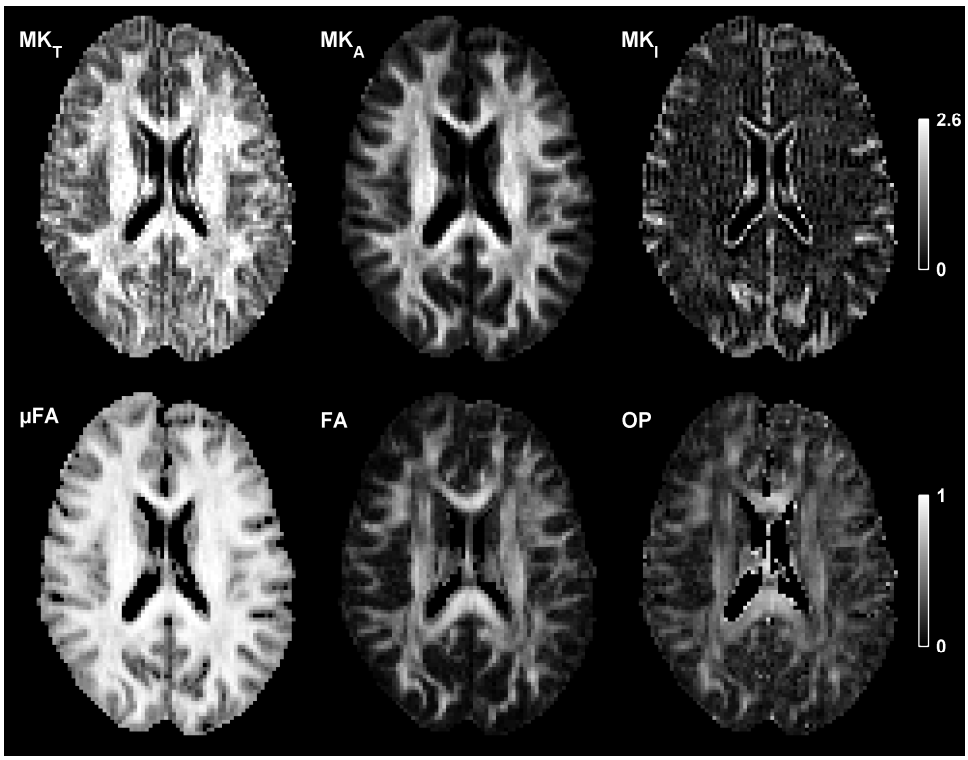

Figure 8 | Parameter maps in an axial slice of a healthy brain. The anisotropic variance is high in regions that contain white matter. The isotropic variance is generally low in brain tissue, and high in regions that interface with cerebrospinal fluid due to partial volume effects. The μFA and FA differ mostly in regions of crossing white matter, and in the gray matter. The data were acquired using the protocols used in Paper VI at a spatial resolution of 2×2×4 mm^3 on a 3 T system with 80-mT/m gradients.

6 Waveform, protocol, and study design

As described in Chapter 4, the diffusional variance components can only be separated if b-tensors with more than one anisotropy are used. The design and implementation of experiments that achieve this depend on a wide range of theoretical and practical considerations. In this chapter, we consider the experimental design at three levels. First, we describe how q-space trajectory encoding is implemented and consider several aspects of gradient waveform optimization. Secondly, we describe how to design the signal sampling protocol to allow for an accurate decomposition of the diffusional variance. Third, we discuss the statistical precision of the estimated parameters and their impact on group-based inferential statistics.

6.1 Waveform design

6.1.1 Q-space trajectory encoding in a spin-echo sequence

In order to explore non-conventional diffusion encoding waveforms, we developed an in-house sequence that allows us to freely specify gradient waveforms to be executed on the scanner. These waveforms can be designed to yield specific trajectories through the q-space, and we therefore refer to the method as q-space trajectory encoding (Paper II, Westin et al., 2016a). For simplicity, and for its clinical relevance, we assume that the QTE is performed within a spin-echo with echo-planar imaging (EPI) readout, although other sequences are also possible (Eriksson et al., 2015, de Almeida Martins and Topgaard, 2016).

The spin-echo sequence has three basic components: excitation, refocusing, and readout (Figure 9). The excitation and refocusing blocks are combinations of radio-frequency pulses and slice selection gradients. The refocusing block also includes

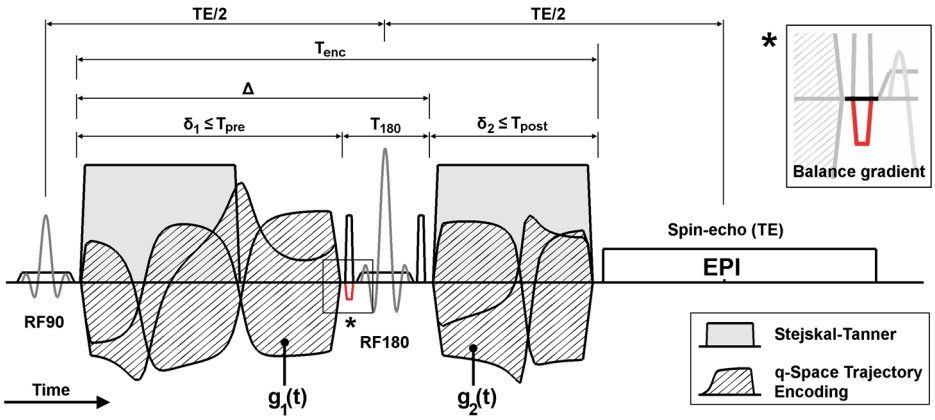

Figure 9 | Schematic spin-echo sequence and its timing variables. The gradient waveforms $\mathbf{g}_1(t)$ and $\mathbf{g}_2(t)$ are executed between the excitation pulse (RF90), the refocusing pulse (RF180), and echo-planar readout (EPI). The timing variables show the maximal time available for encoding (T_{pre} and T_{post}), the duration of each gradient waveform (δ_1 and δ_2), the gradient waveform separation (Δ), the duration of the refocusing block including the crushers (T_{180}), the total encoding time (T_{enc}), and the echo time (TE). The balance gradient (red) is executed at the same time as the first crusher. Note that the Stejskal-Tanner and q-space trajectory encoding gradients are shown together for visual reference, and are not executed simultaneously.

crusher gradients. The EPI readout is centered on the echo time (TE), and can occupy a significant time before and after TE. The diffusion encoding gradient waveforms ($\mathbf{g}_1(t)$ and $\mathbf{g}_2(t)$, see section 4.1) are inserted between these blocks, and the timing is therefore primarily determined by the TE and the duration of each block, as described in Figure 9. Notably, the maximal duration of the encoding after the refocusing pulse is often reduced by the presence of the readout block, referred to as "asymmetric sequence timing". In general, it is beneficial to minimize TE to reduce loss of signal due to transverse relaxation. However, a shorter TE will incur a limitation on the maximal b-value, so there is a trade-off between SNR and encoding strength.

The first implementation of QTE on a clinical MRI system was presented in Paper II, where it was used to yield isotropic diffusion encoding (STE) to estimate the μFA in a phantom. Subsequently, it was employed in vivo to investigate healthy tissue (Paper III) and tumor tissue (Paper V). These studies used magic-angle spinning of the q-vector (qMAS) (Eriksson et al., 2013) to produce STE. We have also used the sequence to render LTE, PTE, and STE in a study of patients with schizophrenia (Westin et al., 2016a). Of course, the QTE sequence can also render trapezoidal waveforms, such as those proposed by Cory et al. (1990), Wong et al. (1995), Mori and van Zijl (1995), and Moffat et al. (2004).

6.1.2 Considerations for waveform design and optimization

In conventional diffusion encoding, the optimization of the gradient waveform is trivial because the maximal b-value for a given encoding time is achieved by maximizing the duration, amplitude, and separation of two identical trapezoid waveforms (Stejskal and Tanner, 1965, Jones et al., 1999). The same is not true for QTE, where the waveform optimization must take into account the prescribed b-tensor shape, and in the case of asymmetric waveforms, the timing asymmetry.

In Paper IV, we presented a method that uses numerical optimization to render waveforms that yield specific b-tensors while respecting limitations imposed by the maximal gradient amplitude, slew rate, energy consumption, and heating. It also allows the user to specify an arbitrary timing of the encoding periods, i.e. the waveform can be designed so that $\delta_1 = T_{\text{pre}}$ and $\delta_2 = T_{\text{post}}$, to take advantage of all available time for encoding (Figure 9). Several factors that influence the design and validity of gradient waveforms for diffusion encoding are discussed below.

6.1.2.1 Gradient amplitude and slew rate

The performance of the gradient system is a vital consideration for the design of a waveform. From Eqs. 14 and 15, we see that $b \propto |\mathbf{g}|^2$, meaning that a gradient system with twice the maximal gradient amplitude can produce four times as strong diffusion encoding. However, the system performance is also limited by the maximal gradient slew rate. This is especially noticeable for short encoding times, where the gradients may never reach their maximal amplitude due to relatively low slew rates compared to the maximal gradient amplitude. The slew rate limitation is most pronounced for PTE and STE, since these are rendered by waveforms that exhibit several transitions between negative and positive gradient amplitudes.

Figure 10 shows the maximal b-values attainable for LTE, PTE, and STE using various waveform designs at maximal gradient amplitudes of 40 and 80 mT/m. The numerically optimized waveforms, denoted "Sjölund" (Paper IV), outperform previous waveform designs.

Of considerable importance is also the risk of causing peripheral nerve stimulation (PNS) (Ham et al., 1997). PNS can be effectively avoided by limiting the slew rate, but such an approach may reduce the encoding efficiency. Alternatively, the risk for PNS can be predicted by a model so that an appropriate waveform may be designed. For example, this could be achieved with the "SAFE" model suggested by Hebrank and Gebhardt (2000).

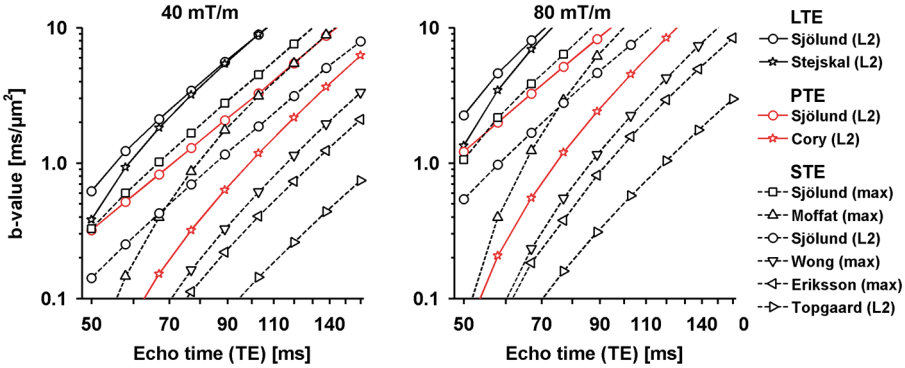

Figure 10 | Maximal b-values for LTE (black lines), PTE (red lines), and STE (dashed lines) for echo times between 50 and 160 ms at 40 and 80 mT/m. The optimization norm of each waveform is denoted in parenthesis at the end of its name where "max" indicates that the waveforms cannot be rotated arbitrarily without incurring a severe performance penalty (see section 6.1.2.2). The b-values are calculated assuming an asymmetric sequence timing (T_{post} is 12 ms shorter than T_{pre}) with a constant gradient-off time of T_{180} = 8 ms, and a maximal slew rate of 100 T/m/s. The most efficient waveforms are the numerically optimized waveforms by Sjölund et al. (2015) (Paper IV). For long echo times, the numerically optimized LTE waveform is only marginally better than the Stejskal-Tanner sequence. The original waveform designs can be found in the following references: Stejskal and Tanner (1965) (SDE), Sjölund et al. (2015) (Paper IV), Eriksson et al. (2013) (qMAS), Topgaard (2016b), Cory et al. (1990) (DDE), Moffat et al. (2004), and Wong et al. (1995).

6.1.2.2 Waveform norm and rotations

It is possible to combine multiple gradient axes to produce gradient strengths beyond the capacity of a single axis. This can be exploited in the design of the waveform where the gradient trajectory can be limited by either the "max-norm"

$$g_{\mathrm{x}}^2 \leq g_{\mathrm{max}}^2 \ , \quad g_{\mathrm{y}}^2 \leq g_{\mathrm{max}}^2 \ , \quad g_{\mathrm{z}}^2 \leq g_{\mathrm{max}}^2 \ , \qquad \text{Eq. 34}$$

or the "L2-norm"

$$g_{\mathrm{x}}^2 + g_{\mathrm{y}}^2 + g_{\mathrm{z}}^2 \leq g_{\mathrm{max}}^2 \ , \qquad \text{Eq. 35}$$

where g_{max} is the maximal gradient amplitude along each axis. These limitations can be seen as constraining the gradients within a cube with a side of $2g_{\mathrm{max}}$ or a sphere with a diameter of $2g_{\mathrm{max}}$, respectively.

The benefit of using the max-norm is that it takes advantage of the combined strength of multiple gradient axes and can therefore yield a higher encoding efficiency (Figure 10). The drawback is that the waveform cannot be rotated along arbitrary directions without violating the gradient amplitude limit. Experiments that demand arbitrary rotations of the b-matrix should therefore be based on waveforms that are constrained to the L2-norm, whereas experiments that demand very few, or no, rotations may benefit from the max-norm. The number of rotations that is required depends on the underlying tissue (Paper VI), as described in section 6.2.1.

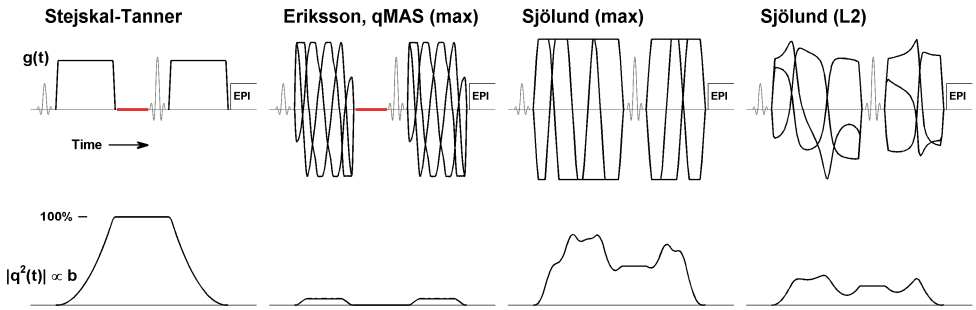

Figure 11 | The top row shows gradient waveforms in a spin-echo sequence with EPI readout. The bottom row shows the magnitude of the squared q-vector, which is proportional to the b-value (see section 4.1), normalized to Stejskal-Tanner encoding to provide a visual cue that reflects their efficiency. Symmetric waveforms (e.g. Stejskal-Tanner and qMAS) do not take advantage of all available encoding time (red lines show interval where gradients are off). Waveforms that return the q-vector to the origin during the refocusing pulse have low efficiency (de Swiet and Mitra, 1996). Asymetric waveforms can use all the encoding time available, which yields superior encoding efficiency (Figure 10). Furthermore, the max-norm employs stronger gradient combinations than the L2-norm, which improves the encoding efficiency. Note that the Stejskal-Tanner waveform renders LTE, whereas the remaining waveforms render STE.

6.1.2.3 Energy consumption and heating

The gradients produced by the MRI system are limited by the energy required by the amplifiers, and the heating of the hardware. Both aspects are factored into the duty cycle of the system, and should be considered and monitored during the design and execution of demanding dMRI experiments (Paper IV). The magnetic field gradient used for diffusion encoding is proportional to the current (I) applied through a coil. The dissipated power (P) is proportional to the square of the current, $P = I^2R \propto |\mathbf{g}|^2$, where R is the circuit resistance (Hidalgo-Tobon, 2010). This means that a doubling of the gradient amplitude will expend four times the energy. The electrical energy is stored in capacitors, which are continuously refilled by the mains power. However, if demanding waveforms are used in rapid succession, the capacitors may be depleted, or fail to recharge between acquisitions. Furthermore, it is possible to deposit more energy in the system than what can be removed by the cooling system, thereby causing net heating – which may affect the signal accuracy (Vos et al., 2016) or cause the system to overheat. Both energy consumption and heating can be mitigated by extending the encoding time so that lower gradient amplitudes can be used to yield a given encoding strength, albeit at a penalty to the SNR.

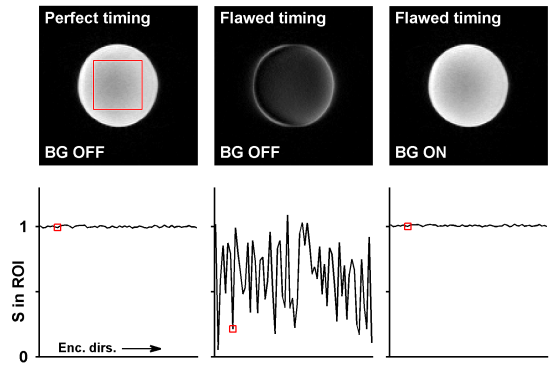

Figure 12 | The top row shows the signal in a water phantom using an asymmetrical waveform for LTE at b = 0.5 ms/μm^2. When the timing is perfect, the waveform is balanced (left). Flawed timing is achieved by extending the duration of the second waveform by 0.1 ms (0.3% of the total encoding time); the waveform is off-balance and gross image artifacts appear (middle). When the balance gradient is engaged, it automatically restores the balance and the signal for perfect timing is recovered (right). The bottom row shows the average signal in a central region of the phantom (red square) along 64 diffusion encoding directions.

6.1.2.4 Waveform symmetry and balance

To characterize some of the features associated with arbitrary waveforms, we use the concepts of waveform symmetry and balance. A waveform is "symmetric" if it is identical on both sides of the refocusing pulse, i.e. if $\mathbf{g}_1(t) = \mathbf{g}_2(t + \Delta)$, where Δ is the time between the onset of the two encoding waveforms (Figure 9). Asymmetric waveforms do not adhere to this rule and can be designed to occupy all available time on both sides of the refocusing pulse (Paper IV). Furthermore, asymmetric waveforms can be designed to encode along different directions before and after the refocusing pulse, whereas symmetric waveforms must repeat the same trajectory twice, which is less effective (Figure 11).

The balance of a waveform is determined by the 0$^{\text{th}}$ moment vector ($\boldsymbol{\mu} = [\mu_x\ \mu_y\ \mu_z]^{\mathrm{T}}$) of the gradient waveform, according to

$$\boldsymbol{\mu} = \gamma \int_{t_1}^{t_2} \mathbf{g}_1(t)\mathrm{d}t - \gamma \int_{t_3}^{t_4} \mathbf{g}_2(t)\mathrm{d}t \ , \qquad \text{Eq. 36}$$

where the integration limits are the beginning and end of each waveform. In order for the accumulated phase to be zero at the time of the spin-echo, the waveform must be designed such that $|\boldsymbol{\mu}| = 0$ (de Swiet and Mitra, 1996). A set of gradients that render $|\boldsymbol{\mu}| = 0$ is called "balanced", whereas $|\boldsymbol{\mu}| \neq 0$ is called "off-balance".

Small errors may be introduced when the waveform is resampled to match the prescribed duration and gradient system raster time. For symmetric waveforms, these errors cancel, and have no discernable effect. If the waveform is asymmetric, seemingly small imperfections may result in significant signal errors. However, timing and interpolation errors can be effectively mitigated by a balance gradient

(Figure 9). The balance gradient automatically negates the residual 0^{th} moment of the encoding gradients and restores the signal properties, as demonstrated in Figure 12.

Generally, asymmetric waveforms are robust to any linear scaling of the gradient amplitude. However, non-linear distortions of the gradient waveform – for example, caused by concomitant fields – may result in image artifacts and signal bias (Bernstein et al., 1998). However, for main magnetic fields above 1.5 T and gradient amplitudes below 300 mT/m, the effects of concomitant fields are negligible. Thus, no additional corrections were implemented in this work, although it is possible to do so in the imaging sequence and post-processing (Meier et al., 2008, Baron et al., 2012).

6.2 Protocol design

The imaging protocol, i.e. the signal sampling scheme, used for diffusional variance decomposition is similar to a multi-shell DKI acquisition in that it uses multiple encoding directions and encoding strengths (Poot et al., 2009, Jensen and Helpern, 2010). However, unlike DKI, it also uses b-tensors with varying anisotropy, and the analysis is based on the powder averaged signal. It therefore has many features in common with the protocol optimization used in DTI and DKI (Basser and Jones, 2002, Cook et al., 2007, Merisaari and Jambor, 2014), but is different enough to warrant a separate investigation of the proper design of the sampling protocol.

The initial implementation of QTE and DIVIDE was based on relatively inefficient waveforms that resulted in long echo times and low spatial resolution. The data was also over-sampled to allow closer inspection of signal characteristics, which limited the spatial coverage (Paper II, III, and V). In Paper VI, we explored the technical feasibility of whole-brain QTE and DVIDE at various MRI systems at clinically feasible times. The considerations pertaining to tissue characteristics and hardware performance are briefly described below.

6.2.1 Impact of tissue characteristics

The design of the protocol depends on the diffusional characteristics of the observed tissue. For example, the diffusivity determines the signal attenuation at a given encoding strength, and will therefore have an impact on the SNR (Jones and Basser, 2004). In Paper VI, we considered how the diffusivity and anisotropy of the tissue affected the assumption of Gaussian phase dispersion (see section 3.4.1) and the accuracy of the powder averaged signal. These considerations could be expressed in

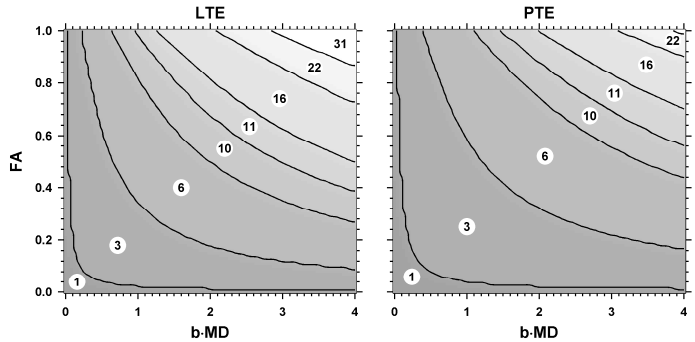

Figure 13 | The miniml number of diffusion encoding directions (n_{min}) required to yield a rotation invariant signal powder average (CV < 1%) for LTE and PTE (Paper VI). Each region is labeled with a circle that shows n_{min} for combinations of anisotropy (FA) and attenuation (b·MD). High anisotropy and attenuation both require more encoding directions. PTE requires fewer directions than LTE, and STE requires only one direction (data not shown).

terms of the maximal encoding strength that was employed, and the required number of diffusion encoding directions. Assuming that the signal should not be attenuated below 10% (Topgaard and Söderman, 2003), the diffusivity of the tissue determined the maximal encoding strength. On the other hand, the tissue anisotropy determined the required number of diffusion encoding directions to render a rotationally invariant signal powder average. As described in sections 4.2 and 5.3.1, the signal powder average is calculated as the average signal across multiple directions. For a finite number of diffusion encoding directions, the signal average across all directions depends on the orientation of the object. However, if the loss of precision due to rotation is negligible compared to the signal uncertainty caused by noise, the signal may be considered to be rotationally invariant. The minimum number of encoding directions for a given b-tensor anisotropy and tissue is then related to the anisotropy (FA) and level of signal attenuation ($b \cdot \mathrm{MD}$) (Paper VI, Szczepankiewicz et al., 2016b). As expected, increasing tissue anisotropy and encoding strength increases the demand on directional resolution, which is a well-known feature in high-angular-resolution dMRI (Frank, 2001, Tournier et al., 2013). Moreover, the directional resolution depends on the b-tensor anisotropy, where PTE requires fewer directions than LTE, and STE requires only one signal acquisition since it yields rotationally invariant signal per definition (Mori and van Zijl, 1995, Wong et al., 1995, Eriksson et al., 2013).

The practical implication of tailoring protocols to the characteristics of specific tissues is that different tissues require different protocols. For example, healthy white matter requires relatively high b-values and a high directional resolution, whereas weaker encoding and few directions are appropriate when investigating a glioma tumor (Paper V and VI).

6.2.2 Impact of static field strength and gradient system performance

The quality of dMRI data depends on both the main magnetic field strength and the gradient system performance (Polders et al, 2011, Setsompop et al, 2013). Thus, the design of a DIVIDE protocol should consider the MRI system performance. As detailed in Figure 10, higher gradient amplitude will render a given b-value at a shorter encoding time, which benefits the SNR and the sampling rate. Assuming high fields and disregarding relaxation, SNR is proportional to the main magnetic field. However, higher magnetic fields also reduce the transversal relaxation times (Stanisz et al., 2005, Uludag et al., 2009, Cox and Gowland, 2010), which counteracts the benefit of increased SNR at sufficiently long echo times. For example, for dMRI based on a spin-echo sequence in the brain, a move from a 3 T to a 7 T system is only motivated if the echo time can be kept below approximately 100 ms (Szczepankiewicz et al., 2016c).

Since the performance of gradient systems in the context of QTE is relatively unexplored, we investigated the feasibility of tensor-valued diffusion encoding with numerically optimized waveforms in systems with different gradient performance (33 to 80 mT/m) and main magnetic field strengths (1.5 to 7 T) (Paper IV). As expected, the gradient system performance was crucial to yield short echo times and high sampling rates. The resulting echo times ranged from 90 to 140 ms, and the resulting SNR maps for a spatial resolution of $2{\times}2{\times}4$ mm^3 at $b = 2$ ms/μm^2 can be seen in Figure 14. We estimate that sufficient SNR, i.e. SNR > 3 (Gudbjartsson and Patz, 1995), is achievable using a 1.5 T scanner with a 33 mT/m gradient system in the whole brain at a spatial resolution of approximately $2.5{\times}2.5{\times}4$ mm^3. For a 7 T system with 60 mT/m gradients, it is possible to achieve echo times below 100 ms, which indicates that DIVIDE based on QTE is also feasible at ultra-high field strengths (Paper VI, Szczepankiewicz et al., 2016c).

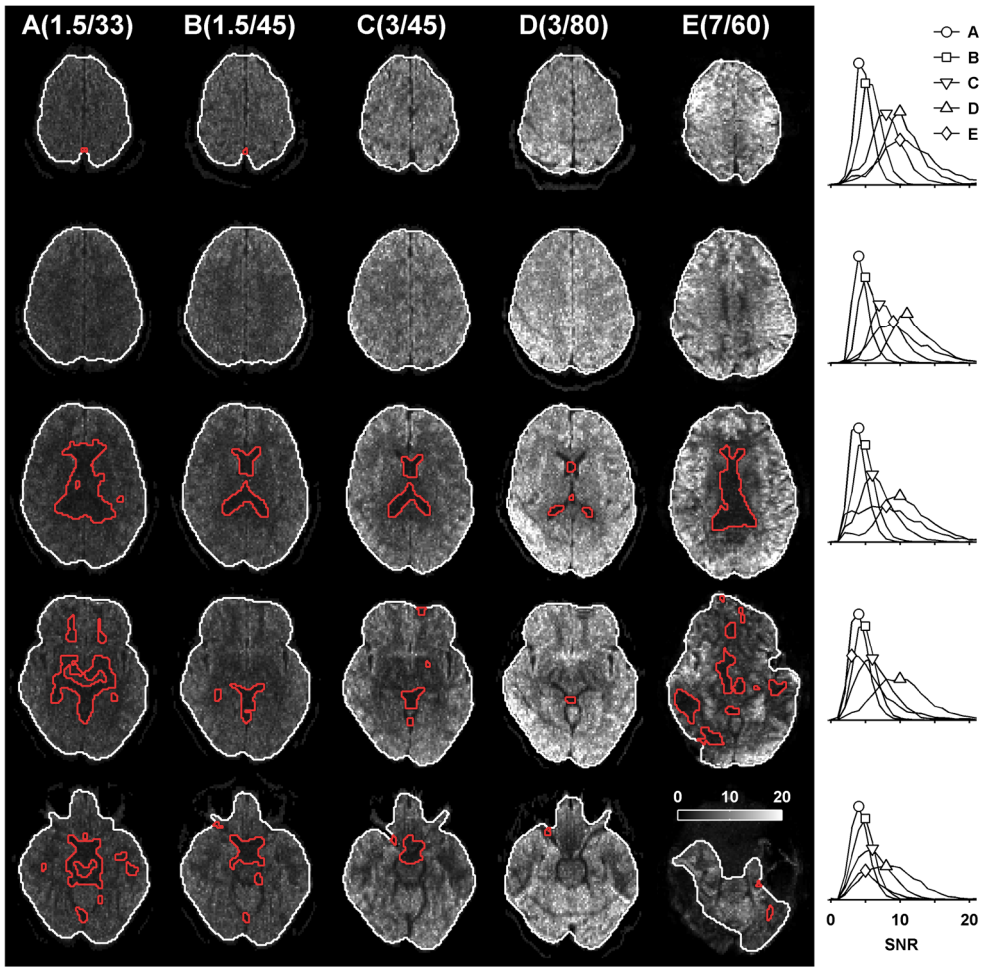

Figure 14 | Signal-to-noise ratio at b = 2 ms/μm^2 in a single healthy volunteer scanned with multiple MRI systems. The red outlines indicate regions where SNR < 3. The labels in parentheses state the main magnetic field strength and the maximal gradient amplitude in units of T and mT/m, respectively. The histograms show the voxel-wise SNR distributions within the white outlines. We note that the 7 T system showed poor signal homogeneity, likely due to RF inhomogeneity (Moser et al., 2012).

6.3 Study design

From a statistical point of view, the preparation, execution, and evaluation of a study may take many forms, and there are several publications to provide guidance on how to do so (Cohen, 1976, Strasak et al., 2007, Vandenbroucke et al., 2007). Here, we discuss the impact of parameter precision on the statistical power and sample size of a t-test, based on a hypothetical comparison of two independent samples.

6.3.1 Statistical power

The statistical power of a test describes the probability of correctly rejecting the null hypothesis. Although the analysis of statistical power is frequently overlooked, a strong case for its usefulness can be made by considering that it lets us predict the probability that a given study will yield a statistically significant result (Cohen, 1976). Since the power depends on the sample size, a statistical power analysis may be used to determine how many subjects should be included in a study to avoid inconclusive results, and may also facilitate more realistic expectations regarding the outcome (Cohen, 1976, Lenth, 2001, Maxwell et al., 2008).

In the context of dMRI, considering the statistical power may also improve interpretation of results. In Paper I, we investigated DKI and DTI parameters, and their statistical precision, in several white matter structures. Interestingly, the statistical power was highly heterogeneous across parameters and locations. The parameter variance was mainly caused by inter-subject differences, and to a lesser extent by measurement noise. Such information can further improve the design of a study by determining if time and resources are best spent on longer scans or larger samples.

Generally, a study and imaging protocol should be designed so that all regions investigated have sufficient power, but this may lead to unfeasible requirements on scan time or sample size. It is worth considering that the statistical power can be improved without increasing the sample size. For example, the design of the study can strive to maximize the effect size by evaluating only regions or parameters where the effect is expected to be largest, and attrition can be avoided by ensuring a high program integrity over the course of the study (Hansen and Collins, 1994). Furthermore, power may be improved by finding and eliminating confounding factors. In Paper I, we found an interaction between dMRI parameters and the size of white matter structures caused by partial volume effects, and we estimated that its removal could reduce the required sample size by up to 60%. Similar effects have

been pointed out in DTI, where interactions between the structure geometry and the imaging raster may reduce the parameter accuracy significantly (Edden and Jones, 2011, Vos et al., 2011).

6.3.2 Estimation of required group sizes

In order to facilitate a preliminary statistical power analysis based on the parameters derived from DIVIDE, values for the group mean and variance are presented in Table 1. We have also estimated the group sizes necessary to yield a statistical power of 0.8 at a relative effect size of 5% using a t-test (Paper I) for several dMRI parameters. The analysis is based on a group of ten healthy volunteers (all male, mean age ± s.d. was 30 ± 4 y, in the interval 24–34 y) as described in Paper IV. Four ROIs were defined to represent the anterior and posterior corpus callous (ACC and PCC), anterior crossing region (ACR), and the corticospinal tract (CST). Each ROI was placed manually in a single axial slice at the level of the lateral ventricles.

Table 1 is intended to provide ballpark figures of the parameter precision and power for future study design and statistical analysis. Notably, the diffusional variance parameters require larger sample sizes than FA and μFA. Furthermore, the μFA showed a high parameter precision, in agreement with previously reported values (Paper III). Apart from the CST, MK_I showed relatively low precision, especially in regions close to the lateral ventricles – possibly due to partial volume effects with cerebrospinal fluid.

Table 1 | Parameter values derived using DIVIDE in a group of ten healthy volunteers, and estimated group sizes (*n*) required to reach statistical power of 0.8 at a relative effect size of 5% for a t-test (independent samples, equal variance, two-tailed, significance threshold 0.05). MD is given in units of $\mu m^2/ms$, and the remaining parameters are unitless.

	ACC		PCC		ACR		CST	
	Mean (s.d.)	*n*	Mean (s.d.)	*n*	Mean (s.d.)	*n*	Mean (s.d.)	*n*
MD	0.88 (0.05)	22	0.90 (0.05)	17	0.95 (0.02)	3	0.93 (0.02)	4
MK_T	2.67 (0.23)	45	3.21 (0.22)	30	2.07 (0.16)	36	2.81 (0.15)	19
MK_A	2.32 (0.20)	48	2.73 (0.22)	41	1.54 (0.10)	27	2.41 (0.14)	22
MK_I	0.34 (0.15)	>200	0.48 (0.15)	>200	0.53 (0.08)	140	0.40 (0.03)	46
μFA	0.97 (0.02)	3	0.99 (0.02)	3	0.88 (0.01)	2	0.98 (0.01)	2
FA	0.84 (0.03)	10	0.80 (0.05)	24	0.33 (0.03)	71	0.68 (0.03)	10

ACC, anterior corpus callosum; PCC, posterior corpus callosum; ACR, anterior crossing region; CST, corticospinal tract; *n*, minimal sample size (per group); MD, mean diffusivity; MK, normalized diffusional variance; FA, fractional anisotropy; μFA, microscopic fractional anisotropy.

7 Interpretation and implications

Diffusional variance decomposition has been performed in healthy brain (Paper III), meningioma and glioma tumors (Paper V), schizophrenia patients (Westin et al., 2016a), and in several phantoms (Paper II, Eriksson et al., 2015, Westin et al., 2016b). Here, we review the preliminary findings currently available in healthy brain tissue and tumor tissue, and compare them to similar methods, such as DKI (Jensen et al., 2005) and techniques based on DDE (Jespersen et al., 2013, Lawrenz and Finsterbusch, 2015). The interpretation of the parameters and the implications for the wider dMRI community are discussed.

7.1 Healthy brain

In the healthy brain, a probe of diffusion anisotropy that is independent of the orientation coherence of tissue is desirable because it may alleviate some of the issues associated with interpretation of voxel-scale anisotropy (Shemesh et al., 2010, Jones et al., 2012). Microscopic diffusion anisotropy has been estimated in monkey brain (Jespersen et al., 2013, 2014a) and human brain (Lawrenz and Finsterbusch, 2013, Hui and Jensen, 2015, Lawrenz et al., 2015, Lawrenz and Finsterbusch, 2015), based on double diffusion encoding. These studies have consistently shown that the diffusion anisotropy on the microscopic scale can be recovered, and that it is high in the white matter, even in regions of crossing pathways where conventional metrics of voxel-level anisotropy, such as FA, are low. Furthermore, the presence of diffusion anisotropy can be probed in tissues that appear isotropic on the voxel scale. For example, microscopic anisotropy has been detected in gray matter, which supports the notion that it contains incoherent anisotropic structures (Komlosh et al., 2007, Shemesh and Cohen, 2011, Jespersen et al., 2013).

In Paper III, we estimated the microscopic anisotropy, based on the DIVIDE approach, in terms of the μFA. The μFA was high in regions of white matter, and relatively low in gray matter and tissues that interface with CSF. The contrast between the μFA and FA was most notable in regions that are known to contain

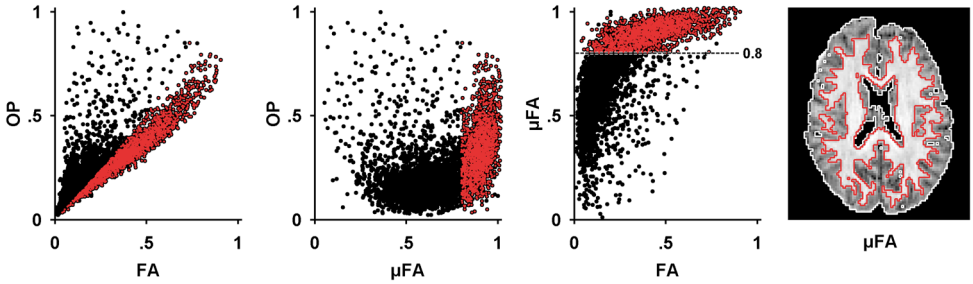

Figure 15 | Association between FA, μFA, and OP. Each point of data corresponds to a voxel in an axial slice of a healthy brain. The red markers show data taken from a region where μFA > 0.8, which corresponds well to the white matter (red outline in μFA map). The OP shows a strong positive correlation to FA, especially in the white matter, indicating that FA mainly reflects the orientation coherence of anisotropic tissue. On the other hand, the μFA and FA show a weak correlation, where a high μFA corresponds to a wide range of FA values, whereas a high FA is always associated with high μFA. This figure is a reproduction of Figure 6 in Paper III, and is based on data that was acquired using the protocols suggested in Paper VI.

crossing white matter pathways, where the μFA was high compared to the FA. These findings are in agreement with those from previous studies (Jespersen et al., 2013, Lawrenz and Finsterbusch, 2013, Lawrenz et al., 2015), and indicate that the different encoding techniques and methods of analysis are sensitive to similar features of the tissue although the mathematical modeling is somewhat different, as discussed by Jespersen et al. (2014b), and Hui and Jensen (2015). We also estimated the OP, which reflects the orientation coherence of the tissue. Note that the OP map bears a striking resemblance to the FA map (Figure 8), which indicates that the FA in white matter is primarily modulated by orientation coherence rather than anisotropy (Paper II and III), which is in agreement with previous results based on biophysical models (Zhang et al., 2012). This result is shown Figure 15, where a strong correlation between the FA and the OP exists in the white matter, whereas μFA is independent of the OP. Our observations of microscopic anisotropy in the gray matter in Paper III were based on data acquired at a low spatial resolution and were therefore sensitive to partial volume effects. In Paper VI, a higher resolution was afforded by the optimized waveforms and shorter echo time, and the μFA in gray matter regions was estimated to be between 0.5–0.6, although it should be noted that μFA below approximately 0.5 may be biased due to noise (Paper II). Although parameters of microscopic diffusion anisotropy have not been independently validated in healthy tissue, recent results comparing high-resolution FA and structural anisotropy support the interpretation of μFA as a marker for anisotropic tissue structures that is independent of voxel-scale orientation coherence (Budde and Frank, 2012, Budde and Annese, 2013, Ronen et al., 2014, Khan et al., 2015).

To our knowledge, we have presented the first studies that isolate and investigate the isotropic variance component in vivo (Paper III and V, Westin et al., 2016a). Westin et al. (2016a) suggested that an elevated V_{I} in the white matter of schizophrenia patients agreed with an increasing free water fraction. However, no independent investigation of what it represents in healthy tissue has been performed. Regardless, it may aid in the interpretation of data. For example, Kaden et al. (2015) proposed that the microscopic anisotropy can be derived from what is effectively the total diffusional variance, but this assumes that all variance is due to anisotropy and it neglects the presence of the isotropic component – an assumption that may introduce a significant bias (Paper III and VI).

7.2 Meningiomas and gliomas

Tumors frequently exhibit both macroscopic and microscopic heterogeneity, caused by factors such as oxygenation, nutrition, metabolism, and interaction with other tissues (Heppner, 1984, Marusyk and Polyak, 2010). Tumor heterogeneity may also be caused by mixtures of divergent cell clones, where clonal diversity may have a strong influence on the malignancy and response to treatment (Shackleton et al., 2009, Marusyk and Polyak, 2010, Magee et al., 2012).

Methods such as DWI and DTI are useful for mapping the macroscopic heterogeneity and geometric extent of tumors (Maier et al., 2010, Ryu et al., 2014, Sternberg et al., 2014, Rozenberg et al., 2016), and also their gross response to treatment (Chenevert et al., 2000, Moffat et al., 2005). On the microscopic scale the heterogeneity may be probed in terms of the diffusional variance. Several studies have shown that the diffusional variance, in terms of the mean kurtosis normalized to normal-appearing white matter ($\mathrm{MK_T}/\mathrm{MK_{NAWM}}$), is superior in differentiating low- and high-grade gliomas (Raab et al., 2010, Van Cauter et al., 2012, Van Cauter et al., 2014, Tietze et al., 2015). These findings presumably reflect a higher degree of tissue heterogeneity in higher-grade tumors. Recently, Hempel et al. (2016) reported an association between $\mathrm{MK_T}/\mathrm{MK_{NAWM}}$ and the molecular profile of gliomas of variable origin, which suggests that a probe of tumor heterogeneity may facilitate more specific diagnosis of tumor subtypes.

In Paper V, we performed diffusional variance decomposition in meningiomas and gliomas. Both tumor types exhibited elevated diffusional variance ($\mathrm{MK_T} > 0$), indicating that both contained heterogeneous tissue. What is remarkable is that the dominant components in the two tumor types were different. In the meningiomas,

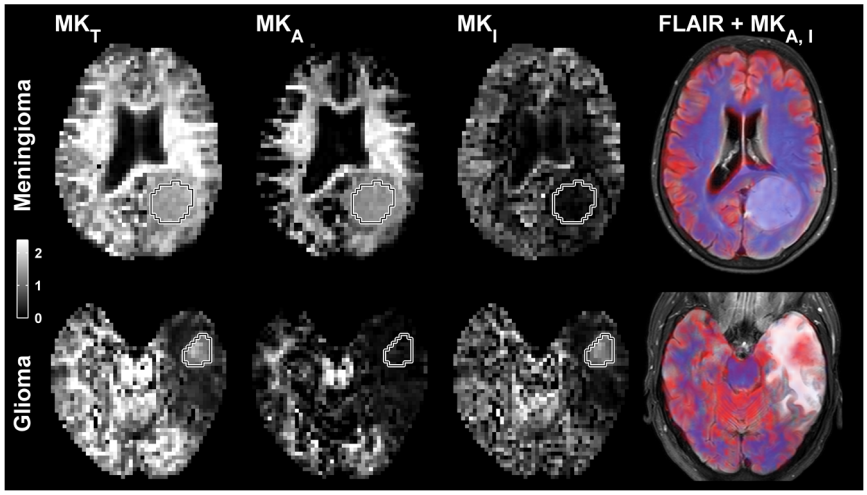

Figure 16 | Examples of diffusional variance parameters in meningioma and glioma tumors (white line shows outline of tumor). The total diffusional variance (MK_T) is high in both tumor types, indicating heterogeneous tissue. However, the tumors differ markedly regarding the source of diffusional variance, where the meningioma and glioma exhibit mostly anisotropic and isotropic diffusional variance, respectively. This is seen in the column on the far right, where the anisotropic (MK_A, blue) and isotropic variance (MK_I, red) are superimposed on a high-resolution FLAIR image. The figure was adapted, with permission, from Paper V by Szczepankiewicz et al. (2016a), published by Elsevier.

the anisotropic diffusional variance was dominant ($MK_A > MK_I$), whereas the opposite was observed in the gliomas ($MK_I > MK_A$). Examples of diffusional variance parameter maps in a meningioma and glioma are shown in Figure 16.

To determine whether the diffusional variance could be interpreted as tissue heterogeneity, an independent analysis of the same tumor tissue by quantitative microscopy was performed. The link between diffusional variance and tissue microstructure was formulated in two hypotheses, which stated that (i) there is a correlation between anisotropic variance and structure anisotropy, and (ii) there is a correlation between isotropic variance and the variance in cell density (Paper V). The tissue anisotropy (H_A) was quantified by "structure tensor analysis" (Bigun, 1987, Knutsson, 1989), which has been used in several studies that show a strong correlation between diffusion and structure anisotropy (Budde and Frank, 2012, Budde and Annese, 2013, Khan et al., 2015). The cell density variance (H_I) was quantified by segmenting and counting cell nuclei in histological images (Malpica et al., 1997, Al-Kofahi et al., 2010). We are not aware of any previous investigations of cell density variance, but the second hypothesis is made plausible by the correlation between diffusivity and cell density that has been reported in several studies (Sugahara et al., 1999, Anderson et al., 2000, Chenevert et al., 2000, Lyng et al., 2000, Kono et al., 2001, Moffat et al., 2004, Kinoshita et al., 2008, Padhani

et al., 2009, Ginat et al., 2012, Chen et al., 2013), although there are exceptions. Examples of quantitative parameter maps derived from histological images are given in Figure 17.

We found strong correlations between parameters derived from dMRI and microscopy, which provides evidence for a link between diffusional variance and structure heterogeneity. Specifically, the anisotropic diffusional variance correlated with structure tensor anisotropy (MK_A vs. H_A, $r = 0.95$), and the isotropic diffusional variance correlated with the cell density variance (MK_I vs. H_I, $r = 0.83$) (Paper V).

We would expect diffusional variance decomposition in tumors to have two relevant implications. First, probing of more specific components of the diffusional variance may facilitate a better understanding and interpretation of tissue heterogeneity and its role in tumor diagnosis and treatment. This also applies to the interpretation of the anisotropic diffusional variance in terms of the μFA. For example, the fact that μFA is not affected by orientation coherence of tissue may be beneficial in determining the presence of anisotropic structures in meningioma tumors for the purpose of predicting their subtype and toughness (Kashimura et al., 2007, Tropine et al., 2007, Jolapara et al., 2010, Sanverdi et al., 2012). Secondly, there may be a purely statistical benefit in separating the two components of diffusional variance, and in treating one as a nuisance parameter (Paper V), as this may remove unwanted variance and therefore improve the statistical power (Paper I).

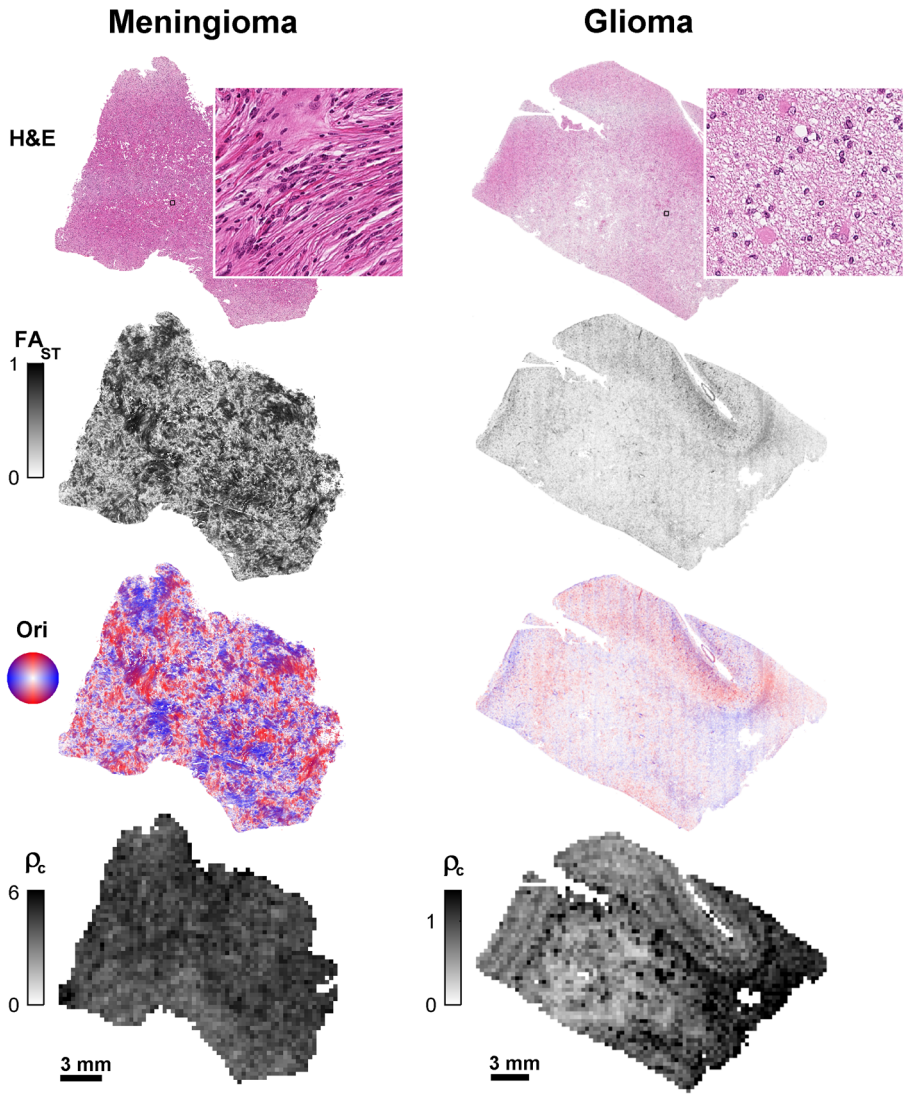

Figure 17 | Quantitative microscopic analysis of tumor tissue. The top row shows the hematoxylin- and eosin-stained section (H&E). The magnifications show a 250×250 μm^2 region of the tissue. The parameter maps show the fractional anisotropy derived from the structure tensor analysis (FA_{ST}), the orientation of the tensor field (Ori), and the cell density (ρ_c in units of 10^3/mm^2). The meningioma is a grade-I fibroblastic subtype (Riemenschneider et al., 2006, Louis et al., 2007), the cell density is relatively homogeneous (ρ_c exhibits low spatial variance), and the tissue mainly contains anisotropic cells and cell structures (high FA_{ST}). The orientation coherence varies across the tumor, and some regions are coherent on the mm length scale (saturated regions in the Ori map). The glioma is a grade-IV glioblastoma multiforme. It is surrounded by normal-appearing cortical gray matter and contains regions of necrotic tissue at its core. The tissue exhibits vanishing levels of structure anisotropy and orientation coherence (low FA_{ST}). However, the cell density varies across the tumor, where necrotic tissue can be seen as regions of low cell density. The figure was adapted, with permission, from Paper V by Szczepankiewicz et al. (2016a) published by Elsevier.

8 Conclusions

This thesis describes initial efforts to probe specific components of diffusional variance, and tissue heterogeneity. The work spanned the development and implementation of novel techniques for diffusion encoding (QTE), tissue modeling (DTD), and parameterization (DIVIDE). We studied healthy and tumor tissues in vivo, and demonstrated that diffusional variance can be decomposed into isotropic and anisotropic components. In the tumors, parameters from DIVIDE were compared to similar parameters from quantitative microscopy. Parameters from the two independent methods showed a strong correlation, which supported the interpretation of isotropic and anisotropic diffusional variance as probes of variable cell density and anisotropic structures, respectively. Although other features of the tissue may affect the diffusional variance, the current results suggest that DIVIDE enables a more specific characterization of tissue heterogeneity than what is possible with previous methods.

Our ability to disentangle anisotropic and isotropic diffusional variance was enabled by the use of b-tensors with variable anisotropy, which require non-conventional diffusion encoding gradient waveforms. To achieve clinically feasible scan times at a wide range of MRI systems, we also worked to developed waveforms with superior efficiency compared to previous designs.

The conclusions of each individual publication were:

I. The diffusional variance and its statistical power is heterogeneous between subjects, across brain regions, and even along specific white matter structures. Studies should take the region-specific statistical power into account when designing studies and interpreting statistical tests.

II. Tensor-valued diffusion encoding by q-space trajectory encoding enables DIVIDE, and is feasible on clinical systems. Diffusional variance in phantoms was caused by isotropic and anisotropic heterogeneity on the microscopic scale.

III. DIVIDE parameters were estimated in healthy volunteers in vivo. Microscopic diffusion anisotropy was probed in terms of the μFA. The μFA

is independent of orientation coherence and may provide a more robust biomarker for structural anisotropy than the conventional FA metric.

IV. Numerical optimization of waveforms for tensor-valued encoding gives superior encoding efficiency. Optimized waveforms provide a significant reduction in the echo time and facilitate higher-data quality with shorter acquisition times.

V. In meningiomas and gliomas, the two variance components estimated by DIVIDE showed a clear association with specific tissue features derived from quantitative microscopy. Tensor-valued diffusion encoding at high b-values improves the interpretation of dMRI in tumors.

VI. Whole-brain DIVIDE is possible in a wide range of MRI systems, and at acquisition times below 8 minutes. Furthermore, the imaging protocol can be tailored to a specific MRI system and tissue to render data of sufficient quality.

8.1 Future work

Future efforts will investigate the assumptions of the DTD model in various tissues in order to establish the impact of time-dependent diffusion and exchange on the accuracy and interpretation of the parameters (Nilsson et al., 2013b, Fieremans et al., 2016). Our investigations of exchange have already yielded preliminary results in healthy brain and tumors (Lampinen et al., 2016), and we expect that the combination of multiple dMRI sequences for specialized measurements will prove valuable in exploring the characteristics of both healthy and diseased tissues.

The interpretation of dMRI parameters should also be informed and substantiated by independent validation. Tools such as microscopy (light, confocal, electron), micro-X-ray, and tissue clearing may contribute valuable information to the continued exploration of tissue microstructure (Chung et al, 2013, Khan et al., 2015, Walton et al., 2015). The challenge remains to investigate large samples at sufficient resolution, and to create a feasible link between tissue microstructure and the diffusion process.

Acknowledgements

I would like to extend my most sincere gratitude to my main supervisor Markus Nilsson, for his tireless support, motivation, friendship, and diligence. Without him at the helm, surely none of this would have been possible.

I would also like to thank my co-supervisors: Jimmy Lätt for always providing support, excellent guidance, and critical thinking; and Freddy Ståhlberg for his uncanny insight into all things MRI and the opportunities that I have enjoyed as a member of the MR group.

Thanks to all my colleagues in the clinic, especially Danielle van Westen for being engaged and honest, and for being an excellent guide to the world of radiology; Pia Sundgren for supporting our ideas and making everything happen; and Elisabet Englund for teaching me the basics of microscopy and pathology, and for inspiring me to do more every day.

I'm also lucky to have wonderful co-authors and colleagues at Physical Chemistry and CR Development: Daniel Topgaard, Stefanie Eriksson, João de Almeida Martins, Karin Bryskhe, and Samo Lasič. Thank you all for being fantastic inventors, scientists, and friends. Thanks to Carl-Fredrik Westin, for all the fruitful collaborations and for hosting us in Boston, and to my remaining co-authors: Alexander Leemans, Hans Knutsson and Jens Sjölund, for letting me benefit from your genius.

Special thanks to Siemens Healthcare and Philips Healthcare for the opportunity to play with your scanners, and for your much needed technical support.

Thanks to all past and current colleagues at Medical Radiation Physics and the MR physics group. Special thanks to my roommate Anna Scherman Rydhög, for your company and for all the crazy discussions; and my old and new friends: Christian Gustafsson, Johan Gustafsson, André Ahlgren, Gustav Brolin, Mikael Petersson, Björn Lampinen, Renata Madru, Mikael Novén and Johan Mårtensson. I am very grateful to Linda Knutsson and Ronnie Wirestam for all your humor, advice, and inspiration. And thanks to Titti Owman and Boel Hansson for your warm welcome, hospitality, and help.

Finally, endless gratitude and love to my family. Thank you!

Funding

This research was supported by:

- The Swedish Research Council
  Grants 2010-36861-78981-35, 13514, 2009-6794, 2010-3034, 2011-4334, 2012-3682, 2014-3910 and K2011-52X-21737-01-3

- The Swedish Cancer Society
  Grants CAN 2009/1076, CAN 2012/597, and CAN 2013/321

- Swedish Foundation for Strategic Research
  Grant AM13-0090

- The National Institutes of Health
  Grants R01MH074794 and P41EB015902

- The Swedish Brain Foundation
  Grant FO2014-0133

- CR Development AB
  Grant MN15

References

Al-Kofahi, Y., Lassoued, W., Lee, W. & Roysam, B. 2010. Improved automatic detection and segmentation of cell nuclei in histopathology images. *IEEE Transactions on Biomedical Engineering,* 57, 841-52.

Alexander, A. L., Hasan, K. M., Lazar, M., Tsuruda, J. S. & Parker, D. L. 2001. Analysis of partial volume effects in diffusion-tensor MRI. *Magnetic Resonance in Medicine,* 45, 770-80.

Alexander, A. L., Lee, J. E., Lazar, M. & Field, A. S. 2007. Diffusion tensor imaging of the brain. *Neurotherapeutics,* 4, 316-29.

Anderson, A. W., Xie, J., Pizzonia, J., Bronen, R. A., Spencer, D. D. & Gore, J. C. 2000. Effects of cell volume fraction changes on apparent diffusion in human cells. *Magnetic Resonance Imaging,* 18, 689-95.

Assaf, Y., Mayk, A. & Cohen, Y. 2000. Displacement imaging of spinal cord using q-space diffusion-weighted MRI. *Magnetic Resonance in Medicine,* 44, 713-722.

Assaf, Y., Blumenfeld-Katzir, T., Yovel, Y. & Basser, P. J. 2008. AxCaliber: a method for measuring axon diameter distribution from diffusion MRI. *Magnetic Resonance in Medicine,* 59, 1347-54.

Assaf, Y. & Pasternak, O. 2008. Diffusion tensor imaging (DTI)-based white matter mapping in brain research: a review. *Journal of Molecular Neuroscience,* 34, 51-61.

Bak, M. & Nielsen, N. C. 1997. REPULSION, A Novel Approach to Efficient Powder Averaging in Solid-State NMR. *Journal of Magnetic Resonance,* 125, 132-9.

Baron, C. A., Lebel, R. M., Wilman, A. H. & Beaulieu, C. 2012. The effect of concomitant gradient fields on diffusion tensor imaging. *Magnetic Resonance in Medicine,* 68, 1190-201.

Basser, P. J., Mattiello, J. & Le Bihan, D. 1994. MR diffusion tensor spectroscopy and imaging. *Biophysical Journal,* 66, 259-67.

Basser, P. J. & Pierpaoli, C. 1996. Microstructural and physiological features of tissues elucidated by quantitative-diffusion-tensor MRI. *Journal of Magnetic Resonance*, 209-2019.

Basser, P. J. & Jones, D. K. 2002. Diffusion-tensor MRI: theory, experimental design and data analysis - a technical review. *NMR in Biomedicine,* 15, 456-67.

Beaulieu, C. 2002. The basis of anisotropic water diffusion in the nervous system - a technical review. *NMR in Biomedicine,* 15, 435-55.

Beck, R. E. & Schultz, J. S. 1970. Hindered diffusion in microporous membranes with known pore geometry. *Science,* 170, 1302-5.

Bernstein, M. A., Zhou, X. J., Polzin, J. A., King, K. F., Ganin, A., Pelc, N. J. & Glover, G. H. 1998. Concomitant gradient terms in phase contrast MR: analysis and correction. *Magnetic Resonance in Medicine,* 39, 300-8.

Bigun, J. 1987. optimal orientation detection of linear symmetry. *In:* Proc. of the IEEE First international conference on computer vision, June 8-11 1987 London. 433-438.

Budde, M. D. & Frank, J. A. 2012. Examining brain microstructure using structure tensor analysis of histological sections. *Neuroimage,* 63, 1-10.

Budde, M. D. & Annese, J. 2013. Quantification of anisotropy and fiber orientation in human brain histological sections. *Frontiers in Integrative Neuroscience,* 7, 3.

Burcaw, L. M., Fieremans, E. & Novikov, D. S. 2015. Mesoscopic structure of neuronal tracts from time-dependent diffusion. *Neuroimage,* 114, 18-37.

Callaghan, P. T. & Pinder, D. N. 1983. A Pulsed Field Gradient NMR-Study of Self-Diffusion in a Polydisperse Polymer System - Dextran in Water. *Macromolecules,* 16, 968-973.

Callaghan, P. T. & Soderman, O. 1983. Examination of the Lamellar Phase of Aerosol Ot-Water Using Pulsed Field Gradient Nuclear Magnetic-Resonance. *Journal of Physical Chemistry,* 87, 1737-1744.

Callaghan, P. T., Coy, A., Macgowan, D., Packer, K. J. & Zelaya, F. O. 1991. Diffraction-Like Effects in NMR Diffusion Studies of Fluids in Porous Solids. *Nature,* 351, 467-469.

Callaghan, P. T. & Komlosh, M. E. 2002. Locally anisotropic motion in a macroscopically isotropic system: displacement correlations measured using double pulsed gradient spin-echo NMR. *Magnetic Resonance in Chemistry,* 40, S15-S19.

Caminiti, R., Carducci, F., Piervincenzi, C., Battaglia-Mayer, A., Confalone, G., Visco-Comandini, F., Pantano, P. & Innocenti, G. M. 2013. Diameter, length, speed, and conduction delay of callosal axons in macaque monkeys and humans: comparing data from histology and magnetic resonance imaging diffusion tractography. *Journal of Neuroscience,* 33, 14501-11.

Catani, M. & Thiebaut De Schotten, M. 2008. A diffusion tensor imaging tractography atlas for virtual in vivo dissections. *Cortex,* 44, 1105-32.

Chen, L., Liu, M., Bao, J., Xia, Y., Zhang, J., Zhang, L., Huang, X. & Wang, J. 2013. The correlation between apparent diffusion coefficient and tumor cellularity in patients: a meta-analysis. *PLoS ONE,* 8, e79008.

Chenevert, T. L., Stegman, L. D., Taylor, J. M., Robertson, P. L., Greenberg, H. S., Rehemtulla, A. & Ross, B. D. 2000. Diffusion magnetic resonance imaging: an early surrogate marker of therapeutic efficacy in brain tumors. *Journal of the National Cancer Institute,* 92, 2029-36.

Cheng, Y. & Cory, D. G. 1999. Multiple scattering by NMR. *Journal of the American Chemical Society,* 121, 7935-7936.

Chuhutin, A., Khan, A. R., Hansen, B. & Jespersen, S. N. 2015. The mean kurtosis evaluation measurements show a considerable disparity from the analytically evaluated ones for a clinically used range of b-values. *In:* Proc. Intl. Soc. Reson. Med. 23, 2015 Toronto, Canada. 2833.

Chung, K., Wallace, J., Kim, S. Y., Kalyanasundaram, S., Andalman, A. S., Davidson, T. J., Mirzabekov, J. J., Zalocusky, K. A., Mattis, J., Denisin, A. K., Pak, S., Bernstein, H., Ramakrishnan, C., Grosenick, L., Gradinaru, V. & Deisseroth, K. 2013. Structural and molecular interrogation of intact biological systems. Nature, 497, 332-7.

Clark, C. A., Hedehus, M. & Moseley, M. E. 2001. Diffusion time dependence of the apparent diffusion tensor in healthy human brain and white matter disease. *Magnetic Resonance in Medicine,* 45, 1126-9.

Cohen, J. 1976. *Statistical power analysis for the behavioral sciences*, Lawrence Erlbaum Associates.

Cook, P. A., Symms, M., Boulby, P. A. & Alexander, D. C. 2007. Optimal acquisition orders of diffusion-weighted MRI measurements. *Journal of Magnetic Resonance Imaging,* 25, 1051-8.

Cory, D. G., Garroway, A. N. & Miller, J. B. 1990. Applications of Spin Transport as a Probe of Local Geometry. *Polym Preprints*, 31, 149-150

Cox, E. F. & Gowland, P. A. 2010. Simultaneous quantification of T2 and T'2 using a combined gradient echo-spin echo sequence at ultrahigh field. *Magnetic Resonance in Medicine,* 64, 1440-5.

Damon, B. M., Froeling, M., Buck, A. K., Oudeman, J., Ding, Z., Nederveen, A. J., Bush, E. C. & Strijkers, G. J. 2016. Skeletal muscle diffusion tensor-MRI fiber tracking: rationale, data acquisition and analysis methods, applications and future directions. *NMR in Biomedicine*.

De Almeida Martins, J. P. & Topgaard, D. 2016. Two-Dimensional Correlation of Isotropic and Directional Diffusion Using NMR. *Physical Review Letters,* 116.

De Santis, S., Jones, D. K. & Roebroeck, A. 2016. Including diffusion time dependence in the extra-axonal space improves in vivo estimates of axonal diameter and density in human white matter. *Neuroimage,* 130, 91-103.

De Swiet, T. M. & Mitra, P. P. 1996. Possible Systematic Errors in Single-Shot Measurements of the Trace of the Diffusion Tensor. *Journal of Magnetic Resonance. Series B,* 111, 15-22.

Does, M. D., Parsons, E. C. & Gore, J. C. 2003. Oscillating gradient measurements of water diffusion in normal and globally ischemic rat brain. *Magnetic Resonance in Medicine,* 49, 206-15.

Douaud, G., Jbabdi, S., Behrens, T. E., Menke, R. A., Gass, A., Monsch, A. U., Rao, A., Whitcher, B., Kindlmann, G., Matthews, P. M. & Smith, S. 2011. DTI measures in crossing-fibre areas: increased diffusion anisotropy reveals early white matter alteration in MCI and mild Alzheimer's disease. *Neuroimage,* 55, 880-90.

Edden, R. A. & Jones, D. K. 2011. Spatial and orientational heterogeneity in the statistical sensitivity of skeleton-based analyses of diffusion tensor MR imaging data. *Journal of Neuroscience Methods,* 201, 213-9.

Edén, M. & Levitt, M. H. 1998. Computation of Orientational Averages in Solid-State NMR by Gaussian Spherical Quadrature. *Journal of Magnetic Resonance,* 132, 220-39.

Edén, M. 2003. Computer simulations in solid-state NMR. III. Powder averaging. *Concepts in Magnetic Resonance Part A,* 18A, 24-55.

Einstein, A. 1905. On the movement of small particles suspended in stationary liquids required by the molecular-kinetic theory of heat. *Annalen der Physik,* 17, 549-560.

Epstein, C. L. & Schotland, J. 2008. The bad truth about Laplace's transform. *Siam Review,* 50, 504-520.

Eriksson, S., Lasič, S. & Topgaard, D. 2013. Isotropic diffusion weighting in PGSE NMR by magic-angle spinning of the q-vector. *Journal of Magnetic Resonance,* 226, 13-8.

Eriksson, S., Lasič, S., Nilsson, M., Westin, C. F. & Topgaard, D. 2015. NMR diffusion-encoding with axial symmetry and variable anisotropy: Distinguishing between prolate and oblate microscopic diffusion tensors with unknown orientation distribution. *Journal of Chemical Physics,* 142, 104201.

Fieremans, E., Burcaw, L. M., Lee, H. H., Lemberskiy, G., Veraart, J. & Novikov, D. S. 2016. In vivo observation and biophysical interpretation of time-dependent diffusion in human white matter. *Neuroimage*.

Frank, L. R. 2001. Anisotropy in high angular resolution diffusion-weighted MRI. *Magnetic Resonance in Medicine,* 45, 935-9.

Ginat, D. T., Mangla, R., Yeaney, G., Johnson, M. & Ekholm, S. 2012. Diffusion-weighted imaging for differentiating benign from malignant skull lesions and correlation with cell density. *AJR: American Journal of Roentgenology,* 198, W597-601.

Gore, J. C., Xu, J., Colvin, D. C., Yankeelov, T. E., Parsons, E. C. & Does, M. D. 2010. Characterization of tissue structure at varying length scales using temporal diffusion spectroscopy. *NMR in Biomedicine,* 23, 745-56.

Gudbjartsson, H. & Patz, S. 1995. The Rician Distribution of Noisy MRI Data. *Magnetic Resonance Imaging*, 910-914.

Hagmann, P., Cammoun, L., Gigandet, X., Gerhard, S., Grant, P. E., Wedeen, V., Meuli, R., Thiran, J. P., Honey, C. J. & Sporns, O. 2010. MR connectomics: Principles and challenges. *Journal of Neuroscience Methods,* 194, 34-45.

Ham, C. L., Engels, J. M., Van De Wiel, G. T. & Machielsen, A. 1997. Peripheral nerve stimulation during MRI: effects of high gradient amplitudes and switching rates. *Journal of Magnetic Resonance Imaging,* 7, 933-7.

Hansen, W. B. & Collins, L. M. 1994. Seven ways to increase power without increasing N. *NIDA Research Monograph,* 142, 184-95.

Hebrank, F. X. & Gebhardt, M. 2000. SAFE-Model - A New Method for Predicting Peripheral Nerve Stimulations in MRI. *In:* Proc. Intl. Soc. Mag. Res. Med., 2000.

Hempel, J. M., Bidsas, S., Schittenhelm, J., Brendle, C., Bender, B., Wassmann, H., Skardelly, M., Tabatabai, G., Vega, S. C., Ernemann, U. & Klose, U. 2016. In vivo molecular profiling of human glioma using diffusion kurtosis imaging. *Journal of Neuro-Oncology*.

Heppner, G. H. 1984. Tumor heterogeneity. *Cancer Research,* 44, 2259-65.

Hidalgo-Tobon, S. S. 2010. Theory of gradient coil design methods for magnetic resonance imaging. *Concepts in Magnetic Resonance Part A,* 36A, 223-242.

Holz, M., Heil, S. R. & Sacco, A. 2000. Temperature-dependent self-diffusion coefficients of water and six selected molecular liquids for calibration in accurate 1H NMR PFG measurements. *Physical Chemistry Chemical Physics,* 2, 4740-4742.

Horsfield, M. A. & Jones, D. K. 2002. Applications of diffusion-weighted and diffusion tensor MRI to white matter diseases - a review. *NMR in Biomedicine,* 15, 570-7.

Hui, E. S. & Jensen, J. H. 2015. Double-pulsed diffusional kurtosis imaging for the in vivo assessment of human brain microstructure. *Neuroimage,* 120, 371-381.

Huisman, T. A. 2003. Diffusion-weighted imaging: basic concepts and application in cerebral stroke and head trauma. *European Radiology,* 13, 2283-97.

Håkansson, B., Nyden, M. & Söderman, O. 2000. The influence of polymer molecular-weight distributions on pulsed field gradient nuclear magnetic resonance self-diffusion experiments. *Colloid and Polymer Science,* 278, 399-405.

Jensen, J. H., Helpern, J. A., Ramani, A., Lu, H. & Kaczynski, K. 2005. Diffusional kurtosis imaging: the quantification of non-gaussian water diffusion by means of magnetic resonance imaging. *Magnetic Resonance in Medicine,* 53, 1432-40.

Jensen, J. H. & Helpern, J. A. 2010. MRI quantification of non-Gaussian water diffusion by kurtosis analysis. *NMR in Biomedicine,* 23, 698-710.

Jensen, J. H., Hui, E. S. & Helpern, J. A. 2014. Double-pulsed diffusional kurtosis imaging. *NMR in Biomedicine,* 27, 363-370.

Jensen, J. H. 2014. Sufficiency of diffusion tensor in characterizing the diffusion MRI signal to leading order in diffusion weighting. *NMR in Biomedicine,* 27, 1005-7.

Jespersen, S. N., Bjarkam, C. R., Nyengaard, J. R., Chakravarty, M. M., Hansen, B., Vosegaard, T., Østergaard, L., Yablonskiy, D., Nielsen, N. C. & Vestergaard-Poulsen, P. 2010. Neurite density from magnetic resonance diffusion measurements at ultrahigh field: Comparison with light microscopy and electron microscopy. *Neuroimage,* 49, 205-216.

Jespersen, S. N., Lundell, H., Sønderby, C. K. & Dyrby, T. B. 2013. Orientationally invariant metrics of apparent compartment eccentricity from double pulsed field gradient diffusion experiments. *NMR in Biomedicine,* 26, 1647-62.

Jespersen, S. N., Lundell, H., Sønderby, C. K. & Dyrby, T. B. 2014a. Erratum: Orientationally invariant metrics of apparent compartment eccentricity from double pulsed field gradient diffusion experiments. *NMR in Biomedicine,* 27, 738-738.

Jespersen, S. N., Lundell, H., Sønderby, C. K. & Dyrby, T. B. 2014b. Commentary on "Microanisotropy imaging: quantification of microscopic diffusion anisotropy and orientation of order parameter by diffusion MRI with magic-angle spinning of the q-vector". *Frontiers in Physics,* 2, 28.

Jeurissen, B., Leemans, A., Tournier, J. D., Jones, D. K. & Sijbers, J. 2013. Investigating the prevalence of complex fiber configurations in white matter tissue with diffusion magnetic resonance imaging. *Human Brain Mapping,* 34, 2747-66.

Jian, B., Vemuri, B. C., Ozarslan, E., Carney, P. R. & Mareci, T. H. 2007. A novel tensor distribution model for the diffusion-weighted MR signal. *Neuroimage,* 37, 164-76.

Jiang, R., Du, F. Z., He, C., Gu, M., Ke, Z. W. & Li, J. H. 2014. The value of diffusion tensor imaging in differentiating high-grade gliomas from brain metastases: a systematic review and meta-analysis. *PLoS ONE,* 9, e112550.

Jolapara, M., Kesavadas, C., Radhakrishnan, V. V., Thomas, B., Gupta, A. K., Bodhey, N., Patro, S., Saini, J., George, U. & Sarma, P. S. 2010. Role of diffusion tensor imaging in differentiating subtypes of meningiomas. *Journal of Neuroradiology,* 37, 277-83.

Jones, D. K., Horsfield, M. A. & Simmons, A. 1999. Optimal strategies for measuring diffusion in anisotropic systems by magnetic resonance imaging. *Magnetic Resonance in Medicine,* 42, 515-25.

Jones, D. K. & Basser, P. J. 2004. "Squashing peanuts and smashing pumpkins": how noise distorts diffusion-weighted MR data. *Magnetic Resonance in Medicine,* 52, 979-93.

Jones, D. K. & Cercignani, M. 2010. Twenty-five pitfalls in the analysis of diffusion MRI data. *NMR in Biomedicine,* 23, 803-20.

Jones, D. K., Knosche, T. R. & Turner, R. 2012. White matter integrity, fiber count, and other fallacies: the do's and don'ts of diffusion MRI. *Neuroimage,* 73, 239-54.

Kaden, E., Kruggel, F. & Alexander, D. C. 2015. Quantitative mapping of the per-axon diffusion coefficients in brain white matter. *Magnetic Resonance in Medicine,* 75, 1752-63.

Kashimura, H., Inoue, T., Ogasawara, K., Arai, H., Otawara, Y., Kanbara, Y. & Ogawa, A. 2007. Prediction of meningioma consistency using fractional anisotropy value measured by magnetic resonance imaging. *Journal of Neurosurgery,* 107, 784-7.

Khan, A. R., Cornea, A., Leigland, L. A., Kohama, S. G., Jespersen, S. N. & Kroenke, C. D. 2015. 3D structure tensor analysis of light microscopy data for validating diffusion MRI. *Neuroimage,* 111, 192-203.

Kindlmann, G. 2004. Superquadric tensor glyphs. *Proc. IEEE TVCG/EG Symp Vis.*

Kingsley, P. B. 2006a. Introduction to diffusion tensor imaging mathematics: Part II. Anisotropy, diffusion-weighting factors, and gradient encoding schemes. *Concepts in Magnetic Resonance Part A,* 28A, 123-154.

Kingsley, P. B. 2006b. Introduction to diffusion tensor imaging mathematics: Part I. Tensors, rotations, and eigenvectors. *Concepts in Magnetic Resonance Part A,* 28A, 101-122.

Kinoshita, M., Hashimoto, N., Goto, T., Kagawa, N., Kishima, H., Izumoto, S., Tanaka, H., Fujita, N. & Yoshimine, T. 2008. Fractional anisotropy and tumor cell density of the tumor core show positive correlation in diffusion tensor magnetic resonance imaging of malignant brain tumors. *Neuroimage,* 43, 29-35.

Kiselev, V. 2011. The cumulant expansion: an overarching mathematical framework for understanding diffusion NMR. *In:* JONES, D. K. (ed.) *Diffusion MRI: Theory, Methods, and Applications.*

Kiselev, V. G. & Il'yasov, K. A. 2007. Is the "biexponential diffusion" biexponential? *Magnetic Resonance in Medicine,* 57, 464-9.

Knutsson, H. 1989. Representing local structure using tensors. *In:* Proc. 6th Scandinavian Conf. on Image Analysis. , 1989 Finland, Oulu. 244-251.

Komlosh, M. E., Horkay, F., Freidlin, R. Z., Nevo, U., Assaf, Y. & Basser, P. J. 2007. Detection of microscopic anisotropy in gray matter and in a novel tissue phantom using double Pulsed Gradient Spin Echo MR. *Journal of Magnetic Resonance,* 189, 38-45.

Kono, K., Inoue, Y., Nakayama, K., Shakudo, M., Morino, M., Ohata, K., Wakasa, K. & Yamada, R. 2001. The role of diffusion-weighted imaging in patients with brain tumors. *AJNR: American Journal of Neuroradiology,* 22, 1081-8.

Lampinen, B., Szczepankiewicz, F., Van Westen, D., Englund, E., Sundgren, P., Lätt, J., Ståhlberg, F. & Nilsson, M. 2016. Optimal experimental design for filter exchange imaging: Apparent exchange rate measurements in the healthy brain and in intracranial tumors. *Magnetic Resonance in Medicine.*

Lasič, S., Szczepankiewicz, F., Eriksson, S., Nilsson, M. & Topgaard, D. 2014. Microanisotropy imaging: quantification of microscopic diffusion anisotropy and orientational order parameter by diffusion MRI with magic-angle spinning of the q-vector. *Frontiers in Physics,* 2, 11.

Lawrenz, M., Koch, M. A. & Finsterbusch, J. 2010. A tensor model and measures of microscopic anisotropy for double-wave-vector diffusion-weighting experiments with long mixing times. *Journal of Magnetic Resonance,* 202, 43-56.

Lawrenz, M. & Finsterbusch, J. 2013. Double-wave-vector diffusion-weighted imaging reveals microscopic diffusion anisotropy in the living human brain. *Magnetic Resonance in Medicine,* 69, 1072-82.

Lawrenz, M., Brassen, S. & Finsterbusch, J. 2015. Microscopic diffusion anisotropy in the human brain: reproducibility, normal values, and comparison with the fractional anisotropy. *Neuroimage,* 109, 283-97.

Lawrenz, M. & Finsterbusch, J. 2015. Mapping measures of microscopic diffusion anisotropy in human brain white matter in vivo with double-wave-vector diffusion-weighted imaging. *Magnetic Resonance in Medicine,* 73, 773-83.

Lazar, M. 2010. Mapping brain anatomical connectivity using white matter tractography. *NMR in Biomedicine,* 23, 821-35.

Le, T. D., Olsson, U., Mortensen, K., Zipfel, J. & Richtering, W. 2001. Nonionic amphiphilic bilayer structures under shear. *Langmuir,* 17, 999-1008.

Lebel, C., Walker, L., Leemans, A., Phillips, L. & Beaulieu, C. 2008. Microstructural maturation of the human brain from childhood to adulthood. *Neuroimage,* 40, 1044-55.

Leemans, A. & Jones, D. K. 2009. The B-matrix must be rotated when correcting for subject motion in DTI data. *Magnetic Resonance in Medicine,* 61, 1336-49.

Lenth, R. V. 2001. Some practical guidelines for effective sample size determination. *The American Statistician,* 55, 187-193.

Li, L., Margolis, D. J., Deng, M., Cai, J., Yuan, L., Feng, Z., Min, X., Hu, Z., Hu, D., Liu, J. & Wang, L. 2015. Correlation of gleason scores with magnetic resonance diffusion tensor imaging in peripheral zone prostate cancer. *Journal of Magnetic Resonance Imaging,* 42, 460-7.

Louis, D. N., Ohgaki, H., Wiestler, O. D., Cavenee, W. K., Burger, P. C., Jouvet, A., Scheithauer, B. W. & Kleihues, P. 2007. The 2007 WHO classification of tumours of the central nervous system. *Acta Neuropathol,* 114, 97-109.

Lundell, H., Sønderby, C. K. & Dyrby, T. B. 2014. Diffusion weighted imaging with circularly polarized oscillating gradients. *Magnetic Resonance in Medicine*.

Lyng, H., Haraldseth, O. & Rofstad, E. K. 2000. Measurement of cell density and necrotic fraction in human melanoma xenografts by diffusion weighted magnetic resonance imaging. *Magnetic Resonance in Medicine,* 43, 828-36.

Lätt, J., Brockstedt, S., Wirestam, R., Larsson, C. & Ståhlberg, F. 2003. Visualisation of displacement-distribution parameters in q-space imaging. *In:* Proc. Intl. Soc. Mag. Reson. Med. 11, 2003. 590.

Lätt, J., Nilsson, M., Van Westen, D., Wirestam, R., Ståhlberg, F. & Brockstedt, S. 2009. Diffusion-weighted MRI measurements on stroke patients reveal water-exchange mechanisms in sub-acute ischaemic lesions. *NMR in Biomedicine,* 22, 619-28.

Löbel, U., Sedlacik, J., Gullmar, D., Kaiser, W. A., Reichenbach, J. R. & Mentzel, H. J. 2009. Diffusion tensor imaging: the normal evolution of ADC, RA, FA, and eigenvalues studied in multiple anatomical regions of the brain. *Neuroradiology,* 51, 253-63.

Magee, J. A., Piskounova, E. & Morrison, S. J. 2012. Cancer stem cells: impact, heterogeneity, and uncertainty. *Cancer Cell,* 21, 283-96.

Maier, S. E., Sun, Y. & Mulkern, R. V. 2010. Diffusion imaging of brain tumors. *NMR in Biomedicine,* 23, 849-64.

Malpica, N., De Solorzano, C. O., Vaquero, J. J., Santos, A., Vallcorba, I., Garcia-Sagredo, J. M. & Del Pozo, F. 1997. Applying watershed algorithms to the segmentation of clustered nuclei. *Cytometry,* 28, 289-97.

Marusyk, A. & Polyak, K. 2010. Tumor heterogeneity: Causes and consequences. *Biochimica et Biophysica Acta (BBA) - Reviews on Cancer,* 1805, 105-117.

Mattiello, J., Basser, P. J. & Lebihan, D. 1997. The b matrix in diffusion tensor echo-planar imaging. *Magnetic Resonance in Medicine,* 37, 292-300.

Maxwell, S. E., Kelley, K. & Rausch, J. R. 2008. Sample size planning for statistical power and accuracy in parameter estimation. *Annual Review of Psychology,* 59, 537-63.

Meier, C., Zwanger, M., Feiweier, T. & Porter, D. 2008. Concomitant field terms for asymmetric gradient coils: consequences for diffusion, flow, and echo-planar imaging. *Magnetic Resonance in Medicine,* 60, 128-34.

Mekkaoui, C., Reese, T. G., Jackowski, M. P., Bhat, H. & Sosnovik, D. E. 2015. Diffusion MRI in the heart. *NMR in Biomedicine*.

Merisaari, H. & Jambor, I. 2014. Optimization of b-value distribution for four mathematical models of prostate cancer diffusion-weighted imaging using b values up to 2000 s/mm : Simulation and repeatability study. *Magnetic Resonance in Medicine*.

Mills, R. 1973. Self-Diffusion in Normal and Heavy-Water in Range 1-45 Degrees. *Journal of Physical Chemistry,* 77, 685-688.

Mitra, P. 1995. Multiple wave-vector extensions of the NMR pulsed-field-gradient spin-echo diffusion measurement. *Physical Review B,* 51, 15074-15078.

Moffat, B. A., Hall, D. E., Stojanovska, J., Mcconville, P. J., Moody, J. B., Chenevert, T. L., Rehemtulla, A. & Ross, B. D. 2004. Diffusion imaging for evaluation of tumor therapies in preclinical animal models. *MAGMA,* 17, 249-59.

Moffat, B. A., Chenevert, T. L., Lawrence, T. S., Meyer, C. R., Johnson, T. D., Dong, Q., Tsien, C., Mukherji, S., Quint, D. J., Gebarski, S. S., Robertson, P. L., Junck, L. R., Rehemtulla, A. & Ross, B. D. 2005. Functional diffusion map: a noninvasive MRI biomarker for early stratification of clinical brain tumor response. *Proceedings of the National Academy of Sciences of the United States of America,* 102, 5524-9.

Mori, S. & Van Zijl, P. 1995. Diffusion Weighting by the Trace of the Diffusion Tensor within a Single Scan. *Magnetic Resonance in Medicine,* 33, 41-52.

Mori, S., Crain, B. J., Chacko, V. P. & Van Zijl, P. C. 1999. Three-dimensional tracking of axonal projections in the brain by magnetic resonance imaging. *Annals of Neurology,* 45, 265-9.

Moseley, M. 2002. Diffusion tensor imaging and aging - a review. *NMR in Biomedicine,* 15, 553-60.

Moseley, M. E., Cohen, Y., Mintorovitch, J., Chileuitt, L., Shimizu, H., Kucharczyk, J., Wendland, M. F. & Weinstein, P. R. 1990a. Early detection of regional cerebral ischemia in cats: comparison of diffusion- and T2-weighted MRI and spectroscopy. *Magnetic Resonance in Medicine,* 14, 330-46.

Moseley, M. E., Kucharczyk, J., Mintorovitch, J., Cohen, Y., Kurhanewicz, J., Derugin, N., Asgari, H. & Norman, D. 1990b. Diffusion-weighted MR imaging of acute stroke: correlation with T2-weighted and magnetic susceptibility-enhanced MR imaging in cats. *AJNR: American Journal of Neuroradiology,* 11, 423-9.

Moser, E., Ståhlberg, F., Ladd, M. E. & Trattnig, S. 2012. 7-T MR--from research to clinical applications? NMR in Biomedicine, 25, 695-716.

Nilsson, M., Lätt, J., Nordh, E., Wirestam, R., Ståhlberg, F. & Brockstedt, S. 2009. On the effects of a varied diffusion time in vivo: is the diffusion in white matter restricted? *Magnetic Resonance Imaging,* 27, 176-187.

Nilsson, M., Alerstam, E., Wirestam, R., Stahlberg, F., Brockstedt, S. & Latt, J. 2010. Evaluating the accuracy and precision of a two-compartment Karger model using Monte Carlo simulations. *Journal of Magnetic Resonance,* 206, 59-67.

Nilsson, M., Lätt, J., Van Westen, D., Brockstedt, S., Lasič, S., Ståhlberg, F. & Topgaard, D. 2013a. Noninvasive mapping of water diffusional exchange in the human brain using filter-exchange imaging. *Magnetic Resonance in Medicine,* 69, 1573-81.

Nilsson, M., Van Westen, D., Ståhlberg, F., Sundgren, P. C. & Lätt, J. 2013b. The role of tissue microstructure and water exchange in biophysical modelling of diffusion in white matter. *MAGMA,* 26, 345-70.

Nilsson, M., Lasič, S., Topgaard, D. & Westin, C. F. 2016. Estimating the Axon Diameter from Intra-Axonal Water Diffusion with Arbitrary Gradient Waveforms: Resolution Limit in Parallel and Dispersed Fibers. *In:* Proc. Intl. Soc. Mag. Reson. Med. 24, 2016 Singapore. 0663.

Novikov, D. S. & Kiselev, V. G. 2010. Effective medium theory of a diffusion-weighted signal. *NMR in Biomedicine,* 23, 682-97.

Ozarslan, E. & Basser, P. J. 2008. Microscopic anisotropy revealed by NMR double pulsed field gradient experiments with arbitrary timing parameters. *Journal of Chemical Physics,* 128, 154511.

Padhani, A. R., Liu, G., Mu-Koh, D., Chenevert, T. L., Thoeny, H. C., Takahara, T., Dzik-Jurasz, A., Ross, B. D., Van Cauteren, M., Collins, D., Hammoud, D. A., Rustin, G. J. S., Taouli, B. & Choyke, P. L. 2009. Diffusion-Weighted Magnetic Resonance Imaging as a Cancer Biomarker: Consensus and Recommendations. *Neoplasia,* 11, 102-125.

Partridge, S. C., Murthy, R. S., Ziadloo, A., White, S. W., Allison, K. H. & Lehman, C. D. 2010. Diffusion tensor magnetic resonance imaging of the normal breast. *Magnetic Resonance Imaging,* 28, 320-8.

Pierpaoli, C., Jezzard, P., Basser, P. J., Barnett, A. & Di Chiro, G. 1996. Diffusion tensor MR imaging of the human brain. *Radiology,* 201, 637-48.

Polders, D. L., Leemans, A., Hendrikse, J., Donahue, M. J., Luijten, P. R. & Hoogduin, J. M. 2011. Signal to noise ratio and uncertainty in diffusion tensor imaging at 1.5, 3.0, and 7.0 Tesla. Journal of Magnetic Resonance Imaging, 33, 1456-63.

Poot, D. H., Den Dekker, A. J., Achten, E., Verhoye, M. & Sijbers, J. 2009. Optimal experimental design for Diffusion Kurtosis Imaging. *IEEE Transactions on Medical Imaging,* 29, 819-829.

Potgieser, A. R., Wagemakers, M., Van Hulzen, A. L., De Jong, B. M., Hoving, E. W. & Groen, R. J. 2014. The role of diffusion tensor imaging in brain tumor surgery: a review of the literature. *Clinical Neurology and Neurosurgery,* 124, 51-8.

Provencher, S. W. 1982. A constrained regularization method for inverting data represented by linear algebraic or integral equations. *Computer Physics Communications,* 27, 213-227.

Quirk, J. D., Bretthorst, G. L., Duong, T. Q., Snyder, A. Z., Springer, C. S., Jr., Ackerman, J. J. & Neil, J. J. 2003. Equilibrium water exchange between the intra- and extracellular spaces of mammalian brain. *Magnetic Resonance in Medicine,* 50, 493-9.

Raab, P., Hattingen, E., Franz, K., Zanella, F. E. & Lanfermann, H. 2010. Cerebral gliomas: diffusional kurtosis imaging analysis of microstructural differences. *Radiology,* 254, 876-81.

Riemenschneider, M. J., Perry, A. & Reifenberger, G. 2006. Histological classification and molecular genetics of meningiomas. *The Lancet Neurology,* 5, 1045-1054.

Ronen, I., Moeller, S., Ugurbil, K. & Kim, D. S. 2006. Analysis of the distribution of diffusion coefficients in cat brain at 9.4 T using the inverse Laplace transformation. *Magnetic Resonance Imaging,* 24, 61-8.

Ronen, I., Budde, M., Ercan, E., Annese, J., Techawiboonwong, A. & Webb, A. 2014. Microstructural organization of axons in the human corpus callosum quantified by diffusion-weighted magnetic resonance spectroscopy of N-acetylaspartate and post-mortem histology. *Brain Structure and Function,* 219, 1773-85.

Rozenberg, R., Thornhill, R. E., Flood, T. A., Hakim, S. W., Lim, C. & Schieda, N. 2016. Whole-Tumor Quantitative Apparent Diffusion Coefficient Histogram and Texture Analysis to Predict Gleason Score Upgrading in Intermediate-Risk 3 + 4 = 7 Prostate Cancer. *AJR: American Journal of Roentgenology,* 206, 775-82.

Ryu, Y. J., Choi, S. H., Park, S. J., Yun, T. J., Kim, J. H. & Sohn, C. H. 2014. Glioma: application of whole-tumor texture analysis of diffusion-weighted imaging for the evaluation of tumor heterogeneity. *PLoS ONE,* 9, e108335.

Röding, M., Bernin, D., Jonasson, J., Sarkka, A., Topgaard, D., Rudemo, M. & Nyden, M. 2012. The gamma distribution model for pulsed-field gradient NMR studies of molecular-weight distributions of polymers. *Journal of Magnetic Resonance,* 222, 105-11.

Röding, M., Williamson, N. H. & Nydén, M. 2015. Gamma convolution models for self-diffusion coefficient distributions in PGSE NMR. *Journal of Magnetic Resonance,* 261, 6-10.

Sanverdi, S. E., Ozgen, B., Oguz, K. K., Mut, M., Dolgun, A., Soylemezoglu, F. & Cila, A. 2012. Is diffusion-weighted imaging useful in grading and differentiating histopathological subtypes of meningiomas? *European Journal of Radiology,* 81, 2389-95.

Scherrer, B., Schwartzman, A., Taquet, M., Sahin, M., Prabhu, S. P. & Warfield, S. K. 2015. Characterizing brain tissue by assessment of the distribution of anisotropic microstructural environments in diffusion-compartment imaging (DIAMOND). *Magnetic Resonance in Medicine*.

Scholz, J., Klein, M. C., Behrens, T. E. & Johansen-Berg, H. 2009. Training induces changes in white-matter architecture. *Nature Neuroscience,* 12, 1370-1.

Setsompop, K., Kimmlingen, R., Eberlein, E., Witzel, T., Cohen-Adad, J., Mcnab, J. A., Keil, B., Tisdall, M. D., Hoecht, P., Dietz, P., Cauley, S. F., Tountcheva, V., Matschl, V., Lenz, V. H., Heberlein, K., Potthast, A., Thein, H., Van Horn, J., Toga, A., Schmitt, F., Lehne, D., Rosen, B. R., Wedeen, V. & Wald, L. L. 2013. Pushing the limits of in vivo diffusion MRI for the Human Connectome Project. *Neuroimage*, 80, 220-33.

Shackleton, M., Quintana, E., Fearon, E. R. & Morrison, S. J. 2009. Heterogeneity in cancer: cancer stem cells versus clonal evolution. *Cell,* 138, 822-9.

Shemesh, N., Ozarslan, E., Komlosh, M. E., Basser, P. J. & Cohen, Y. 2010. From single-pulsed field gradient to double-pulsed field gradient MR: gleaning new microstructural information and developing new forms of contrast in MRI. *NMR in Biomedicine,* 23, 757-80.

Shemesh, N. & Cohen, Y. 2011. Microscopic and compartment shape anisotropies in gray and white matter revealed by angular bipolar double-PFG MR. *Magnetic Resonance in Medicine,* 65, 1216-27.

Shemesh, N., Jespersen, S. N., Alexander, D. C., Cohen, Y., Drobnjak, I., Dyrby, T. B., Finsterbusch, J., Koch, M. A., Kuder, T., Laun, F., Lawrenz, M., Lundell, H., Mitra, P. P., Nilsson, M., Ozarslan, E., Topgaard, D. & Westin, C. F. 2016. Conventions and

nomenclature for double diffusion encoding NMR and MRI. *Magnetic Resonance in Medicine,* 75, 82-7.

Sjölund, J., Szczepankiewicz, F., Nilsson, M., Topgaard, D., Westin, C. F. & Knutsson, H. 2015. Constrained optimization of gradient waveforms for generalized diffusion encoding. *Journal of Magnetic Resonance,* 261, 157-168.

Song, S.-K., Sun, S.-W., Ramsbottom, M. J., Chang, C., Russell, J. & Cross, A. H. 2002. Dysmyelination Revealed through MRI as Increased Radial (but Unchanged Axial) Diffusion of Water. *Neuroimage,* 17, 1429-1436.

Sotak, C. H. 2002. The role of diffusion tensor imaging in the evaluation of ischemic brain injury - a review. *NMR in Biomedicine,* 15, 561-9.

Stanisz, G. J., Szafer, A., Wright, G. A. & Henkelman, R. M. 1997. An analytical model of restricted diffusion in bovine optic nerve. *Magnetic Resonance in Medicine,* 37, 103-11.

Stanisz, G. J., Odrobina, E. E., Pun, J., Escaravage, M., Graham, S. J., Bronskill, M. J. & Henkelman, R. M. 2005. T1, T2 relaxation and magnetization transfer in tissue at 3T. *Magnetic Resonance in Medicine,* 54, 507-12.

Stejskal, E. O. 1965. Use of Spin Echoes in a Pulsed Magnetic-Field Gradient to Study Anisotropic, Restricted Diffusion and Flow. *The Journal of Chemical Physics,* 43, 3597.

Stejskal, E. O. & Tanner, J. E. 1965. Spin Diffusion Measurement: Spin echoes in the Presence of a Time-Dependent Field Gradient. *The Journal of Chemical Physics,* 42, 288-292.

Sternberg, E. J., Lipton, M. L. & Burns, J. 2014. Utility of diffusion tensor imaging in evaluation of the peritumoral region in patients with primary and metastatic brain tumors. *AJNR: American Journal of Neuroradiology,* 35, 439-44.

Strasak, A. M., Zaman, Q., Pfeiffer, K. P., Gobel, G. & Ulmer, H. 2007. Statistical errors in medical research--a review of common pitfalls. *Swiss Medical Weekly,* 137, 44-9.

Sugahara, T., Korogi, Y., Kochi, M., Ikushima, I., Shigematu, Y., Hirai, T., Okuda, T., Liang, L. X., Ge, Y. L., Komohara, Y., Ushio, Y. & Takahashi, M. 1999. Usefulness of diffusion-weighted MRI with echo-planar technique in the evaluation of cellularity in gliomas. *Jmri-Journal of Magnetic Resonance Imaging,* 9, 53-60.

Sullivan, E. V. & Pfefferbaum, A. 2006. Diffusion tensor imaging and aging. *Neuroscience and Biobehavioral Reviews,* 30, 749-61.

Sun, S. W., Liang, H. F., Le, T. Q., Armstrong, R. C., Cross, A. H. & Song, S. K. 2006. Differential sensitivity of in vivo and ex vivo diffusion tensor imaging to evolving optic nerve injury in mice with retinal ischemia. *Neuroimage,* 32, 1195-204.

Sykova, E. & Nicholson, C. 2008. Diffusion in brain extracellular space. *Physiological Reviews,* 88, 1277-340.

Szczepankiewicz, F., Van Westen, D., Englund, E., Westin, C. F., Stahlberg, F., Latt, J., Sundgren, P. C. & Nilsson, M. 2016a. The link between diffusion MRI and tumor heterogeneity: Mapping cell eccentricity and density by diffusional variance decomposition (DIVIDE). *Neuroimage*.

Szczepankiewicz, F., Westin, C. F., Ståhlberg, F., Lätt, J. & Nilsson, M. 2016b. Minimum number of diffusion encoding directions required to yield a rotationally invariant powder average signal in single and double diffusion encoding. *In:* Proc. Intl. Soc. Mag. Reson. Med. 24, 2016b Singapore. 2065.

Szczepankiewicz, F., Westin, C. F., Ståhlberg, F., Lätt, J. & Nilsson, M. 2016c. Microscopic Anisotropy Imaging at 7T Using Asymmetrical Gradient Waveform Encoding. *In:* Proc. Intl. Soc. Mag. Reson. Med. 24, 2016c Singapore. 1081.

Tanner, J. E. & Stejskal, E. O. 1968. Restricted Self-Diffusion of Protons in Colloidal Systems by the Pulsed-Gradient, Spin-Echo Method. *The Journal of Chemical Physics,* 49, 1768.

Taouli, B., Beer, A. J., Chenevert, T., Collins, D., Lehman, C., Matos, C., Padhani, A. R., Rosenkrantz, A. B., Shukla-Dave, A., Sigmund, E., Tanenbaum, L., Thoeny, H., Thomassin-Naggara, I., Barbieri, S., Corcuera-Solano, I., Orton, M., Partridge, S. C. & Koh, D. M. 2016. Diffusion-weighted imaging outside the brain: Consensus statement from an ISMRM-sponsored workshop. *Journal of Magnetic Resonance Imaging,* 44, 521-40.

Tietze, A., Hansen, M. B., Ostergaard, L., Jespersen, S. N., Sangill, R., Lund, T. E., Geneser, M., Hjelm, M. & Hansen, B. 2015. Mean Diffusional Kurtosis in Patients with Glioma: Initial Results with a Fast Imaging Method in a Clinical Setting. *AJNR: American Journal of Neuroradiology,* 36, 1472-8.

Topgaard, D. & Söderman, O. 2003. Experimental determination of pore shape and size using q-space NMR microscopy in the long diffusion-time limit. *Magnetic Resonance Imaging,* 21, 69-76.

Topgaard, D. 2016a. NMR methods for studying microscopic diffusion anisotropy. *In:* VALIULLIN, R. (ed.) *Diffusion NMR in Confined Systems: Fluid Transport in Porous Solids and Heterogeneous Materials.* Royal Society of Chemistry, Cambridge, UK.

Topgaard, D. 2016b. Director orientations in lyotropic liquid crystals: diffusion MRI mapping of the Saupe order tensor. *Physical Chemistry Chemical Physics,* 18, 8545-53.

Tournier, J. D., Mori, S. & Leemans, A. 2011. Diffusion tensor imaging and beyond. *Magnetic Resonance in Medicine,* 65, 1532-56.

Tournier, J. D., Calamante, F. & Connelly, A. 2013. Determination of the appropriate b value and number of gradient directions for high-angular-resolution diffusion-weighted imaging. *NMR in Biomedicine,* 26, 1775-86.

Tropine, A., Vucurevic, G., Delani, P., Boor, S., Hopf, N., Bohl, J. & Stoeter, P. 2004. Contribution of diffusion tensor imaging to delineation of gliomas and glioblastomas. *Journal of Magnetic Resonance Imaging,* 20, 905-12.

Tropine, A., Dellani, P. D., Glaser, M., Bohl, J., Ploner, T., Vucurevic, G., Perneczky, A. & Stoeter, P. 2007. Differentiation of fibroblastic meningiomas from other benign subtypes using diffusion tensor imaging. *Journal of Magnetic Resonance Imaging,* 25, 703-8.

Uludag, K., Muller-Bierl, B. & Ugurbil, K. 2009. An integrative model for neuronal activity-induced signal changes for gradient and spin echo functional imaging. *Neuroimage,* 48, 150-65.

Walton, L. A., Bradley, R. S., Withers, P. J., Newton, V. L., Watson, R. E. B., Austin, C. & Sherratt, M. J. 2015. Morphological Characterisation of Unstained and Intact Tissue Micro-architecture by X-ray Computed Micro- and Nano-Tomography. *Scientific Reports,* 5, 10074.

Van Cauter, S., Veraart, J., Sijbers, J., Peeters, R. R., Himmelreich, U., De Keyzer, F., Van Gool, S. W., Van Calenbergh, F., De Vleeschouwer, S., Van Hecke, W. & Sunaert, S. 2012. Gliomas: diffusion kurtosis MR imaging in grading. *Radiology,* 263, 492-501.

Van Cauter, S., De Keyzer, F., Sima, D. M., Sava, A. C., D'arco, F., Veraart, J., Peeters, R. R., Leemans, A., Van Gool, S., Wilms, G., Demaerel, P., Van Huffel, S., Sunaert, S. & Himmelreich, U. 2014. Integrating diffusion kurtosis imaging, dynamic susceptibility-

weighted contrast-enhanced MRI, and short echo time chemical shift imaging for grading gliomas. *Neuro Oncol,* 16, 1010-21.

Vandenbroucke, J. P., Von Elm, E., Altman, D. G., Gotzsche, P. C., Mulrow, C. D., Pocock, S. J., Poole, C., Schlesselman, J. J., Egger, M. & Initiative, S. 2007. Strengthening the Reporting of Observational Studies in Epidemiology (STROBE): explanation and elaboration. *PLoS Medicine,* 4, e297.

Vanderhart, D. L. & Gutowsky, H. S. 1968. Rigid-Lattice NMR Moments and Line Shapes with Chemical-Shift Anisotropy. *The Journal of Chemical Physics,* 49, 261-271.

Westin, C. F., Szczepankiewicz, F., Pasternak, O., Özarslan, E., Topgaard, D., Knutsson, H. & Nilsson, M. 2014. Measurement tensors in diffusion MRI: Generalizing the concept of diffusion encoding. *Med Image Comput Comput Assist Interv,* 17 (Pt 5), 217-225.

Westin, C. F., Knutsson, H., Pasternak, O., Szczepankiewicz, F., Özarslan, E., Van Westen, D., Mattisson, C., Bogren, M., O'donnell, L. J., Kubicki, M., Topgaard, D. & Nilsson, M. 2016a. Q-space trajectory imaging for multidimensional diffusion MRI of the human brain. *Neuroimage,* 135, 345-62.

Westin, C. F., Szczepankiewicz, F., Pasternak, O., Witzel, T., Özarslan, E., Bryskhe, K., Lasič, S., Knutsson, H., Topgaard, D. & Nilsson, M. 2016b. Q-space Trajectory Imaging (QTI) and the Hex Phantom. *In:* ISMRMR workshop, 2016b Portugal, Lisbon.

Whittall, K. P. & Mackay, A. L. 1989. Quantitative Interpretation of NMR Relaxation Data. *Journal of Magnetic Resonance,* 84, 134-152.

Woessner, D. E. 1963. N.M.R. Spin-Echo Self-Diffusion Measurements on Fluids Undergoing Restricted Diffusion. *The Journal of Physical Chemistry,* 67, 1365-1367.

Wong, E. C., Cox, R. W. & Song, A. W. 1995. Optimized isotropic diffusion weighting. *Magnetic Resonance in Medicine,* 34, 139-43.

Vos, S. B., Jones, D. K., Viergever, M. A. & Leemans, A. 2011. Partial volume effect as a hidden covariate in DTI analyses. *Neuroimage,* 55, 1566-76.

Vos, S. B., Tax, C. M., Luijten, P. R., Ourselin, S., Leemans, A. & Froeling, M. 2016. The importance of correcting for signal drift in diffusion MRI. *Magnetic Resonance in Medicine*.

Yablonskiy, D. A., Bretthorst, G. L. & Ackerman, J. J. 2003. Statistical model for diffusion attenuated MR signal. *Magnetic Resonance in Medicine,* 50, 664-9.

Yablonskiy, D. A. & Sukstanskii, A. L. 2010. Theoretical models of the diffusion weighted MR signal. *NMR in Biomedicine,* 23, 661-81.

Zatorre, R. J., Fields, R. D. & Johansen-Berg, H. 2012. Plasticity in gray and white: neuroimaging changes in brain structure during learning. *Nature Neuroscience,* 15, 528-36.

Zhang, H., Schneider, T., Wheeler-Kingshott, C. A. & Alexander, D. C. 2012. NODDI: practical in vivo neurite orientation dispersion and density imaging of the human brain. *Neuroimage,* 61, 1000-16.

Paper I

NeuroImage 76 (2013) 145–154

Contents lists available at SciVerse ScienceDirect

NeuroImage

journal homepage: www.elsevier.com/locate/ynimg

Variability in diffusion kurtosis imaging: Impact on study design, statistical power and interpretation

Filip Szczepankiewicz [a,*], Jimmy Lätt [b], Ronnie Wirestam [a], Alexander Leemans [c], Pia Sundgren [b,d], Danielle van Westen [d], Freddy Ståhlberg [a,d,e], Markus Nilsson [e]

[a] Department of Medical Radiation Physics, Lund University, Lund, Sweden
[b] MR Department, Centre for Medical Imaging and Physiology, Lund University Hospital, Lund, Sweden
[c] Image Sciences Institute, University Medical Center Utrecht, Utrecht, The Netherlands
[d] Department of Diagnostic Radiology, Lund University, Lund, Sweden
[e] Lund University Bioimaging Center, Lund University, Lund, Sweden

ARTICLE INFO

Article history:
Accepted 25 February 2013
Available online 16 March 2013

Keywords:
Diffusion kurtosis imaging
Statistical power
Study design
Group size
Tractography

ABSTRACT

Diffusion kurtosis imaging (DKI) is an emerging technique with the potential to quantify properties of tissue microstructure that may not be observable using diffusion tensor imaging (DTI). In order to help design DKI studies and improve interpretation of DKI results, we employed statistical power analysis to characterize three aspects of variability in four DKI parameters; the mean diffusivity, fractional anisotropy, mean kurtosis, and radial kurtosis. First, we quantified the variability in terms of the group size required to obtain a statistical power of 0.9. Second, we investigated the relative contribution of imaging and post-processing noise to the total variance, in order to estimate the benefits of longer scan times versus the inclusion of more subjects. Third, we evaluated the potential benefit of including additional covariates such as the size of the structure when testing for differences in group means. The analysis was performed in three major white matter structures of the brain: the superior cingulum, the corticospinal tract, and the mid-sagittal corpus callosum, extracted using diffusion tensor tractography and DKI data acquired in a healthy cohort. The results showed heterogeneous variability across and within the white matter structures. Thus, the statistical power varies depending on parameter and location, which is important to consider if a pathogenesis pattern is inferred from DKI data. In the data presented, inter-subject differences contributed more than imaging noise to the total variability, making it more efficient to include more subjects rather than extending the scan-time per subject. Finally, strong correlations between DKI parameters and the structure size were found for the cingulum and corpus callosum. Structure size should thus be considered when quantifying DKI parameters, either to control for its potentially confounding effect, or as a means of reducing unexplained variance.

Introduction

Diffusion kurtosis imaging (DKI) is a technique that has been suggested to show higher sensitivity and specificity than diffusion tensor imaging (DTI) in detecting and differentiating alterations of tissue microstructure (Cauter et al., 2012; Cheung et al., 2009; Grossman et al., 2012; Wang et al., 2011; Wu and Cheung, 2010). Being an extension of DTI, DKI provides conventional DTI-based parameters, such as the mean diffusivity (MD) and the fractional anisotropy (FA), and unique parameters that describe the degree to which the water diffusion is non-Gaussian. This information is most commonly represented by the mean diffusional kurtosis (MK) and radial diffusional kurtosis (RK) (Jensen and Helpern, 2010; Jensen et al., 2005), that can be related to properties of the tissue microstructure, for example, the axonal water fraction and the tortuosity of the extracellular space in white matter (WM) (Fieremans et al., 2011). In its application to clinical research, DKI has rendered promising results in studies of, for example, reactive astrogliosis (Zhuo et al., 2012), age-related diffusional changes (Falangola et al., 2008), and has been reported to outperform conventional DTI in the detection of Parkinson's disease (Wang et al., 2011) and in the grading of gliomas (Cauter et al., 2012). DKI has also been performed outside of the brain, for example, in the spinal cord (Hori et al., 2012; Szczepankiewicz et al., 2011).

In light of the emerging popularity of DKI, it is interesting to elucidate the statistical characteristics of the extracted parameters. Using a statistical power analysis, the variability of any parameter can be evaluated in terms of, for example, the minimal group size required to detect a true difference in means (effect size) at a predefined probability (statistical power) (Cohen, 1976; Lenth, 2001; Maxwell et al., 2008). It may also inform better interpretation of experimental results by complementing statistical significance tests with information

* Corresponding author at: Lund University, Department of Medical Radiation Physics, Barngatan 2, 22185 Lund, Sweden.
E-mail address: filip.szczepankiewicz@med.lu.se (F. Szczepankiewicz).

1053-8119/$ – see front matter © 2013 Elsevier Inc. All rights reserved.
http://dx.doi.org/10.1016/j.neuroimage.2013.02.078

about the probability at which the test successfully rejects a false null hypothesis (Cohen, 1976).

A prerequisite to perform a power analysis is knowledge of the parameter variance and relevant effect size. Several studies have been dedicated to analyzing variability in DTI parameters. Heiervang et al. (2006) performed a statistical power analysis for several WM structures and various tracking methods, showing that inter-subject coefficients of variation (CV) for MD and FA were below 8% and 10%, respectively. Variations in the mean and standard deviation of DTI parameters have also been demonstrated *within* WM structures (Colby et al., 2012; Corouge et al., 2006; Wakana et al., 2007). Wakana et al. (2007) investigated the reproducibility in FA and structure size in several WM structures, and found that a 10% difference in fiber-bundle volume required a group size 10 times larger than that required to detect a 10% difference in FA, indicating a higher variance in the size parameter compared to FA. Variability is also introduced by the hardware and the post-processing of data. Pfefferbaum et al. (2003) compared within- and between-scanner reliability on two similar but not identical scanners, and reported a systematic mean bias across scanners with CVs of 7.5% and 4.5% for MD and FA, respectively. Few studies have analyzed the variability of DKI-specific parameters, however, data reported by Lätt et al. (2012), on the mean and standard deviations in 21 manually segmented structures, can be used to calculate CVs for the most frequently used DKI parameters. The CV, averaged across all structures, was the lowest for MD and MK, with values of 5% and 8%, respectively, and the highest in FA and RK with values of 10% and 14%, respectively. These values indicate that the variability in MK and RK is larger but comparable to that found for MD and FA. However, more detailed information could improve study design and aid the interpretation of experimental results.

The aim of this study was, therefore, to evaluate three aspects of DKI parameter variability: the global and along-tract variability, the inter- and intra-subject variability, and the amount of variability explained by the WM structure size. The results were used to estimate the minimal group sizes required to find a physiologically relevant effect size, to quantify the advantage of increasing group size versus extending scan time per subject, and to estimate whether the introduction of additional covariates, such as the structure size, may lower demands on group size. The study was based on three major WM structures in the brain, defined using tractography-based segmentation.

Theory

Statistical power and group size

The power of a statistical test (π) represents its probability to correctly reject the null-hypothesis, i.e., "there is no significant difference in means between two groups". For a *t*-test, π can be estimated from the *t* statistic and the number of samples in each group, here referred to as the group size (n), given a predefined significance level (α) and an effect size defined as the absolute ($\Delta\mu$) or relative ($\Delta\mu/\mu$) difference in group means, respectively. The *t* statistic used for testing whether the means of two groups are significantly different is given by

$$t = \frac{\Delta\mu}{\mathrm{SE}(\Delta\mu)} = \frac{\Delta\mu}{\sqrt{2V/n}}, \tag{1}$$

where $\mathrm{SE}(\Delta\mu)$ is the standard error of the difference in group mean values, given by $\mathrm{SE}(\Delta\mu) = (2V/n)^{1/2}$ if the two groups are equal in size and have equal variance (V) (Vittinghoff et al., 2005).

Statistical power analysis may also be used to predict how a modification to an experimental protocol will influence the minimal group size. Below, we analyzed the influence on group size requirements from study-design alterations such as extending the acquisition time or correcting for hidden covariates.

Parameter variance

Since the statistical power is related to the variance of the parameter under investigation, reducing the variance will reduce the required group size. The measured parameters can be modeled by a stochastic variable Y, described by the population mean (μ), the group-dependent deviation from the mean, that is the effect size ($\Delta\mu$), and a stochastic error term (E_{total}), according to

$$Y = \mu + \Delta\mu \cdot G + E_{\mathrm{total}}, \tag{2}$$

where $G = [0,1]$ is a discrete index of group affiliation ($G = 0$ for controls and $G = 1$ for the experimental or patient group) (Vittinghoff et al., 2005). The error term can be described by a two-level random-effects model, where E_{total} is the sum of two independent error terms $E_{\mathrm{total}} = E_{\mathrm{inter}} + E_{\mathrm{noise}}$ (Clayden et al., 2006; Laird and Ware, 1982). Here, E_{inter} and E_{noise} represent the inter-subject variability and the variability introduced by imaging and post-processing noise, with variances V_{inter} and V_{noise}, respectively. The total variance is thus the sum of the inter-subject and noise variances, according to

$$V_{\mathrm{total}} = V_{\mathrm{inter}} + V_{\mathrm{noise}}. \tag{3}$$

Estimating the total variance in a new acquisition protocol (V'_{total}) is possible by studying how the noise component is modified, according to

$$V'_{\mathrm{total}}(g) = V_{\mathrm{inter}} + \frac{V_{\mathrm{noise}}}{g^2}. \tag{4}$$

Two important factors affecting g are the signal-to-noise ratio per signal acquisition (SNR), and the acquisition time (T) of the new and the old protocol: $g \propto (T'/T)^{1/2} \cdot (\mathrm{SNR}'/\mathrm{SNR})$, assuming that T is proportional to the total number of acquired images. The factor g, and the new group size (n') both have an effect on the denominator in Eq. (1), according to

$$\mathrm{SE}(\Delta\mu') = \mathrm{SE}(\Delta\mu) \cdot \sqrt{\left(1 - RV_{\mathrm{noise}} \cdot \left(1 - \frac{1}{g^2}\right)\right) \cdot \frac{n}{n'}}, \tag{5}$$

where $RV_{\mathrm{noise}} = V_{\mathrm{noise}}/V_{\mathrm{total}}$ is the relative variance contribution from noise in the old protocol. Assuming large groups, the new and old protocol will have equal power if $\mathrm{SE}(\Delta\mu') = \mathrm{SE}(\Delta\mu)$, and the new group size will be given by

$$n' \approx n \cdot \left(1 - RV_{\mathrm{noise}} \cdot \left(1 - \frac{1}{g^2}\right)\right). \tag{6}$$

Eq. (6) shows that an increase in g has the strongest effect on n' when RV_{noise} is relatively large, that is when most of the total variance is due to noise. In other words, for a fixed statistical power, an increase in SNR or T can reduce the demand on group size n'. Likewise, a reduction in total scan time would increase the demand on the group size.

Parameter covariance

DKI parameters are influenced by properties of the tissue microstructure (Fieremans et al., 2011), but may also be affected by other factors, such as the partial volume effect (PVE) (Cao and Gold, 2008; Vos et al., 2011), image distortions, subject motion and post-processing, among many others (Jones and Cercignani, 2010). Some of these effects may be corrected for by expanding the model in Eq. (2) to include

additional predictors. The addition of one predictor (x) to Eq. (2) results in

$$Y = \mu' + \Delta\mu' \cdot G + k \cdot x + E'_{\text{total}}, \tag{7}$$

where k denotes the regression coefficient of the predictor, and E'_{total} is the new error term (Vittinghoff et al., 2005). Identifying significant predictors means that their contribution to the variance of the error factor can be removed, resulting in a modified residual variance, according to

$$V'_{\text{total}} = V_{\text{total}} \cdot \frac{1-R^2_{Y,[G,X]}}{1-R^2_{Y,G}} \cdot \frac{2n-2}{2n-3}, \tag{8}$$

where $R^2_{Y,G}$ is the coefficient of determination for regression of Y on the group term G, and $R^2_{Y,[G,x]}$ is the coefficient of determination for regression of Y on G and the predictor x. The effect on the standard error of the estimated effect size is

$$\text{SE}(\Delta\mu') = \text{SE}(\Delta\mu) \cdot \sqrt{\frac{V'_{\text{total}}}{V_{\text{total}}} \cdot \frac{n}{n'} \cdot \frac{1}{1-R^2_{G,x}}}, \tag{9}$$

where the term $(1 - R^2_{G,x})^{-1}$ is commonly referred to as the variance inflation factor, since it inflates the standard error of $\Delta\mu$ in cases where correlation between G and x exists, and may even outweigh the benefits of an additional predictor (Vittinghoff et al., 2005). However, if the groups are matched with respect to x, i.e., the two groups have equal mean values of x, the value of $R^2_{G,x}$ is zero, resulting in no inflation and a guaranteed reduction in the standard error of the estimated effect size. Assuming that the compared groups are large ($2n - 2 \approx 2n - 3$, in Eq. (8)) and matched with respect to x ($R_{G,x} = 0$, in Eq. (9)), the minimal group size after accounting for the additional covariate is given by

$$n' \approx n \cdot \frac{1-R^2_{Y,[G,X]}}{1-R^2_{Y,G}}. \tag{10}$$

In analogy with the improvements arising from increased SNR or extended acquisition times, Eqs. (9) and (10) show that reducing the standard error of $\Delta\mu$, by accounting for covariates, can be translated into increased statistical power or reduced demands on group size.

Methods

Data acquisition and post-processing

In order to assess the variability characteristics of DKI parameters, DKI was performed on 31 healthy volunteers (12 male, 19 female, age 36 ± 13 years). The study was approved by the local ethics committee and informed consent was obtained from all volunteers. Imaging was performed on a Philips Achieva 3 T MRI scanner, with a maximum gradient amplitude of 80 mT/m, using an 8-channel head coil. The DKI protocol consisted of one volume acquired with $b = 0$ s/mm^2, followed by 60 diffusion-weighted volumes in which the diffusion encoding was applied in 15 non-collinear encoding directions with b-values of 500, 1000, 2500 and 2750 s/mm^2. The selection of b-values was based on the protocol optimized by Poot et al. (2010). The image volume consisted of 35 contiguous axial slices at a spatial resolution of $2 \times 2 \times 2$ mm^3, covering the CG, CC and CST (from the cerebral peduncle to the centrum semiovale). The echo time (TE) was 76 ms, repetition time (TR) was 7855 ms, half-scan factor was 0.78, SENSE factor was 2, and bandwidth was 2970 Hz, resulting in a scan time of 8:15 min. Motion and eddy current distortions were corrected in *ExploreDTI* (Leemans et al., 2009) where *ElastiX* (Klein et al., 2010) was used to register the images. The images were inspected for motion, ensuring that no image volume was rotated more than 2.5° during the acquisition. Parameter maps, including MD, FA, MK and RK, were calculated using in-house developed software, implemented in Matlab (The Mathworks, Natick, MA, USA). In this procedure, the diffusion-weighted images were modulated with the Jacobian determinant (Jones and Cercignani, 2010). In order to mitigate the potential effects of Gibbs ringing artifacts, all image volumes were smoothed using an isotropic 3D Gaussian kernel with a full width at half maximum of 2 mm (Veraart et al., in press). This kernel size has little effect on sensitivity and specificity (Van Hecke et al., 2009), thus, it is not expected to significantly influence the parameter precision.

Bootstrapping

To estimate the variance component caused by noise, one oversampled set of data was acquired to facilitate a bootstrap analysis (Jones and Pierpaoli, 2005). This data was acquired in an extended imaging session for one of the volunteers, in which the DKI protocol was repeated in seven subsequent acquisitions with a total scan time of approximately 65 min. The subject was not repositioned between acquisitions. By randomly selecting one out of the seven image volumes for every combination of encoding strength and direction, 200 bootstrapped data sets were created, each with a composition corresponding to those acquired in the control group. This number of bootstraps, given the seven original data sets with 60 direction and b-value combinations in each, is expected to generate a reliable distribution of parameters (O'Goreman and Jones, 2006), where the CV of the relative noise contribution is given by $\text{CV}(RV_{\text{noise}}) = (2/N)^{1/2}$, i.e., 10% for $N = 200$. Individual post-processing and parameter calculation was performed on all of the simulated sets of data in a way identical to that performed in the control group. The bootstrapping generated unique noise realizations, allowing the resulting parameter variance to be attributed to imaging and post-processing noise only and thereby provide an estimate of V_{noise} in Eq. (3).

Structure definition

Three major WM structures were investigated: the superior cingulum bundle (CG), the medial motor corticospinal tract (CST) and the mid-sagittal corpus callosum (CC). These structures were selected to represent some of the structures most commonly investigated with diffusion tensor tractography, which also offer a variety of features, such as proximity to CSF and gray matter (GM), and varying geometrical configurations. The structures were defined in native space using manually defined geometrical inclusion criteria (AND-gates, commonly referred to as ROIs) as shown in Fig. 1. The structures were segmented from a whole-brain tractography (diffusion tensor was fit to $b = 0$, 500 and 1000 s/mm^2), generated in *TrackVis* (Wang et al., 2007), using a deterministic interpolated streamline algorithm. Track termination was based on a FA threshold of 0.2 and an angle threshold of 30°.

The CG was delineated using three AND-gates, combined in gate pairs, and positioned to include the superior CG bundle (Fig. 1A). Gates were defined in coronal projections and the mid-sagittal CC was employed as an anatomical reference. The gates were aligned with the anterior (Ant), central (Cent) and posterior (Post) part of the mid-sagittal CC body, and landmarks were placed at the center of each gate. The CST was delineated using two AND-gates (Fig. 1D), defined in axial projections and placed around the peduncle (Inf) and the medial motor area of the cortex (Sup). Landmarks were defined at each gate and at the level of the ventricles (Cent). The CC was extracted using two AND-gates, separated by 12 mm and centered on the mid-sagittal plane, that excluded the tracts outside of the intersections so that a truncated mid-sagittal segment was selected (Fig. 1G). The landmarks were placed at the inferior edges of the genu (Ant) and splenium (Post), as well as at the boundary between the body and the genu (PreA) and the splenium (PreP), respectively.

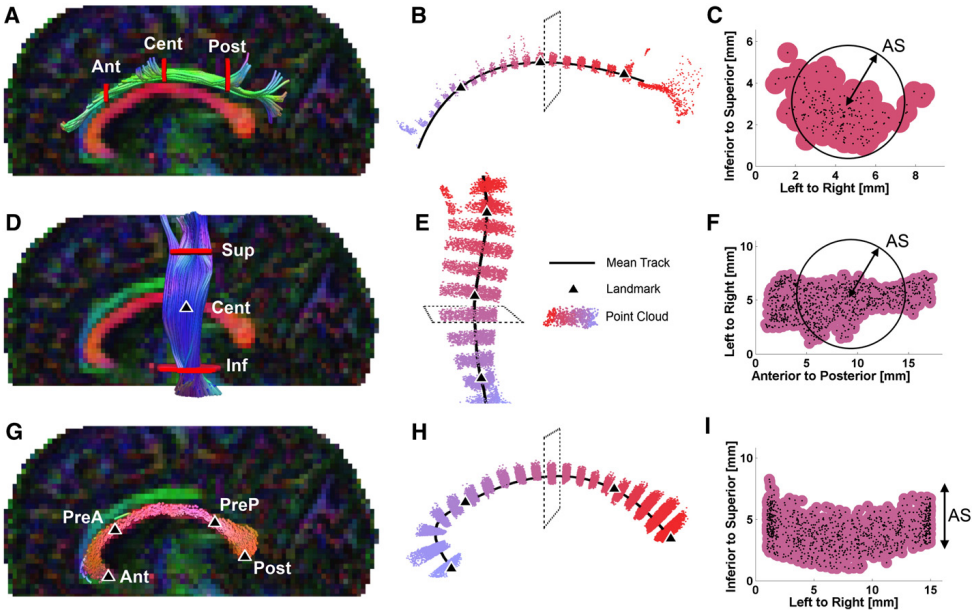

Fig. 1. The left column shows tractographies of the left hand side CG (A) and CST (D), as well as the mid-sagittal truncation of the CC (G), superimposed on a color FA-map. The AND-gates, used for structure delineation, are shown as red lines, and the anatomical landmarks are shown as black triangles (note that landmarks that coincide with AND-gates are not shown, and that the gates defining the CC are not displayed). The middle column (B, E and H) shows the mean track (black line), the point cloud that defines the tracts in 3D-space (red to blue dots), the landmarks (black triangles), and the selected cross section (dashed line) for display in the right column. Every other interval of the point cloud is omitted in order to visualize the path of the mean track (note that only points between the outermost landmarks were used in the evaluation and that the figures are not to scale). The parametric information contained within each sub-interval of the point cloud is projected onto the mean track, thus creating parameter vectors of MD, FA, MK and RK, that can be normalized across subjects with respect to the anatomical landmarks. The right column (C, F and I) shows cross sections of the point cloud, in a plane that is perpendicular to the mean track. Each point is the center of a circle with a radius of 0.5 mm. The area of the cross section, created in each interval, was used to quantify the apparent size (AS) of the structures. In the CG (C) and CST (F) the AS was defined as the radius of a circle with the same area as the structure. In the CC (I) the AS was defined as the thickness of the point cloud.

The sub-segments of each structure were defined by the intervals between landmarks, creating two sub-segments in the CG and CST, and three sub-segments in the CC. Tractography and parameter extraction were performed independently on all of the bootstrapped data sets.

Parameter evaluation

Diffusion parameters were calculated as a function of position to retain spatial information along the tract, employing an evaluation method resembling that presented by Colby et al. (2012). The evaluation was performed in three steps. First, a single *mean track* was created to represent the geometrical features of the track bundle. Second, diffusion parameters were projected onto the mean track to create parameter vectors. In the final step, the parameter vectors were normalized across subjects using anatomical landmarks as points of reference. Fig. 1 shows representative tractographies of the CG, CST and CC (Figs. 1A, D, G), along with the *point cloud* that makes up the tracts and constituted the cross-sections selected along the mean track (Figs. 1B, E, H). All calculations were performed using in-house developed software, implemented in Matlab, and details on the three steps are given below.

The first step was to calculate the mean track, which was represented by a number of consecutive points in 3D-space (m_i), with each point placed at the center of mass of the cross section of the track bundle. Note that the mean track in the CG and CST is directed *along* the WM fibers, while in the CC it runs *perpendicular* to the WM fibers (Fig. 1).

In the second step, projection of the diffusion parameters to the mean track was performed by averaging the parameter values from all points in the cross section associated with m_i. The cross section included at most one point per track, with the point selected being the one closest to a plane with normal $n = m_{i+1} - m_i$, with its origin in m_i. Only points within 1 mm distance from each plane were included in the cross section, resulting in a cross section thickness of 2 mm. The calculation of the apparent structure size (AS) was performed by determining the apparent *radius* (in the case of the CG and CST) or *thickness* (in the case of the CC) of the tract bundle mask at each cross section. The area of the mask was calculated by representing each point in the cross-section by a circle with radius 0.5 mm (Figs. 1C, F, I). Only non-overlapping parts of the circles contributed to the AS.

In the third step, the individual parameter vectors were normalized in order to align them with respect to the anatomical landmarks. Each landmark was first associated with the point on the mean track closest to the landmark, which allowed the calculation of average interval lengths, i.e., the mean path track lengths between two landmarks. Next, the mean tracks and their associated parameter vectors were linearly interpolated so that the interval lengths of the individual mean tracks conformed to the average interval lengths. Further, the mean tracks were resampled to contain 100 equidistant elements

Table 1
Relative effect sizes ($\Delta\mu/\mu$) of various conditions as observed in DTI and DKI parameters, and group sizes investigated (n, reported as size of control group + patient group). The values of $\Delta\mu/\mu$ are reported in regions where significant differences in group means were found. The coefficient of variation (CV) is the value reported for the control group specified for each parameter separately. In cases where the variability was not reported it is marked with a dash (–).

Source	Condition	Region	Parameter	CV [%]	$\Delta\mu/\mu$ [%]	n
Wang et al. (2011)	PD	Caudate, putamen, globus palidus, substantia nigra	MK	13	15–30	30 + 30
Grossman et al. (2012)	mTBI	Thalamus, internal capsule, splenium of the CC, centum semiovale	MK	1–2	2–3	14 + 22
			FA	2	3	
			MD	1–4	1–2	
Kim et al. (2006)	PTSD	CG bundle	FA	11–18	12–26	21 + 21
Zhang et al. (2011)	MDD	Right uncinate	FA	7	7	21 + 21
			RD	7	5	
Ito et al. (2008)	PSP	Anterior CC	MD	17	15–34	19 + 7
			FA	8	12–17	
Bozzali et al. (2012)	AD	Cingulum	MD	6	17	14 + 31
			FA	8	12	
Stenset et al. (2011)	MCI	Cingulum, genu CC	FA	10–15	7–13	26 + 12
			RD	17–29	11–22	
Tang et al. (2010)	EOS	Right anterior cingulum	FA	–	14	38 + 38

AD Alzheimer's disease, EOS early-onset schizophrenia, MDD major depressive disorder, mTBI mild traumatic brain injury, NAWM normal appearing white matter, PD Parkinson's disease, PSP progressive supranuclear palsy, PTSD posttraumatic stress disorder, RD radial diffusivity.

per DKI parameter and WM structure, on which the final analysis was performed. To simplify the presentation of results for bilateral structures, the CG and CST estimates were evaluated as the average of both sides for each individual subject.

Statistical analysis

The statistical analysis comprised three aspects, all performed to improve the design of future DKI studies: first, calculating the group size required to find a subtle difference in group means, second, answering the question of whether to scan longer per subject or more subjects by analyzing the relative contribution of noise to the total variance, and third, analyzing the potential reduction in group size requirement resulting from the addition of relevant covariates.

The group sizes required to obtain a statistical power of $\pi = 0.9$ at a relative effect size of 5% (i.e., absolute effect size was $\Delta\mu = 0.05 \cdot \mu$) were calculated for whole structures and sub-segments. We assumed that the difference in group mean values was tested using a two-tailed Student's t-test at a significance level of $\alpha = 0.05$, assuming that the control and experimental groups were of equal sizes. Furthermore, the analysis assumed equal variance in both groups, with a value given by that observed in the group of healthy volunteers. Even at a moderate departure from the assumption of equal group size and variance, the analysis is expected to produce robust estimates of the t-statistic and the statistical power of the study (Cohen, 1976). The effect size was chosen to represent a subtle but physiologically relevant change in DKI parameters, according to a survey of relevant DTI and DKI studies of the brain (Table 1). In this compilation, the approximate span of relative effect sizes is between 1 and 30%. However, it should be noted that the relative effect size can be much higher for more severe tissue alterations such as tumors and edema (Cauter et al., 2012; Harris et al., 2008; Jensen et al., 2011). Required group sizes were calculated by iteratively adjusting n until the desired statistical power was reached.

The total variance, measured in the control group, was separated into inter-subject variance and imaging noise variance in order to determine the effect of increasing scan time or group size (Eq. (6)). The

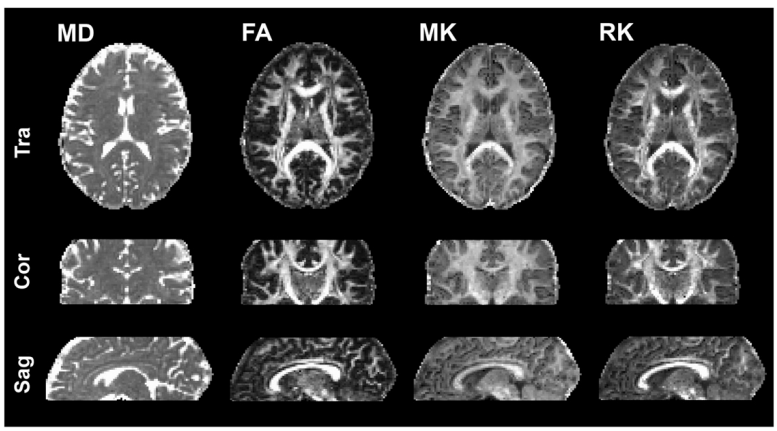

Fig. 2. The image depicts transversal (Tra), coronal (Cor), and sagittal (Sag) projections of the DKI parameter maps (MD, FA, MK and RK, respectively). The FA map displays the highest contrast between WM and GM, followed by RK and MK, in descending order. MD displays a high contrast when comparing CSF to WM and GM, but is low when comparing WM to GM.

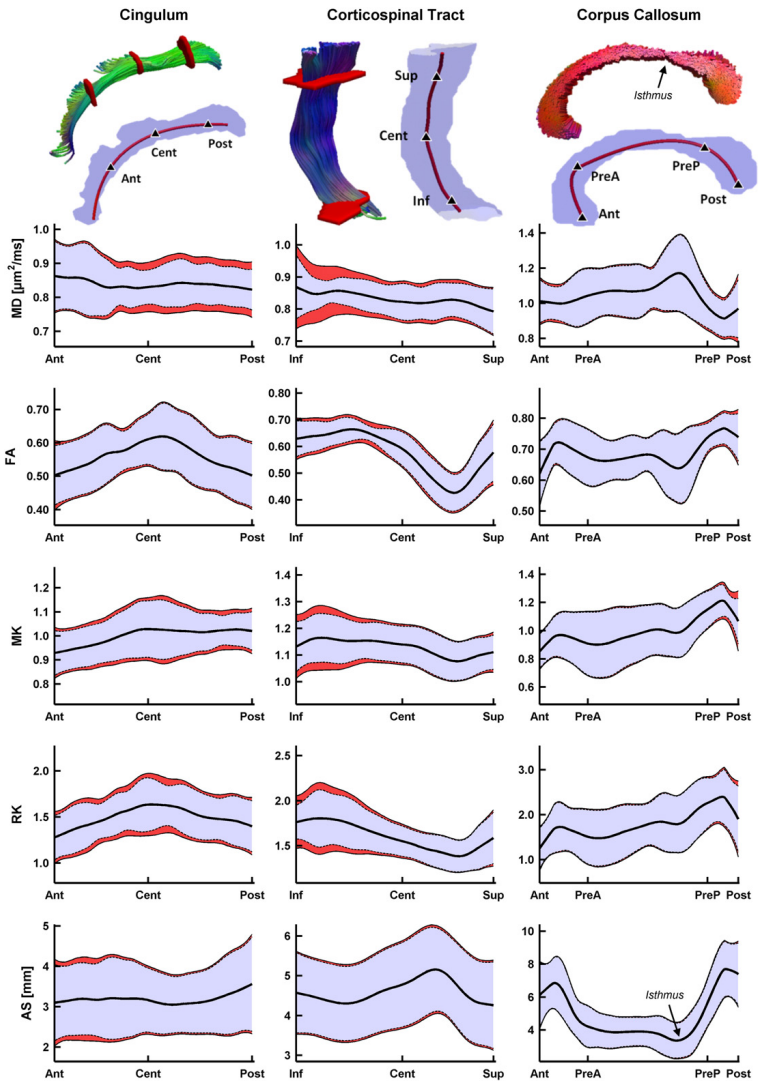

Fig. 3. The tractographies (top row) show a representative right-hand side CG (green tracts), CST (blue tracts), and a mid-sagittal truncation of the CC (red tracts) together with the AND-gates (red) used to segment the structures from the whole-brain tractography (not shown for the CC). The figure also shows a transparent representation of the same structures (blue) containing the mean track (red tract), and the landmarks (black triangles) used to normalize data. The plots show the group mean values (bold black line) of the apparent size (AS, bottom row) and the DKI parameters (MD, FA, MK and RK) as a function of anatomical position along the structures. The parameter variability is visualized by thin black lines, where the solid lines show two standard deviations from the mean ($2V_{\mathrm{tot}}^{1/2}$), and the dashed lines show two standard deviations from the mean after the contribution from noise has been removed ($2V_{\mathrm{inter}}^{1/2}$, Eq. (3)). The red field visualizes the variability contributed by noise. In the CG, MD displays a high inter-subject variability in the anterior regions, whereas MK has its highest variability in the central region. Both FA and RK peak at the center, tapering off towards the anterior and posterior endpoints. Parameter variations along the CST are most prominent for the FA, probably due to the crossing-fiber region in the superior segment. The variability of all parameters, except the FA and AS, is elevated in the inferior parts of the structure. Similarly to the CST, the CC displays significant parameter variation along the structure. In the thinnest region, the *isthmus* (black arrows), MD and FA are strongly elevated and reduced, respectively, probably due to the PVE at the WM/CSF interface. The CC also displays a much smaller relative dependence on noise (red area) compared with the CG and CST. It is also notable how the AS and the FA both follow the same trend, which showcases the modulating effect of PVE on diffusion parameters due to tract morphology.

noise component (V_{noise}) was estimated from the bootstrapped data, by assuming that the variance in the simulated data was due to noise. To obtain V_{inter}, the noise component was subtracted from the total variance according to Eq. (3).

DKI parameter correlation with the apparent structure size was assessed using Pearson's correlation coefficient (r). The effects of correlation on the statistical power were calculated according to Eq. (9), assuming that the two groups were matched with respect to AS, i.e., that there was no inflation due to predictor covariance ($R^2_{c,AS} = 0$).

Results

Fig. 2 shows axial projections of the DKI parameter maps in one representative subject. Visually, the MK and RK maps are similar to the FA maps, with the highest values found in the WM. MK and RK maps are similar, since MK is partly determined by RK just as RD is partly determined by MD. The numerical values of the MK, RK, and FA maps are the lowest in the ventricles, as expected, due to the nearly unrestricted water diffusion in the ventricular cerebrospinal fluid (CSF).

Fig. 3 shows the DKI parameters and AS, and their variability, as a function of anatomical position along each WM structure. The variability is represented by two components: the blue area shows two standard deviations from the mean of the inter-subject variability and the blue and red areas together show the total variability. The evaluation of parameters along structures allowed within-structure details to be resolved. For example, FA was reduced in the superior parts of the CST where the tract intersects with the CC. In the CC, MD was elevated and FA was reduced at the thinnest part (isthmus), probably due to stronger PVE with CSF at this location. This mode of visualization also supplies insight into the parameter covariance; MK generally showed inverse correlation with MD, whereas the variation of RK exhibited similar patterns to FA and MK. The influence of noise and inter-subject variability was also dependent on position. For example, DKI parameters were more affected by noise and inter-subject variability in the inferior parts of the CST than in its superior parts (Fig. 3, center column). Table 2 presents these results in a condensed format, showing average parameter values with coefficients of variation in the sub-segments, compared with values from whole tract averages. Table 2 also shows the relative variability induced by imaging and post-processing noise, as calculated from the bootstrapped noise simulations. In most of the structures and parameters, less than 30% of the total variance was attributed to the influence of noise. The magnitude of the noise component was heterogeneous along the structures, indicated by a varying thickness of the red area in Fig. 3. The value of RV_{noise} was found to be at its highest in the inferior segment of the CST, where it contributed with as much as 54% of the total variance in MD and approximately 35% of the variance in other DKI parameters (Fig. 3 and Table 2). The lowest relative noise contribution was found in the CC.

Table 3
Calculated group sizes (n) for DKI parameters (MD, FA, MK and RK) and apparent structure size (AS), required in order to generate a statistical power of $\pi = 0.9$ at an effect size of 5% and a significance level of $\alpha = 0.05$. The group sizes show the number of subjects needed in each group and were estimated for whole structures as well as sub-structures. The values of n mainly reflects the total parameter variability, meaning that a low V_{total} makes it easier to detect the proposed 5% change, making the required group size comparatively small.

		MD	FA	MK	RK	AS
CG	Ant	21	39	21	63	183
	Post	18	51	18	59	147
	Whole	14	34	17	47	148
CST	Inf	17	17	15	55	109
	Sup	13	38	11	30	108
	Whole	13	17	11	37	106
CC	Ant	32	28	65	199	100
	Cent	36	18	68	181	122
	Post	38	13	22	146	101
	Whole	26	14	48	137	85

Table 3 shows the group size requirements in whole structures and in structure sub-segments, as calculated from the parameter variance. The most precise parameters, requiring the smallest group sizes, were MD (n = 10–40), followed by FA (n = 10–50). The kurtosis and structure size parameters generally demanded larger group sizes, where MK was the most precise (n = 10–70). The parameters RK and AS tended to require more than twice the number of subjects compared to any of the other parameters (n = 30–200, and n = 80–180, respectively). The worst case was found in the anterior CC where 200 subjects were required for detecting subtle group-wise differences in RK. Note that RK, in this case, correlated strongly with MK ($r = 0.93$), suggesting that RK may not add substantially to the information already provided by the more precise MK. Evaluating whole structures, without dividing them into sub-segments, generally resulted in a lower group size requirement, although some combinations of structure segments and parameters exhibited behavior contrary to this generalization, for example, the MK in the posterior sub-segment of the CC. This indicates that sub-structures may exhibit smaller inter-subject variability compared to whole structures, despite having a smaller volume, thus increasing the statistical power when evaluated as a sub-structure.

Correlations between the investigated DKI parameters and the apparent structure size are shown in Table 4. Significant correlations between AS and several DKI parameters were found in the CG and CC. The most prominent correlation was found for FA in the CG (r = 0.80, $p < 10^{-7}$, for whole structure, Fig. 4) and for MD in the CC ($r = -0.53$, $p < 10^{-3}$, for posterior sub-segment). Adding the AS as a covariate could reduce the group size requirement by 30–60% in the

Table 2
DKI parameter values in the group of healthy volunteers (n = 31), calculated in the cingulum (CG), corticospinal tract (CST) and corpus callosum (CC). The mean value (μ) is presented along with the coefficient of variation (CV in %) and the relative noise contribution to variance (RV_{noise} in %). Average whole-structure CVs were 4.2, 4.7, 4.9 and 8.8% for MD, FA, MK and RK, respectively. The most prominent contributor to variance was generally the inter-subject variability (reflected by a low RV_{noise}).

		MD [μm²/ms]			FA			MK			RK		
		μ	CV	RV_{noise}	μ	CV	RV_{noise}	μ	CV	RV_{noise}	μ	CV	RV_{noise}
CG	Ant	0.84	4.6	20	0.56	6.6	8	0.98	4.7	20	1.47	8.4	25
	Post	0.84	4.2	47	0.57	7.6	5	1.02	4.2	28	1.53	8.2	25
	Whole	0.84	3.7	42	0.56	6.1	6	1.00	4.1	22	1.50	7.2	28
CST	Inf	0.85	4.2	54	0.64	4.1	35	1.15	3.8	36	1.72	7.9	35
	Sup	0.82	3.6	24	0.50	6.4	16	1.10	3.1	9	1.46	5.7	8
	Whole	0.83	3.6	42	0.57	4.1	33	1.13	3.2	25	1.60	6.4	25
CC	Ant	1.01	5.9	12	0.69	5.5	6	0.94	8.6	5	1.59	15.2	6
	Cent	1.09	6.3	5	0.67	4.2	5	0.98	8.8	5	1.75	14.5	4
	Post	0.93	6.5	17	0.76	3.6	19	1.17	4.8	35	2.27	13.0	14
	Whole	1.04	5.3	8	0.69	3.6	8	1.00	7.4	5	1.80	12.6	4

Table 4
Pearson's correlation coefficient (r) describing the association of DKI parameters (MD, FA, MK and RK) with the apparent structure size (AS). As expected, AS correlated with DKI parameters in the CG and CC which means that structure size may account for some of the measured variability. No significant correlation was found in the CST, as was expected due to the high AS dependence on AND-gate definition. No correction for multiple comparisons was done; however, no more than 5 significant correlations are expected on the 5% level for 40 independent comparisons.

		MD	FA	MK	RK
CG	Ant	−0.23	0.57‡	0.33	0.17
	Post	−0.31	0.69‡	0.37†	0.48‡
	Whole	−0.32	0.80‡	0.40†	0.45†
CST	Inf	−0.12	0.06	−0.10	0.01
	Sup	−0.11	0.17	0.02	0.29
	Whole	−0.12	0.17	−0.07	0.13
CC	Ant	−0.48‡	0.26	0.11	−0.14
	Cent	−0.44†	0.42†	0.18	0.15
	Post	−0.58‡	−0.12	−0.24	−0.44†
	Whole	−0.53‡	0.32	0.05	−0.09

† $p < 0.05$.
‡ $p < 0.01$.

CG and 20–30% in the CC (Eq. (10)). No correlations between DKI parameters and AS were found in the CST.

Discussion

In this study, we investigated the group sizes required to find subtle differences in group means of DKI parameters in three WM structures with a statistical power of 0.9. The results, with respect to group sizes required, not only showed a large heterogeneity between the various DKI parameters and between the three WM structures investigated, but also heterogeneity between different sub-segments within the structures (Table 3). A similar heterogeneity in group size requirement has been found for DTI by Heiervang et al. (2006) when comparing the CG, CST and CC. The heterogeneity in variability implies that, for a fixed relative effect size, the statistical power varies between structures and their sub-segments, as well as between parameters. For example, in the data presented, finding a difference in MK between two groups is more likely in the posterior CC than in its anterior part even if the relative effect size in these sub-structures is equal. Knowledge of this spatial and parameter-specific variation is expected to benefit studies aiming at early diagnosis, and it is critical when a pathogenesis pattern is inferred from the observation of significant alterations in one part of the brain before another. In other words, the conclusion that a disease did not have its origin in a given part of the brain must be accompanied by the knowledge that an effect was likely to have been discovered if, in fact, it was there. Thus, awareness of statistical power is crucial both for study design and for interpretation of results from DTI and DKI studies. Knowledge of these characteristics allows studies to be designed in a way that ensures sufficient power in all structures investigated, since the structure with the lowest statistical power defines the lower limit of the required group size. Such a procedure could result in some structures becoming overpowered, a potential downside for a study (Ferguson, 2009), hence all statistically significant group-wise differences should be scrutinized with respect to the effect size, considering its practical or physiological relevance using similar studies as a guideline (Table 1).

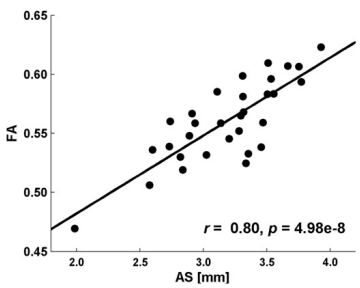

Fig. 4. Correlation between the mean FA and mean AS in the CG, for the 31 healthy subjects. The regression line (black line) shows that a CG bundle with a high AS is likely to exhibit a high FA. Note that the correlation coefficient value of $r = 0.8$ indicates that 64% of the variance in FA can be explained by its association to AS. If AS is known, this variance contribution can be removed (Eq. (10)).

The analysis of the variations in variability along the structures could also be used to reduce group size demands, by sampling only those parts of a structure where the variability is expected to be low, assuming, of course, that homogeneous whole-structure alterations are expected. This conclusion is somewhat contra-intuitive, since inclusion of larger volumes normally reduces the standard error of the mean. It should also be pointed out that the segment exhibiting minimal variability might vary depending on the evaluated parameter. An example of high group-wise variability can be seen in the superior part of the CST, where the group size for FA is three times larger than compared to the inferior part, which is likely due to the presence of crossing fibers in this region (Jeurissen et al., 2013; Vos et al., 2012). By contrast, group size demands for RK are a factor of two smaller in the superior part of CST. Thus, some WM structures could benefit from being subsampled, avoiding regions where variability is known to be high, resulting in favorable reductions in group size demands.

Two other strategies may also increase the power of a study or reduce the group size demands; first, to discern whether to prioritize longer scan times or to include more subjects when designing the study, and second, to incorporate hidden covariates in the data analysis (Vos et al., 2011). The first strategy was investigated by determining the portion of variability that could be attributed to effects other than the true differences between subjects, i.e., variability introduced by imaging and post-processing noise. This investigation was performed under the assumption that the variance of the noise component can be reduced by increasing the scan time dedicated to each subject (Eq. (5)). In most structures, imaging and post-processing noise contributed with 5 to 25% of the total variance. In segments with $RV_{\text{noise}} \leq 25\%$, doubling the scan time for each subject would result in group size reductions of only 10%. In segments with higher values of RV_{noise}, such as the posterior CG, inferior CST and posterior CC, the corresponding reduction is 20%. The values of RV_{noise} reported herein are lower than those reported for a similar selection of WM structures by Clayden et al. (2009) for DTI performed at 1.5 T. In that study, the noise component was generally dominant for both MD and FA, indicating that scan time extension could provide a viable power improvement at that field strength. By contrast, our study suggests that the gain in statistical power resulting from measuring twice as long per subject, for the DKI protocol employed here, is comparable with increasing the group size by no more than 5–20%. Therefore, it could be more profitable to invest resources in the inclusion of more patients rather than extending the individual scan time, provided that it is practically feasible.

The second strategy to increase the statistical power described in this report is to include hidden covariates in the analysis. The potential efficacy of this strategy was investigated by using the structure size as a covariate, which showed that correcting for correlations with AS could lower group size requirements by up to 60% for FA in the CG, and 30% for MD in the CC. We expected the correlation between AS and DKI parameters to be the highest for structures and parameters showing a high contrast to the surrounding tissue, as the probable mechanism responsible for the correlation is the variable amounts of partial volume effects induced by variations in structure size (Vos

et al., 2011). Further, we expected this mechanism to be stronger for small structures, in which surrounding tissue comprises a larger partial volume fraction. In the data presented, the CG demonstrated these effects in accordance with our predictions in that FA, which exhibited the highest contrast between the WM of the CG and the surrounding GM (Fig. 1, coronal projections), had the strongest correlation to the size of the structure, followed by RK and MK. Further, MD did not correlate significantly with AS, again explained by the low contrast between the WM of the CG and the GM surrounding it. In the CC, MD was strongly correlated to AS, probably due to the large interface with the CSF-filled lateral ventricles. As expected, correlations with size were absent in the CST, since its AS is highly dependent on the inclusion gate geometry rather than the structure size itself (Wakana et al., 2007). Although the strength and direction of correlation with volume may vary across the brain (Fjell et al., 2008), the presence of an association implies that any measured difference in diffusion parameters may be due to either alterations in tissue microstructure or in the amount of PVE. Disentangling these effects requires a correction for size, as described by Vos et al. (2011). For example, our results indicate that a 4% difference in FA may be induced by a radius difference of 10% in the CG, even if the microstructure is otherwise equal. Therefore, the search and correction for hidden covariates such as structure size, has the potential not only to increase the power of a given study, but also to allow for better interpretations of the results (Bendlin et al., 2010; Cao and Gold, 2008; Vos et al., 2011). Similarly the effects of age can be easily included by expanding the currently used methods. However, since the effects of aging are well documented elsewhere (Lebel et al., 2008; Löbel et al., 2009; Sullivan and Pfefferbaum, 2006), age was only considered as a possible confounder in the association between diffusion parameters and the structure size, and was found to have no significant correlation ($\alpha = 0.05$) with AS in any WM structure or sub-structure.

Finally, investigating group-wise AS differences would require much larger group sizes than for the DKI parameters, as it exhibits a large inter-subject variation (CV = 10–15% in all evaluated structures). This result is in agreement with multiple studies of the volumes of the healthy brain and individual structures, in which the CVs have been reported to be in the range of 10–20% (Choo et al., 2010; Flashman et al., 1997; Kristo et al., 2012; Pitel et al., 2010; Teipel et al., 2003). This indicates that a 5% effect in AS, as used in this study, may be regarded to be small (Cohen, 1976) compared to the effect in diffusion parameters. The group size requirements in DKI as compared to DTI are expected to be higher, since diffusional kurtosis can only be probed at relatively high *b*-values with higher signal attenuation. Higher *b*-values also demands longer echo times. Taking this into account, DKI may still be preferable to DTI in tissue where the DTI model is invalid, for example, in regions with complex fiber organization. An example of this may be found in Alzheimer's disease, where the FA unexpectedly increases in areas of crossing fibers, probably due to the removal of one fiber population (Douaud et al., 2011). Notably, the MK maps are smooth in regions where the FA shows the characteristic reduction due to fiber crossings (Fig. 2).

A limiting factor in the study is the bootstrapping procedure used to estimate the influence from noise since it is not exactly equivalent to repeated measurements. Although it is capable of assessing the contribution of specific sources of error (Jones and Pierpaoli, 2005), we believe that the reported magnitude of the noise component is slightly overestimated. This conclusion is supported by the observation that the variability between the seven repeated scans (data not shown), used as the base for bootstrapping, was generally lower than that found in the bootstrapped data and that it cannot be entirely explained by the expected precision in the estimation of the contribution from bootstrapping noise. For example, the seven repeated scans exhibited less of the elevated variance otherwise found in the inferior CST and posterior CG. The overestimation of variance in the bootstrapped parameter maps could be due to the large temporal spacing between images, resulting in exaggerated movement compared to a normal acquisition. However, the conclusion derived from this evaluation, i.e., that increased group sizes improve the statistical power more than extended scan times, is still valid.

Conclusion

The variability in DKI parameters varies across the brain, and was seen to vary even within single WM structures. This implies that the statistical power is dependent on location, which could be a serious confound in studies aiming at early diagnosis of disease. Such studies typically focus on finding the region from which the alteration of cerebral microstructure originates. Lack of attention to the risk of being underpowered in some of the evaluated regions may lead to an incorrect interpretation of the results, i.e., the absence of significance may be interpreted as the absence of true effect. Although this study was based on the DKI model it should be noted that, since DKI includes the DTI model, these conclusions are also valid for conventional DTI.

An increase in statistical power can be achieved by extending the scan time per subject, although this was shown to be less potent than spending that time on scanning more subjects. Another strategy that may enhance the statistical power is to correct for hidden covariates, such as the size of the structure. In WM structures where the DKI parameters correlated significantly with the size of the structure, such a correction could reduce the group size requirements to approximately half of their initial size. In order to disentangle effects of variable PVE and alterations of underlying microstructure on group-wise differences in DTI and DKI parameters, correction for structure size should be performed in group comparisons, at least in the corpus callosum and cingulum.

Acknowledgments

This research project was supported by the Swedish Research Council, grants no. 2010-36861-78981-35 and 13514, and the Swedish Cancer Society grant no. CAN 2009/1076.

Conflict of interest statement

The authors declare that there is no conflict of interest.

References

Bendlin, B.B., Fitzgerald, M.E., Ries, M.L., Xu, G., Kastman, E.K., Thiel, B.W., Rowley, H.A., Lazar, M., Alexander, A.L., Johnson, S.C., 2010. White matter in aging and cognition: a cross-sectional study of microstructure in adults aged eighteen to eighty-three. Dev. Neuropsychol. 35, 257–277.

Bozzali, M., Giulietti, G., Basile, B., Serra, L., Spanò, B., Perri, R., Giubilei, F., Marra, C., Caltagirone, C., Cercignani, M., 2012. Damage to the cingulum contributes to Alzheimer's disease pathophysiology by deafferentation mechanism. Hum. Brain Mapp. 33, 1295–1308.

Cao, N., Gold, B., 2008. Partial volume effect of cingulum tract in diffusion-tensor MRI. Proc. SPIE 6916, 1U.

Cauter, S., Veraart, J., Sijbers, J., Peeters, R.R., Himmelreich, U., Keyzer, F., Gool, S.W., Calenbergh, F., Vleeschouwer, S., Hecke, W., Sunaert, S., 2012. Gliomas: diffusion kurtosis MR imaging in grading. Radiology 263, 492–501.

Cheung, M.M., Hui, E.S., Chan, K.C., Helpern, J.A., Qi, L., Wu, E.X., 2009. Does diffusion kurtosis imaging lead to better neural tissue characterization? A rodent brain maturation study. NeuroImage 45, 386–392.

Choo, I.H., Lee, D.Y., Oh, J.S., Lee, J.S., Lee, D.S., Song, I.C., Youn, J.C., Kim, S.G., Kim, K.W., Jhoo, J.H., Woo, J.I., 2010. Posterior cingulate cortex atrophy and regional cingulum disruption in mild cognitive impairment and Alzheimer's disease. Neurobiol. Aging 31, 772–779.

Clayden, J.D., Bastin, M.E., Storkey, A.J., 2006. Improved segmentation reproducibility in group tractography using a quantitative tract similarity measure. NeuroImage 33, 482–492.

Clayden, J.D., Storkey, A.J., Maniega, S.M., Bastin, M.E., 2009. Reproducibility of tract segmentation between sessions using an unsupervised modelling-based approach. NeuroImage 45, 377–385.

Cohen, J., 1976. Statistical Power Analysis for the Behavioral Sciences, 2nd edition. Lawrence Erlbaum Associates, Publishers.

Colby, J.B., Soderberg, L., Lebel, C., Dinov, I.D., Thompson, P.M., Sowell, E.R., 2012. Along-tract statistics allow for enhanced tractography analysis. NeuroImage 59, 3227–3242.

Corouge, I., Fletcher, P.T., Joshi, S., Gouttard, S., Gerig, G., 2006. Fiber tract-oriented statistics for quantitative diffusion tensor MRI analysis. Med. Image Anal. 10, 786–798.
Douaud, G., Jbabdi, S., Behrens, T.E.J., Menke, R.A., Gass, A., Monsch, A.U., Rao, A., Whitcher, B., Kindlmann, G., Matthews, P.M., Smith, S., 2011. DTI measures in crossing-fibre areas: increased diffusion anisotropy reveals early white matter alteration in MCI and mild Alzheimer's disease. NeuroImage 55, 880–890.
Falangola, M.F., Jensen, J.H., Babb, J.S., Hu, C., Castellanos, F.X., Martino, A., Ferris, S.H., Helpern, J.A., 2008. Age-related non-Gaussian diffusion patterns in the prefrontal brain. J. Magn. Reson. Imaging 28, 1345–1350.
Ferguson, C., 2009. An effect size primer: a guide for clinicians and researchers. Prof. Psychol.-Res. Pr. 40, 532–538.
Fieremans, E., Jensen, J.H., Helpern, J.A., 2011. White matter characterization with diffusional kurtosis imaging. NeuroImage 58, 177–188.
Fjell, A.M., Westlye, L.T., Greve, D.N., Fischl, B., Benner, T., Van Der Kouwe, A.J.W., Kouwe, A.J., Salat, D., Bjørnerud, A., Due-Tønnessen, P., Walhovd, K.B., 2008. The relationship between diffusion tensor imaging and volumetry as measures of white matter properties. NeuroImage 42, 1654–1668.
Flashman, L., Andreasen, N., Flaum, M., Swayze, V., 1997. Intelligence and regional brain volumes in normal controls. Intelligence 25, 149–160.
Grossman, E.J., Ge, Y., Jensen, J.H., Babb, J.S., Miles, L., Reaume, J., Silver, J.M., Grossman, R.I., Inglese, M., Ge, Y., Jensen, J.H., Babb, J.S., Miles, L., Reaume, J., Silver, J.M., Grossman, R.I., 2012. Thalamus and cognitive impairment in mild traumatic brain injury: a diffusional kurtosis imaging study. J. Neurotrauma 29, 2318–2327.
Harris, G.J., Jaffin, S.K., Hodge, S.M., Kennedy, D., Caviness, V.S., Marinkovic, K., Papadimitriou, G.M., Makris, N., Oscar-Berman, M., 2008. Frontal white matter and cingulum diffusion tensor imaging deficits in alcoholism. Alcohol. Clin. Exp. Res. 32, 1001–1013.
Heiervang, E., Behrens, T.E., Mackay, C.E., Robson, M.D., Johansen-Berg, H., 2006. Between session reproducibility and between subject variability of diffusion MR and tractography measures. NeuroImage 33, 867–877.
Hori, M., Fukunaga, I., Masutani, Y., Nakanishi, A., Shimoji, K., Kamagata, K., Asahi, K., Hamasaki, N., Suzuki, Y., Aoki, S., 2012. New diffusion metrics for spondylotic myelopathy at an early clinical stage. Eur. Radiol. 22, 1797–1802.
Ito, S., Makino, T., Shirai, W., Hattori, T., 2008. Diffusion tensor analysis of corpus callosum in progressive supranuclear palsy. Neuroradiology 50, 981–985.
Jensen, J.H., Helpern, J.A., 2010. MRI quantification of non-Gaussian water diffusion by kurtosis analysis. NMR Biomed. 23, 698–710.
Jensen, J.H., Helpern, J.A., Ramani, A., Lu, H., Kaczynski, K., 2005. Diffusional kurtosis imaging: the quantification of non-Gaussian water diffusion by means of magnetic resonance imaging. Magn. Reson. Med. 53, 1432–1440.
Jensen, J.H., Falangola, M.F., Hu, C., Tabesh, A., Rapalino, O., Lo, C., Helpern, J.A., 2011. Preliminary observations of increased diffusional kurtosis in human brain following recent cerebral infarction. NMR Biomed. 24, 452–457.
Jeurissen, B., Leemans, A., Tournier, J., Jones, D.K., Sijbers, J., 2013. Investigating the prevalence of complex fiber configurations in white matter tissue with diffusion magnetic resonance imaging. Hum. Brain Mapp. http://dx.doi.org/10.1002/hbm.22099.
Jones, D.K., Cercignani, M., 2010. Twenty-five pitfalls in the analysis of diffusion MRI data. NMR Biomed. 23, 803–820.
Jones, D.K., Pierpaoli, C., 2005. Confidence mapping in diffusion tensor magnetic resonance imaging tractography using a bootstrap approach. Magn. Reson. Med. 53, 1143–1149.
Kim, S.J., Jeong, D., Sim, M.E., Bae, S.C., Chung, A., Kim, M.J., Chang, K.H., Ryu, J., Renshaw, P.F., Lyoo, I.K., 2006. Asymmetrically altered integrity of cingulum bundle in posttraumatic stress disorder. Neuropsychobiology 54, 120–125.
Klein, S., Staring, M., Murphy, K., Viergever, M.A., Pluim, J.P., 2010. ElastiX: a toolbox for intensity-based medical image registration. IEEE Trans. Med. Imaging 29, 196–205.
Kristo, G., Leemans, A., Gelder, B., Raemaekers, M., Rutten, G., Ramsey, N., 2012. Reliability of the corticospinal tract and arcuate fasciculus reconstructed with DTI-based tractography: implications for clinical practice. Eur. Radiol. http://dx.doi.org/10.1007/s00330-012-2589-9.
Laird, N.M., Ware, J.H., 1982. Random-effects models for longitudinal data. Biometrics 38, 963–974.
Lätt, J., Nilsson, M., Wirestam, R., Ståhlberg, F., Karlsson, N., Johansson, M., Sundgren, P.C., Van Westen, D., 2012. Regional values of diffusional kurtosis estimates in the healthy brain. J. Magn. Reson. Imaging. http://dx.doi.org/10.1002/jmri.23857.
Lebel, C., Walker, L., Leemans, A., Phillips, L., Beaulieu, C., 2008. Microstructural maturation of the human brain from childhood to adulthood. NeuroImage 40, 1044–1055.
Leemans, A., Jeurissen, B., Sijbers, J., Jones, D.K., 2009. ExploreDTI: a graphical toolbox for processing, analyzing, and visualizing diffusion MR data. Proc. Int. Soc. Magn. Reson. Med. 17, 3536.
Lenth, R., 2001. Some practical guidelines for effective sample size determination. Am. Stat. 55, 187–193.
Löbel, U., Sedlacik, J., Güllmar, D., Kaiser, W.A., Reichenbach, J.R., Mentzel, H.-J., 2009. Diffusion tensor imaging: The normal evolution of ADC, RA, FA and eigenvalues studied in multiple anatomical regions of the brain. Neuroradiology. 51, 253–263.
Maxwell, S.E., Kelley, K., Rausch, J.R., 2008. Sample size planning for statistical power and accuracy in parameter estimation. Annu. Rev. Psychol. 59, 537–563.
O'Goreman, R.L., Jones, D.K., 2006. Just how much data need to be collected for reliable bootstrap DT-MRI? Magn. Reson. Med. 56, 884–890.
Pfefferbaum, A., Adalsteinsson, E., Sullivan, E.V., 2003. Replicability of diffusion tensor imaging measurements of fractional anisotropy and trace in brain. J. Magn. Reson. Imaging 18, 427–433.
Pitel, A., Chanraud, S., Sullivan, E.V., Pfefferbaum, A., Chanraud, S., 2010. Callosal microstructural abnormalities in Alzheimer's disease and alcoholism: same phenotype, different mechanisms. Psychiatry Res. Neuroimaging 184, 49–56.
Poot, D.H., Dekker, A.J., Achten, E., Verhoye, M., Sijbers, J., 2010. Optimal experimental design for diffusion kurtosis imaging. IEEE Trans. Med. Imaging 29, 819–829.
Stenset, V., Bjørnerud, A., Fjell, A.M., Walhovd, K.B., Hofoss, D., Due-Tønnessen, P., Gjerstad, L., Fladby, T., 2011. Cingulum fiber diffusivity and CSF T-tau in patients with subjective and mild cognitive impairment. Neurobiol. Aging 32, 581–589.
Sullivan, E.V., Pfefferbaum, A., 2006. Diffusion tensor imaging and aging. Neurosci. Biobehav. Rev. 30, 749–761.
Szczepankiewicz, F., Nilsson, M., Mårtensson, J., Westen, D., Ståhlberg, F., Lätt, J., 2011. Automated quantification of diffusion tensor imaging (DTI) and diffusion kurtosis imaging (DKI) parameters along the cervical spine using tractography-based voxel selection. Proc. Eur. Soc. Magn. Reson. Med. Biol. 27, 262–263.
Tang, J., Liao, Y., Zhou, B., Tan, C., Liu, T., Hao, W., Hu, D., Chen, X., 2010. Abnormal anterior cingulum integrity in first episode, early-onset schizophrenia: a diffusion tensor imaging study. Brain Res. 1343, 199–205.
Teipel, S.J., Schapiro, M.B., Alexander, G.E., Krasuski, J.S., Horwitz, B., Hoehne, C., Möller, H., Rapoport, S.I., Hampel, H., 2003. Relation of corpus callosum and hippocampal size to age in nondemented adults with Down's syndrome. Am. J. Psychiatry 160, 1870–1878.
Van Hecke, W., Leemans, A., De Backer, S., Jeurissen, Parizel, P.M., Sijbers, J., 2009. Comparing isotropic and anisotropic smoothing for voxel-based DTI analyses: a simulation study. Hum. Brain Mapp. 31, 98–114.
Veraart, J., Rajan, J., Peeters, R.R., Leemans, A., Sunaert, S., Sijbers, J., in press. Comprehensive framework for accurate diffusion MRI parameter estimation. Magn Reson Med. 2012 Nov 6. http://dx.doi.org/10.1002/mrm.24529 [Epub ahead of print] PubMed PMID: 23132517.
Vittinghoff, E., Glidden, D.V., Shiboski, S.C., Mcculloch, C.E., 2005. Regression Methods in Biostatistics. Springer, New York.
Vos, S.B., Jones, D.K., Viergever, M.A., Leemans, A., 2011. Partial volume effect as a hidden covariate in DTI analyses. NeuroImage 55, 1566–1576.
Vos, S.B., Jones, D.K., Jeurissen, B., Viergever, M.A., Leemans, A., 2012. The influence of complex white matter architecture on the mean diffusivity in diffusion tensor MRI of the human brain. NeuroImage 59, 2208–2216.
Wakana, S., Caprihan, A., Panzenboeck, M.M., Fallon, J.H., Perry, M., Gollub, R.L., Hua, K., Zhang, J., Jiang, H., Dubey, P., Blitz, A., Zijl, P., Mori, S., 2007. Reproducibility of quantitative tractography methods applied to cerebral white matter. NeuroImage 36, 630–644.
Wang, R., Benner, T., Sorensen, A., 2007. Diffusion toolkit: a software package for diffusion imaging data processing and tractography. Proc. Int. Soc. Magn. Reson. Med. 15, 3720.
Wang, J., Lin, W., Lu, C., Weng, Y., Ng, S., Wang, C., Liu, H., Hsieh, R., Wan, Y., Wai, Y., 2011. Parkinson disease: diagnostic utility of diffusion kurtosis imaging. Radiology 261, 210–217.
Wu, E.X., Cheung, M.M., 2010. MR diffusion kurtosis imaging for neural tissue characterization. NMR Biomed. 23, 836–848.
Zhang, A., Leow, A., Ajilore, O., Lamar, M., Yang, S., Joseph, J., Medina, J., Zhan, L., An, Kumar, Kumar, A., 2011. Quantitative tract-specific measures of uncinate and cingulum in major depression using diffusion tensor imaging. Neuropsychopharmacology 37, 959–967.
Zhuo, J., Xu, S., Proctor, J.L., Mullins, R.J., Simon, J.Z., Fiskum, G., Gullapalli, R.P., 2012. Diffusion kurtosis as an in vivo imaging marker for reactive astrogliosis in traumatic brain injury. NeuroImage 59, 467–477.

Paper II

frontiers in PHYSICS

ORIGINAL RESEARCH ARTICLE
published: 27 February 2014
doi: 10.3389/fphy.2014.00011

Microanisotropy imaging: quantification of microscopic diffusion anisotropy and orientational order parameter by diffusion MRI with magic-angle spinning of the q-vector

Samo Lasič[1]*, Filip Szczepankiewicz[2], Stefanie Eriksson[3], Markus Nilsson[4] and Daniel Topgaard[3]

[1] *CR Development AB, Lund, Sweden*
[2] *Department of Medical Radiation Physics, Lund University, Lund, Sweden*
[3] *Division of Physical Chemistry, Center for Chemistry and Chemical Engineering, Lund University, Lund, Sweden*
[4] *Lund University Bioimaging Center, Lund University, Lund, Sweden*

Edited by:
Michal Cifra, Academy of Sciences of the Czech Republic, Czech Republic

Reviewed by:
Itamar Ronen, Leiden University Medical Center, Netherlands
Frank Stallmach, University Leipzig, Germany

****Correspondence:***
Samo Lasič, CR Development AB, Getingevägen 60, Lund, SE 22100, Sweden
e-mail: samo@crdev.se

Diffusion tensor imaging (DTI) is the method of choice for non-invasive investigations of the structure of human brain white matter (WM). The results are conventionally reported as maps of the fractional anisotropy (FA), which is a parameter related to microstructural features such as axon density, diameter, and myelination. The interpretation of FA in terms of microstructure becomes ambiguous when there is a distribution of axon orientations within the image voxel. In this paper, we propose a procedure for resolving this ambiguity by determining a new parameter, the microscopic fractional anisotropy (μFA), which corresponds to the FA without the confounding influence of orientation dispersion. In addition, we suggest a method for measuring the orientational order parameter (OP) for the anisotropic objects. The experimental protocol is capitalizing on a recently developed diffusion nuclear magnetic resonance (NMR) pulse sequence based on magic-angle spinning of the *q*-vector. Proof-of-principle experiments are carried out on microimaging and clinical MRI equipment using lyotropic liquid crystals and plant tissues as model materials with high μFA and low FA on account of orientation dispersion. We expect the presented method to be especially fruitful in combination with DTI and high angular resolution acquisition protocols for neuroimaging studies of gray and white matter.

Keywords: microscopic diffusion anisotropy, single shot isotropic diffusion weighting, q-MAS, fractional anisotropy, microscopic fractional anisotropy, order parameter, orientation dispersion, diffusion distribution

INTRODUCTION

Molecular self-diffusion measured with nuclear magnetic resonance (NMR) [1, 2] can be used to non-invasively probe the microstructure of porous materials [3–5] and tissues [6]. The apparent self-diffusion coefficient, as measured in a pulsed gradient spin echo (PGSE) experiment, reflects the average diffusivity, which is a sum of contributions from different water compartments in a complex system. The diffusion is influenced by several properties of the medium, e.g., pore size and shape [7, 8], pore size distribution, pore interconnectivity [9, 10], permeability of cell membranes [11], and anisotropy [12]. The anisotropy of the tissue morphology renders the water self-diffusion anisotropic, a feature that is the basis for non-invasive mapping of muscle and nerve fiber orientations by diffusion tensor imaging (DTI) [13, 14]. DTI is commonly used to study the white matter (WM) of the brain, where the nerve fibers have a dominant direction on macroscopic length scales. Because of the limited spatial resolution in DTI, a majority of the voxels in WM contain fiber bundles with different orientations, thus making the interpretation of the DTI data ambiguous [15]. Due to the significance of accurate quantification of the level of anisotropy in the brain, techniques for detecting fiber orientation dispersion are being developed [16, 17].

The degree of the macroscopic diffusion anisotropy is often quantified by the dimensionless fractional anisotropy (FA) [12]. The FA parameter is sensitive to alterations in several tissue properties, e.g., axonal diameter, axonal packing density, and degree of myelination. Changes in these properties may be associated with normal brain development, learning, and healthy ageing, but also with disorders such as Alzheimer's disease, autism, schizophrenia, mild cognitive impairment, multiple sclerosis, amyotrophic lateral sclerosis, epilepsy, Tourette's syndrome, Parkinson's disease, and Huntington's disease [16, 18, 19]. Because fiber orientation dispersion and several other tissue properties are inherently entangled in the echo attenuation of the PGSE experiment, changes in FA are not specific to any particular tissue characteristics [16]. This fact is known to confound the use of FA as a diagnostic parameter in regions of dispersing or crossing WM fibers [17], and also detracts from the usability of FA in macroscopically isotropic tissues such as the gray matter (GM) of the nervous system [20].

Despite several experimental approaches attempting to assess the microscopic diffusion anisotropy in the nervous system [21], disentangling underlying tissue properties from the effects of orientation dispersion remains challenging and has inspired the development of analytical models extending beyond the standard

DTI approach [22, 23]. For materials consisting of randomly oriented anisotropic microcrystallites, e.g., lyotropic liquid crystals, the presence of microscopic anisotropy can be inferred from the characteristic functional form of the PGSE signal attenuation [24, 25]. This approach becomes ambiguous for more complex materials where several mechanisms could give the same signal attenuation. More recently, the microscopic anisotropy is detected in double-PGSE experiments by diffusion encoding in two separate time periods [26], giving characteristic signal modulations for data obtained with collinear and orthogonal displacement encoding [27–29] or when systematically varying the angle between the directions of displacement encoding [26, 30, 31]. A double-PGSE scheme to quantify microscopic anisotropy in terms of compartment eccentricity, independent of the macroscopic anisotropy, has recently been suggested [32]. A two-dimensional correlation approach [33] gives the currently most complete separation of the underlying diffusion components, albeit at the expense of being far too time consuming for clinical use.

We have recently shown that microscopic anisotropy can be efficiently detected with an acquisition protocol including single-shot isotropic diffusion weighting (DW) using magic-angle spinning of the q-vector (q-MAS) [34]. Comparisons between the q-MAS and other single-shot DW approaches [35, 36] can be found in [37]. Here we implement a numerically optimized version of the q-MAS pulse sequence [37] on a high-performance microimaging system, limited to specimens with maximum 10 mm diameter, and on a standard whole-body clinical scanner. The efficiency of the q-MAS sequence is demonstrated using two materials with pronounced water diffusion anisotropy: lyotropic liquid crystals [24, 25, 27, 34, 38–40] and pureed asparagus [41–44]. For contrast, a yeast cells suspension is used, exhibiting two isotropic diffusion components [34, 45–47].

We introduce a new parameter, the microscopic fractional anisotropy (μFA), for quantification of the microscopic anisotropy, and suggest a method to estimate the value of μFA by analysis of a set of diffusion MRI data acquired with both isotropic and conventional DW. The new μFA and the standard FA parameters have the same dependence on the size, shape, and density of the underlying anisotropic compartments, but differ in their sensitivity to the distribution of compartment orientations in the image voxel. The information from FA and μFA can be combined to quantify the orientation dispersion. In the literature, there are previous definitions of an orientation dispersion index based on a specific model of the orientation distribution function [23, 48, 49]. We quantify orientation dispersion with the order parameter (OP), a well-established measure of the orientational order in the field of liquid crystals [50]. A wide range of experimental techniques have been used to estimate OP for liquid crystalline systems, e.g., NMR spectroscopy, fluorescence polarization, and X-ray scattering. We derive an expression that relates OP to FA and μFA. The analysis presented here allows disentangling the two contributions to FA, i.e., the microscopic anisotropy and the orientational order of the micro-domains.

Figure 1 illustrates idealized scenarios of microstructural organization and the corresponding μFA, OP, and FA parameters. For a purely isotropic system, FA and μFA are both zero regardless of compartment size polydispersity. For anisotropic systems on the other hand, μFA reflects anisotropy of the underlying microscopic structures but not their organization on the voxel level. For identical micro-domains with identical μFA values, a reduced FA is expected for increased orientation dispersion reflected by a reduced OP. Both FA and μFA are reduced in the presence of isotropic structures. Because of its insensitivity to orientation dispersion, μFA could potentially be used as a relevant biomarker in clinical applications. It can provide additional information about the microstructure in tissue where conventional anisotropy measures are confounded by the voxel-scale tissue organization, thus improving the diagnostic specificity. Further, μFA and OP may generate novel diagnostic information in tissue that appears isotropic on a macroscopic scale but has sub-voxel anisotropic components, such as that found in cortical GM [20].

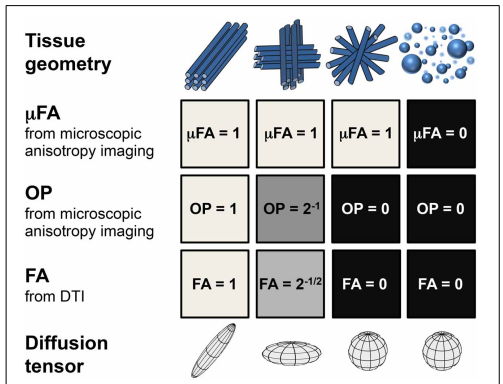

FIGURE 1 | Idealized tissue geometries with corresponding structure parameters. Consecutive rows show values of the microscopic fractional anisotropy, μFA; orientational order parameter, OP; fractional anisotropy, FA; and diffusion tensors. Decreasing values of OP from **left** to **right** in columns 1–3 leads to a reduction of FA while μFA remains constant. For isotropic structures (column 4), both FA and μFA vanish.

THEORY

DIFFUSION DISPERSION

In complex systems like tissue, the MRI signal attenuation often reflects multiple diffusion processes, including restricted, hindered, and free diffusion. Restricted diffusion may give rise to both isotropic and anisotropic contributions. Although restricted diffusion is fundamentally a non-Gaussian process, at a low DW and at the experimental times typical for diffusion NMR/MRI, it can be characterized by the apparent diffusion coefficient, D_g, along the applied gradient direction **g**. For a multi-component system, the echo attenuation intensity is given by the sum over all the different contributions,

$$S_g = \sum_i S_{0i} e^{-bD_{gi}}, \quad (1)$$

where S_{0i} is the relaxation weighted intensity of component i.

Equation (1) can be expressed as the Laplace transform of the probability distribution of apparent diffusivities, $P(D)$ [25, 51, 52]. For a macroscopically anisotropic system, the distribution $P(D)$ depends on the diffusion encoding direction, as indicated by the subscript g in Equation (1). The arithmetic average of the signal intensity over all directions, also known as the powder average, mimics a uniform orientation dispersion of anisotropic micro-domains and thus, yields $P(D)$ independent of the orientation dispersion. Provided that $P(D)$ is normalized to unity, the distribution is well described by the mean value,

$$\overline{D} = \int_0^\infty DP(D)\, dD \tag{2}$$

and by the central moments

$$\mu_m = \int_0^\infty \left(D - \overline{D}\right)^m P(D)\, dD. \tag{3}$$

While the mean diffusivity, $\overline{D}$, gives the initial slope of the echo attenuation, the second central moment, μ_2, represents the initial deviation from mono-exponential attenuation, corresponding to the second term in the cumulant expansion [53] of the normalized signal intensity, $E = S(b)/S_0$, according to

$$\ln E(b) = -\overline{D}b + \frac{\mu_2}{2}b^2 - .... \tag{4}$$

The second central moment, μ_2, is often expressed in terms of the kurtosis coefficient K as $\mu_2 = \overline{D}^2 K/3$ [42]. For Gaussian diffusion in each component, as assumed in Equation (1), the value of μ_2 corresponds to the variance of apparent diffusion coefficients. For brevity, we refer to μ_2 as the variance. In the case of a two-component isotropic system, e.g., intra and extracellular diffusion in a yeast cell suspensions [34], the value of μ_2 increases with the difference between the two diffusivities and is maximized when the two contributions are represented with equal probabilities.

MICROSCOPIC FRACTIONAL ANISOTROPY (μFA)

The anisotropy of a medium is reflected by the diffusion tensor, $\mathbf{D} = \mathbf{R}\Lambda\mathbf{R}^{-1}$, where Λ is the diagonal representation of $\mathbf{D}$ in the principal axis system given by the eigenvalues λ_1, λ_2, and λ_3 and $\mathbf{R}$ is the Euler rotation matrix. In DTI, the diffusion tensor can be constructed based on measurements of signal intensity along several non-collinear gradient directions, $\hat{\mathbf{g}}$, using the expression

$$S_g = S_0 \exp\left[-b\,\hat{\mathbf{g}}\cdot\mathbf{D}\cdot\hat{\mathbf{g}}^T\right]. \tag{5}$$

The anisotropy on a voxel level is quantified in terms of FA and expressed as an invariant of the three independent diffusion tensor eigenvalue [12],

$$\mathrm{FA} = \sqrt{\frac{3}{2}}\sqrt{\frac{\left(\lambda_1 - \overline{D}\right)^2 + \left(\lambda_2 - \overline{D}\right)^2 + \left(\lambda_3 - \overline{D}\right)^2}{\lambda_1^2 + \lambda_2^2 + \lambda_3^2}}, \tag{6}$$

where the mean diffusivity is given by

$$\overline{D} = \frac{\lambda_1 + \lambda_2 + \lambda_3}{3}. \tag{7}$$

The diffusion tensor eigenvalues can be combined in several ways to represent different invariant measures characterizing the diffusion tensor shape. To quantify the degree to which the diffusion tensor reflects the planar geometry, we use the planar measure C_p [54],

$$C_p = \frac{\lambda_2 - \lambda_3}{\lambda_1}, \tag{8}$$

assuming a descending order of the eigenvalues, $\lambda_1 \geq \lambda_2 \geq \lambda_3$.

For randomly oriented anisotropic domains represented by a single set of diffusion tensor eigenvalues, corresponding to the powder average, the variance of the observed $P(D)$ is given by [55]

$$\mu_2 = \frac{4}{45}\left[(\lambda_1 - \lambda_3)^2 + (\lambda_2 - \lambda_1)(\lambda_2 - \lambda_3)\right]. \tag{9}$$

For axially symmetric diffusion tensors, FA is given by

$$\mathrm{FA} = \frac{\left|D_{||} - D_\perp\right|}{\sqrt{D_{||}^2 + 2D_\perp^2}}, \tag{10}$$

where $D_{||}$ is the axial diffusivity and $D_\perp$ is the radial diffusivity. For macroscopically isotropic systems, with axially symmetric anisotropic micro-domains, the signal attenuation and the corresponding $P(D)$ can be expressed in a compact form (see Equations 34 and 35 in [34]).

The mean diffusivity and the variance are given by the axial and radial diffusivities as

$$\begin{aligned} \overline{D} &= \tfrac{D_{||}+2D_\perp}{3} \\ \mu_2 &= \tfrac{4}{45}\left(D_{||} - D_\perp\right)^2. \end{aligned} \tag{11}$$

For a diffusion tensor with oblate shape, where $D_{||} < D_\perp$, the upper limit of the variance is given by $\mu_{2\,\max} = \overline{D}^2/5$, while for a prolate shape, where $D_{||} > D_\perp$, $\mu_{2\,\max} = 4\overline{D}^2/5$. For randomly oriented axially symmetric micro-domains, the FA in Equation (10) can be expressed in terms of $\overline{D}$ and μ_2 using the relations in Equation (11) as

$$\mathrm{FA} = \sqrt{\frac{3}{2}}\left(1 + \frac{2}{5}\cdot\frac{1}{\widetilde{\mu_2}}\right)^{-1/2}, \tag{12}$$

where the ratio $\widetilde{\mu_2} = \mu_2/\overline{D}^2$ represents the scaled variance.

Isotropic DW can be achieved with q-MAS if the water molecules stay within an anisotropic micro-domain throughout the duration of the diffusion encoding [34]. In a system consisting of a single type of micro-domain, the variance μ_2, observed in the powder-averaged DW experiment, is a consequence of domain anisotropy and independent of orientation dispersion. In such a case, the isotropic DW yields $\mu_2^{\mathrm{iso}} = 0$. Since the difference $\Delta\mu_2 = \mu_2 - \mu_2^{\mathrm{iso}}$ is expected to vanish when all diffusion

contributions are isotropic, and it is maximized for systems where the deviation from mono-exponential echo decay is purely due to microscopic anisotropy, the difference $\Delta\mu_2$ can be used to quantify microscopic anisotropy. In case of macroscopically isotropic systems, or equivalently, for an isotropically averaged intensity, the mean diffusivity is expected to be identical for both isotropic and powder-averaged DW data. This can be implemented as an advantageous constraint in data analysis.

Substituting the $\widetilde{\mu}_2$ in Equation (12) with its "bias-corrected" counterpart, here named the difference in scaled variance,

$$\Delta\widetilde{\mu}_2 = \frac{\mu_2 - \mu_2^{\text{iso}}}{\overline{D}^2}. \tag{13}$$

suggests a definition for the microscopic fractional anisotropy, μFA, according to

$$\mu\text{FA} = \sqrt{\frac{3}{2}}\left(1 + \frac{2}{5}\cdot\frac{1}{\Delta\widetilde{\mu}_2}\right)^{-1/2}. \tag{14}$$

Equation (14) is the key equation to quantify microscopic anisotropy, since $\Delta\widetilde{\mu}_2$ is the measurable difference in curvature between powder-averaged and isotropic signal-vs.-b data, while μFA is the desired microstructural parameter. The relation between $\Delta\widetilde{\mu}_2$ and μFA is shown in **Figure 2A**.

The values of μFA are equal to the FA when diffusion is locally purely anisotropic and determined by coherently oriented axially symmetric diffusion tensors. For two-dimensional diffusion between parallel planes, $\mu\text{FA} = \text{FA} = \sqrt{1/2}$ and for one-dimensional diffusion within narrow tubes, $\mu\text{FA} = \text{FA} = 1$.

ORDER PARAMETER (OP)

The OP is well-established for characterization of the orientational order in liquid crystals [50]. Here we use the OP to quantify the orientation dispersion of anisotropic micro-domains. Consider a typical macroscopic voxel consisting of an ensemble of anisotropic micro-domains characterized by axially symmetric diffusion tensors with axial and radial diffusivities, $D_{||}$ and $D_{\perp}$, respectively, and varying orientation of the domain's symmetry axis **d**. Further, assume that the distribution of sub-voxel domain orientations is also axially symmetric around the voxel symmetry axis **u**, where $\mathbf{u}\cdot\mathbf{d} = \cos\theta$.

The diffusivity along the voxel symmetry axis is given by the contributions from all the micro-domains with different polar angles θ. Each micro-domain contributes

$$D(\theta) = D_{||}\cos^2\theta + D_{\perp}\sin^2\theta. \tag{15}$$

Note the similarity with the expression describing the chemical shift anisotropy (see Equation 23 in [56]). The above expression can be rewritten as

$$D(\theta) = \overline{D} + \frac{2}{3}\left(D_{||} - D_{\perp}\right)P_2(\cos\theta), \tag{16}$$

where $P_2(x) = (3x^2-1)/2$ is the second Legendre polynomial. The axial and radial diffusivities observed on a voxel level are given by

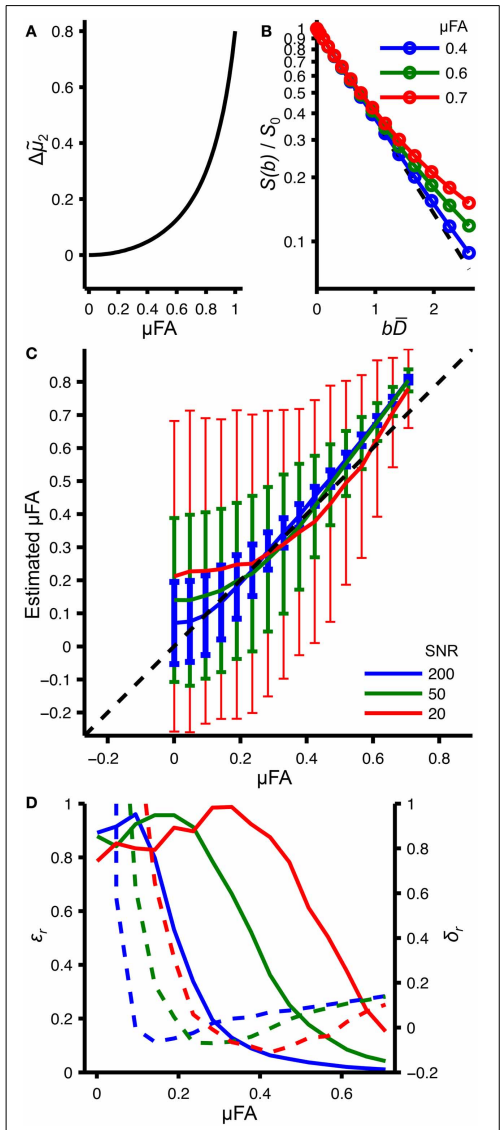

FIGURE 2 | Random and systematic errors in estimating the microscopic fractional anisotropy. (A) Relation between microscopic fractional anisotropy (μFA) and the difference in variance, $\Delta\widetilde{\mu}_2 = \left(\mu_2 - \mu_2^{\text{iso}}\right)/\overline{D}^2$, calculated with Equation (14). **(B)** Powder-averaged signal attenuation, $S(b)/S_0$, for an axially symmetric anisotropic system corresponding to different μFA values (solid lines with circles), calculated based on Equation 35 in [34] using the relations in

(Continued)

FIGURE 2 | Continued
Equations (11) and (14). The dashed line corresponds to the isotropic DW with $\mu_2^{\mathrm{iso}} = 0$. **(C)** Relation between true μFA values and their estimation from fitting Equation (25) to data generated in the same way as the data shown in panel **(B)**. Shown are the mean values (solid lines) and standard deviations (error bars) resulting from 1000 fitting iterations with synthetic noise corresponding to different SNRs [66]. **(D)** Relative systematic (δ_r, dashed line) and random errors (ε_r, solid lines) calculated from data shown in panel **(C)**. In panel **(B)**, the red, green, and blue colors correspond to different μFA values, while in panels **(C,D)**, the colors correspond to different SNR levels.

the ensemble averages

$$\begin{aligned}\langle D_{||}\rangle &= \overline{D} + \frac{2}{3}\left(D_{||} - D_{\perp}\right)\langle P_2(\cos\theta)\rangle,\\ \langle D_{\perp}\rangle &= \overline{D} + \frac{2}{3}\left(D_{||} - D_{\perp}\right)P_2\left(\cos\frac{\pi}{2}\right)\langle P_2(\cos\theta)\rangle\\ &= \overline{D} - \frac{1}{3}\left(D_{||} - D_{\perp}\right)\langle P_2(\cos\theta)\rangle. \end{aligned} \tag{17}$$

The OP (see [50]) is defined by

$$\mathrm{OP} = \langle P_2(\cos\theta)\rangle. \tag{18}$$

As we see from Equation (17), the OP can be determined by the relation between the micro-domain diffusivities and the ensemble average diffusivities,

$$\mathrm{OP} = \frac{\langle D_{||}\rangle - \langle D_{\perp}\rangle}{D_{||} - D_{\perp}}. \tag{19}$$

For randomly oriented domains, the OP = 0, while for completely aligned domains, the OP = 1. The OP defined here is similar to the one calculated from motionally averaged chemical shift anisotropy or dipolar powder patterns in [50].

The definition of OP in Equation (19) is suitable for purely anisotropic systems with axial symmetry, for which $\mu_2^{\mathrm{iso}} = 0$, and it can be determined from DW experiments performed in several non-collinear directions using multiple *b*-values. The ensemble average diffusivities, $\langle D_{||}\rangle$ and $\langle D_{\perp}\rangle$, are the diffusion tensor's eigenvalues, while the difference of the micro-domain diffusivities, $D_{||} - D_{\perp}$, is related to the variance μ_2 in Equation (11) and can be determined by analyzing the powder-averaged signal attenuation (4). If the FA is converted into the corresponding scaled variance according to Equation (12),

$$\widetilde{\mu}_2^{\mathrm{FA}} = \frac{4}{5}\left(\frac{3}{\mathrm{FA}^2} - 2\right)^{-1}, \tag{20}$$

the OP in Equation (19) can be rewritten as $\mathrm{OP} = \sqrt{\widetilde{\mu}_2^{\mathrm{FA}}/\widetilde{\mu}_2}$. However, the FA is not only reduced due to orientation dispersion but also due to isotropic contributions, characterized by $\mu_2^{\mathrm{iso}} > 0$. To account for the isotropic contributions in the calculation of the OP, the difference in variance should be used, suggesting the definition

$$\mathrm{OP} = \sqrt{\frac{\widetilde{\mu}_2^{\mathrm{FA}}}{\Delta\widetilde{\mu}_2}} = \sqrt{\frac{3\mu\mathrm{FA}^{-2} - 2}{3\mathrm{FA}^{-2} - 2}}. \tag{21}$$

Equation (21) provides the link between the FA and μFA and allows quantifying the orientation dispersion of anisotropic structures. Since the ratio $\mathrm{FA}/\mu\mathrm{FA} < 1$, the OP is always in the range 0–1. The macroscopic parameter, FA, can be interpreted in terms of two underlying mechanism, i.e., the anisotropy of micro-domains, given by μFA, and the domain organization, given by the OP. Inverting Equation (21) gives

$$\mathrm{FA} = \mathrm{OP}\left[\mu\mathrm{FA}^{-2} + \frac{2}{3}\left(\mathrm{OP}^2 - 1\right)\right]^{-1/2}. \tag{22}$$

The above equation quantifies the relation between the anisotropy of microscopic structures and their macroscopic organization. For large FA, both the OP and the μFA need to be large, while a reduction of either OP or μFA gives reduced FA (see **Figure 1**).

ESTIMATING MICROSCOPIC FRACTIONAL ANISOTROPY

In the case of high signal-to-noise and a well-sampled echo attenuation signal, the variance μ_2 could be estimated by regressing Equation (4) onto the isotropic and powder-averaged DW data. However, it can be shown that the convergence of the cumulant expansion is very slow in the case of randomly oriented anisotropic domains, for which the echo intensity can be expressed in a simple analytical form (see Equation 35 in [34]). The problem of analyzing the echo intensity data can instead be considered from the perspective of finding a suitable approximation to the $P(D)$ or its first two moments, see Equations (2) and (3). A convenient functional form to approximate $P(D)$ for complex systems with both isotropic and anisotropic components should have a simple analytical Laplace transform and it should be able to capture a wide range of diffusion distributions with only a few parameters. The gamma distribution function,

$$P(D) = D^{\alpha-1}\frac{e^{-D/\beta}}{\Gamma(\alpha)\,\beta^{\alpha}} \tag{23}$$

proves to be an efficient and physically plausible model for describing complex polydisperse systems such as polymer solutions [57]. The mean and the dispersion value of the gamma distribution are given by the so-called shape parameter α and the scale parameter β, where $\overline{D} = \alpha\cdot\beta$ and $\mu_2 = \alpha\cdot\beta^2$, respectively. The Laplace transform of the gamma distribution takes a simple analytical form,

$$E(b) = (1 + b\beta)^{-\alpha}, \tag{24}$$

which can expressed as

$$S(b) = S_0\left(1 + b\frac{\mu_2}{\overline{D}}\right)^{-\frac{\overline{D}^2}{\mu_2}} \tag{25}$$

for data-fitting purposes.

Figure 2 summarizes the key aspects of the microscopic anisotropy analysis, which are discussed in more detail throughout the Results and Discussion section. The functional form of Equation (14) is shown in **Figure 2A**. The expected signal attenuation for an axially symmetric anisotropic system with varying μFA values is depicted in **Figure 2B**, illustrating that only rather large μFA values give rise to a detectable deviation from monoexponential decay. The systematic and random errors of μFA estimation resulting from fitting Equation (25) to the synthetic data in **Figure 2B** are presented in **Figures 2C,D.**

MATERIALS AND METHODS

LIQUID CRYSTAL/YEAST PHANTOM

A liquid crystalline sample was prepared by mixing the nonionic surfactant triethylene glycol monodecyl ether $C_{10}E_3$ (Nikko Chemical Co., Tokyo, Japan) with water containing 95 wt% D_2O (Sigma Aldrich, Steinheim, Germany) and 5 wt% H_2O (MilliQ purified) in an NMR tube with 5 mm outer diameter, giving 40 wt% surfactant concentration and 0.5 ml sample volume. A water bath was used to heat the sample to 50°C where it separates into two phases: nearly pure water and a concentrated surfactant solution with reverse micelles [58], both phases having low viscosity. After removing the tube from the water bath and exposing it to room temperature air, it was held horizontally and rotated manually about its long axis until, after approximately 2 min, the sample turned viscous. The temperature decrease leads to a phase transition into the lamellar liquid crystalline phase [58], while the rotation aligns the lamellae with respect to the inner surface of the tube [59]. The preferential orientation of the lamellae extends less than a millimeter from the glass surface, thus leaving the interior of the sample randomly oriented (see **Figure 3**). The sample was equilibrated at room temperature (21°C) for 24 h with the tube in the vertical direction.

Fresh baker's yeast was purchased at a local supermarket. A cell suspension was prepared by shaking equal volumes of the yeast with tap water in a glass tube. The suspension was allowed to sediment overnight at room temperature. The clear supernatant was discarded and 1 ml of the loosely packed cell sediment was transferred to a 10 mm NMR tube using a syringe with a 1 mm diameter needle.

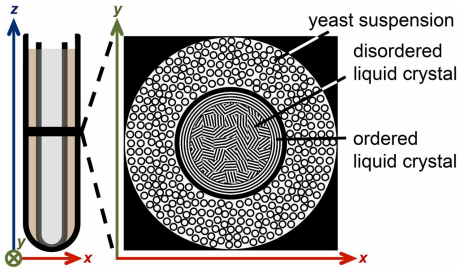

FIGURE 3 | Illustration of the liquid crystal/yeast MRI phantom. A 5 mm NMR tube, containing 40 wt% of the surfactant $C_{10}E_3$ in water, is inserted into a 10 mm NMR tube with yeast cells in water. The black horizontal line in the **left** schematic indicates the slice of the 2D MR image. The **top** view of the phantom is depicted on the **right**. The anisotropic liquid crystal domains are mostly randomly oriented, while a narrow layer of aligned domains is formed near the tube walls.

The 5 mm NMR tube with the liquid crystal was inserted into the 10 mm NMR tube with the yeast sediment, creating an MRI phantom with an inner cylindrical compartment with water diffusion anisotropy and an outer cylindrical shell having a broad distribution of isotropic water diffusivities (see **Figure 3**). Before the MRI measurements, the sample was equilibrated for 2 h at 25°C within the magnet of the microimaging equipment.

PUREED ASPARAGUS PHANTOM

Fresh asparagus (*Asparagus officinalis*), obtained from a local supermarket, was prepared in a plastic container that consisted of two cylindrical compartments with a diameter of approximately 8 cm. The first compartment contained water and intact asparagus stems cut to an appropriate length. The second compartment was filled with water and asparagus which was processed in a kitchen blender, resulting in a grainy puree with particle sizes well below one imaging voxel. The pureed asparagus was compressed to the bottom of the container in order to decrease the free water component in the puree. Measurements were performed at room temperature on the whole-body MR scanner.

MICROIMAGING

The liquid crystal/yeast phantom was measured on an 11.7 T Bruker AVII-500 spectrometer equipped with a Bruker MIC-5 microimaging probe having a maximum gradient strength of 3 Tm^{-1} and a 10 mm saddle coil radio frequency (RF) insert. Images were acquired with a TopSpin 2.1 implementation of the pulse sequence shown in **Figure 4** using a single-shot RARE [60] signal read-out with 9 × 9 mm field-of-view, 64 × 32 acquisition matrix (read × phase), 10 mm slice thickness, and 65 ms duration of the echo train. The spin-echo DW block with total duration of 45 ms included two identical gradient waveforms bracketing the 180° RF pulse. Isotropic DW was achieved with the optimized *q*-MAS gradient modulation scheme [37]. Directional DW employed a gradient waveform giving the same time-dependence of the magnitude of the *q*-vector as the *q*-MAS modulation. The *q*-MAS gradient waveform was executed with duration $\tau = 20$ ms and amplitude $G = 0.405$ Tm^{-1}, yielding a *b*-value of 5200 s/mm^2 according to the equation $b = NC\gamma^2G^2\tau^3$, where $\gamma = 2.675.10^8$ $radT^{-1}s^{-1}$ is the ^1H gyromagnetic ratio, $C = 0.0278$ is a constant specific for the optimized *q*-MAS modulation [37], and $N = 2$ is the number of repetitions of the *q*-MAS modulation. Images were acquired for 16 *b*-values and 15 non-collinear gradient directions, as well as 15 repetitions of the isotropic DW, giving a total data set of 480 images. The *b*-values were incremented by linear steps in the gradient amplitude, while the gradient directions were chosen according to the electrostatic repulsion scheme [61, 62]. Each image was recorded as the sum of four transients with phase cycling of the RF pulses and the receiver [63]. A 1 s recycle delay gave a total experiment time of 30 min.

Image processing was performed with in-house Matlab code. Before Fourier transformation, the acquired data was zero-filled

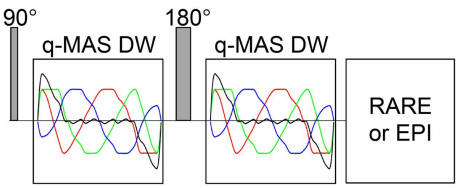

FIGURE 4 | Schematic of the diffusion MRI pulse sequence with isotropic or directional diffusion weighting. The 90 and 180° RF pulses produce a spin echo, which is acquired with a single-shot RARE sequence at the high field spectrometer or EPI sequence at the clinical scanner. Identical DW blocks are inserted on each side of the 180° pulse. Isotropic DW is achieved with a numerically optimized *q*-MAS gradient modulation scheme [37] as shown with the green (G_x), blue (G_y), and red (G_z) lines. The black line indicates the directional gradient waveform that yields the same magnitude of dephasing [34] as the *q*-MAS modulation.

to 128 × 128 points [64] and multiplied with a 2D Gaussian function giving 0.2 mm × 0.2 mm image smoothing.

WHOLE-BODY SCANNER

Experiments on the pureed asparagus phantom were performed on a whole-body Philips Achieva 3 T scanner equipped with an eight-channel head coil. The gradient system delivered a maximum gradient strength of 80 $\mathrm{mTm^{-1}}$ at the maximal slew rate of 100 $\mathrm{mTm^{-1}s^{-1}}$. DW images were recorded with an echo planar read-out [65] using an echo time of 160 ms, half-scan factor of 0.8, SENSE factor of 2, and a slice thickness of 10 mm. The field of view was 288 × 288 mm with an acquisition matrix of 96 × 96, resulting in a spatial resolution of $3 \times 3 \times 10\,\mathrm{mm^3}$. Isotropic and directional DW were achieved during $\tau = 62.9$ ms, before and after the 180° RF pulse, using the same waveform as in the microimagning experiment. Images were acquired for 16 *b*-values, between 50 and 2800 $\mathrm{s/mm^2}$. The directional DW was performed in 15 non-collinear gradient directions spread out according to the repulsion scheme [61, 62]. The isotropic encoding was repeated 15 times for each *b*-value in order to generate an equal amount of acquisitions with the isotropic and directional DW. The repetition time was 2 s, resulting in acquisition times of 8:06 min for both the directional and isotropic data.

One high resolution T_2-weighted volume was acquired to visualize the different components of the phantom, and reconstructed at a spatial resolution of $0.45 \times 0.45 \times 8.00\,\mathrm{mm^3}$.

The standard scanner reconstruction software was used to convert the raw data into two series of 240 images each, which were exported to Matlab for further analysis.

DATA ANALYSIS

Maps of the eigenvalues and eigenvectors of the diffusion tensor, as well as the $\overline{D}$ and FA values were obtained by non-linear least squares fitting of directional DW data using Equation (5) with S_0, λ_1, λ_2, λ_3 and three Euler angles as adjustable parameters.

The images with directional DW (16 *b*-values and 15 directions) were converted to a powder-averaged series of images (16 *b*-values) by arithmetic averaging over the gradient directions. The multiple acquisitions of images with isotropic DW (16 *b*-values and 15 repetitions) were averaged to a single series (16 *b*-values). Equation (25) was regressed onto the isotropic and powder-averaged DW data, using S_0, $\overline{D}$, μ_2, and μ_2^{iso} as fit parameters. S_0 and $\overline{D}$ were constrained to be identical for both datasets, while μ_2 and μ_2^{iso} correspond to the powder-averaged and isotropic data, respectively. The values of μ_2 and μ_2^{iso} were constrained to be in the physically reasonable range from 0 to $\overline{D}^2$. The standard deviations of the fit parameters were estimated by a Monte Carlo error analysis [66]. Finally, the μFA and OP indexes were calculated with Equations (14) and (21).

RESULTS AND DISCUSSION

Phantoms, constructed to exhibit varied degree of microscopic and macroscopic anisotropy, were probed by directional and isotropic DW as well as with DTI. Results are presented and discussed in three sections; the microimaging experiments are followed by the experiments on a whole-body scanner and finally the significance of the novel microstructural measures is discussed. The microimaging section discusses the liquid crystal/yeast phantom and its micro-/macro-structural features, which are compared to the results of the μFA and DTI analysis. The difference between diffusion variance in directional and isotropic DW is thoroughly discussed in relation to the microstructural properties of the phantom. The meaning of the newly introduced parameters μFA and OP is demonstrated and the limitations of the *q*-MAS DW experiment and its analysis are discussed. The following section presents the results on the asparagus phantom obtained at a whole-body scanner. In the third section, the potential of μFA and OP as novel biomarkers and the key aspects of the *q*-MAS DW implementation in a clinical setting are considered.

MICROIMAGING

Experimental results for the liquid crystal/yeast phantom are shown in **Figure 5** as parametric images and histograms. We recapitulate that the concentric phantom is designed to have an outer compartment with a broad distribution of isotropic diffusivities and an inner compartment with microscopic diffusion anisotropy as well as varying degrees of voxel-scale anisotropy on account of the alignment of the underlying anisotropic objects with respect to the glass wall separating the two compartments (see **Figure 3**).

The map of the mean diffusivity $\overline{D}$ in **Figure 5A** shows clear differences between the surfactant/water mixture and the yeast suspension, with values of 0.51 and 1.5 $\mu\mathrm{m^2/ms}$, respectively, at the maxima of the narrow distributions in the histogram. A reference experiment with pure H_2O (data not shown) gives $\overline{D} = 2.3\,\mu\mathrm{m^2/ms}$, in good agreement with the literature value [67]. A wide range of microscopic mechanisms could cause the observed reduction of $\overline{D}$ from the value for pure H_2O: from confinement of the water in more or less impermeable micrometer-scale pores [68] to the presence of colloidal obstacles at high concentrations [69]. The values of $\overline{D}$ are by themselves not sufficient to make any detailed inferences on microstructure.

Diffusion tensor

The FA map in **Figure 5B** shows that the water diffusion is essentially isotropic in the yeast suspension (FA < 0.05). A closer look

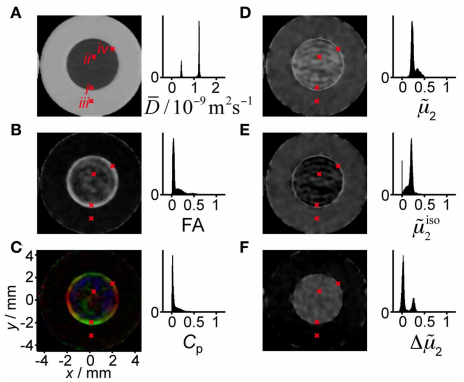

FIGURE 5 | Parameter maps and histograms for the liquid crystal/yeast phantom. The panels show **(A)** mean diffusivity $\bar{D}$, **(B)** fractional anisotropy FA, **(C)** planar index C_p, **(D)** scaled variance $\tilde{\mu}_2$, **(E)** scaled isotropic variance $\tilde{\mu}_2^{iso}$, and **(F)** the difference in scaled variance $\Delta\tilde{\mu}_2$. The red crosses, numbered with roman numerals in panel **(A)**, point out pixels for which the acquired signal is shown in detail in **Figure 6**. The colors in the C_p map indicate the direction of the vector corresponding to the minimum eigenvalue of the diffusion tensor (red: *x*, green: *y*, blue: *z*). Pixels with signal below a threshold value are shown in black in the parameter maps and excluded from the calculation of the histograms.

at the FA histogram reveals that the values for the yeast have an approximately Gaussian distribution with mean value 0.04 and standard deviation 0.02. The positive bias at low values of FA originates from the fact that any deviation from the equality $\lambda_1 = \lambda_2 = \lambda_3$ gives a positive value of FA according to Equation (6). In the surfactant/water mixture, the values of FA cover the range from 0 to 0.6, with the highest values concentrated in a 0.5 mm wide band along the outer edge of the compartment. Information about the shape and orientation of the diffusion tensor can be obtained from the planar index, C_p, color-coded with the direction of the eigenvector $\mathbf{v}_3$, corresponding to the minimum eigenvalue λ_3. In **Figure 5C**, values of C_p above 0.7 can be observed at the rim of the interior compartment, indicating an essentially planar diffusion tensor. The radial orientation of $\mathbf{v}_3$ verifies that the lamellar planes have the same orientation as the adjacent glass surface. A perfectly oriented lamellar liquid crystal, with $D_{||} << D_\perp$, would give FA $= \sqrt{1/2} \approx 0.71$ and $C_p = 1$. The values observed experimentally, FA ≈ 0.6 and $C_p = 0.7$, are smaller than the ideal ones, indicating that there is a distribution of lamellar domain orientations within the voxels and/or that $D_{||}$ is not negligible in comparison to $D_\perp$. The values of FA and C_p are by themselves not sufficient to distinguish between the two cases. The interior of the tube with the surfactant/water mixture contains extensive regions where FA and C_p are close to zero. From the conventional DTI parameters, one could be tempted to draw the conclusion that these regions contain an isotropic phase, e.g., a sponge phase or cubic liquid crystalline phase, rather than the lamellar liquid crystalline phase that is expected from the sample composition and the equilibrium phase diagram [58].

Diffusion variance in directional and isotropic DW

Figure 5D shows the scaled variance of the distribution of apparent diffusivities $P(D)$, $\tilde{\mu}_2 = \mu_2/\bar{D}^2$, for the powder-averaged data acquired with directional DW. We reiterate that $\tilde{\mu}_2$ is a measure of the width of the $P(D)$ and the curvature of log$S(b)$, and is closely related to the diffusional kurtosis [43]. Non-zero values of $\tilde{\mu}_2$ can result from diffusion anisotropy and/or the presence of more than one microscopic environment for the water. As shown in **Figure 2A**, diffusion anisotropy can by itself give a maximum $\tilde{\mu}_2$ value of 0.8. Both the liquid crystal and the yeast suspension display $\tilde{\mu}_2$ values being substantially different from zero. The histogram in **Figure 5D** features two overlapping distributions with maxima at 0.35 and 0.23 for the surfactant/water mixture and the yeast suspension, respectively. Since FA for the yeast is zero within experimental noise, it seems safe to assume that the non-zero values of $\tilde{\mu}_2$ originate from the presence of multiple microenvironments. In the case of a yeast suspension, these microenvironments correspond to the intra- and extracellular spaces [70]. Conversely, comparison between **Figures 5B,D** shows that, for the surfactant/water mixture, high values of $\tilde{\mu}_2$ occur for regions with both high and low values of FA, thus making the interpretation of $\tilde{\mu}_2$ in terms of either diffusion anisotropy or multiple environments highly ambiguous. The crucial information needed for discriminating between the two cases can be found in **Figure 5E**, displaying the scaled variance for data acquired with isotropic DW, $\tilde{\mu}_2^{iso} = \mu_2^{iso}/\bar{D}^2$. This parameter is insensitive to diffusion anisotropy and is non-zero only if there are multiple environments with distinct isotropic diffusivities. While the surfactant/water mixture has values close to zero, the values for the yeast suspension are, within experimental noise, identical in **Figures 5D,E**, confirming the presence of a distribution of environments with different isotropic diffusivity. On account of the limited spatial resolution, the voxels at the border between the surfactant/water mixture and the yeast suspension contain signal from both compartments, leading to exceptionally high values of $\tilde{\mu}_2^{iso}$ which can be observed as a thin bright circle in **Figure 5E**.

As shown in **Figure 5F**, taking the difference $\Delta\tilde{\mu}_2 = (\mu_2 - \mu_2^{iso})/\bar{D}^2$ isolates the effect of diffusion anisotropy. Non-zero values of $\Delta\tilde{\mu}_2$ are expected when the microscopic structure is anisotropic on the length scale of the molecular displacements during the diffusion time, typically tens of micrometers. If during the diffusion encoding, molecules would have enough time to migrate between anisotropic domains with different orientations, this would affect the diffusion variance in both isotropic and directional DW. In the limit of long diffusion times, the variance observed in a directional DW vanishes [38], while in isotropic DW the variance is expected to increase due to incoherent averaging across microdomains. The dependence of the *q*-MAS DW on diffusion time can be viewed in analogy to the effects of the MAS in solid-state NMR spectroscopy. The broadening of $P(D)$ in isotropic DW corresponds to the broadening of the sidebands at low frequencies of sample MAS when the rates of spinning and reorientation are similar [71]. The $\Delta\tilde{\mu}_2$ values for the yeast

suspension are close to zero, consistent with isotropic diffusion. Detailed inspection of the histogram in **Figure 5F** reveals that the yeast data can be described with an approximately Gaussian distribution with mean 0.03 and standard deviation 0.03, thus spanning both positive and negative values. The data for the surfactant/water mixture is centered at $\Delta\widetilde{\mu}_2 = 0.25$ and, as for the yeast, has a standard deviation of 0.03. Assuming that the true value is homogeneous in both the liquid crystal and the yeast compartments, the observed standard deviation of 0.03 can be interpreted as the precision in the estimation of $\Delta\widetilde{\mu}_2$ at the current experimental settings. The observation of $\Delta\widetilde{\mu}_2$ values well above zero for the surfactant/water mixture is a strong indication that the water resides in an anisotropic microenvironment, in agreement with the presence of a lamellar liquid crystalline phase. In contrast to FA, the values of $\Delta\widetilde{\mu}_2$ do not depend on the details of the orientation distribution of the anisotropic objects within the voxel, and is consequently better suited for detecting diffusion anisotropy.

Taken together, the parameters shown in **Figure 5** give a rather complete description of the nature of the water environments within each voxel. Whereas the yeast suspension contains multiple water environments ($\widetilde{\mu}_2^{\mathrm{iso}} > 0$) that are isotropic ($\Delta\widetilde{\mu}_2 = 0$), the surfactant/water mixture consists of a single type of environment ($\widetilde{\mu}_2^{\mathrm{iso}} = 0$) with diffusion anisotropy on the microscopic scale ($\Delta\widetilde{\mu}_2 > 0$) and varying degrees of orientation coherence on the voxel scale, from random orientations (FA = 0) to preferential alignment with the lamellae following the curvature of the glass surface (FA > 0, radial orientation of $\mathbf{v}_3$).

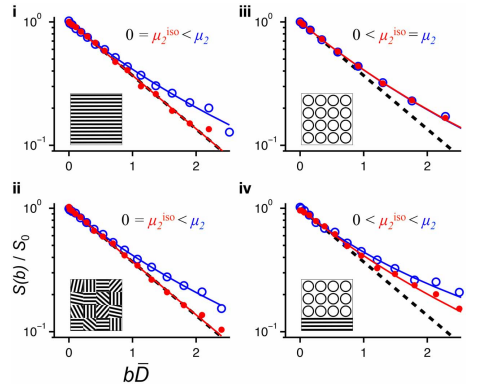

FIGURE 6 | Normalized signal $S(b)/S_0$ vs. normalized diffusion weighting $b\overline{D}$ for selected pixels in Figure 5. The roman numerals of the panels correspond to the pixel labels in **Figure 5A**. Powder-averaged directional and isotropic data is shown with open blue and solid red circles, respectively. The solid lines indicate fits of Equation (25) to the data using S_0, $\overline{D}$, μ_2, and μ_2^{iso} as adjustable parameters. The dashed lines show the single-exponential decay $S/S_0 = exp(-b\overline{D})$. The inserts illustrate the microstructure, with water occupying the white space between the black barriers: **(i)** single-orientation anisotropic, **(ii)** randomly oriented anisotropic domains, **(iii)** water inside and between spherical compartments, and **(iv)** mixed case with spherical compartments and anisotropic domains. The panels are labeled with the characteristic relations between μ_2 and μ_2^{iso}.

Fractional microscopic anisotropy

The information about microscopic diffusion anisotropy lies in the difference between $S(b)$ data acquired with isotropic or powder-averaged directional DW. We believe that it is good practice to inspect the raw data to make sure that the fitted parameters are consistent with the features that can be observed visually. **Figure 2B** illustrates that very small deviations from a mono-exponential form of $S(b)$ correspond to relatively large μFA values, potentially leading to erroneous conclusion when noisy data is used to estimate μFA. Data for four representative voxels can be found in **Figure 6**. Plotting the data as a function of $b\overline{D}$ rather than b emphasizes the deviation from mono-exponential decay and facilitates the comparison of data from voxels having different values of $\overline{D}$ [72]. The data for voxels *i* and *ii* originate from lamellar liquid crystalline phases that are coherently oriented (FA = 0.54) and randomly oriented (FA = 0.08), respectively. The mono-exponential decay of the isotropic data shows that there is a single type of water environment within the voxel, while the pronounced multi-exponential decay of the powder-averaged data proves that this environment is anisotropic. The similarity of the data for the voxels *i* and *ii* verifies that there is no influence from the voxel-scale orientation distribution of the anisotropic objects. Completely different behavior can be observed in the data from the yeast suspension in voxel *iii*. In this case both the isotropic and the powder-averaged data feature pronounced and identical signal attenuation, consistent with the presence of multiple isotropic water environments. Voxel *iv* is located at the border between the liquid crystal and yeast suspension compartments and shows signs of both multiple environments (the isotropic data) and diffusion anisotropy (pronounced multi-exponentiality for the powder-averaged data). For now, we refrain from trying to disentangle the contributions from multiple environments with varying degrees of anisotropy, but we conjecture that our approach with isotropic DW could add sufficient information to make such deconvolution feasible in a manner analogous to the separation of isotropic and anisotropic contributions to the chemical shift in solid-state NMR spectroscopy [73].

The parameter $\Delta\widetilde{\mu}_2$ is in itself an adequate measure of diffusion anisotropy. The values of $\Delta\widetilde{\mu}_2$ are related to the eigenvalues of the diffusion tensor through Equation (11), covering the range from 0, for isotropic diffusion, to 0.4 when $D_{||} << D_{\perp}$ and 0.8 if $D_{||} >> D_{\perp}$. The FA index has been adopted as the standard measure for voxel-scale diffusion anisotropy, and it is thus desirable to convert $\Delta\widetilde{\mu}_2$ to a parameter that is directly comparable with FA. As described in the theory section, we define the microscopic fractional anisotropy, μFA, as the value of FA that would be observed if all the anisotropic objects had the same orientation throughout the voxel. The value of μFA can be calculated from $\Delta\widetilde{\mu}_2$ using Equation (14), which is also shown as a graph in **Figure 2A**. A comparison of FA and μFA data for the liquid crystal/yeast phantom is shown in **Figure 7**. Because of the highly non-linear relation between μFA and $\Delta\widetilde{\mu}_2$, even moderate fit errors in $\Delta\widetilde{\mu}_2$ get greatly amplified in the conversion to μFA when the values of $\Delta\widetilde{\mu}_2$ are smaller than approximately 0.1

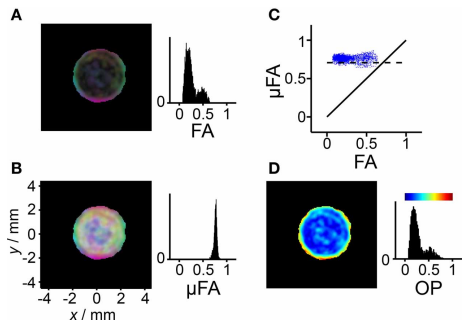

FIGURE 7 | Diffusion anisotropy and orientation dispersion in the liquid crystal. The analysis is performed on the data from **Figure 6** fulfilling the conditions $\overline{D} < 1\mu m^2/ms$ and $\Delta\widetilde{\mu}_2 > 0.15$, thus excluding pixels dominated by signal from the yeast suspension. **(A)** Parametric map with brightness given by the fractional anisotropy (FA) and color-coding according to D_{xx}/λ_1 (red), D_{yy}/λ_1 (green), and D_{zz}/λ_1 (blue), where D_{xx}, D_{yy}, and D_{zz} are elements of the laboratory-frame diffusion tensor and λ_1 is its largest eigenvalue. **(B)** As in panel **(A)**, but with brightness given by the microscopic fractional anisotropy (μFA) calculated from $\Delta\widetilde{\mu}_2$ in **Figure 5F** using Equation (14). Bright pixels with weak color saturation are observed when μFA >> FA. **(C)** Scatter plot showing the correlation between μFA and FA. The solid and dashed lines indicate μFA = FA and $\mu\text{FA} = \sqrt{1/2}$, respectively, the latter being expected for a liquid crystal with ideal lamellar geometry. **(D)** Parametric map and histogram of the order parameter (OP) calculated with Equation (21). The color-scale is given by the bar above the histogram. Pixels not included in the analysis are shown in black.

(see **Figures 2C,D**). Consequently, we select the pixels for which the conversion can be reliably performed by applying a threshold value of 0.15. With this threshold, only the pixels from the liquid crystal are included in the analysis. The histograms in **Figures 7A,B** show that FA covers the range from 0 to 0.6 while the values of μFA are centered at 0.76 with a standard deviation of 0.03. No correlation between μFA and FA can be discerned in the scatter plot in **Figure 7C**, indicating that the observed spread in μFA can be attributed to the precision of the experiment rather than any true inhomogeneity of the liquid crystal sample. Even when taking into account the spread of the data, the experimental values are consistently located above the line μFA = 0.71 which is the theoretical maximum for oblate diffusion tensors. This discrepancy originates from our procedure for estimating the values of μ_2 from the experimental data using Equation (25) as a fitting function. A positive bias of μFA, visible in **Figures 2C,D**, arises due to the interplay between the functional form of Equation (25) and the rather extended range of b-values used for the fit. When the gamma distribution is used to approximate the diffusion dispersion due to the orientation dispersion in purely anisotropic systems, the attenuation data can be described accurately by the function in Equation (25) only for a limited range of b-values. In the case of anisotropy with axial symmetry, for which the echo attenuation can be calculated analytically (see Equation 35 in [34]) and the exact values for $\overline{D}$ and μ_2 are given by Eq. (11), the function in Eq (25) increasingly underestimates the signal intensity at $b\overline{D} > 1$. Thus, the μ_2 value tends to be overestimated when Equation (25) is regressed onto the dataset with too high b-values resulting in an overestimation of the μFA. The bias could be reduced by limiting the range of b-values, but unfortunately at the expense of a severe loss in precision of the fitted parameters. Finding the optimal fitting function and b-values could be decisive for the success of transferring our approach to *in vivo* measurements. Still, we choose to postpone further investigations of this subject.

In the FA and μFA parameter maps in **Figures 7A,B,** the RGB levels are based on the three diagonal elements of the diffusion tensor in the laboratory frame of reference. The alignment of the lamellar planes at the glass surface gives rise to an intensely colored band at the outer edge of the liquid crystal compartment in both the FA and μFA maps. In stark contrast to the FA map, the brightness of the μFA map is constant on account of the nearly uniform values of μFA. Weakly colored bright pixels can be found in the interior of the compartment where there is no preferential orientation of the lamellar microcrystallites. The corresponding pixels in the FA map are nearly black because of the absence of voxel-scale anisotropy.

Order parameter

While the μFA parameter contains information about the microscopic diffusion anisotropy, the value of FA additionally includes the effect of voxel-scale alignment of the underlying anisotropic objects. Consequently, it seems logical to use the values of FA and μFA to define a parameter quantifying the orientational order or, alternatively, disorder. In the field of liquid crystals, the orientational ordering is conventionally described with an OP, defined as an ensemble average in Equation (18). In cases of lower than uniaxial symmetry, the scalar OP is generalized to an order matrix. Complete alignment of the anisotropic objects gives OP = 1, while random orientations correspond to OP = 0. Equations (19) and (21) describe how OP can be calculated from the measured diffusion tensor eigenvalues and the variances of the diffusion distribution, respectively. The eigenvalues and variances correspond to the information contained in the FA and μFA parameters, respectively. The resulting OP map for the liquid crystal is shown in **Figure 7D**. In line with the previous results, a highly ordered region can be found next to the glass surface, while the interior of the liquid crystal displays low order. Since the values of μFA are nearly constant, and there is a monotonous, albeit nonlinear, relation between FA and OP, as described by Equations (21) and (22), the corresponding histograms in **Figures 7A,D** have similar shapes. The benefit of using OP, rather than some more directly calculated measure such as the ratio FA/μFA, is that it has a simple geometrical definition through Equation (18), and that it is a well-established parameter in other fields of science.

WHOLE-BODY SCANNER

Measurements of μFA were also successfully implemented on a clinical system. The highly efficient single-shot isotropic DW protocol, based on the optimized q-MAS gradient modulation [37], allows to achieve high DW even at a standard clinical scanner with significant gradient amplitude and

energy constrains. It is worth noting that, although the clinical scanner was equipped with gradients capable of 80 mT/m on axis, the maximum b-value of 2800 ms/mm^2 for a total diffusion encoding time of 125.8 ms was mainly restricted by the power available to the gradient amplifiers. The results for the whole-body scanner imaging experiments are shown in **Figure 8** as parametric maps, histograms and signal curves. The measurements were performed on a phantom consisting of one compartment that contained coherent micro domains (intact asparagus stems) and another compartment that contained small domains with high orientation dispersion (pureed asparagus).

The FA map for the intact asparagus phantom indicates a high degree of voxel scale anisotropy, as seen in **Figure 8B**. However, when the coherent geometry of the asparagus stem is distorted, as in the pureeing process, the anisotropy on the voxel scale is strongly suppressed (see **Figure 8G**). By contrast, the microscopic anisotropy is visible in the μFA both before and after the pureeing process, as seen in **Figures 8C,H**. The effects on FA and μFA were quantified using two ROIs placed in specific regions of the phantom in order to reduce the influence from the free water. The first ROI was placed over several intact asparagus stems and the second included the central parts of the asparagus puree. Notice that several stems of asparagus exhibited hyperintensity in the T_2 map, and were also found to have lower values of FA and μFA, suggesting that the microarchitecture of these stems was compromised, possibly due to mechanical damage or natural degradation. In order to avoid such damaged tissue, these stems were excluded from the ROIs. The mean parameter value in the two ROIs was $\mathrm{FA}_{\mathrm{intact}} = 0.50$ and $\mathrm{FA}_{\mathrm{puree}} = 0.06$, and $\mu\mathrm{FA}_{\mathrm{intact}} = 0.75$ and $\mu\mathrm{FA}_{\mathrm{puree}} = 0.50$, respectively. The FA value of intact asparagus is in agreement with other experiments that have employed similar diffusion times [41]. The distributions of parameter values are presented in histograms in **Figures 8D,I**. The histogram visualizes the high contrast between the FA and the μFA in the pureed tissue, demonstrating how the μFA is still sensitive to the anisotropic diffusion at the scale of each asparagus fragment even if the diffusion is approximately isotropic on the voxel scale. The fact that the μFA is decreased in the pureed tissue can be attributed to the loss of anisotropy in the tissue microstructure and the relatively large water component introduced in the pureeing process.

The fitted lines for the representative voxels, resulting from regression of Equation (25), are shown in **Figures 8E,J**. The fit parameters in the intact asparagus were $\overline{D} = 1.55 \pm 0.05\,\mu\mathrm{m}^2/\mathrm{ms}$, $\mu_2^{\mathrm{iso}} = 0.60 \pm 0.12\,\mu\mathrm{m}^4/\mathrm{ms}^2$ ($\mu_2^{\mathrm{iso}}/\overline{D}^2 \approx 0.25$) and $\mu_2 = 1.24 \pm 0.18\,\mu\mathrm{m}^4/\mathrm{ms}^2$ ($\mu_2/\overline{D}^2 \approx 0.52$) resulting in a μFA value of 0.77 ± 0.03. The corresponding values in the pureed asparagus were $\overline{D} = 1.96 \pm 0.02\,\mu\mathrm{m}^2/\mathrm{ms}$, $\mu_2^{\mathrm{iso}} = 0.17 \pm 0.06\,\mu\mathrm{m}^4/\mathrm{ms}^2$ ($\mu_2^{\mathrm{iso}}/\overline{D}^2 \approx 0.04$) and $\mu_2 = 0.64 \pm 0.06\,\mu\mathrm{m}^4/\mathrm{ms}^2$ ($\mu_2/\overline{D}^2 \approx 0.17$) result in a μFA value of 0.60 ± 0.02. The standard deviations were estimated by a Monte Carlo error analysis [66]. The high apparent diffusivity in the pureed asparagus tissue further supports the notion that the calculation of μFA in the pureed tissue was affected by a free water component.

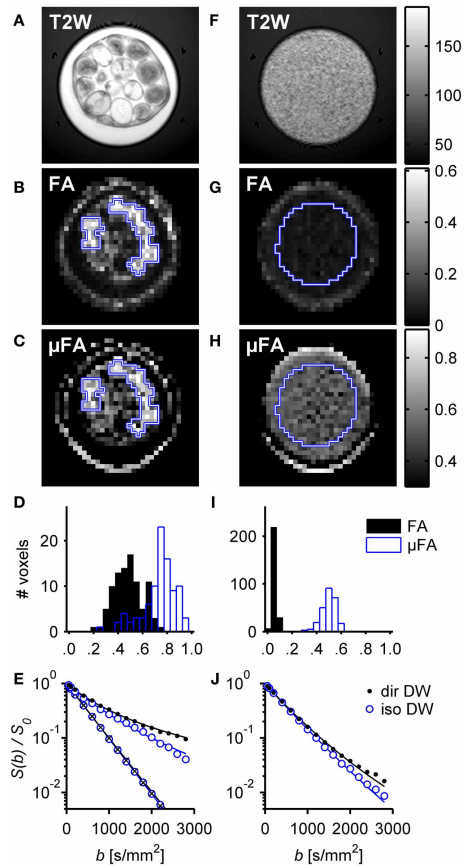

FIGURE 8 | Results of the whole-body scanner experiment on water in intact and pureed asparagus. The left column **(A–E)** shows the resulting images in the intact asparagus, and the right column **(F–J)** shows corresponding images for the pureed asparagus. The top row shows high resolution T_2-weighted images. The second and third rows show FA and μFA maps, respectively. A high FA is only observed in the intact asparagus while μFA can be observed in both intact and pureed asparagus. The histograms show the distribution of FA and μFA in the ROIs (blue outline superimposed on FA and μFA maps). The bottom row shows normalized signal intensity vs. diffusion weighting, $S(b)/S_0$, for representative voxels found in the ROIs (signal from isotropic DW: empty blue circles; powder-averaged directional DW: filled black circles). The bottom left plot **(E)** includes the signal from a region consisting of unobstructed water measured by directional (crosses) and isotropic DW (circles). The fitted regression lines, according to Equation (25), correspond to μFA values of 0.77 and 0.47 in the intact and pureed asparagus, respectively.

Parts of the phantom with intact asparagus consist purely of unobstructed water and thus serve as a reference to validate that in these regions the isotropic and directional DW indeed yield identical signal attenuation. The signal from one such

region with unobstructed water (ROI not shown), is depicted by circles and crosses in **Figure 8E**. The data coincide and show mono-exponential attenuation, thus verifying that the isotropic and directional experiments give the same DW for an isotropic liquid.

SIGNIFICANCE AND IMPLEMENTATION OF MICROSCOPIC ANISOTROPY BIOMARKERS

Biophysical modeling of WM is a field that has attracted much activity lately [74], and the need to disentangle orientation dispersion from dispersion in compartment size is now obvious [23, 75, 76]. Isotropic *q*-MAS DW could be an important tool to help disentangle the two phenomena. We suggest that the implementation of the isotropic DW in combination with the standard high *b*-value directional DW may generate new valuable biomarkers, such as the μFA and OP, that would allow identifying more specific mechanisms in cases where confounders would otherwise lower the specificity of parameters such as FA. This could be particularly helpful in selective WM atrophy in crossing geometries where the removal of one fiber population would cause the FA to increase, creating an opposite effect size as compared to unidirectional geometries [17]. Unlike the FA, the μFA is not restricted to macroscopically anisotropic tissue and it is thus suited for diagnosing also macroscopically isotropic tissue such as GM, where it could detect changes in the anisotropic diffusion, a feature that is useful in the mapping of GM deterioration. The μFA could also assist in the pre-surgical planning of tumor removal by differentiating different types of tissue consistency [77].

The application of the method for *in vivo* quantification of microscopic anisotropy should be straight forward, but was outside the scope of this paper. Previous studies employing non-conventional diffusion encoding have produced promising results in the human brain despite the long echo times required by the signal preparation [78–80]. For accurate μFA quantification, especially in tissue close to cerebrospinal fluid, such as the cortical GM, the partial volume effect needs to be considered. Ignoring this problem is known to bias the results of conventional DTI and non-conventional diffusion MRI such as filter-exchange imaging [78, 81]. The most straightforward means of mitigating the partial volume effect would be to include an isotropic component with high-diffusivity and zero anisotropy in addition to Equation (25) for the tissue signal. Once a suitable signal model is constructed, the experiment design can be optimized to minimize the influence of noise on parameter estimates [82]. Finally, the noise-induced variance should be compared to the biological variance in μFA, to aid the design of clinical studies [83].

CONCLUSION

We demonstrated that the microscopic anisotropy can be quantified based on the comparison between isotropic and powder-averaged directional DW data. Proof-of-principle experiments were carried out on selected phantoms at a high-field spectrometer as well as on a standard clinical scanner. The spin-echo implementation of the optimized single-shot *q*-MAS DW provides efficient diffusion encoding. On the clinical scanner, *q*-MAS DW using echo-time of 160 ms yields *b*-values comparable to DKI experiments.

While adding the isotropic DW experiment to the standard DTI requires only minor additional experimental time, it adds valuable information to the powder-averaged directional DW data. In addition to FA, available from the DTI, the experiment with isotropic DW allows disentangling the contributions of microscopic anisotropy and orientation dispersion of microdomains, which can be quantified by the herein introduced μFA and OP parameters. The μFA is not affected by the orientation dispersion of microscopic structures and it corresponds to the values of FA in the absence of orientation dispersion. Since the μFA is not sensitive to the macroscopic organization of anisotropic structures, like crossing fibers of the WM, the μFA could provide a valuable new biomarker to characterize tissue.

AUTHOR AND CONTRIBUTORS

All the authors of this manuscript: Samo Lasič, Filip Szczepankiewicz, Stefanie Eriksson, Markus Nilsson, Daniel Topgaard, fulfill the authorship criteria according to Substantial contributions to the conception or design of the work; or the acquisition, analysis, or interpretation of data for the work; Drafting the work or revising it critically for important intellectual content; Final approval of the version to be published; and Agreement to be accountable for all aspects of the work in ensuring that questions related to the accuracy or integrity of any part of the work are appropriately investigated and resolved.

ACKNOWLEDGMENTS

The work was financially supported by the Swedish Research Council (2009–6794, 2011–4334, K2011-52x-21737-01-3), the Swedish Cancer Society (04 0421) and the National Institute of Health (NIH R01MH074794). Fruitful discussions with Carl-Fredrik Westin are gratefully acknowledged.

REFERENCES

1. Callaghan PT. *Translational Dynamics and Magnetic Resonance: Principles of Pulsed Gradient Spin Echo NMR*. Oxford: Oxford University Press (2011).
2. Price W. *NMR Studies of Translational Motion: Principles and Applications*. Cambridge: Cambridge University Press (2009).
3. Hürlimann MD, Helmer KG, Latour LL, Sotak CH. Restricted diffusion in sedimentary rocks. Determination of surface-area-to-volume ratio and surface relaxivity*J Magn Reson Ser A* (1994) **111**:169–78. doi: 10.1006/jmra.1994.1243
4. Topgaard D, Söderman O. Self-diffusion of nonfreezing water in porous carbohydrate polymer systems studied with nuclear magnetic resonance. *Biophys J.* (2002) **83**:3596–606. doi: 10.1016/S0006-3495(02)75360-5
5. Lasič S, Åslund I, Topgaard D. Spectral characterization of diffusion with chemical shift resolution: highly concentrated water-in-oil emulsion. *J Magn Reson.* (2009) **199**:166–72. doi: 10.1016/j.jmr.2009.04.014
6. Le Bihan D. Looking into the functional architecture of the brain with diffusion MRI. *Nat Rev Neurosci.* (2003) **4**:469–80. doi: 10.1038/nrn1119
7. Latour LL, Mitra PP, Kleinberg RL, Sotak CH. Time-dependent diffusion coefficient of fluids in porous media as a probe of surface-to-volume ratio. *J Magn Reson Ser A* (1993) **101**:342–6. doi: 10.1006/jmra.1993.1056
8. Topgaard D, Söderman O. Experimental determination of pore shape and size using *q*-space NMR microscopy in the long diffusion-time limit. *Magn Reson Imaging* (2003) **21**:69–76. doi: 10.1016/s0730-725x(02)00626-4
9. Latour LL, Kleinberg RL, Mitra PP, Sotak CH. Pore-size distributions and tortuosity in heterogeneous porous media. *J Magn Reson Ser A* (1995) **112**:83–91. doi: 10.1006/jmra.1995.1012

10. Topgaard D, Söderman O. Diffusion of water absorbed in cellulose fibers studied with ^{1}H-NMR. *Langmuir* (2001) **17**:2694–702. doi: 10.1021/la0009821
11. Lasič S, Nilsson M, Lätt J, Ståhlberg F, Topgaard D. Apparent exchange rate mapping with diffusion MRI. *Magn Reson Med.* (2011) **66**:356–65. doi: 10.1002/mrm.22782
12. Basser PJ, Pierpaoli C. Microstructural and physiological features of tissues elucidated by quantitative-diffusion-tensor MRI. *J Magn Reson Ser B* (1996) **111**:209–19. doi: 10.1006/jmrb.1996.0086
13. Basser PJ, Mattiello J, LeBihan D. MR diffusion tensor spectroscopy and imaging. *Biophys J.* (1994) **66**:259–67. doi: 10.1016/S0006-3495(94)80775-1
14. Moseley ME, Kucharczyk J, Asgari HS, Norman D. Anisotropy in diffusion-weighted MRI. *Magn Reson Med.* (1991) **19**:321–6. doi: 10.1002/mrm.1910190222
15. Jeurissen B, Leemans A, Tournier J-D, Jones DK, Sijbers J. Investigating the prevalence of complex fiber configurations in white matter tissue with diffusion magnetic resonance imaging. *Hum Brain Mapp.* (2013) **34**:2747–66. doi: 10.1002/hbm.22099
16. Jones DK, Knösche TR, Turner R. White matter integrity, fiber count, and other fallacies: the do's and don'ts of diffusion MRI. *Neuroimage* (2013) **73**:239–54. doi: 10.1016/j.neuroimage.2012.06.081
17. Douaud G, Jbabdi S, Behrens TEJ, Menke RA, Gass A, Monsch AU, et al. DTI measures in crossing-fibre areas: increased diffusion anisotropy reveals early white matter alteration in MCI and mild Alzheimer's disease. *Neuroimage* (2011) **55**:880–90. doi: 10.1016/j.neuroimage.2010.12.008
18. Sundgren PC, Dong Q, Gómez-Hassan D, Mukherji SK, Maly P, Welsh R. Diffusion tensor imaging of the brain: review of clinical applications. *Neuroradiology* (2004) **46**:339–50. doi: 10.1007/s00234-003-1114-x
19. Assaf Y, Pasternak O. Diffusion tensor imaging (DTI)-based white matter mapping in brain research: a review. *J Mol Neurosci.* (2008) **34**:51–61. doi: 10.1007/s12031-007-0029-0
20. McNab JA, Jbabdi S, Deoni SCL, Douaud G, Behrens TEJ, Miller KL. High resolution diffusion-weighted imaging in fixed human brain using diffusion-weighted steady state free precession. *Neuroimage* (2009) **46**:775–85. doi: 10.1016/j.neuroimage.2009.01.008
21. Beaulieu C. The basis of anisotropic water diffusion in the nervous system—a technical review. *NMR Biomed.* (2002) **15**:435–55. doi: 10.1002/nbm.782
22. Assaf Y, Basser PJ. Composite hindered and restricted model of diffusion (CHARMED) MR imaging of the human brain. *Neuroimage* (2005) **27**:48–58. doi: 10.1016/j.neuroimage.2005.03.042
23. Zhang H, Schneider T, Wheeler-Kingshott CA, Alexander DC. NODDI: practical *in vivo* neurite orientation dispersion and density imaging of the human brain. *Neuroimage* (2012) **61**:1000–16. doi: 10.1016/j.neuroimage.2012.03.072
24. Callaghan PT, Söderman O. Examination of the lamellar phase of Aerosol OT/water using pulsed field gradient nuclear magnetic resonance. *J Phys Chem.* (1983) **87**:1737–44. doi: 10.1021/j100233a019
25. Topgaard D, Söderman O. Self-diffusion in two- and three-dimensional powders of anisotropic domains: an NMR study of the diffusion of water in cellulose and starch. *J Phys Chem B* (2002) **106**:11887–92. doi: 10.1021/jp020130p
26. Mitra P. Multiple wave-vector extensions of the NMR pulsed-field-gradient spin-echo diffusion measurement. *Phys Rev B* (1995) **51**:15074–8. doi: 10.1103/PhysRevB.51.15074
27. Callaghan PT, Komlosh ME. Locally anisotropic motion in a macroscopically isotropic system: displacement correlations measured using double pulsed gradient spin-echo NMR. *Magn Reson Chem.* (2002) **40**:S15–S19. doi: 10.1002/mrc.1122
28. Komlosh ME, Horkay F, Freidlin RZ, Nevo U, Assaf Y, Basser PJ. Detection of microscopic anisotropy in gray matter and in a novel tissue phantom using double Pulsed Gradient Spin Echo MR. *J Magn Reson.* (2007) **189**:38–45. doi: 10.1016/j.jmr.2007.07.003
29. Komlosh ME, Lizak MJ, Horkay F, Freidlin RZ, Basser PJ. Observation of microscopic diffusion anisotropy in the spinal cord using double-pulsed gradient spin echo MRI. *Magn Reson Med.* (2008) **59**:803–9. doi: 10.1002/mrm.21528
30. Shemesh N, Adiri T, Cohen Y. Probing microscopic architecture of opaque heterogeneous systems using double-pulsed-field-gradient NMR. *J Am Chem Soc.* (2011) **133**:6028–35. doi: 10.1021/ja200303h
31. Shemesh N, Cohen Y. Microscopic and compartment shape anisotropies in gray and white matter revealed by angular bipolar double-PFG MR. *Magn Reson Med.* (2011) **65**:1216–27. doi: 10.1002/mrm.22738
32. Jespersen SN, Lundell H, Sønderby CK, Dyrby TB. Orientationally invariant metrics of apparent compartment eccentricity from double pulsed field gradient diffusion experiments. *NMR Biomed.* (2013) **26:**1647–62. doi: 10.1002/nbm.2999
33. Bernin D, Topgaard D. NMR diffusion and relaxation correlation methods: new insights in heterogeneous materials. *Curr Opin Colloid Interface Sci.* (2013) **18**:166–72. doi: 10.1016/j.cocis.2013.03.007
34. Eriksson S, Lasič S, Topgaard D. Isotropic diffusion weighting in PGSE NMR by magic-angle spinning of the *q*-vector. *J Magn Reson.* (2013) **226**:13–8. doi: 10.1016/j.jmr.2012.10.015
35. Mori S, van Zijl PC. Diffusion weighting by the trace of the diffusion tensor within a single scan. *Magn Reson Med.* (1995) **33**:41–52. doi: 10.1002/mrm.1910330107
36. Wong EC, Cox RW, Song AW. Optimized isotropic diffusion weighting. *Magn Reson Med.* (1995) **34**:139–43. doi: 10.1002/mrm.1910340202
37. Topgaard D. Isotropic diffusion weighting in PGSE NMR: numerical optimization of the *q*-MAS PGSE sequence. *Micropor Mesopor Mat.* (2013) **178**:60–3. doi: 10.1016/j.micromeso.2013.03.009
38. Åslund I, Cabaleiro-Lago C, Söderman O, Topgaard D. Diffusion NMR for determining the homogeneous length-scale in lamellar phases. *J Phys Chem B* (2008) **112**:2782–94. doi: 10.1021/jp076174l
39. Hubbard PL, McGrath KM, Callaghan PT. Orientational anisotropy in the polydomain lamellar phase of a lyotropic liquid crystal. *Langmuir* (2006) **22**:3999–4003. doi: 10.1021/la052998n
40. Hubbard PL, McGrath KM, Callaghan PT. Evolution of a lamellar domain structure for an equilibrating lyotropic liquid crystal. *J Phys Chem B* (2006) **110**:20781–8. doi: 10.1021/jp0601872
41. Lätt J, Nilsson M, Rydhög A, Wirestam R, Ståhlberg F, Brockstedt S. Effects of restricted diffusion in a biological phantom: a q-space diffusion MRI study of asparagus stems at a 3T clinical scanner. *MAGMA* (2007) **20**:213–22. doi: 10.1007/s10334-007-0085-z
42. Jansen JFA, Stambuk HE, Koutcher JA, Shukla-Dave A. Non-gaussian analysis of diffusion-weighted MR imaging in head and neck squamous cell carcinoma: a feasibility study. *Am J Neuroradiol.* (2010) **31**:741–8. doi: 10.3174/ajnr.A1919
43. Jensen JH, Helpern JA, Ramani A, Lu H, Kaczynski K. Diffusional kurtosis imaging: the quantification of non-gaussian water diffusion by means of magnetic resonance imaging. *Magn Reson Med.* (2005) **53**:1432–40. doi: 10.1002/mrm.20508
44. Paulsen JL, Cho H, Cho G, Song Y-Q. Acceleration of multi-dimensional propagator measurements with compressed sensing. *J Magn Reson.* (2011) **213**:166–70. doi: 10.1016/j.jmr.2011.08.025
45. Silva MD, Helmer KG, Lee J-H, Han SS, Springer CS, Sotak CH. Deconvolution of compartmental water diffusion coefficients in yeast-cell suspensions using combined T_1 and diffusion measurements. *J Magn Reson.* (2002) **156**:52–63. doi: 10.1006/jmre.2002.2527
46. Åslund I, Topgaard D. Determination of the self-diffusion coefficient of intracellular water using PGSE NMR with variable gradient pulse length. *J Magn Reson.* (2009) **201**:250–4. doi: 10.1016/j.jmr.2009.09.006
47. Åslund I, Nowacka A, Nilsson M, Topgaard D. Filter-exchange PGSE NMR determination of cell membrane permeability. *J Magn Reson.* (2009) **200**:291–5. doi: 10.1016/j.jmr.2009.07.015
48. Zhang H, Hubbard PL, Parker GJM, Alexander DC. Axon diameter mapping in the presence of orientation dispersion with diffusion MRI. *Neuroimage* (2011) **56**:1301–15. doi: 10.1016/j.neuroimage.2011.01.084
49. Sotiropoulos SN, Behrens TEJ, Jbabdi S. Ball and rackets: inferring fiber fanning from diffusion-weighted MRI. *Neuroimage* (2012) **60**:1412–25. doi: 10.1016/j.neuroimage.2012.01.056
50. Emsley JW. (ed.). *Nuclear Magnetic Resonance of Liquid Crystals*. Dordrecht: D. Reidel Publishing Company (1985).
51. Ronen I, Moeller S, Ugurbil, K, Kim D-S. Analysis of the distribution of diffusion coefficients in cat brain at 9.4 T using the inverse Laplace transformation. *Magn Reson Imaging* (2006) **24**:61–8. doi: 10.1016/j.mri.2005.10.023

52. Johnson CS Jr. Diffusion ordered nuclear magnetic resonance spectroscopy: principles and applications. *Prog Nucl Magn Reson Spectrosc.* (1999) **34**:203–56. doi: 10.1016/s0079-6565(99)00003-5
53. Frisken BJ. Revisiting the method of cumulants for the analysis of dynamic light-scattering data. *Appl Opt.* (2001) **40**:4087. doi: 10.1364/AO.40.004087
54. Westin CF, Maier SE, Mamata H, Nabavi A, Jolesz FA, Kikinis R. Processing and visualization for diffusion tensor MRI. *Med Image Anal.* (2002) **6**:93–108. doi: 10.1016/S1361-8415(02)00053-1
55. VanderHart DL, Gutowsky HS. Rigid-lattice NMR moments and line shapes with chemical-shift anisotropy. *J Chem Phys.* (1968) **49**:261. doi: 10.1063/1.1669820
56. Bloembergen N, Rowland TJ. On the nuclear magnetic resonance in metals and alloys. *Acta Metall.* (1953) **1**:731–46. doi: 10.1016/0001-6160(53)90033-9
57. Röding M, Bernin D, Jonasson J, Särkkä A, Topgaard D, Rudemo M, et al. The gamma distribution model for pulsed-field gradient NMR studies of molecular-weight distributions of polymers. *J Magn Reson.* (2012) **222**:105–11. doi: 10.1016/j.jmr.2012.07.005
58. Le TD, Olsson U, Mortensen K, Zipfel J, Richtering W. Nonionic amphiphilic bilayer structures under shear. *Langmuir* (2001) **17**:999–1008. doi: 10.1021/la001227a
59. Oliviero C, Coppola L, Gianferri R, Nicotera I, Olsson U. Dynamic phase diagram and onion formation in the system $C_{10}E_3/D_2O$. *Colloids Surface A* (2003) **228**:85–90. doi: 10.1016/S0927-7757(03)00356-X
60. Hennig J, Nauerth A, Friedburg H. RARE imaging: a fast imaging method for clinical MR. *Magn Reson Med.* (1986) **3**:823–33. doi: 10.1002/mrm.1910030602
61. Bak M, Nielsen N. REPULSION, a novel approach to efficient powder averaging in solid-state NMR. *J Magn Reson.* (1997) **125**:132–9. doi: 10.1006/jmre.1996.1087
62. Jones DK, Horsfield MA, Simmons A. Optimal strategies for measuring diffusion in anisotropic systems by magnetic resonance imaging. *Magn Reson Med.* (1999) **42**:515–25. doi: 10.1002/(SICI)1522-2594(199909)42:3<515::AID-MRM14>3.0.CO;2-Q
63. Bodenhausen G, Freeman R, Turner DL. Suppression of artifacts in two-dimensional *J* spectroscopy. *J Magn Reson.* (1977) **27**:511–4. doi: 10.1016/0022-2364(77)90016-6
64. Zhu X, Tomanek B, Sharp J. A pixel is an artifact: on the necessity of zero-filling in fourier imaging. *Concepts Magn Reson Part A* (2013) **42**:32–44. doi: 10.1002/cmr.a.21256
65. Mansfield P. Multi-planar image formation using NMR spin echoes. *J Phys C Solid State Phys.* (1977) **10**:L55–L58. doi: 10.1088/0022-3719/10/3/004
66. Alper JS, Gelb RI. Standard errors and confidence intervals in nonlinear regression: comparison of Monte Carlo and parametric statistics. *J Phys Chem.* (1990) **94**:4747–51. doi: 10.1021/j100374a068
67. Price WS, Ide H, Arata Y. Self-diffusion of supercooled water to 238 K using PGSE NMR diffusion measurements. *J Phys Chem A* (1999) **103**:448–50. doi: 10.1021/jp9839044
68. Stejskal EO. Use of spin echoes in a pulsed magnetic-field gradient to study anisotropic, restricted diffusion and flow. *J Chem Phys.* (1965) **43**:3597. doi: 10.1063/1.1696526
69. Jönsson B, Wennerström H, Nilsson PG, Linse P. Self-diffusion of small molecules in colloidal systems. *Colloid Polym Sci.* (1986) **264**:77–88. doi: 10.1007/BF01410310
70. Malmborg C, Sjöbeck M, Brockstedt S, Englund E, Söderman O, Topgaard D. Mapping the intracellular fraction of water by varying the gradient pulse length in *q*-space diffusion MRI. *J Magn Reson.* (2006) **180**:280–5. doi: 10.1016/j.jmr.2006.03.005
71. Suwelack D, Rothwell WP, Waugh JS. Slow molecular motion detected in the NMR spectra of rotating solids. *J Chem Phys.* (1980) **73**:2559. doi: 10.1063/1.440491
72. Svensson A, Topgaard D, Piculell L, Söderman O. Molecular self-diffusion in micellar and discrete cubic phases of an ionic surfactant withmixed monovalent/polymeric counterions. *J Phys Chem B* (2003) **107**:13241–50. doi: 10.1021/jp0348225
73. Tycko R, Dabbagh G, Mirau PA. Determination of chemical-shift-anisotropy lineshapes in a two-dimensional magic-angle-spinning NMR experiment. *J Magn Reson.* (1989) **85**:265–74. doi: 10.1016/0022-2364(89)90142-X
74. Nilsson M, van Westen D, Ståhlberg F, Sundgren PC, Lätt J. The role of tissue microstructure and water exchange in biophysical modelling of diffusion in white matter. *MAGMA* (2013) **26**:345–70. doi: 10.1007/s10334-013-0371-x
75. Nilsson M, Lätt J, Ståhlberg F, van Westen D, Hagslätt H. The importance of axonal undulation in diffusion MR measurements: a Monte Carlo simulation study. *NMR Biomed.* (2012) **25**:795–805. doi: 10.1002/nbm.1795
76. Ronen I, Budde M, Ercan E, Annese J, Techawiboonwong A, Webb A. Microstructural organization of axons in the human corpus callosum quantified by diffusion-weighted magnetic resonance spectroscopy of N-acetylaspartate and post-mortem histology. *Brain Struct Funct.* (2013) 1–13. doi: 10.1007/s00429-013-0600-0
77. Tropine A, Dellani PD, Glaser M, Bohl J, Plöner T, Vucurevic G, et al. Differentiation of fibroblastic meningiomas from other benign subtypes using diffusion tensor imaging. *J Magn Reson Imaging* (2007) **25**:703–8. doi: 10.1002/jmri.20887
78. Nilsson M, Lätt J, van Westen D, Brockstedt S, Lasič S, Ståhlberg F, et al. Noninvasive mapping of water diffusional exchange in the human brain using filter-exchange imaging. *Magn Reson Med.* (2013) **69**:1572–80. doi: 10.1002/mrm.24395
79. Avram AV, Özarslan E, Sarlls JE, Basser PJ. *In vivo* detection of microscopic anisotropy using quadruple pulsed-field gradient (qPFG) diffusion MRI on a clinical scanner. *Neuroimage* (2013) **64**:229–39. doi: 10.1016/j.neuroimage.2012.08.048
80. Lawrenz M, Finsterbusch J. Double-wave-vector diffusion-weighted imaging reveals microscopic diffusion anisotropy in the living human brain. *Magn Reson Med.* (2012) **69**:1072–82. doi: 10.1002/mrm.24347
81. Pasternak O, Sochen N, Gur Y, Intrator N, Assaf Y. Free water elimination and mapping from diffusion MRI. *Magn Reson Med.* (2009) **62**:717–30. doi: 10.1002/mrm.22055
82. Alexander DC. A general framework for experiment design in diffusion MRI and its application in measuring direct tissue-microstructure features. *Magn Reson Med.* (2008) **60**:439–48. doi: 10.1002/mrm.21646
83. Szczepankiewicz F, Lätt J, Wirestam R, Leemans A, Sundgren P, van Westen D, et al. Variability in diffusion kurtosis imaging: impact on study design, statistical power and interpretation. *Neuroimage* (2013) **76**:145–54. doi: 10.1016/j.neuroimage.2013.02.078

Conflict of Interest Statement: Patent applications in Sweden nr:1250453-6 and 1250452-8, applications in USA nr: 61/642 594, 61/642 589, PCT applications PCT/SE2013/050492 and PCT/SE2013/050493

Received: 04 December 2013; paper pending published: 14 January 2014; accepted: 09 February 2014; published online: 27 February 2014.
Citation: Lasič S, Szczepankiewicz F, Eriksson S, Nilsson M and Topgaard D (2014) Microanisotropy imaging: quantification of microscopic diffusion anisotropy and orientational order parameter by diffusion MRI with magic-angle spinning of the q-vector. Front. Physics ***2****:11. doi: 10.3389/fphy.2014.00011*
This article was submitted to Biophysics, a section of the journal Frontiers in Physics.

Paper III

NeuroImage 104 (2015) 241–252

Contents lists available at ScienceDirect

NeuroImage

journal homepage: www.elsevier.com/locate/ynimg

Quantification of microscopic diffusion anisotropy disentangles effects of orientation dispersion from microstructure: Applications in healthy volunteers and in brain tumors

Filip Szczepankiewicz [a,*], Samo Lasič [b], Danielle van Westen [c,d], Pia C. Sundgren [c,d], Elisabet Englund [e], Carl-Fredrik Westin [f], Freddy Ståhlberg [a,c,h], Jimmy Lätt [d], Daniel Topgaard [g], Markus Nilsson [h]

[a] Clinical Sciences, Lund, Department of Medical Radiation Physics, Lund University, Lund, Sweden
[b] CR Development, AB, Lund, Sweden
[c] Diagnostic Radiology, Department of Clinical Sciences, Lund, Lund University, Lund, Sweden
[d] Medical Imaging and Physiology, Skåne University Hospital, Lund, Sweden
[e] Division of Oncology and Pathology, Department of Clinical Sciences, Lund, Lund University, Skåne University Hospital, Lund, Sweden
[f] Laboratory for Mathematics in Imaging, Department of Radiology, Brigham and Women's Hospital, Harvard Medical School, Boston, MA, USA
[g] Division of Physical Chemistry, Department of Chemistry, Lund University, Lund, Sweden
[h] Lund University Bioimaging Center, Lund University, Lund, Sweden

ARTICLE INFO

Article history:
Accepted 25 September 2014
Available online 2 October 2014

Keywords:
Diffusion weighted imaging
Microscopic anisotropy
Microscopic fractional anisotropy
Order parameter
Magic angle spinning of the q-vector

ABSTRACT

The anisotropy of water diffusion in brain tissue is affected by both disease and development. This change can be detected using diffusion MRI and is often quantified by the fractional anisotropy (FA) derived from diffusion tensor imaging (DTI). Although FA is sensitive to anisotropic cell structures, such as axons, it is also sensitive to their orientation dispersion. This is a major limitation to the use of FA as a biomarker for "tissue integrity", especially in regions of complex microarchitecture. In this work, we seek to circumvent this limitation by disentangling the effects of microscopic diffusion anisotropy from the orientation dispersion.

The microscopic fractional anisotropy (μFA) and the order parameter (OP) were calculated from the contrast between signal prepared with directional and isotropic diffusion encoding, where the latter was achieved by magic angle spinning of the q-vector (qMAS). These parameters were quantified in healthy volunteers and in two patients; one patient with meningioma and one with glioblastoma. Finally, we used simulations to elucidate the relation between FA and μFA in various micro-architectures.

Generally, μFA was high in the white matter and low in the gray matter. In the white matter, the largest differences between μFA and FA were found in crossing white matter and in interfaces between large white matter tracts, where μFA was high while FA was low. Both tumor types exhibited a low FA, in contrast to the μFA which was high in the meningioma and low in the glioblastoma, indicating that the meningioma contained disordered anisotropic structures, while the glioblastoma did not. This interpretation was confirmed by histological examination.

We conclude that FA from DTI reflects both the amount of diffusion anisotropy and orientation dispersion. We suggest that the μFA and OP may complement FA by independently quantifying the microscopic anisotropy and the level of orientation coherence.

Introduction

The most established technique for non-invasive investigations of the microstructure of the central nervous system is diffusion tensor imaging (DTI) (Basser et al., 1994). DTI provides a means of estimating the rate of diffusion and the diffusional anisotropy in tissue, frequently expressed in terms of the mean diffusivity (MD) and the fractional anisotropy (FA), respectively. The diffusion anisotropy has been shown to correlate with the progression of a wide variety of conditions (Kubicki et al., 2002). For example, reduced FA is observed during aging (Hsu et al., 2010; Sullivan and Pfefferbaum, 2006), and in neurodegenerative diseases such as dementia (Englund et al., 2004; Santillo et al., 2013), Parkinson's disease (Surova et al., 2013), Alzheimer's disease (Sjobeck et al., 2010), and multiple sclerosis (Rovaris et al., 2005). By contrast, the value of FA tends to increase during white matter (WM) maturation (Lebel

* Corresponding author at: Department of Medical Radiation Physics, Clinical Sciences, Lund, Lund University, SE-22185 Lund, Sweden. Fax: +46 46 178540.
E-mail address: filip.szczepankiewicz@med.lu.se (F. Szczepankiewicz).

http://dx.doi.org/10.1016/j.neuroimage.2014.09.057

et al., 2008; Löbel et al., 2009) and after specific forms of training, such as juggling (Scholz et al., 2009).

While FA is clearly sensitive to microstructural alterations, such as demyelination, it also reflects a wide variety of non-specific and possibly confounding effects. One of the most prominent confounders of FA is the partial volume effect (PVE). Partial volume effects are especially relevant for diffusion-MRI (dMRI) where voxel volumes are typically on the scale of ~10 mm^3, resulting in a high probability for the MR signal to originate from water residing in different types of tissue. This includes voxels that are located at the interface between nerve bundles with different orientation, and at the interface between brain tissue and cerebrospinal fluid (CSF). Thus, the signal from individual voxels frequently reflects an average of different diffusion profiles. This invariably leads to less pronounced diffusion directionality, i.e., lower FA (Oouchi et al., 2007; Westin et al., 2002). Consequently, FA correlates with structure size since smaller structures include a larger fraction of voxels that interface with surrounding tissue than larger structures (Szczepankiewicz et al., 2013; Vos et al., 2011). Another aspect of PVE is the presence of crossing, kissing, fanning, and other irregular WM geometries within a voxel, which reduce the FA by inducing a higher degree of orientation dispersion (Alexander et al., 2001; Nilsson et al., 2012). Thus, the utility of FA as a biomarker in regions of complex WM architecture is impeded because it entangles multiple effects into a single value. Although frequently overlooked, this is not an idle theoretical issue but has practical consequences. For example, elevated values of FA have been found in crossing fibers in patients with Alzheimer's disease (Douaud et al., 2011; Teipel et al., 2014). This seemingly counter-intuitive result is explained by the selective damage to one of the fiber populations in the region (Douaud et al., 2011), resulting in reduced orientation dispersion and thus elevated FA. It is also worth noting that FA is an intrinsically poor biomarker in gray matter (GM) due to the high orientation dispersion of neurites in the cortex (Shemesh and Cohen, 2011). Thus, reliable use of FA may be confined to regions of highly coherent WM (De Santis et al., 2013), which is estimated to account for less than 10% of the total white matter of the human brain (Vos et al., 2012). This has prompted the search for methods that accurately model microscopic changes in complex neural tissue.

It has been shown that the effects of orientation and restriction can be disentangled by extending the conventional single pulsed-field-gradient (sPFG) experiment (Stejskal and Tanner, 1965) to include double, or multiple, pulsed-field-gradients (dPFG and mPFG, respectively) (Mitra, 1995). In dPFG experiments information can be derived from the dependence of the signal amplitude on the angle between two successive encoding blocks. Several methods have been proposed for the quantification of microscopic anisotropy from such data. To this end, Lawrenz and Finsterbusch (2013) used a fourth-order tensor parameterization suggested by Lawrenz et al. (2010) to map the microscopic diffusion anisotropy in human white matter in vivo. Jespersen et al. (2013) developed a rotationally invariant dPFG encoding scheme and mapped the microscopic anisotropy in an excised monkey brain in terms of the fractional eccentricity.

Recently, Lasič et al. (2014) formulated a framework for the quantification of microscopic diffusion anisotropy and orientation dispersion in terms of the microscopic fractional anisotropy (μFA) and order parameter (OP), respectively. These parameters were derived from the contrast between the signal acquired in diffusion weighting (DW) experiments that used conventional diffusion encoding as well as isotropic encoding based on magic angle spinning of the q-vector (qMAS) (Eriksson et al., 2013). Briefly, magic angle spinning is an established NMR spectroscopy method where a sample is rotated around its own axis at a specific angle relative to the B_0-field to minimize the influence of chemical shift anisotropy on the observed NMR spectrum. In qMAS, harmonic gradient modulation is used to create a q-vector that performs a precession at the magic angle in order to exert equal diffusion encoding in all spatial directions while the sample remains stationary. Although isotropic encoding can be achieved by combining multiple trapezoidal encoding blocks (Butts et al., 1997; Wong et al., 1995), the qMAS technique offers a time efficient gradient modulation scheme (Topgaard, 2013). The qMAS-encoded signal attenuation becomes independent of contributions from anisotropic diffusion, and is sensitive only to the rate of isotropic diffusion (Eriksson et al., 2013). As a proof-of-principle, Lasič et al. (2014) implemented the qMAS technique on a NMR spectrometer and a clinical scanner, showing that microscopic anisotropy could be detected in phantoms that contained ordered and disordered anisotropic micro-domains.

In this work we performed the first in vivo experiments using qMAS diffusion encoding, and we parameterize the microscopic anisotropy of the human brain based on the framework presented by Lasič et al. (2014). We also demonstrated the feasibility of quantifying microscopic anisotropy in a clinical setting by using it to infer information on tissue structure in two types of brain tumors. Finally, we compared the results to simulated data to elucidate how the measures of anisotropy respond to various changes in micro-architecture, and expanded on the possibilities to use this novel method in clinical research to access information that is unavailable when using conventional methods.

Theory

In conventional DTI, the diffusion on the voxel scale is assumed to be Gaussian and is described by a rank-2 tensor ($\mathbf{D}$) (Basser et al., 1994). The same description can be employed at a sub-voxel scale; meaning that each coherent segment of the underlying microgeometry can be considered as a *domain* in which the diffusion is Gaussian and described by a domain diffusion tensor ($\mathbf{D}_k$). The voxel scale tensor can be described as the average of all domain tensors, according to Eq. (1)

$$\mathbf{D} = \langle \mathbf{D}_k \rangle, \tag{1}$$

where $\mathbf{D} = \mathbf{D}_k$ only when the voxel contains identical domains that are perfectly aligned. In all other cases $\mathbf{D}$ will depend on the distribution of domain tensor eigenvalues, and their orientation (Fig. 1). Here, we denote objects pertaining to microscopic domains by a subscript 'k'. Consider three common parameterizations of $\mathbf{D}$: the mean diffusivity (MD), the variance of the diffusion tensor eigenvalues (V_λ), and the fractional anisotropy (FA), defined in Eqs. (2), (3), and (4) respectively (Basser and Pierpaoli, 1996)

$$\mathrm{MD} = \mathcal{f}(\mathbf{D}) = \frac{\mathrm{Tr}(\mathbf{D})}{3}, \tag{2}$$

$$V_\lambda = \mathcal{g}(\mathbf{D}) = \mathrm{Var}\big(\mathrm{Eig}(\mathbf{D})\big), \tag{3}$$

$$\mathrm{FA} = \mathcal{h}(\mathrm{MD}, V_\lambda) = \sqrt{\frac{3}{2}} \cdot \left(1 + \frac{\mathrm{MD}^2}{V_\lambda}\right)^{-\frac{1}{2}}. \tag{4}$$

Note that $\mathcal{f}(\mathbf{D}_k)$, $\mathcal{g}(\mathbf{D}_k)$ and $\mathcal{h}\big(\mathrm{MD}_k, V_{\lambda,k}\big)$ yield the corresponding parameters for a single domain, denoted MD_k, $V_{\lambda,k}$ and FA_k, respectively. From Eq. (1) to Eq. (4), it is clear that the FA represents the amount of microscopic anisotropy that persists to the voxel scale and is determined by the coherence of the domain orientations (Westin et al., 2002). To circumvent this dependency, Lasič et al. (2014) suggested a method to measure the microscopic anisotropy in terms of the microscopic fractional anisotropy (μFA). Conceptually, in a system of identical and parallel domains the diffusion

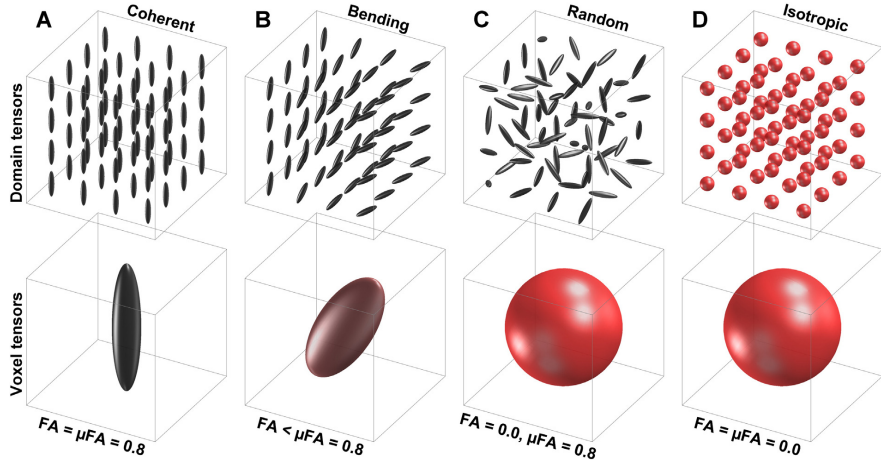

Fig. 1. Schematic examples showing the effects of tensor averaging. The top row shows individual domain tensors ($\mathbf{D}_k$) in the voxel volume, and the bottom row shows the corresponding voxel tensors ($\mathbf{D}$) in tissue containing coherent, bending, random and isotropic domains. In this example, the domains in panels A, B and C have $FA_k = 0.8$, while $FA_k = 0.0$ in panel D. Effects of averaging across multiple orientations are seen in the shape of the voxel scale tensors. Note that FA cannot distinguish between randomly oriented anisotropic domains (C) and isotropic domains (D) since it is zero in both cases.

anisotropy of each domain will persists to the voxel scale, rendering $FA = \mu FA = FA_k$ (Fig. 1A). By contrast, randomly oriented domains exhibit isotropic voxel scale diffusion, rendering $FA = 0$, however, the microscopic anisotropy is unaffected by the orientation dispersion and thus $\mu FA = FA_k$ (Fig. 1C).

It should be clear that individual domains cannot be probed directly using conventional DTI. Instead, the microscopic anisotropy can be inferred from the amount by which the diffusion weighted signal deviates from monoexponential attenuation, commonly referred to as the diffusional kurtosis (Jensen et al., 2005). However, kurtosis is not specific to microscopic anisotropy since it is also sensitive to the presence of multiple diffusion coefficients. Further, Mitra (1995) showed that these two effects cannot be distinguished in a conventional sPFG experiment, but that it could be done using dPFG experiments. Here, we separate the two effects by using the contrast between conventional and isotropic diffusion encoding (Lasič et al., 2014). The concept is understood by considering the MR signal (S) as a function of the magnitude of diffusion encoding (b), and the distribution of diffusion coefficients (P), according to Eq. (5)

$$S_{\mathbf{N}}(b) = S_0 \int_0^\infty P(D|\mathbf{N}) \cdot e^{-bD} dD, \tag{5}$$

where $P(D|\mathbf{N})$ reads as the probability distribution of diffusion coefficients when employing the *encoding tensor* $\mathbf{N}$, and $D = \mathbf{N} : \mathbf{D}$, where ':' denotes the double inner product. The encoding tensor is introduced to facilitate the analysis of both conventional and isotropic encoding (Westin et al., 2014). Conventional diffusion encoding is *anisotropic*, i.e., the diffusion sensitizing gradient is employed in one specific direction $\mathbf{n}$, where $\mathbf{n} = [n_x\ n_y\ n_z]^T$ and $|\mathbf{n}| = 1$. The corresponding encoding tensor is defined as $\mathbf{N} = \mathbf{n}\mathbf{n}^T$ (3×3 matrix with a single non-zero eigenvalue), and the b-matrix is given by $\mathbf{B} = b \cdot \mathbf{N}$ (Basser et al., 1994).

For low to moderately high b-values, the signal described in Eq. (5) mainly depends on the expected value and the variance of the distribution of diffusion coefficients. The expected value, or first moment, of P is reflected in the initial slope of the signal attenuation, and is equal to the apparent diffusion coefficient in the direction defined by $\mathbf{N}$, according to $ADC = \mathrm{E}[P(D|\mathbf{N})]$. The variance, or second central moment, of P is reflected in the departure of the signal attenuation from monoexponentiality, and is related to the apparent diffusional kurtosis (K) mapped in DKI, such that $\mathrm{Var}(P(D|\mathbf{N})) = K \cdot ADC^2/3$ (Jensen et al., 2005).

The dependence of the distribution of diffusion coefficients on $\mathbf{N}$ is essential to understanding the calculation of the microscopic anisotropy. We highlight this dependence by considering an *ideal system* that contains an ensemble of anisotropic domains that are randomly oriented and axially symmetric, i.e., the system is rotationally invariant and all domain tensors are defined by two eigenvalues. This system is anisotropic on the microscopic scale, but isotropic on the voxel scale, hence $FA = 0$. However, the microscopic anisotropy can be recovered from the variance of the distribution of diffusion coefficients reflected in the departure from monoexponential signal attenuation. In the ideal system, the average variance of the domain tensor eigenvalues ($\langle V_{\lambda,k} \rangle$) is related to the variance of the distribution of diffusion coefficients (V_a) according to Eq. (6)(Lasič et al., 2014)

$$\left\langle V_{\lambda,k} \right\rangle = \frac{5}{2} V_a, \tag{6}$$

where $V_a = \mathrm{Var}(P(D|\mathbf{N}))$. The subscript 'a' indicates that the variance is induced only by the presence of anisotropy. The microscopic fractional anisotropy is defined by substituting V_λ in Eq. (4) with the right hand side of Eq. (6), according to Eq. (7)(Lasič et al., 2014; Topgaard and Lasič, 2013)

$$\mu FA = \mathcal{h}\left(MD, \frac{5}{2} V_a\right) = \sqrt{\frac{3}{2}} \left(1 + \frac{MD^2}{\frac{5}{2} V_a}\right)^{-\frac{1}{2}}. \tag{7}$$

The definition in Eq. (7) was originally suggested by Topgaard and Lasič (2013), but an analogous parameter, the fractional eccentricity (FE), was independently developed by Jespersen et al. (2013). Note that the μFA and FE differ only by a constant factor such that $\mu FA = \sqrt{3/2} \cdot FE$ (Jespersen et al., 2014a,b; Lasič et al., 2014).

Applying Eq. (7) to an ideal system is able to perfectly describe the μFA as an analog to FA that is not sensitive to the effects of orientation dispersion (Fig. 1). However, assumptions made in the ideal system may not be valid in biological tissue. In such cases, the μFA can still be quantified by relaxing the demands of the ideal system and compensating for the introduced error. Here we consider departure from rotation invariance, and the presence of multiple sources of variance.

Rotation invariance can be achieved by constructing the powder average of the signal and is required in systems that exhibit residual anisotropy (FA > 0). The powder average is the arithmetic average of the signal across multiple rotations of the diffusion encoding gradients, and will render a signal that is insensitive to rotations of the object. Here we denote the powder averaged signal and distribution function as $\overline{S}$ and $\overline{P}$, respectively. Note that the expected value of the powder averaged distribution yields the mean diffusivity, i.e., $\langle \overline{P}(D|\mathbf{N}) \rangle = \mathrm{MD}$.

Variance in the distribution of diffusion coefficients can be a consequence of both anisotropy and presence of multiple isotropic components. This is relevant for the evaluation of Eq. (7) where only the variance arising due to the presence of microscopic anisotropy is considered. Thus, in cases where all domains cannot be assumed to have equal isotropic diffusivity, i.e., the domains have different $\mathrm{MD_k}$, the contribution to total variance (V_t) from isotropic components (V_i) must be quantified and removed, according to Eq. (8)

$$V_a = V_t - V_i. \tag{8}$$

To calculate V_a according to Eq. (8) we must find an independent means of measuring V_t and V_i. We know from DKI that V_t can be quantified by performing a conventional diffusion experiment, according to $V_t = \mathrm{Var}(\overline{P}(D|\mathbf{N}))$. Since $\overline{P}$ is affected not only by the underlying microenvironment, but also by the *shape* of the encoding tensor, V_i can be quantified by employing isotropic diffusion encoding that is designed to exert equal encoding strength in all spatial directions in a single preparation of the signal. We define the isotropic encoding tensor ($\mathbf{I}$, 3×3 matrix) as one-third of the identity matrix so that all its eigenvalues are equal, and $\mathrm{Tr}(\mathbf{I}) = 1$. This mode of encoding is insensitive to the domain orientations, and if the diffusion is approximately Gaussian, it is rotationally invariant and independent of microscopic anisotropy. Note that when isotropic encoding is used, $\overline{P}$ and P are interchangeable since $\mathbf{I}$ has no defined direction. For isotropic encoding the signal in Eq. (5) is a function of $P(D|\mathbf{I})$ which denotes the distribution of domain mean diffusivities since $\mathbf{I}{:}\mathbf{D_k} = \mathrm{MD_k}$. The remaining variance is due to heterogeneous domain mean diffusivities, and is defined as $V_i = \mathrm{Var}(P(D|\mathbf{I}))$. In summary, anisotropic and isotropic diffusion encoding at sufficiently high b-values can be used to quantify V_t and V_i, respectively. The μFA can then be calculated according to Eqs. (7) and (8).

Finally, we note that the interpretation of V_a in Eq. (8) is valid if the two probability distribution functions are related in terms of a convolution, according to $\overline{P}(D|\mathbf{N}) = R(D) \otimes \overline{P}(D|\mathbf{I})$ (see Fig. 2), where $R(D)$ is the anisotropy response function and $V_a = \mathrm{Var}(R(D))$, according to probability theory and the arithmetic of random variables. Thus, the analysis assumes that the variance of the anisotropy response function is equal for all domains. This assumption may be invalid, for example, in mixtures of WM and CSF where the anisotropy response functions are expected to be markedly different. The effects of such unfavorable conditions on the validity of μFA calculations are investigated in the Simulation experiments.

Methods

Imaging protocols

Data was acquired using a Philips Achieva 3T system, equipped with 80 mT/m gradients with a maximum slew rate of 100 mT/m/ms on axis, and an eight channel head coil.

The in vivo experiment was designed to evaluate the validity of the μFA model and was therefore acquired using a high b-value sampling rate, employing ten equidistant b-values between 100 and 2800 s/mm^2. Thereby, the sequence was limited to five image slices. Each set of data (one set per subject) contained images prepared with both the isotropic qMAS and harmonically modulated anisotropic encoding (Fig. 3). Harmonic modulation is preferred to trapezoidal encoding to ensure equal diffusion times for both types of encoding (Eriksson et al., 2013). All DW data were acquired using an echo time of 160 ms, repetition time of 2000 ms, 96×96 acquisition matrix, spatial resolution of $3 \times 3 \times 3$ mm^3, partial Fourier factor of 0.8, and a SENSE factor of 2. Regardless of encoding technique, each encoding block, before and after the 180°-pulse, lasted 62.5 ms. Anisotropic encoding was performed in 15 directions for each b-value using harmonically modulated gradients according to Lasič et al. (2014). The directions were distributed using an electrostatic repulsion scheme (Jones et al., 1999). The isotropic encoding was repeated 15 times per b-value. This resulted in equal amounts of images and scan time for both techniques. The combined scan time for the isotropic and anisotropic encoding sequences was 10:12 min.

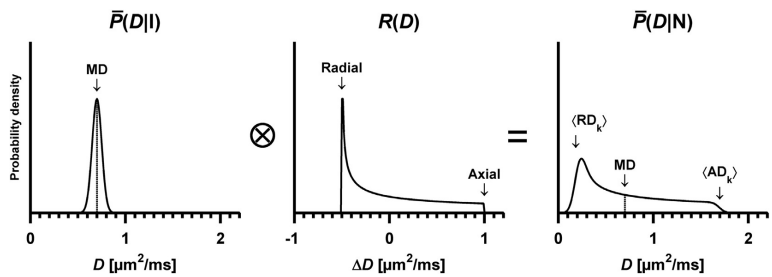

Fig. 2. Schematic example of the distribution of diffusion coefficients when employing encoding that is isotropic (left, $\overline{P}(D|\mathbf{I})$) and anisotropic (right, $\overline{P}(D|\mathbf{N})$). The convolution visualizes how the variance of $\overline{P}(D|\mathbf{I})$ is added to the variance of the anisotropy response function $R(D)$, rendering the total variance in $\overline{P}(D|\mathbf{N})$. This example depicts a system that contains axially symmetric and randomly oriented domains where $\mathrm{MD_k} = 0.70 \pm 0.05$ μm^2/ms, and the axial and radial domain diffusion is $\mathrm{AD_k} = \mathrm{MD_k} + 1.0$ μm^2/ms and $\mathrm{RD_k} = \mathrm{MD_k} - 0.5$ μm^2/ms, respectively (middle panel). Thus, the variance of the anisotropy response function is equal for all domains. The fact that the system contains anisotropic domains is reflected in the width of $R(D)$, indicating that there is a difference between the eigenvalues of the domain tensors. The prolate symmetry of the domain tensors can be discerned from the shape of $R(D)$, where the slow diffusion ($\mathrm{RD_k}$) is the most probable while the fast diffusion ($\mathrm{AD_k}$) is the least probable (Eriksson et al., 2013). Note that the area under each distribution equals unity, and that the y-axes have been adjusted to improve legibility.

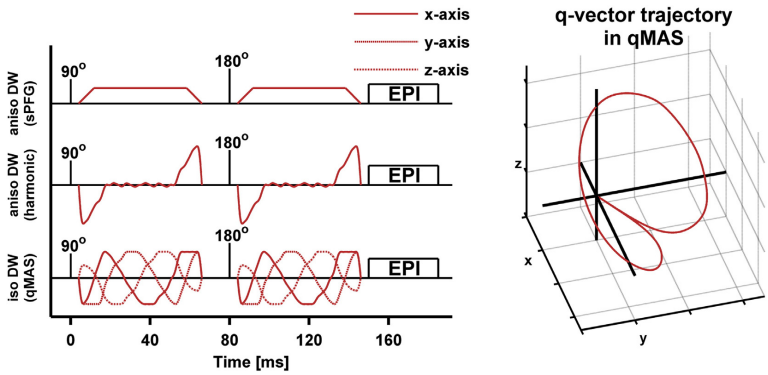

Fig. 3. Schematic comparison of sequences (left) and qMAS q-vector trajectory (right). The sequences show a spin-echo experiment where different types of diffusion encoding blocks (red lines) have been inserted on both sides of the 180°-pulse. The first two rows show examples of anisotropic diffusion encoding that use trapezoidal and harmonic gradient modulation, respectively. The bottom row shows the harmonic gradient modulation in isotropic qMAS. The q-vector trajectory in the qMAS experiment (right) follows the surface of a cone with an aperture of twice the magic angle resulting in the same encoding strength in all directions for each encoding block. Note that the speed of the qMAS q-vector along the trajectory varies as a function of its magnitude (low magnitude entails low speed), and that the magnitude of the qMAS encoding is zero during the 180°-pulse.

Additionally, two whole-brain morphological sequences were acquired. One T1-weighted (T1W) 3D turbo-field-echo, reconstructed at a spatial resolution of $1 \times 1 \times 1$ mm^3; and one T2-weighted (T2W) FLAIR, reconstructed at a spatial resolution of $0.5 \times 0.5 \times 6$ mm^3. The scan time for the T1W and T2W images was 6:28 and 4:48 min, respectively.

Post-processing and parameterization

Motion correction and eddy-current correction was applied to DWI data using *ElastiX* (Klein et al., 2010). The first moment, and the second central moment of the distribution of diffusion coefficients was estimated by regressing the inverse Laplace transform of the gamma distribution function onto the acquired signal (Lasič et al., 2014; Roding et al., 2012). The signal was modeled, according to Eq. (9)

$$\bar{S}(b) = S_0\left(1 + \frac{b \cdot V}{\mathrm{MD}}\right)^{-\frac{\mathrm{MD}^2}{V}}, \tag{9}$$

where MD and V were the fitting variables representing the initial slope and curvature of the signal attenuation function, respectively. Note that V in Eq. (9) corresponds to V_t and V_i when the model is regressed onto data from the powder averaged anisotropic and isotropic diffusion encoding experiments, respectively. Three constraints were introduced in the fitting procedure to eliminate non-physical results. First, the MD was constrained to be equal in the two acquisitions by assuming that $\langle \overline{P}(D|\mathbf{N})\rangle = \langle \overline{P}(D|\mathbf{I})\rangle = \mathrm{MD}$. This assumption is reasonable since the choice of encoding technique should not affect the mean diffusivity unless the diffusion time and the time required for the diffusing medium to probe the relevant restrictions are at the same scale, which is rarely the case for DWI in vivo (Nilsson et al., 2009, 2013). Second, V_i was constrained to the range between the total variance and zero ($V_t \geq V_i \geq 0$). Finally, signal that was attenuated below 5% ($\bar{S}(b) < 0.05 \cdot S_0$) was excluded from the fitting procedure. This was done to avoid detection of false variance in regions where a strong diffusion weighting rendered a signal that was elevated due to the noise floor. This is expected to affect only voxels where MD > 1.1 μm^2/ms.

FA was calculated through conventional DTI analysis from the data employing anisotropic encoding for encoding strengths $b \leq 1000$ s/mm^2. The μFA was calculated according to Eq. (8). Finally, the orientation coherence of the domains was quantified by the order parameter which is a well-established parameter for describing the order in liquid crystals. It is defined as $\mathrm{OP} = \langle (3\cos^2(\theta_k) - 1)/2 \rangle$, where θ_k is the angle between the domain and voxel scale symmetry axes. Thus, the OP provides a measure of orientation dispersion that has a simple geometric interpretation where $\mathrm{OP} = 1$ indicates perfectly coherent alignment and $\mathrm{OP} = 0$ indicates randomly oriented domain orientations. The OP can also be calculated from the microscopic and voxel scale variance, according to Eq. (10)(Lasič et al., 2014)

$$\mathrm{OP} = \sqrt{\frac{V_\Lambda}{\langle V_{\lambda,k} \rangle}}. \tag{10}$$

Note that OP is not equivalent to the orientation dispersion index used in NODDI (Zhang et al., 2012), and that it can be calculated for any given orientation distribution function.

In vivo experiments

Imaging was performed on eight healthy volunteers (age 32 ± 4 years, all male) and two patients with brain tumors (one female, 62 years, with meningioma, WHO grade I; and one male, 46 years, with glioblastoma, WHO grade IV). Written consent was obtained from all subjects and the study was approved by the Regional Ethical Review Board at Lund University.

Analysis of diffusion parameters was performed at the group level, as well as in a single representative subject. Three regions of interest (ROI) were selected in the WM; the splenium of the corpus callosum (CC), the corticospinal tract (CST), and the anterior crossing region (CR) where frontal projection fibers from the genu of the corpus callosum and thalamic radiation of the internal capsule intersect (see Assaf and Pasternak,2008). One ROI was also placed in the superior part of the thalamus (THA), which contains a mixture of WM and GM. The ROIs were delineated manually, using MD, FA and μFA maps for guidance; the operator was instructed to avoid voxels that contained GM or CSF.

The healthy individual was investigated with respect to the signal parameterization and parameter distribution in all four ROIs. One additional ROI was placed in the lateral ventricles to investigate the signal attenuation in the isotropic and rapidly diffusing CSF. The analysis of

the parameter distribution was based on the ROIs while the signal and model fit was inspected in a single voxel in each ROI. Further, the voxel-wise correlation between combinations of FA, μFA and OP were evaluated. This analysis was performed in one axial slice of the image volume and the parameter maps were masked to remove interference from irrelevant regions of the head. The strength of the association was quantified by the coefficient of determination (r^2, Pearson's linear correlation coefficient squared).

The healthy volunteer group was investigated with respect to the parameter distribution in the CC, CST, CR and THA. In order to elucidate if the three WM regions were different with respect to parameter mean values, F-tests (one-way ANOVA, assuming independent samples) were performed on the distributions of MD, FA, μFA, OP, V_i and V_a in the CC, CST and CR. The threshold for significance was set at $\alpha = 0.05/6$ (Bonferroni correction for six tests).

The tumors were compared with respect to their FA and μFA by placing ROIs in one axial slice through each tumor. The ROIs were defined manually and the inclusion of WM, GM and CSF was avoided. Both tumors were resected one day after the MRI procedure and histological evaluation of the tumors was performed, in accordance with local clinical routine. Each tumor specimen was fixed in 4% buffered formaldehyde solution, embedded in paraffin, and sectioned at 4 μm. The sections were stained with hematoxylin–eosin in order to visualize the tissue structure and cell morphology. Microscopy was performed on an Olympus BX50. The cell shape and presence of tissue fascicles was investigated qualitatively and compared to corresponding diffusion parameters. Finally, structure tensor analysis (Peyré, 2011) was performed on the microphotos to enhance the visibility of cell structure orientations.

Simulation experiments

Simulation experiments were performed to investigate the qualitative behavior of FA and μFA in scenarios where the underlying system contained complex diffusion profiles. These scenarios were designed to mimic a range of effects that may be found in experimental data. The results were evaluated in terms of the value, effect size, effect direction, and accuracy of the FA and μFA.

The simulations included three types of model components (C) with varying water fractions (f). The first component was designed to represent the anisotropic diffusion in WM (C_a). For simplicity, all anisotropic domains were assumed to be axially symmetric and were described by their radial (RD_k) and axial diffusivity (AD_k). These were set to $AD_k = 1.7$ and $RD_k = 0.2$ μm^2/ms. The orientation dispersion was modeled with the Watson distribution (Sra and Karp, 2013; Zhang et al., 2011) where the concentration parameter (κ) is related to the order parameter according to Eq. (11)

$$\mathrm{OP} = \frac{1}{2} \cdot \frac{\mathcal{M}(3/2, 5/2, \kappa)}{\mathcal{M}(1/2, 3/2, \kappa) - 1}, \tag{11}$$

where $\mathcal{M}$ is the confluent hypergeometric function. The order parameter could be varied to produce geometries between fully coherent (OP = 1) and fully dispersed (OP = 0) orientations. The two remaining environments were designed to represent diffusion in damaged neural tissue (C_i) and CSF (C_{CSF}). The diffusion in these environments was assumed to be isotropic, with a domain mean diffusivity of $MD_k = 1.7$ and 3.0 μm^2/ms in C_i and C_{CSF}, respectively.

Damaged WM was simulated by gradually replacing C_a with C_i. This was done in four geometries; the first three included one, two and three coherent (OP = 1) and orthogonal C_a components, and the last contained one C_a component with randomly oriented domains (OP = 0). The isotropic component replaced one anisotropic component while the remaining anisotropic components were unaltered. For example, in the case of two crossing fibers (C_{a1} and C_{a2}), the damaged anisotropic component C_{a1}, had a volume fraction f_{a1}. Initially, f_{a1} made up half the volume, but was gradually reduced to zero, and the fraction lost in C_{a1} was replaced by C_i, i.e., $f_{a1} = 1/2 \rightarrow 0$, and $f_i = 1/2 - f_{a1}$. During this process the fraction of C_{a2} was constant ($f_{a2} = 1/2$).

The response to increasing radial diffusivity, mimicking demyelination, was simulated in a coherent C_a component (OP = 1), where the radial diffusivity was increased from its starting value until it exhibited no anisotropy ($RD_k = 0.2 \rightarrow 1.7$ μm^2/ms). Effects of orientation dispersion were investigated using a single C_a component with variable amount of dispersion, from dispersed to coherent (OP = 0 → 1). The effect of the crossing angle between two coherent C_a components was simulated by varying the angle from a parallel to a perpendicular geometry ($\varphi = 0 \rightarrow 90°$). Finally, the effects of CSF contamination were simulated by gradually replacing a coherent C_a component (OP = 1) with C_{CSF} ($f_a = 1 \rightarrow 0$, and $f_{CSF} = 1 - f_a$). In all cases, the effects of noise were simulated for five equidistant points along each process by adding Rice-distributed noise to the signal (Sijbers and den Dekker, 2004). The signal was generated in accordance with the imaging protocol, i.e., using the same b-values, number of directions and parameterization, at a S_0 signal-to-noise ratio (SNR) of 20. The model was regressed onto 1000 realizations of the noisy signal to render a reliable median and interquartile range of the parameters.

Results

In vivo experiments

Maps of FA, μFA and OP for one healthy volunteer are shown in Fig. 4. As expected, the μFA is high in regions comprised of WM and lower in GM. Most notably, the FA and μFA maps differ in regions where a high orientation dispersion is expected, for example, in crossing WM and

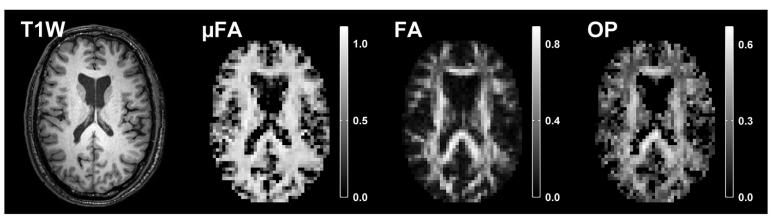

Fig. 4. T1W, μFA, FA and OP maps from one healthy volunteer. The μFA is similar to the FA map in that it highlights the WM of the brain, but does so regardless of the local orientation dispersion. The μFA exhibits high values in areas where FA values are low due to crossing, bending and fanning fibers. Thus, the μFA map exhibits strong resemblance to the WM morphology in the T1W image, although the latter is not quantitative. The GM is visible in the μFA-map at a slightly lower intensity, indicating that the microscopic anisotropy is lower in GM as compared to WM. The OP displays similar contrast to the FA, in regions of WM.

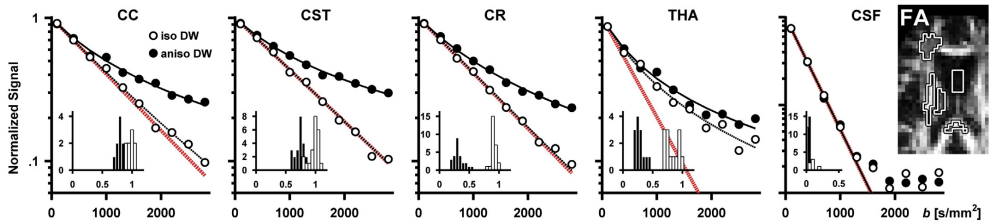

Fig. 5. Signal vs. *b* curves and parameter distributions in the corpus callosum (CC), corticospinal tract (CST), anterior crossing region (CR), thalamus (THA) and the cerebrospinal fluid in the lateral ventricles (CSF) in one healthy volunteer. The ROIs are shown in the FA map (right, black–white outline). The signal plots show the powder averaged signal from a single voxel in each region as measured with isotropic and anisotropic diffusion encoding (white and black circles), as well as the model fit (dashed and solid lines). The red lines are a visual reference showing monoexponential attenuation at the estimated mean diffusivity. The signal attenuation in all three WM regions is similar, where the isotropic encoding shows little deviation from monoexponential attenuation, while the anisotropic encoding exhibits a curvature in the signal attenuation, indicating that all regions contain microscopic anisotropy. In the THA, both the isotropic and anisotropic encoding shows a strong deviation from monoexponential attenuation, although the presence of microscopic anisotropy is made clear by the separation of the two curves. Note that the signal from the CSF was fitted only for signal values above 5% of the signal at $b = 0$ s/mm^2, and that the y-axis in the CSF plot has a larger range than the other plots. The inserted histograms show the parameter distribution in each ROI where black and white bars represent FA and μFA, respectively. The histograms show that the μFA is similar in the three WM ROIs and that the largest difference between FA and μFA can be found in the CR and THA.

the interface between WM pathways, in accordance with Lawrenz and Finsterbusch (2014). Another prominent difference can be seen in the GM where FA is close to zero, whereas μFA indicates that the GM contains detectable microscopic anisotropy. Fig. 5 shows the parameter distribution in the CC, CST, CR, THA and CSF, and the powder averaged signal originating from a single voxel in each region. As expected for WM tissue, the departure from monoexponential attenuation was smaller for the isotropic encoding than the anisotropic encoding. The THA exhibited a relatively high isotropic variance, but the presence of microscopic anisotropy is clearly visible from the separation of the two signal curves. In the CSF, the signal was attenuated below 5% of its initial value, and it is apparent that the fitting would detect a false variance if high *b*-value data was not excluded. The resulting parameterization of the signal seen in Fig. 5 was: μFA = 0.98, 1.03, 0.96, 0.76, and 0.00; MD = 0.91, 0.84, 0.89, 1.60, and 2.95 μm^2/m; V_i = 0.07, 0.00, 0.01, 1.66, and 0.01 μm^4/ms^2; and V_a = 0.57, 0.66, 0.51, 0.65, and 0.00 μm^4/ms^2 in the CC, CST, CR, THA and CSF, respectively.

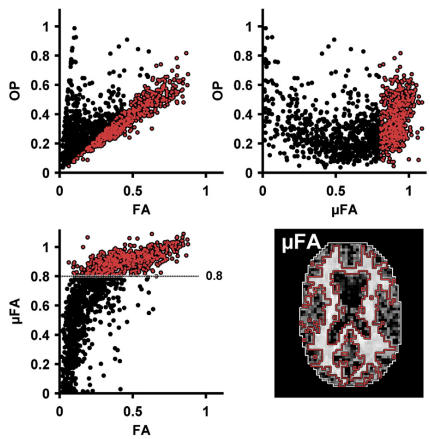

Fig. 6. Voxel-wise parameter dependency between FA, μFA and OP in one healthy volunteer. The strongest correlation was found for the OP and FA (top left, see text for details). Separating the distribution at a threshold of μFA = 0.8 (red and black dots show μFA above and below 0.8, respectively) revealed a clear spatial dependency where high values of μFA are associated with the WM of the brain (voxels within red outline). The correlation between OP and FA in the WM indicates that FA is strongly dependent on the OP, i.e., the FA is strongly dependent on the coherence of WM fibers.

The voxel-wise correlation between μFA, OP and FA is presented in Fig. 6. The relation between FA and μFA resembles the relation between the corresponding parameters reported by Jespersen et al. (2013) in that high FA entails high μFA, although not vice versa. The correlation between μFA and FA was found to exhibit two distinct modes, which were separated by introducing an arbitrary threshold at the shoulder of the distribution (μFA = 0.8). The interval containing high values of μFA was found to correspond well to regions of WM (μFA > 0.8, red outline in Fig. 6) and the low μFA was found in a mixture of peripheral WM, GM and CSF (μFA < 0.8, white outline in Fig. 6). In the WM region, a strong correlation was found between OP and FA ($r^2 = 0.9$), while only weak correlations were found between μFA and OP ($r^2 = 0.1$), and between μFA and FA ($r^2 = 0.4$). No relevant correlations were found in the peripheral region (all $r^2 < 0.3$).

The investigation of the parameter distribution in the group of healthy volunteers is summarized in Table 1. All parameter mean values, except the MD and V_i, were found to have significantly different mean values in the three WM ROIs. This was expected for the FA since the ROIs include both coherent and crossing WM tissue. The μFA was also found to differ significantly between the three regions, albeit at a much smaller effect size compared to the FA. The group level variability detected in MD and V_i indicated that the absence of significance is likely due to a small effect size and large variance, respectively.

The anisotropy parameters measured in the two tumor types are presented in Fig. 7, and corresponding microphotos of the excised tumors are presented in Fig. 8. The meningioma tissue exhibited a low voxel scale anisotropy (mean ± standard deviation, FA = 0.19 ± 0.06) and high microscopic anisotropy (μFA = 0.88 ± 0.08). Likewise, the glioblastoma tissue exhibited low voxel scale anisotropy (FA = 0.07 ± 0.05). However, it exhibited markedly lower microscopic

Table 1
Diffusion parameters (group mean ± standard deviation) in four ROIs in the group of healthy volunteers ($n = 8$). The ANOVA indicated significantly different mean values in the CC, CST and CR for all parameters except MD and V_i. Note that the number of voxels in each ROI (#Vox) is shown but was not included in any tests.

		THA	CC	CST	CR	
MD	[μm^2/ms]	1.09 ± 0.20	0.98 ± 0.11	0.96 ± 0.05	1.00 ± 0.06	
FA		0.31 ± 0.04	0.86 ± 0.03	0.64 ± 0.04	0.38 ± 0.04	†
μFA		0.82 ± 0.09	1.02 ± 0.02	0.97 ± 0.01	0.93 ± 0.01	†
OP		0.26 ± 0.02	0.64 ± 0.04	0.47 ± 0.03	0.27 ± 0.03	†
V_a	[μm^4/ms^2]	0.50 ± 0.12	0.96 ± 0.19	0.65 ± 0.07	0.57 ± 0.07	†
V_i	[μm^4/ms^2]	0.54 ± 0.40	0.30 ± 0.21	0.17 ± 0.05	0.22 ± 0.11	
#Vox		12 ± 3	5 ± 3	32 ± 5	24 ± 5	

† ANOVA shows significant difference between parameter mean values ($p \ll 0.05/6$) in the CC, CST and CR.

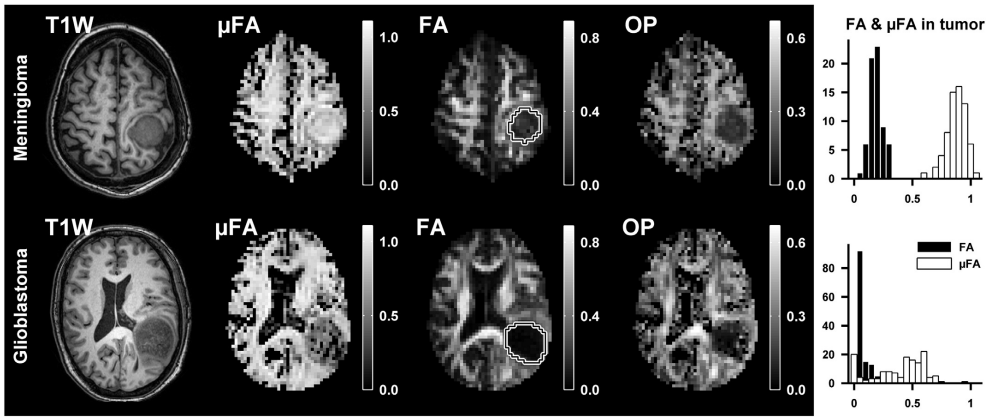

Fig. 7. Parameter maps from the meningioma (top row) and glioblastoma (bottom row). The ROIs used for quantitative evaluation of diffusion parameters are shown in the FA maps (white–black outline). Both tumors exhibited low FA, while the μFA was high in the meningioma and low in the glioblastoma (histogram).

anisotropy compared to the meningioma (μFA $= 0.39 \pm 0.22$). Although both tumors exhibited low FA values, the FA in the meningioma was elevated compared to the glioblastoma, indicating that the tissue is organized enough to create a weak but detectable diffusion anisotropy on the voxel scale. The high vs. low microscopic anisotropy in the meningioma and glioblastoma was corroborated by the histological examination of the two tumors, shown in Fig. 8. The histological examination of the meningioma demonstrated a dense fascicular pattern of growth with elongated tumor cells, consistent with low FA and high μFA; and a more loose assemblage of rounded cells of variable size along with patchy areas of necrosis in the glioma, consistent with both low FA and low μFA.

Simulation experiment

Figs. 9 and 10 showcase how the FA and μFA are altered when the underlying diffusion profiles are manipulated.

When a coherent anisotropic component was replaced by an isotropic component (Fig. 9A), the FA decreased approximately linearly as a function of the isotropic tissue fraction. In the same system, the μFA

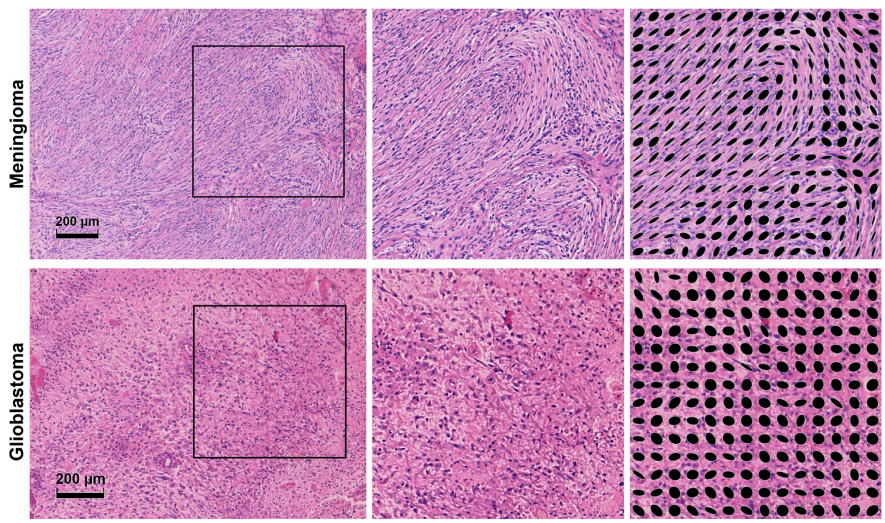

Fig. 8. Microphotos of excised meningioma (top row) and glioblastoma (bottom row) tissue. The meningioma exhibited a dense fascicular pattern of growth with elongated tumor cells in a mostly monomorph structure. As seen in the upper left image, the fascicles in the meningioma could stretch for distances comparable to the voxel size (~1 mm). The glioblastoma exhibited a loose assemblage of rounded cells of variable size, along with patchy areas of necrosis. Blood vessels had thickened walls with endothelial cell proliferation and multiple small bleedings were included. The images on the right show magnified areas of the tumor tissue as well as structure tensors (black ellipses) that illustrate the local orientation of the tissue. The structure tensors in the meningioma showcase the presence of locally ordered structures, while few such structures are appear in the glioblastoma.

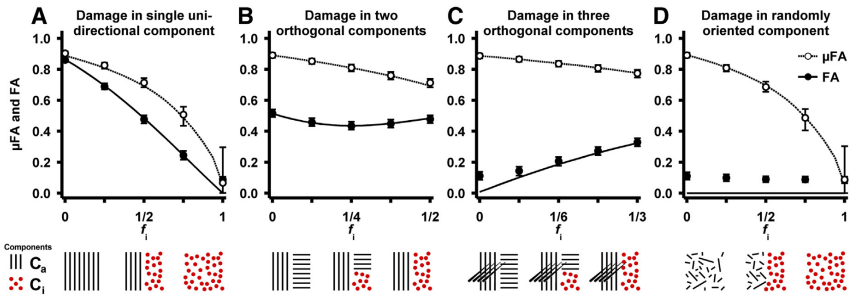

Fig. 9. Response in FA and μFA in four geometries where one anisotropic component is replaced by an isotropic component to mimic tissue damage. The solid and broken lines show the noise free FA and μFA, respectively. The circular markers show the median parameter value when the SNR is 20, using the imaging protocol and parameterization detailed in the Methods section. The error bars show the influence of noise as the interquartile range. The geometries and processes are illustrated with graphics below the plots showing the anisotropic (black lines) and isotropic components (circles). Generally, the FA and μFA differ in all processes. In the single damaged WM component (A), the FA and μFA should be equal, but a positive bias in the μFA is induced due to the increasing presence of the isotropic component. In the double crossing (B), the FA can both increase and decrease due to the selective removal of anisotropic domains, whereas the μFA is strictly decreasing as a function of the reduction of anisotropy. In the triple crossing (C), the FA and μFA exhibit opposing effects, where FA increases and μFA decreases. The randomly oriented domains (D) illustrate that FA has no sensitivity to any changes in this case, while the μFA still reflects the presence of microscopic anisotropy.

followed a similar pattern, but had a less pronounced initial slope indicating that the μFA is overestimated when the distribution of diffusion coefficients contains both isotropic and anisotropic components. In the absence of noise, both parameters approached zero for purely isotropic systems. In the crossing geometry, where one anisotropic component was replaced by an isotropic component (Fig. 9B), the FA first decreased due to the relatively rapid increase of the isotropic component. However, when a majority of the receding component had been removed ($f_i > 1/2$), the FA instead *increased* due to the dominance of the remaining anisotropic component. By contrast, μFA decreased strictly. This demonstrates a case where μFA may exhibit superior sensitivity and specificity over FA, since the direction of the effect is constant. Further, the effect size is larger for μFA since it is not confounded by the same counteracting mechanisms. Similar results are shown for a triple crossing geometry (Fig. 9C). In this case the FA started at a low value because the tissue was macroscopically isotropic with its three orthogonal fiber populations, and increased as one of the fiber populations was replaced by isotropic tissue. Again, the positive direction of the effect, caused by the reduction in orientation dispersion, may be confounding. By contrast, μFA reflected only the presence of microscopic anisotropy and responded as expected to the simulated damage. In the case of damage in randomly oriented microdomains (Fig. 9D), the macroscopic anisotropy is zero, rendering FA insensitive to any changes in tissue microstructure while the μFA reflects the amount of microscopic anisotropy that is lost.

The effect of gradually increasing domain radial diffusivity, resulted in similar effects for FA and μFA (Fig. 10A). However, as the system approaches isotropic conditions, the uncertainty in the μFA increases considerably. Fig. 10B shows how dispersion influences the FA, while the μFA is constant. A similar pattern is seen when simulating crossing fibers with varying crossing angles (Fig. 10C). As expected the FA was highest when the two fiber structures were parallel and had its lowest value when they were perpendicular. These results show the potential benefits of quantifying a measure for anisotropy that is not sensitive to confounds such as crossing, bending, fanning, and kissing fiber geometries. Finally, the effects of CSF contamination exhibit similar effects as the simulated damage in a single coherent WM system (compare Figs. 9A and 10D). This simulation highlights the overestimation of μFA due to multiple isotropic components. Generally, the μFA is increasingly susceptible to noise as the simulated systems approach zero microscopic anisotropy, resulting in reduced accuracy.

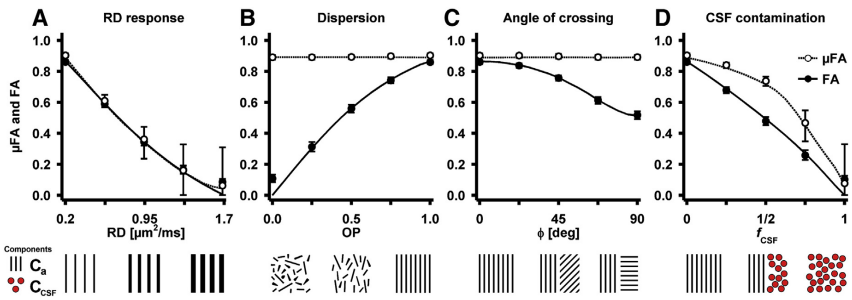

Fig. 10. Response in FA and μFA due to changes in microstructure geometry. The plot objects are described in the caption of Fig. 9. The response to increasing radial diffusivity (A) is equivalent for FA and μFA, however, the quantification of μFA displays a higher uncertainty. Both the effects of dispersion (B) and angle of crossing (C) have no effect on the μFA, while the FA is strongly modulated. The effect of CSF contamination (D) shows a positive bias in μFA compared to FA, similar to that found in Fig. 9A. Note that the values of FA and μFA in the simulation of CSF contamination are expected to be lower than the corresponding values in Fig. 9A. The similarity arises from the model fitting, where the bias is positive in both cases, but more so in the case of CSF since the model violation is larger. The varying degree of bias works to counteract the underlying difference between the two environments. Generally, in environments with low levels of microscopic anisotropy, μFA exhibits a higher level of statistical uncertainty as compared to FA. Note that the noise prevents both FA and μFA from assuming values close to zero.

Discussion

In this study we present the first implementation of qMAS for the purpose of probing the microscopic anisotropy in vivo on a clinical MRI system. The parameters μFA and OP, as well as conventional DTI parameters FA and MD, were quantified in healthy subjects and in two different types of tumor tissue. Unlike the voxel scale anisotropy, measured in terms of the FA, the microscopic anisotropy measured by μFA was relatively homogeneous in large portions of the WM. This finding is in agreement with other studies that have aimed to remove effects of orientation dispersion from the quantification of local anisotropy (Jensen et al., 2014; Jespersen et al., 2013; Lawrenz and Finsterbusch, 2013, 2014). The notion that FA is sensitive to local orientation dispersion is supported by the strong correlation found between the FA and OP (Fig. 6). However, the three WM regions chosen for analysis exhibited small but statistically significant differences also in μFA (Table 1), indicating that orientation dispersion is not the only difference between these regions. This could possibly be explained by varying levels of domain anisotropy, for example, caused by variable axonal packing density.

In the tumor tissue, FA was generally low, which indicated that the meningioma and the glioblastoma were approximately isotropic on the voxel scale. By contrast, the μFA was able to reliably differentiate between the two tumors, and indicated that microscopic diffusion anisotropy was more pronounced in the meningioma than the glioblastoma. Thus, the information provided by both FA and μFA was instrumental in predicting the tumor cell structures which were later confirmed by the histological exam (Fig. 8).

To elucidate some of the underlying mechanisms that affect FA and μFA, simulations of different micro-environments visualized the parameters as a function of several relevant processes. For example, in the case of increased radial diffusivity of parallel fibers, the responses in FA and μFA are approximately equal, meaning that the two representations of anisotropy share a common interpretation. On the other hand, scenarios that include any form of orientation dispersion demonstrate prominent differences between FA and μFA. For example, the combination of two and three orthogonal anisotropic components (Figs. 9B and C) were used to reproduce the effects of selective atrophy in a crossing WM geometry, as reported by Douaud et al. (2011), where the effect direction in FA was found to be positive in a damaged region of crossing WM. The simulations also illuminated the bias that arises when μFA is quantified in systems that violate the assumptions used in the parameterization, e.g., in complex mixtures of anisotropic and isotropic tissue. Although these scenarios invalidate the μFA as a direct metric of the microscopic anisotropy, it is worth noting that it retains sensitivity to the relevant effect and does so in a more consistent manner than the FA.

Although the comparison between FA and μFA showcases the effects of orientation dispersion as a confounder for FA, it does not invalidate previous studies that employ FA as a biomarker. Instead, the origin of the effect can be better understood, possibly allowing an improved interpretation of the FA and its relation to the microstructural integrity. We expect that μFA may not only contribute to the investigation of complex WM geometries, but also in detecting microscopic anisotropy in tissues that are approximately isotropic on the voxel scale, for example, in GM (McNab et al., 2013; Truong et al., 2014). Further, the μFA and OP may provide complementing information to the FA and tensor shape analysis previously used in the differentiation of classic and atypical meningioma (Toh et al., 2008), detection of fibroblastic meningioma (Tropine et al., 2007), and in the preoperative estimation of tumor consistency (Kashimura et al., 2007), by removing the confounding effects of orientation dispersion which are otherwise ignored.

It is important to stress that the signal acquired with conventional anisotropic encoding used in this study is identical to that needed for DKI analysis. However, because DKI makes no effort to distinguish between the origins of the diffusional kurtosis (herein referred to as variance in diffusion coefficients) it is not directly associated to microscopic anisotropy. The framework presented here is also related to the dPFG-methods employed by Jespersen et al. (2013) and Lawrenz and Finsterbusch (2014). In terms of the analysis presented here, dPFG encoding can be described with an encoding tensor which renders a signal that is sensitive to a weighted sum of V_i and V_a, where the weighting depends on the direction of the encoding blocks (Westin et al., 2014). It appears that the framework based on qMAS combined with anisotropic encoding probes the μFA more directly and may therefore provide a faster technique for measuring microscopic anisotropy compared to the dPFG methods. Finally, we note that the implementation and use of qMAS is no more complicated than a similar DKI protocol. Other techniques that take orientation dispersion into account include, for example, NODDI which quantifies the magnitude of fiber dispersion and the neurite density (Zhang et al., 2012). From this information it is possible to calculate a parameter analogous to the μFA. However, like DTI and DKI, the NODDI technique cannot distinguish between randomly oriented anisotropic domains and multiple isotropic components. Another drawback of model-based approaches, such as NODDI, is the demand for a priori assumptions about the tissue that is investigated, which may limit their use in abnormal tissues such as tumors.

In the present study, several factors affected the accuracy, i.e., the trueness and precision, of the estimated μFA. The imaging protocol features a long echo time which impacted the SNR and thus also the precision of μFA. Sufficient SNR for a robust signal parameterization was achieved by increasing the voxel size. Consequently, this increased the amount of PVE, especially in tissue interfacing with CSF, thereby reducing the trueness in such regions. Note that the present protocol was designed to test the validity of the suggested model by acquiring a densely sampled signal. However, the experimental design can be adjusted to allow whole brain coverage at feasible acquisition times by optimizing the acquisition protocol (Alexander, 2008). Further, a relatively low number of encoding directions were acquired, which may have reduced the trueness by introducing a weak directional dependency in the powder averaged signal, although simulations (data not shown) indicate a negligible μFA bias even for highly anisotropic tissue. A further limitation of μFA is that it may suffer from low accuracy when the model assumptions are violated or when investigating tissue with little or no microscopic anisotropy. The effects of such unfavorable conditions are demonstrated in the simulations (Figs. 9 and 10). The reduced accuracy in tissue with low anisotropy ($\mu FA < 0.4$) can be understood by considering Eq. (7) for V_a approaching zero; where the restriction on V_a to be positive may reduce trueness, and low levels of variance in V_a will render a poor precision in μFA. Thus, it is likely that the μFA calculated in the glioblastoma exhibited a positive bias since the histological exam of the glioblastoma found few anisotropic structures (Fig. 8). Although the accuracy of the estimated μFA in the glioblastoma may be poor, the tumors could be reliably differentiated based on the difference in their microscopic anisotropy. Finally, a limitation may be that the assumption of Gaussian diffusion is not valid, i.e., that the signal attenuation may be dependent on diffusion time. We do not expect this to be the case in white matter for the current diffusion time regime (Nilsson et al., 2009, 2013). However, tumor tissue may contain larger cell structures, which could make μFA dependent on experimental parameters. This is a topic that deserves further attention, especially since qMAS exhibits an anisotropic time dependency due to the varying speed of the q-vector through q-space (Fig. 3).

Conclusion

This study demonstrates the feasibility of mapping the microscopic anisotropy of the brain in vivo in terms of the μFA. The Results suggest that the contrast found in conventional FA maps is strongly modulated by the orientation dispersion of the anisotropic domains contained within each imaging voxel. By contrast, our analysis quantifies the microscopic anisotropy and orientation dispersion separately in terms of the μFA and OP. Unlike the conventional FA derived from DTI, μFA may

therefore provide a robust biomarker that probes the relevant diffusion anisotropy even in complex WM configurations. The potential benefit of μFA was demonstrated in two brain tumors. Although both tumors appeared isotropic on the voxel scale, the μFA could be used to distinguish between them based on their microscopic anisotropy. Additionally, simulations of complex tissue microstructures suggested that μFA exhibits a more intuitive interpretation than FA.

We predict that the combination of FA, μFA and OP can be useful in clinical and research applications, by enabling detection of microstructural degeneration in complex neural tissue, detection of fibrous tissue in tumors for pre-surgical classification of consistency, and quantification of microscopic anisotropy in macroscopically isotropic tissue.

Acknowledgments

This research was supported by the Swedish Research Council (grant nos. 2009-6794, 2010-3034, 2011-4334, 2012-3682 and K2011-52X-21737-01-3), the Swedish Cancer Society (grant no. CAN 2009/1076), Swedish Foundation for Strategic Research (grant no. AM13-0090), and the National Institutes of Health (grant nos. R01MH074794 and P41EB015902).

Conflict of interest statement

SL, DT and MN declare patent applications in Sweden (1250453-6 and 1250452-8), USA (61/642 594 and 61/642 589), and PCT (SE2013/050492 and SE2013/050493). The remaining authors declare no conflict of interest.

References

Alexander, D.C., 2008. A general framework for experiment design in diffusion MRI and its application in measuring direct tissue-microstructure features. Magn. Reson. Med. 60, 439–448.
Alexander, A.L., Hasan, K.M., Lazar, M., Tsuruda, J.S., Parker, D.L., 2001. Analysis of partial volume effects in diffusion-tensor MRI. Magn. Reson. Med. 45, 770–780.
Assaf, Y., Pasternak, O., 2008. Diffusion tensor imaging (DTI)-based white matter mapping in brain research: a review. J. Mol. Neurosci. 34, 51–61.
Basser, P.J., Pierpaoli, C., 1996. Microstructural and physiological features of tissues elucidated by quantitative-diffusion-tensor MRI. J. Magn. Reson. 209–2019.
Basser, P.J., Mattiello, J., Le Bihan, D., 1994. MR diffusion tensor spectroscopy and imaging. Biophys. J. 66, 259–267.
Butts, K., Pauly, J., de Crespigny, A., Moseley, M., 1997. Isotropic diffusion-weighted and spiral-navigated interleaved EPI for routine imaging of acute stroke. Magn. Reson. Med. 38, 741–749.
De Santis, S., Drakesmith, M., Bells, S., Assaf, Y., Jones, D.K., 2013. Why diffusion tensor MRI does well only some of the time: variance and covariance of white matter tissue microstructure attributes in the living human brain. Neuroimage 89C, 35–44.
Douaud, G., Jbabdi, S., Behrens, T.E., Menke, R.A., Gass, A., Monsch, A.U., Rao, A., Whitcher, B., Kindlmann, G., Matthews, P.M., Smith, S., 2011. DTI measures in crossing-fibre areas: increased diffusion anisotropy reveals early white matter alteration in MCI and mild Alzheimer's disease. Neuroimage 55, 880–890.
Englund, E., Sjobeck, M., Brockstedt, S., Latt, J., Larsson, E.M., 2004. Diffusion tensor MRI post mortem demonstrated cerebral white matter pathology. J. Neurol. 251, 350–352.
Eriksson, S., Lasič, S., Topgaard, D., 2013. Isotropic diffusion weighting in PGSE NMR by magic-angle spinning of the q-vector. J. Magn. Reson. 226, 13–18.
Hsu, J.L., Van Hecke, W., Bai, C.H., Lee, C.H., Tsai, Y.F., Chiu, H.C., Jaw, F.S., Hsu, C.Y., Leu, J.G., Chen, W.H., Leemans, A., 2010. Microstructural white matter changes in normal aging: a diffusion tensor imaging study with higher-order polynomial regression models. Neuroimage 49, 32–43.
Jensen, J.H., Helpern, J.A., Ramani, A., Lu, H., Kaczynski, K., 2005. Diffusional kurtosis imaging: the quantification of non-Gaussian water diffusion by means of magnetic resonance imaging. Magn. Reson. Med. 53, 1432–1440.
Jensen, J.H., Hui, E.S., Helpern, J.A., 2014. Double-pulsed diffusional kurtosis imaging. NMR Biomed. 27, 363–370.
Jespersen, S.N., Lundell, H., Sønderby, C.K., Dyrby, T.B., 2013. Orientationally invariant metrics of apparent compartment eccentricity from double pulsed field gradient diffusion experiments. NMR Biomed. 26, 1647–1662.
Jespersen, S.N., Lundell, H., Sønderby, C.K., Dyrby, T.B., 2014a. Commentary on "Microanisotropy imaging: quantification of microscopic diffusion anisotropy and orientation of order parameter by diffusion MRI with magic-angle spinning of the q-vector". Front. Phys. 2, 28.
Jespersen, S.N., Lundell, H., Sønderby, C.K., Dyrby, T.B., 2014b. Erratum: orientationally invariant metrics of apparent compartment eccentricity from double pulsed field gradient diffusion experiments. NMR Biomed. 27 (738-738).
Jones, D.K., Horsfield, M.A., Simmons, A., 1999. Optimal strategies for measuring diffusion in anisotropic systems by magnetic resonance imaging. Magn. Reson. Med. 42, 515–525.
Kashimura, H., Inoue, T., Ogasawara, K., Arai, H., Otawara, Y., Kanbara, Y., Ogawa, A., 2007. Prediction of meningioma consistency using fractional anisotropy value measured by magnetic resonance imaging. J. Neurosurg. 107, 784–787.
Klein, S., Staring, M., Murphy, K., Viergever, M.A., Pluim, J.P., 2010. Elastix: a toolbox for intensity-based medical image registration. IEEE Trans. Med. Imaging 29, 196–205.
Kubicki, M., Westin, C.F., Maier, S.E., Mamata, H., Frumin, M., Ersner-Hershfield, H., Kikinis, R., Jolesz, F.A., McCarley, R., Shenton, M.E., 2002. Diffusion tensor imaging and its application to neuropsychiatric disorders. Harv. Rev. Psychiatry 10, 324–336.
Lasič, S., Szczepankiewicz, F., Eriksson, S., Nilsson, M., Topgaard, D., 2014. Microanisotropy imaging: quantification of microscopic diffusion anisotropy and orientational order parameter by diffusion MRI with magic-angle spinning of the q-vector. Front. Phys. 2, 11.
Lawrenz, M., Finsterbusch, J., 2013. Double-wave-vector diffusion-weighted imaging reveals microscopic diffusion anisotropy in the living human brain. Magn. Reson. Med. 69, 1072–1082.
Lawrenz, M., Finsterbusch, J., 2014. Mapping measures of microscopic diffusion anisotropy in human brain white matter in vivo with double-wave-vector diffusion-weighted imaging. Magn. Reson. Med. http://dx.doi.org/10.1002/mrm.25140.
Lawrenz, M., Koch, M.A., Finsterbusch, J., 2010. A tensor model and measures of microscopic anisotropy for double-wave-vector diffusion-weighting experiments with long mixing times. J. Magn. Reson. 202, 43–56.
Lebel, C., Walker, L., Leemans, A., Phillips, L., Beaulieu, C., 2008. Microstructural maturation of the human brain from childhood to adulthood. Neuroimage 40, 1044–1055.
Löbel, U., Sedlacik, J., Gullmar, D., Kaiser, W.A., Reichenbach, J.R., Mentzel, H.J., 2009. Diffusion tensor imaging: the normal evolution of ADC, RA, FA, and eigenvalues studied in multiple anatomical regions of the brain. Neuroradiology 51, 253–263.
McNab, J.A., Polimeni, J.R., Wang, R., Augustinack, J.C., Fujimoto, K., Stevens, A., Triantafyllou, C., Janssens, T., Farivar, R., Folkerth, R.D., Vanduffel, W., Wald, L.L., 2013. Surface based analysis of diffusion orientation for identifying architectonic domains in the in vivo human cortex. Neuroimage 69, 87–100.
Mitra, P., 1995. Multiple wave-vector extensions of the NMR pulsed-field-gradient spin-echo diffusion measurement. Phys. Rev. B 51, 15074–15078.
Nilsson, M., Lätt, J., Nordh, E., Wirestam, R., Ståhlberg, F., Brockstedt, S., 2009. On the effects of a varied diffusion time in vivo: is the diffusion in white matter restricted? Magn. Reson. Imaging 27, 176–187.
Nilsson, M., Latt, J., Stahlberg, F., van Westen, D., Hagslatt, H., 2012. The importance of axonal undulation in diffusion MR measurements: a Monte Carlo simulation study. NMR Biomed. 25, 795–805.
Nilsson, M., van Westen, D., Stahlberg, F., Sundgren, P.C., Latt, J., 2013. The role of tissue microstructure and water exchange in biophysical modelling of diffusion in white matter. MAGMA 26, 345–370.
Oouchi, H., Yamada, K., Sakai, K., Kizu, O., Kubota, T., Ito, H., Nishimura, T., 2007. Diffusion anisotropy measurement of brain white matter is affected by voxel size: underestimation occurs in areas with crossing fibers. AJNR Am. J. Neuroradiol. 28, 1102–1106.
Peyré, G., 2011. The numerical tours of signal processing — advanced computational signal and image processing. IEEE Comput. Sci. Eng. 13, 94–97.
Roding, M., Bernin, D., Jonasson, J., Sarkka, A., Topgaard, D., Rudemo, M., Nyden, M., 2012. The gamma distribution model for pulsed-field gradient NMR studies of molecular-weight distributions of polymers. J. Magn. Reson. 222, 105–111.
Rovaris, M., Gass, A., Bammer, R., Hickman, S.J., Ciccarelli, O., Miller, D.H., Filippi, C.G., 2005. Diffusion MRI in multiple sclerosis. Neurology 65, 1526–1532.
Santillo, A.F., Martensson, J., Lindberg, O., Nilsson, M., Manzouri, A., Landqvist Waldo, M., van Westen, D., Wahlund, L.O., Latt, J., Nilsson, C., 2013. Diffusion tensor tractography versus volumetric imaging in the diagnosis of behavioral variant frontotemporal dementia. PLoS One 8, e66932.
Scholz, J., Klein, M.C., Behrens, T.E., Johansen-Berg, H., 2009. Training induces changes in white-matter architecture. Nat. Neurosci. 12, 1370–1371.
Shemesh, N., Cohen, Y., 2011. Microscopic and compartment shape anisotropies in gray and white matter revealed by angular bipolar double-PFG MR. Magn. Reson. Med. 65, 1216–1227.
Sijbers, J., den Dekker, A.J., 2004. Maximum likelihood estimation of signal amplitude and noise variance from MR data. Magn. Reson. Med. 51, 586–594.
Sjobeck, M., Elfgren, C., Larsson, E.M., Brockstedt, S., Latt, J., Englund, E., Passant, U., 2010. Alzheimer's disease (AD) and executive dysfunction. A case–control study on the significance of frontal white matter changes detected by diffusion tensor imaging (DTI). Arch. Gerontol. Geriatr. 50, 260–266.
Sra, S., Karp, D., 2013. The multivariate Watson distribution: maximum-likelihood estimation and other aspects. J. Multivar. Anal. 114, 256–269.
Stejskal, E.O., Tanner, J.E., 1965. Spin diffusion measurement: spin echoes in the presence of a time-dependent field gradient. J. Chem. Phys. 42, 288–292.
Sullivan, E.V., Pfefferbaum, A., 2006. Diffusion tensor imaging and aging. Neurosci. Biobehav. Rev. 30, 749–761.
Surova, Y., Szczepankiewicz, F., Latt, J., Nilsson, M., Eriksson, B., Leemans, A., Hansson, O., van Westen, D., Nilsson, C., 2013. Assessment of global and regional diffusion changes along white matter tracts in Parkinsonian disorders by MR tractography. PLoS One 8, e66022.

Szczepankiewicz, F., Latt, J., Wirestam, R., Leemans, A., Sundgren, P., van Westen, D., Stahlberg, F., Nilsson, M., 2013. Variability in diffusion kurtosis imaging: impact on study design, statistical power and interpretation. Neuroimage 76, 145–154.

Teipel, S.J., Grothe, M.J., Filippi, M., Fellgiebel, A., Dyrba, M., Frisoni, G.B., Meindl, T., Bokde, A.L., Hampel, H., Kloppel, S., Hauenstein, K., 2014. Fractional anisotropy changes in Alzheimer's disease depend on the underlying fiber tract architecture: a multiparametric DTI study using joint independent component analysis. J. Alzheimers Dis. 41, 69–83.

Toh, C.H., Castillo, M., Wong, A.M., Wei, K.C., Wong, H.F., Ng, S.H., Wan, Y.L., 2008. Differentiation between classic and atypical meningiomas with use of diffusion tensor imaging. AJNR Am. J. Neuroradiol. 29, 1630–1635.

Topgaard, D., 2013. Isotropic diffusion weighting in PGSE NMR: numerical optimization of the q-MAS PGSE sequence. Microporous Mesoporous Mater. 178, 60–63.

Topgaard, D., Lasič, S., 2013. Patent: Analys för kvantifiering av mikroskopisk diffusionsanisotropi (Analysis for the Quantification of Microscopic Diffusion Anisotropy). (Language: Swedish. IPC: A61B5/055, G01N24/00, G01R33/563. Filed: 2012-05-04, Issued: 2013-11-05).

Tropine, A., Dellani, P.D., Glaser, M., Bohl, J., Ploner, T., Vucurevic, G., Perneczky, A., Stoeter, P., 2007. Differentiation of fibroblastic meningiomas from other benign subtypes using diffusion tensor imaging. J. Magn. Reson. Imaging 25, 703–708.

Truong, T.K., Guidon, A., Song, A.W., 2014. Cortical depth dependence of the diffusion anisotropy in the human cortical gray matter in vivo. PLoS One 9, e91424.

Vos, S.B., Jones, D.K., Viergever, M.A., Leemans, A., 2011. Partial volume effect as a hidden covariate in DTI analyses. Neuroimage 55, 1566–1576.

Vos, S.B., Jones, D.K., Jeurissen, B., Viergever, M.A., Leemans, A., 2012. The influence of complex white matter architecture on the mean diffusivity in diffusion tensor MRI of the human brain. Neuroimage 59, 2208–2216.

Westin, C.F., Maier, S.E., Mamata, H., Nabavi, A., Jolesz, F.A., Kikinis, R., 2002. Processing and visualization for diffusion tensor MRI. Med. Image Anal. 6, 93–108.

Westin, C.F., Szczepankiewicz, F., Pasternak, O., Özarslan, E., Topgaard, D., Knutsson, H., Nilsson, M., 2014. Measurement tensors in diffusion MRI: generalizing the concept of diffusion encoding. Med. Image Comput. Comput. Assist. Interv. 17 (Pt 5), 217–225.

Wong, E.C., Cox, R.W., Song, A.W., 1995. Optimized isotropic diffusion weighting. Magn. Reson. Med. 34, 139–143.

Zhang, H., Hubbard, P.L., Parker, G.J., Alexander, D.C., 2011. Axon diameter mapping in the presence of orientation dispersion with diffusion MRI. Neuroimage 56, 1301–1315.

Zhang, H., Schneider, T., Wheeler-Kingshott, C.A., Alexander, D.C., 2012. NODDI: practical in vivo neurite orientation dispersion and density imaging of the human brain. Neuroimage 61, 1000–1016.

Paper IV

Journal of Magnetic Resonance 261 (2015) 157–168

Contents lists available at ScienceDirect

Journal of Magnetic Resonance

journal homepage: www.elsevier.com/locate/jmr

Constrained optimization of gradient waveforms for generalized diffusion encoding

Jens Sjölund [a,b,c,*], Filip Szczepankiewicz [d], Markus Nilsson [e], Daniel Topgaard [f], Carl-Fredrik Westin [g], Hans Knutsson [b,c]

[a] Elekta Instrument AB, Kungstensgatan 18, Box 7593, SE-103 93 Stockholm, Sweden
[b] Department of Biomedical Engineering, Linköping University, Linköping, Sweden
[c] Center for Medical Image Science and Visualization (CMIV), Linköping University, Sweden
[d] Department of Medical Radiation Physics, Lund University, Lund, Sweden
[e] Lund University Bioimaging Center, Lund University, Lund, Sweden
[f] Department of Chemistry, Lund University, Lund, Sweden
[g] Brigham and Women's Hospital, Harvard Medical School, Boston, MA, USA

ARTICLE INFO

Article history:
Received 24 March 2015
Revised 19 October 2015
Available online 31 October 2015

Keywords:
Diffusion MR
Generalized gradient waveforms
Q-space trajectory imaging
Optimization
Hardware constraints

ABSTRACT

Diffusion MRI is a useful probe of tissue microstructure. The conventional diffusion encoding sequence, the single pulsed field gradient, has recently been challenged as more general gradient waveforms have been introduced. Out of these, we focus on q-space trajectory imaging, which generalizes the scalar *b*-value to a tensor valued entity. To take full advantage of its capabilities, it is imperative to respect the constraints imposed by the hardware, while at the same time maximizing the diffusion encoding strength. We provide a tool that achieves this by solving a constrained optimization problem that accommodates constraints on maximum gradient amplitude, slew rate, coil heating and positioning of radio frequency pulses. The method's efficacy and flexibility is demonstrated both experimentally and by comparison with previous work on optimization of isotropic diffusion sequences.

1. Introduction

Diffusion MRI probes the structure of biological tissue structure on a microscopic scale using the random translational motion of water molecules [1–3]. In the brain, tissue components—such as cell membranes, nerve fibers and macromolecules—impede the diffusion, making its characteristics different from that of freely diffusing water. In particular, the organization of white matter tracts into fiber bundles with preferential directions makes the diffusion anisotropic [4]. In diffusion tensor imaging (DTI), the diffusion in a voxel is described by a tensor with six degrees of freedom [5,6]. Consequently, it requires the acquisition of at least six diffusion-weighted images. The trace of the diffusion tensor, which relates to the mean diffusivity (MD), is a useful biomarker e.g. when studying tumor cellularity [7] or diagnosing stroke [8]. In fact, the mean diffusivity can be determined by single-shot isotropic diffusion weighting [9], i.e. without doing full DTI. Although a good idea this has rarely been done in practice—until recently. The recent revival has been spurred by advancements on both the methodological and the technical sides. On the methodological side, isotropic diffusion weighting has been shown useful when studying microscopic diffusion anisotropy [10] and, in combination with directional diffusion weighting, it can be used to distinguish between microscopic anisotropy and orientational order [11,12]. On the technical side, the limited gradient amplitudes achievable in clinical scanners have made it challenging to obtain sufficient diffusion weighting when using isotropic encoding. Rapid progress is being made on the hardware side [13,14] but in the numerical optimization of gradient waveforms there is still room for improvement, although there has been some promising research in this direction [15,16]. A gradient waveform that yields isotropic diffusion encoding can—in theory—easily be remapped to achieve a general diffusion encoding [17], which can be tuned to maximize sensitivity to the microstructure parameters of interest [18,19].

In some of the earlier work [15,16] the numerical optimization was strongly model driven, with constraints implicitly incorporated into a parametrization of the pulse sequence which was then optimized with respect to the parameters. This makes the obtained optimization less transparent and less adaptable to a new setting. Remapping a waveform with isotropic diffusion encoding into a

* Corresponding author at: Elekta Instrument AB, Kungstensgatan 18, Box 7593, SE-103 93 Stockholm, Sweden.
E-mail address: jens.sjolund@liu.se (J. Sjölund).

http://dx.doi.org/10.1016/j.jmr.2015.10.012
1090-7807/

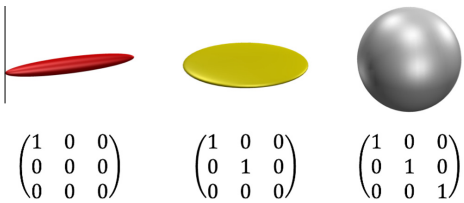

$$\begin{pmatrix}1&0&0\\0&0&0\\0&0&0\end{pmatrix} \quad \begin{pmatrix}1&0&0\\0&1&0\\0&0&0\end{pmatrix} \quad \begin{pmatrix}1&0&0\\0&1&0\\0&0&1\end{pmatrix}$$

Fig. 1. Measurement tensors: the top row is the graphical representation of the corresponding matrix representations in the bottom row. In the graphical representation, the magnitudes of the eigenvalues are mapped to red–green–blue. Note that in this case the *b*-value of the rightmost tensor is three times as high as that of the leftmost one. (For interpretation of the references to color in this figure legend, the reader is referred to the web version of this article.)

generalized diffusion measurement [17] does not take the inherent constraints into account. Subsequently adjusting the remapped gradient waveform to make it feasible comes at the cost of efficiency.

In this work, we propose a new optimization framework for these gradient waveforms that makes far less modeling assumptions than previous work while it is at the same time easily adaptable to hardware constraints on maximum gradient amplitude, slew rate, heating and positioning of RF pulses. Taking gradient heating into account is of particular interest for diffusion imaging where the power dissipation can otherwise hinder operation at a high duty cycle [13,14]. A further generalization of our approach is that it allows arbitrary positioning of time intervals with zero gradients (or slice-selective gradients), during which an RF pulse can be applied, and not requiring a mirror-symmetric gradient waveform.

2. Optimization

The most common pulse sequence in diffusion MRI is single diffusion encoding (SDE) by a pair of short gradient pulses separated by a diffusion time [20]. Each repetition of such a measurement probes the diffusion in one direction. In this work we consider more general scenarios with time-varying gradients that probe trajectories in so-called q-space [17]. The q-space trajectory is determined by gradient waveforms $\mathbf{g}(t) = (g_x(t), g_y(t), g_z(t))^T$ according to

$$\mathbf{q}(t) = \gamma \int_0^t \mathbf{g}(t')dt', \tag{1}$$

where γ is the gyromagnetic ratio. It is the q-space trajectories $\mathbf{q}(t)$ that constitute the degrees of freedom that we consider in the optimization.

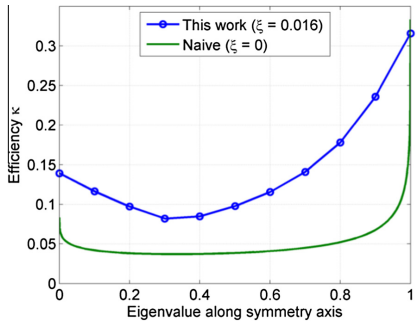

Fig. 3. Efficiency κ for sequences with diagonal, axially symmetric, measurement tensors as the eigenvalue along the symmetry axis is varied.

Restricted diffusion does not follow the Gaussian behavior that is characteristic of free diffusion [1]. Nevertheless, the model of diffusion—on the voxel scale—as a mixture of Gaussians has found widespread use [21–23] and captures relevant information about the tissue microstructure [2].

Under the Gaussian approximation, the geometry of the diffusion encoding is captured by the measurement tensor [1,17]

$$\mathbf{B} = \int_0^\tau \mathbf{q}(t)\mathbf{q}(t)^T dt, \tag{2}$$

where τ is the echo time. The measurement tensor extends the conventional *b*-value to a matrix-valued entity (the conventional *b*-value is given by the trace of **B**). The rank of the measurement tensor depends on the q-space trajectory: it is one in the case of SDE, two for double diffusion encoding (DDE) [24], and three in the isotropic encoding case. Fig. 1 shows the correspondence between the graphical- and the matrix representations of measurement tensors used in this work.

By definition, isotropic diffusion encoding corresponds to a measurement tensor

$$\mathbf{B}_{\text{iso}} = b\begin{pmatrix}1/3&0&0\\0&1/3&0\\0&0&1/3\end{pmatrix}. \tag{3}$$

There is a direct link between the diffusion tensor in a voxel,

$$\mathbf{D} = \begin{pmatrix}D_{xx}&D_{xy}&D_{xz}\\D_{yx}&D_{yy}&D_{yz}\\D_{zx}&D_{zy}&D_{zz}\end{pmatrix}, \tag{4}$$

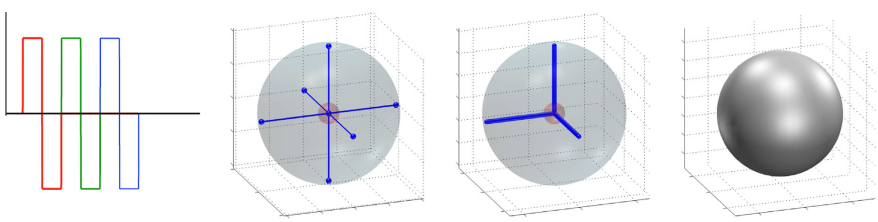

Fig. 2. An example of a naïve gradient waveform used for comparison throughout this work. From left to right: the *x*–*y*–*z* gradients in red–green–blue; gradient trajectory; q-space trajectory and the resulting measurement tensor (isotropic in case). (For interpretation of the references to color in this figure legend, the reader is referred to the web version of this article.)

and the measurement tensor $\mathbf{B}$; the normalized echo amplitude $E(\mathbf{q})$ in a diffusion experiment is [1]

$$-\log(E(\mathbf{q})) = \int_0^\tau \mathbf{q}(t')^T \mathbf{D}\mathbf{q}(t')dt' = \sum_{\alpha,\beta} D_{\alpha\beta} \int_0^\tau q_\alpha(t') q_\beta(t')\, dt' = \mathrm{Tr}(\mathbf{DB}), \tag{5}$$

where $\alpha, \beta \in \{x, y, z\}$. From the basics of the trace operator it follows that the attenuation is directly related to the sum of the eigenvalues of the matrix product $\mathbf{DB}$. In particular $\mathbf{B} = \mathbf{B}_{\mathrm{iso}}$ gives $\mathrm{Tr}(\mathbf{DB}) = b(\lambda_1 + \lambda_2 + \lambda_3)/3 = b\bar{D}$, where $\bar{D}$ is usually referred to as the mean diffusivity.

It is convenient to define a general measurement tensor as $\mathbf{B} = b\hat{\mathbf{B}}$, where $\mathrm{Tr}(\hat{\mathbf{B}}) = 1$, because then b is the conventional b-value and $\mathrm{Tr}(\mathbf{DB}) = b \cdot \mathrm{Tr}(\mathbf{D}\hat{\mathbf{B}})$. Combining this with Eq. (5) it is evident that—independent of the choice of $\hat{\mathbf{B}}$—maximizing the diffusion weighting amounts to maximizing b. However, the hardware imposes a multitude of constraints that prevents a universally optimal formula. It might seem a bit backwards to optimize b for a given echo time, instead of the converse, but in practice it is not an issue: using bisection the minimum echo time for a given b can be found in a small number of optimization runs. In return, the problem can be formulated as a constrained optimization problem in a more natural way.

2.1. Constraints

A pulse sequence optimization needs to respect a number of hardware dependent and sequence dependent constraints. We will describe these constraints in an idealized, continuous, scenario; implementation details can be found in Appendix A. To facilitate the numerical treatment, we phrase the optimization problem in terms of $\mathbf{q}(t)$, rather than working directly with the gradient waveforms $\mathbf{g}(t)$. Converting in between is straightforward: it follows from Eq. (1) that $\mathbf{g}(t) = \frac{1}{\gamma}\frac{d\mathbf{q}}{dt}$.

2.1.1. Sequence dependent constraints

There are three constraints specific to the sequence desired. First, we want to achieve a given diffusion encoding as described by a (normalized) measurement tensor $\hat{\mathbf{B}}$, i.e.

$$\int_0^\tau \mathbf{q}(t)\mathbf{q}(t)^T dt = b\hat{\mathbf{B}}. \tag{6}$$

Second, in order for the sequence to produce an echo at the desired echo time, τ, it must hold that

$$\mathbf{q}(0) = \mathbf{q}(\tau) = 0. \tag{7}$$

Third, it may be desirable to enforce the gradients to be zero (or active only in the slice encoding direction) during certain time intervals, I_t, to allow for RF pulses. Since the gradients are found by differentiating $\mathbf{q}(t)$ this is to say

$$\left.\frac{d\mathbf{q}}{dt}\right|_{t\in I_t} = 0. \tag{8}$$

In particular, we will impose throughout that the gradients are zero at the start and end of the pulse sequence.

2.1.2. Hardware constraints

The hardware constraints considered are the maximum gradient strength, slew rate and heating. The gradient amplitude, $G_{\max}$, is one of the most severe factors limiting the diffusion encoding strength [2,14] and it is therefore important to account for it explicitly in the optimization. This is done through the constraint

$$\left\|\frac{d\mathbf{q}}{dt}\right\| \leqslant \gamma G_{\max}, \tag{9}$$

where the norm is either the max-norm, $\|(x_1, x_2, x_3)\|_\infty = \max(|x_1|, |x_2|, |x_3|)$, or the Euclidean norm, $\|(x_1, x_2, x_3)\|_2 = \sqrt{x_1^2 + x_2^2 + x_3^2}$. The first corresponds to obtain the actual scanner constraints whereas the latter can be used to obtain a rotationally invariant waveform (more on that in Section 4.1).

A similar, but often not as severe, constraint is the maximum slew rate (rate of change), $R_{\max}$, of the gradients, which translates into

$$\left\|\frac{d^2\mathbf{q}}{dt^2}\right\|_\infty \leqslant \gamma R_{\max}. \tag{10}$$

An additional—at times overlooked—part of an efficient pulse sequence is the ability to perform at a high duty-cycle without inactive cool-down periods. An intense diffusion encoding block often requires a rather long idle time, which reduces the number of samples per unit of time and thereby the effective signal-to-noise ratio. This means that there is much to gain by accounting for the heat dissipation when optimizing the pulse sequence. Assuming resistive heating [13], the heat dissipation in gradient coil α is proportional to the time integral of $g_\alpha(t)^2$. This can be captured by the constraint

$$\int_0^\tau \left(\frac{dq_\alpha}{dt}\right)^2 dt \leqslant \eta\gamma^2 G_{\max}^2 \tau, \quad \alpha = x, y, z, \tag{11}$$

where $\eta \in [0, 1]$ is a dimensionless scalar. Varying the parameter η allows us to balance heat dissipation against diffusion encoding.

2.2. The optimization problem

Taken together, we arrive at the optimization problem

$$\begin{aligned}
\underset{\mathbf{q}, b}{\text{maximize}} \quad & b \\
\text{subject to} \quad & \int_0^\tau \mathbf{q}(t)\mathbf{q}(t)^T dt = b\hat{\mathbf{B}} \\
& \mathbf{q}(0) = \mathbf{q}(\tau) = 0 \\
& \left.\frac{d\mathbf{q}}{dt}\right|_{t\in I_t} = 0 \\
& \left\|\frac{d\mathbf{q}}{dt}\right\| \leqslant \gamma G_{\max}, \\
& \left\|\frac{d^2\mathbf{q}}{dt^2}\right\|_\infty \leqslant \gamma R_{\max} \\
& \int_0^\tau \left(\frac{dq_\alpha}{dt}\right)^2 dt \leqslant \eta\gamma^2 G_{\max}^2 \tau, \quad \alpha = x, y, z.
\end{aligned} \tag{12}$$

To solve this problem we discretize $\mathbf{q}(t)$ and replace the derivatives and integrals with finite difference approximations (see Appendix A). To achieve better convergence, we also relax the equality in the measurement tensor constraint by allowing a small violation ϵ in Frobenius norm. These steps turn the problem into a form in which it can be solved efficiently using sequential quadratic programming. This is a deterministic algorithm, meaning that it always returns the same solution for a given initial guess. Our experience is that a random initialization works best and, with large[1] probability, results in one out of a number of different but equally good (same

[1] Running 100 optimizations with random initial guesses, isotropic diffusion encoding, and the remaining settings as in Sections 4.1 and 4.2 (the only difference being max-norm or Euclidean norm in the gradient amplitude constraint) the best objective function value was found in 54 and 86 cases, respectively. In all the remaining cases the objective function value was within 1% of the best one.

objective function value) solutions. To further increase this probability, it is of course possible to run the optimization multiple times, with different initial guesses, and choose the best solution. The numerical results presented in Sections 4.1 and 4.2 all use the same random initial guess, i.e. a single starting configuration.

Incidentally, note that this optimization problem does not impose any particular shape on $\mathbf{q}(t)$, only that its diffusion encoding matches the desired measurement tensor. The shape can be important when considering restricted diffusion. However, if a particular shape is desired it is straightforward to check which constraint will be the limiting one and set the magnitude accordingly.

2.3. Evaluation

The performance of the different gradient waveforms can be compared with respect to their diffusion weighting and the amount of dissipated heat. In general, the b-value of any gradient waveform can be expressed as

$$b = \kappa \frac{\gamma^2 G_{\max}^2 \tau^3}{4}, \tag{13}$$

where κ is a dimensionless efficiency factor that depends on the gradient waveform. For a single coil, the maximum efficiency, $\kappa = 1/3$, results from applying maximum gradient in one direction for half the echo time and in the opposite direction for the other half of the time. It thus requires an infinite slew rate. Only by applying this gradient sequence in the three coils simultaneously is it possible to attain $\kappa = 1$.

To capture the slew rate limitation we introduce another dimensionless parameter, $\xi \in [0, 1]$, as

$$\xi = \frac{G_{\max}}{R_{\max}\tau}. \tag{14}$$

In other words, ξ is the fraction of the echo time it takes to increase the gradient amplitude from zero to max.

2.4. Heat dissipation and repetition times

The signal-to-noise ratio (SNR) of a measurement can be increased by repeating the measurement n times and averaging the results. A short repetition time T_R allows more repetitions in a given time. A short and intense gradient sequence suffers less from transverse relaxation but dissipates more heat—and may therefore require longer T_R—than a more gentle gradient sequence. A relevant question is therefore: provided a set amount of time, how to choose τ and T_R to maximize the SNR?

We will answer this question by considering two gradient sequences referred to as A and B. Gradient sequence A, with corresponding τ_A and η_A, is held fixed while we change gradient sequence B and record the ratio of their SNRs. In general, for a repeated spin echo experiment

$$\mathrm{SNR} \propto \sqrt{n}\exp(-\tau/T_2)\left(1 - \exp\left(-\frac{T_R - \tau/2}{T_1}\right)\right). \tag{15}$$

To proceed we make the following two assumptions: first, that Eq. (13), with $\kappa = \kappa(\eta)$ (as will be shown in Fig. 5), holds as τ and η are varied. This is a reasonable approximation as long as the slew rate is not a major limitation (ξ small). Second, that the average heat dissipation per unit time is sufficient to represent the thermal dynamics and that the system adjusts $T_R^{(A)}$ so that the average heat dissipation is precisely as high as acceptable. If this is not the case, it is best to simply use the most intense gradient sequence possible. As shown in Appendix B, the resulting ratio of the pulse sequences SNRs is

$$\frac{\mathrm{SNR}_B}{\mathrm{SNR}_A} = \left(\frac{\eta_A}{\eta_B}\right)^{1/2} \Psi^{-1/2} \exp\left((1-\Psi)\frac{\tau_A}{T_2}\right) \cdot \frac{1 - \exp\left(\Psi \frac{\tau_A}{2T_1}\right)\exp\left(-\Psi \frac{\eta_B}{\eta_A}\frac{T_R^{(A)}}{T_1}\right)}{1 - \exp\left(\frac{\tau_A}{2T_1}\right)\exp\left(-\frac{T_R^{(A)}}{T_1}\right)}, \tag{16}$$

where $\Psi = (\kappa(\eta_A)/\kappa(\eta_B))^{1/3}$. The highest SNR can be found by maximizing the ratio with respect to η_B, which in turn yields τ_B and $T_R^{(B)}$.

3. Experiments

We performed two types of experiments: the first, detailed in Appendix C, aimed to verify that optimized waveforms achieve isotropic diffusion encoding when intended to; the second, detailed below, considers the implementation of optimized waveforms on a clinical MRI scanner.

3.1. In vivo experiments

To demonstrate that the optimized waveforms could be implemented on a clinical scanner system, MRI data was acquired in 10 healthy volunteers (all male, mean age (standard deviation) was 30 (4) y, interval [24, 34] y), using a Siemens Skyra 3 T system, equipped with 43 mT/m gradients with a maximum slew rate of 200 mT/m/ms, and a 20-channel receiver head coil. Written consent was received from all volunteers prior to scanning. The diffusion experiments were based on those reported by Szczepankiewicz et al. [12], although using another sequence implementation. Briefly, the experiment combines equal amounts of images acquired with directional and isotropic diffusion encoding at b-values 100, 500, 1000, 1500 and 2000 s/mm^2. The directional encoding in each shell was performed in 6, 6, 12, 20 and 48 directions, respectively, and the isotropic encoding was repeated the same number of times for each shell. The directions were optimized across all b-shells simultaneously using a charged container model [25]. All images were acquired in 11 contiguous axial slices using an echo time (τ) of 130 ms, repetition time (T_R) of 2500 ms, 128×128 acquisition matrix, spatial resolution of $2 \times 2 \times 4$ mm^3, partial Fourier factor of 6/8, bandwidth of 1500 Hz/voxel, and a GRAPPA factor of 2. The diffusion encoding was performed during 55.44 ms and 48.16 ms before and after the refocusing pulse, respectively; the duration of the refocusing pulse and slice-selection gradients was 7.76 ms. The waveform was optimized to this timing using 2-norm, $\eta = 0.6$, $G_{\max} = 43$ mT/m, $R_{\max} = 130$ T/m/s and $N = 200$ discretization points. The maximum slew rate was limited to avoid peripheral nerve stimulation. Total scan time for the isotropic and anisotropic encoding sequences was 8:00 min. All data was smoothed with a 3D Gaussian kernel (FWHM 2 mm) to mitigate Gibbs ringing artefacts [26], and corrected for motion and eddy-current distortions using ElastiX [27] with extrapolated references [28]. Parameter maps of the mean diffusivity (MD) and microscopic fractional anisotropy (μFA), were calculated according to the framework suggested by Lasič et al. [11,12]. The conventional fractional anisotropy (FA) was calculated from the directionally encoded data, using standard diffusion tensor analysis [29,12]. The potential benefit of using optimized waveforms was evaluated by comparing the maximal b-values that could be achieved by the qMAS waveforms, used in Szczepankiewicz et al. [12], to the optimized waveforms.

In addition to this, a separate investigation of the SNR was performed in a single volunteer where optimized waveforms were compared to qMAS. To this end, the in vivo protocol was modified to contain only isotropic encoding at a single b-value of

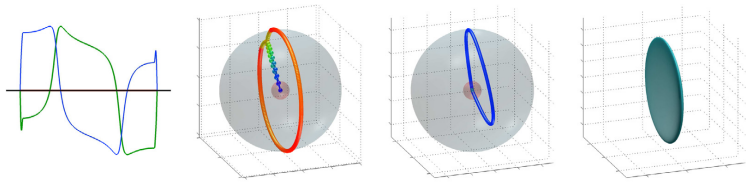

(a) $\lambda_{\text{axial}} = 0$, $b/b_{\max} = 0.44$

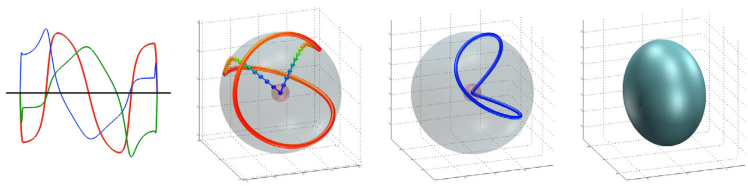

(b) $\lambda_{\text{axial}} = 0.2$, $b/b_{\max} = 0.31$

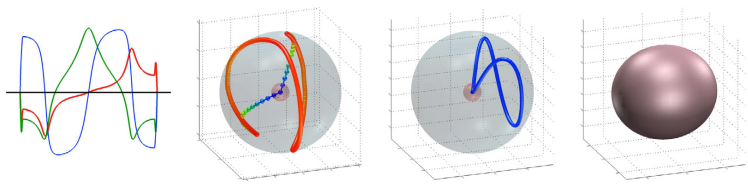

(c) $\lambda_{\text{axial}} = 0.4$, $b/b_{\max} = 0.27$

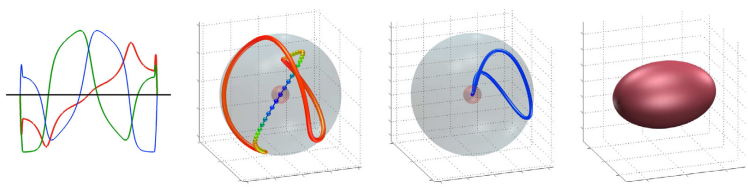

(d) $\lambda_{\text{axial}} = 0.6$, $b/b_{\max} = 0.37$

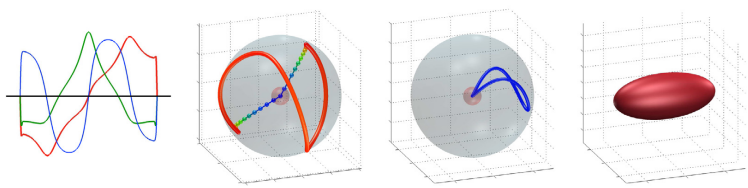

(e) $\lambda_{\text{axial}} = 0.8$, $b/b_{\max} = 0.56$

Fig. 4. Optimized gradient waveforms and trajectories. Columns from left to right: gradients, gradient trajectory, q-space trajectory and measurement tensor. The trajectories are color coded according to rate of change: from slow (red), through intermediate (green) to fast (blue). The fourth column shows the resulting measurement tensor; the magnitudes of the eigenvalues are mapped to red–green–blue. (For interpretation of the references to color in this figure legend, the reader is referred to the web version of this article.)

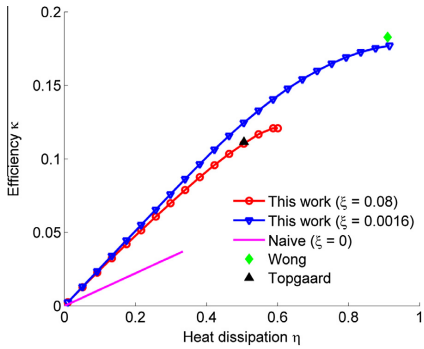

Fig. 5. Sequence efficiency factor κ and relative heat dissipation η for isotropically encoding sequences optimized in this work and in previous work. The larger η is the more heat is generated by the sequence. Two sets of optimizations were done using different slew rates, as specified by the dimensionless constant ξ.

2000 s/mm^2. The echo time was minimized and the repetition time was set to 4000 ms to not incur restrictions on the maximal echo time. This measurement was repeated 20 times and the SNR was calculated in each voxel as the mean signal divided by the signal's standard deviation across all repetitions.

4. Results

We first present results from numerical studies and then experimental results. The numerical studies consider, in turn, varying the measurement tensor, varying the heat dissipation and the heat dissipation's effect on the total SNR. Then, the results of the in vivo experiments follow. The result of the experiment aimed to verify the isotropic encoding of an optimized waveform is presented in Appendix C.

4.1. Optimization of axisymmetric measurement tensors

Axially symmetric tensors are of particular interest since they can be used to distinguish between prolate and oblate microscopic diffusion tensors with unknown orientation distribution [30].

Often, it is desirable to use a pulse sequence that can be rotated to achieve arbitrary directional encoding. This means that the total gradient magnitude can never exceed what a single gradient coil can generate, i.e. $\|\mathbf{g}(t)\|_2 \leqslant G_{\max}$. Geometrically, the gradient trajectory is then constrained to lie inside a sphere of radius $G_{\max}$. In what follows we will only consider diagonal measurement tensors; provided that the rotational dependence of the slew rate constraint can be neglected, this assumption incurs no loss of generality.

For comparison we consider a naïve approach: consecutive application of a conventional SDE sequence in each gradient direction as shown in Fig. 2. Assuming infinite slew rate and $\tau_x = \alpha\tau,\ \tau_y = \tau_z = (1-\alpha)\tau/2$, where $\alpha \in [0,1]$, this gives $\lambda_{\text{axial}} = (\alpha^3\gamma^2 G_{\max}^2\tau^3)/12$ and a resulting efficiency

$$\kappa_{\text{naïve}} = \frac{1}{3}\left(\alpha^3 + \frac{(1-\alpha)^3}{4}\right). \tag{17}$$

Fig. 3 compares the efficiency of this approach compared to an optimization, as proposed in this work, for axially symmetric measurement tensors

$$\hat{\mathbf{B}}(\lambda_{\text{axial}}) = \operatorname{diag}\left(\lambda_{\text{axial}}, \frac{1-\lambda_{\text{axial}}}{2}, \frac{1-\lambda_{\text{axial}}}{2}\right), \tag{18}$$

where $\lambda_{\text{axial}} \in [0,1]$. These optimizations were done using $G_{\max} = 80$ mT/m, $R_{\max} = 100$ T/m/s ($\xi = 0.016$), $\eta = 1$, $\tau = 50$ ms, $\epsilon = 10^{-4}$ and $N = 100$ discretization points. Fig. 4 shows five of the optimized trajectories. To achieve the same b-value, it follows from Eq. (13) that the optimized waveforms allow reductions in echo time by 16% and 22% in the double diffusion encoding ($\lambda_{\text{axial}} = 0$) and triple diffusion encoding ($\lambda_{\text{axial}} = 1/3$) cases, respectively.

4.2. The trade-off between heat dissipation and efficiency

We explored the trade-off between heat dissipation and efficiency by fixing the measurement tensor to be isotropic and varying the heat dissipation η. Again, we used the settings $G_{\max} = 80$ mT/m, $\tau = 50$ ms, $\epsilon = 10^{-4}$ and $N = 100$. However, to investigate the influence of the slew rate, we repeated the experiment twice: first with $R_{\max} = 100$ T/m/s ($\xi = 0.016$) and then with $R_{\max} = 20$ T/m/s ($\xi = 0.08$). The resulting efficiencies as a function of the heat dissipation are shown in Fig. 5, which also shows the results from previous work and compares with a naïve sequence defined as in Section 4.1 but with the gradient magnitudes scaled to meet the heat dissipation requirement. Fig. 6 shows five trajectories optimized with $\xi = 0.016$ and different values of η. As the allowable heat dissipation is varied from low to high, the gradient waveforms transition from smooth, almost sinusoidal, to rectangular.

The fact that the gradient amplitude and slew rate apply to each coil separately means that the gradients are constrained by a cube with its sides at $\pm G_{\max}$. The strongest diffusion encoding is achieved in the corners of this cube (recall that the b-value scales quadratically with the gradient). So, whenever heat dissipation can be neglected, this is where we expect to find the gradients. The slew rate then limits how fast the gradient trajectory transitions between corners. This behavior is clearly visible in Fig. 6e.

4.3. Heat dissipation and repetition times

To illustrate the heat dissipation's effect on SNR, as described in Section 2.4, we consider the optimized sequences from Section 4.2 with $\xi = 0.016$ that are shown in Fig. 5 and the corresponding naïve sequences. Fig. 7 shows the ratio of SNRs, for $T_R^{(A)} \in \{1000\text{ ms}, 2500\text{ ms}\}$, when gradient sequence A is taken to be the most intense one. Here, we used $T_1 = 1331$ ms and $T_2 = 110$ ms for gray matter (GM); $T_1 = 832$ ms and $T_2 = 80$ ms for white matter (WM) [31].

4.4. In vivo experiments

All volunteers were successfully scanned. A qualitative examination of the diffusion weighted images showed that the image quality was good, and that no prominent artefacts were introduced by the optimized waveforms. Parameter maps of a subject are shown in Fig. 8.

The maximal b-value achievable for isotropic encoding with $\tau = 130$ ms (see Section 3.1) was 3000 s/mm^2 for the optimized waveforms, and 1050 s/mm^2 for the qMAS waveforms, respectively. Thus, to achieve a b-value of 3000 s/mm^2 the echo time could be reduced from 180 ms to 130 ms when employing the optimized waveforms.

A b-value of 2000 s/mm^2 was achievable with an echo time of 116 and 170 ms for the optimized waveform and qMAS waveforms, respectively. Due to transverse relaxation effects, the signal at $b = 2000$ s/mm^2 is thus expected to increase by 63% and 96% for gray matter ($T_2 = 110$ ms) and white matter ($T_2 = 80$ ms), respectively. To make these statements more tangible, Fig. 9 shows an

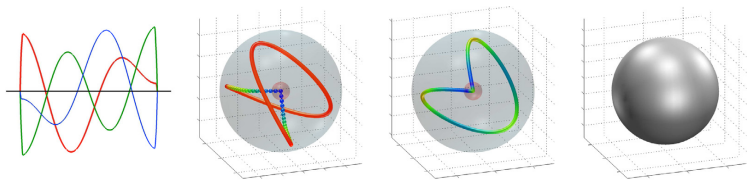

(a) $\eta = 0.26,\ b/b_{\max} = 0.37$

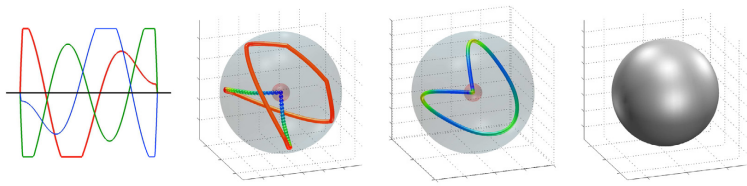

(b) $\eta = 0.42,\ b/b_{\max} = 0.60$

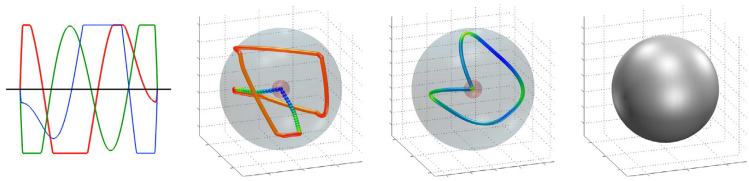

(c) $\eta = 0.59,\ b/b_{\max} = 0.79$

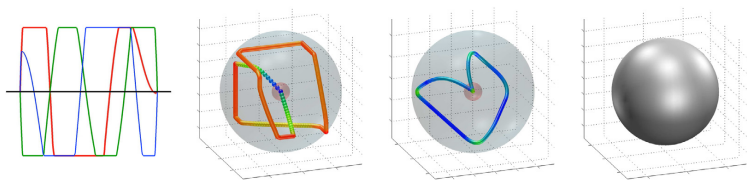

(d) $\eta = 0.75,\ b/b_{\max} = 0.93$

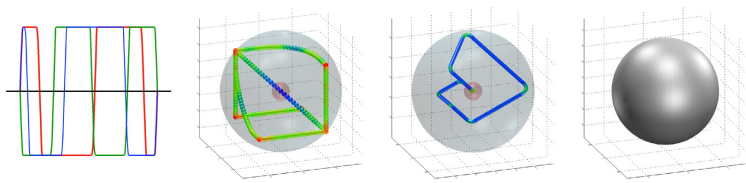

(e) $\eta = 0.92,\ b/b_{\max} = 1$

Fig. 6. Gradient waveforms optimized with $\xi = 0.016$ and different values of η. Columns from left to right: gradients, gradient trajectory, q-space trajectory and measurement tensor. Color coding as in Fig. 4. (For interpretation of the references to color in this figure legend, the reader is referred to the web version of this article.)

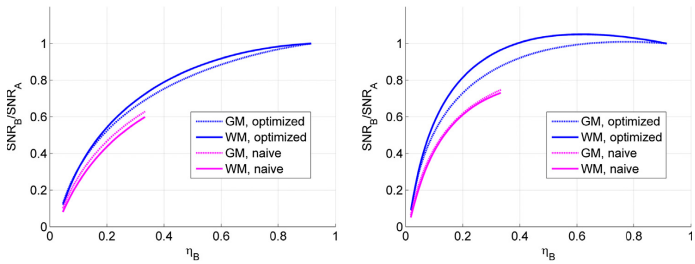

(a) $T_R^{(A)} = 1000$ ms. (b) $T_R^{(A)} = 2500$ ms.

Fig. 7. Comparison of signal-to-noise ratio in gray matter (GM) and white matter (WM) as the heat dissipation of the gradient sequences from Section 4.2 is varied. The baseline, gradient sequence A, is the most intense gradient sequence and is assumed to require a repetition time $T_R^{(A)}$ to reach a sustainable average heat dissipation. The naïve gradient sequence consists of consecutive SDE sequences in each gradient direction and the resulting heat dissipation can thus be at most $\eta_B = 1/3$.

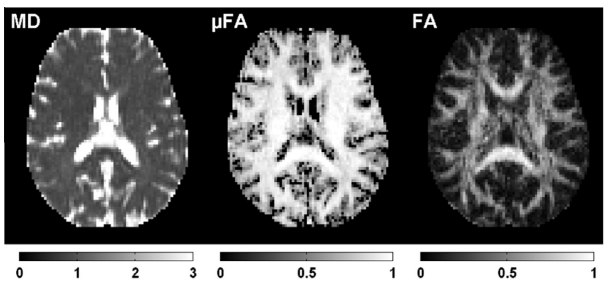

Fig. 8. Parameter maps in axial slice through the corpus callosum in a healthy volunteer. Data quality for all volunteers was qualitatively good, and no additional artefacts were observed as a result of employing the optimized waveforms. As previously reported by Szczepankiewicz et al. [12], the μFA map is homogeneous in regions of white matter, and the difference between the μFA and FA maps is most prominent in regions where complex white matter architecture is expected, such as in crossing white matter pathways.

example of raw diffusion weighted images acquired with the different methods together with a histogram of the voxelwise SNR. As expected, the shorter echo time, facilitated by the optimized waveform, rendered a markedly higher SNR in the images.

5. Discussion

In optimization, a good practice is to formulate a problem that is a caricature of the real problem—capturing all the essential characteristics and ignoring the rest. This often makes solving the problem more reliable, thereby producing a better end result than a too detailed model. In addition, the problem formulation will be easier to adapt to a different setting.

An example of this is the model of the signal as a mixture of Gaussians, from which our objective function derives. This is not a physically well-founded model for restricted diffusion but it has found widespread use. With this work, we do not attempt to answer whether this is the most appropriate way of modeling the signal; instead our hope is to provide a tool that researchers in the field will find useful. Consequently, we have assumed that the object of interest is the measurement tensor, but we have left its application undetermined. On the other hand, we have placed virtually no other restrictions on the shape of the gradient waveforms other than those imposed by the hardware. This makes the model much more flexible than if deciding upon particular basis functions or similar. This means our formulation can, without modifications, be used for a range of experiments—be it in NMR or in vivo diffusion MRI. Another example of this flexibility is the possibility to impose zero-gradient intervals, or intervals with specified slice encoding gradients, at arbitrary points in time, i.e. not requiring the gradient waveform to be symmetric. This was taken advantage of in our in vivo experiments and was one of the reasons why it was possible to reduce the echo time from 180 ms to 130 ms. It can, however, be expected that the slice selection gradient will perturb the obtained measurement tensor, but only by a little.

The importance of explicitly taking the hardware constraints into account can be appreciated from the q-space trajectories in Fig. 4, where the total gradient magnitude is limited by what a single gradient coil can generate (in order to allow arbitrary rotation of the resulting waveforms). The lack of dynamics in the color coding reflects that this constraint is active throughout almost the entire trajectory—an indication of the solutions high quality and a feat that would otherwise be very difficult to accomplish.

As another example, a more intense gradient sequence may reduce the echo time at the cost of prolonging the repetition time (to allow for cooling). A general procedure to maximize the SNR using the methods we have presented would be as follows. First, given a desired b-value, use bisection to find—with no concern for heat dissipation ($\eta = 1$)—the shortest echo time possible. Then, test what the minimum repetition time allowed by the scanner is. If it appears that cooling is not a limitation then stop, else maximize Eq. (16) with respect to η_B either numerically or graphically. Fig. 7 suggests that beyond a certain value of the repetition time it

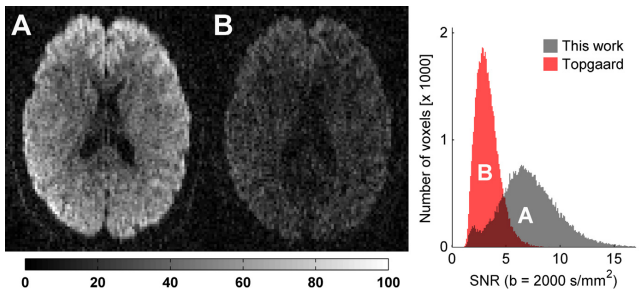

Fig. 9. Raw diffusion weighted images in an axial slice through the corpus callosum in a healthy volunteer. The encoding strength is $b = 2000$ s/mm^2 in both images. The measured signal is markedly higher in the images encoded with the optimized waveform (A, echo time 116 ms) compared to the qMAS waveform (B, echo time 170 ms) suggested by Topgaard et al. [15]. The histogram shows the distribution of voxelwise SNR from brain tissue located within the imaging slab. There is a clear tendency towards higher SNR for the optimized waveform, due to the shorter echo time.

becomes more efficient to decrease the pulse's heat dissipation than to use the most intense one. Incidentally, the figure also shows that compared with a naïve sequence for isotropic diffusion encoding, the optimized sequences can increase the SNR by about 60%.

Our experiments have shown that the optimized waveforms can achieve the expected isotropic encoding and that it is possible to implement optimized waveforms on a clinical MRI scanner with a drastically reduced echo time yet no prominent artefacts. The latter finding is in line with our theoretical comparison with naïve double diffusion encoding (DDE) and triple diffusion encoding (TDE), that showed that reductions in echo time by 16% and 22%, respectively, are possible.

6. Conclusions

We have proposed a new framework for optimization of gradient waveforms that maximizes the b-value for a given measurement tensor and echo time. From this it is straightforward to obtain gradient waveforms that minimize the echo time for a given b. The formulation as a constrained optimization problem allows explicit control of hardware requirements, including maximum gradient amplitude, slew rate, heating and positioning of RF pulses.

Based on two reasonable assumptions, we have derived an expression for the signal-to-noise ratio's dependence on the heat dissipation and outlined how this can be used to strike a balance between gradient intensity and heat dissipation that maximizes the signal-to-noise ratio.

We have verified by experiments on a water/surfactant mixture that the method can achieve the desired diffusion encoding. By in vivo experiments and numerical comparisons with previous work, we have shown that substantial gains in terms of reduced echo times and better signal-to-noise ratio's can be achieved, in particular as compared with naïve double diffusion encoding (DDE) and triple diffusion encoding (TDE).

Acknowledgments

The authors acknowledge the Swedish Research Council (VR) Grants 2012-4281, 2012-3682, 2011-5176 and 2014-3910; the Swedish Foundation for Strategic Research (SSF) Grant AM13-0090; EUREKA ITEA BENEFIT Grant 2014-00593; NIH Grants R01MH074794 and P41EB015902; and the Linneaus center CADICS.

Appendix A. Explicit problem formulation

In summary, we strive to find the q-space trajectory $\mathbf{q}(t)$ that maximizes b, everything else is considered fixed parameters. This is done by discretizing $\mathbf{q}(t)$ into N time steps of length $\Delta t = \tau/N$, forming the $N \times 3$ matrix

$$\mathbf{Q} = \begin{pmatrix} q_{x,1} & q_{y,1} & q_{z,1} \\ \vdots & \vdots & \vdots \\ q_{x,N} & q_{y,N} & q_{z,N} \end{pmatrix}, \tag{A.1}$$

where we have used the notation $q_{\alpha,k} = q_\alpha((k-1/2)\Delta t)$. To discretize the measurement tensor constraint in Eq. (6), we first introduce a diagonal "integration matrix" corresponding to the trapezoid rule

$$\mathbf{\Theta} = \Delta t \begin{pmatrix} 1/2 & & & & \\ & 1 & & & \\ & & \ddots & & \\ & & & 1 & \\ & & & & 1/2 \end{pmatrix}, \tag{A.2}$$

so that the discretized version of Eq. (6) reads

$$\mathbf{Q}^T\mathbf{\Theta}\mathbf{Q} = b\hat{\mathbf{B}}. \tag{A.3}$$

However, because nonlinear equality constraints should be avoided, we relax this and instead require

$$\|\mathbf{Q}^T\mathbf{\Theta}\mathbf{Q} - b\hat{\mathbf{B}}\|_F^2 \leqslant (b\epsilon)^2, \tag{A.4}$$

where we have introduced a tolerance ϵ on the isotropy violation.

Many of the remaining constraints involve the gradients; these are easily implemented through a finite difference scheme. We used a central difference scheme shifted by half a time step,

$$\left.\frac{d\mathbf{q}_\alpha}{dt}\right|_{k+1/2} \approx \frac{q_{\alpha,k+1} - q_{\alpha,k}}{\Delta t}, \tag{A.5}$$

which can also be interpreted as the average value over the bin centered at $k\Delta t$. The boundary constraints on the gradients, which are of Dirichlet type, were implemented using ghost points. The $(N-1)$ internal derivatives were thus approximated using the $(N-1) \times N$-matrix

$$\mathbf{A}_1 = \frac{1}{\Delta t}\begin{pmatrix} -1 & 1 & & \\ & \ddots & \ddots & \\ & & -1 & 1 \end{pmatrix}. \tag{A.6}$$

Similarly, the second derivatives were approximated using the $N \times N$-matrix

$$\mathbf{A}_2 = \frac{1}{(\Delta t)^2}\begin{pmatrix} -2 & 1 & & & & \\ 1 & -2 & 1 & & & \\ & \ddots & \ddots & \ddots & & \\ & & 1 & -2 & 1 & \\ & & & 1 & -2 & \end{pmatrix}. \tag{A.7}$$

In Euclidean norm, a constraint on the gradient amplitude can thus be written as the nonlinear inequality constraints (interpreted componentwise)

$$(\mathbf{A}_1\mathbf{q}_x)^2 + (\mathbf{A}_1\mathbf{q}_y)^2 + (\mathbf{A}_1\mathbf{q}_z)^2 \leqslant \gamma^2 G_{\max}^2. \tag{A.8}$$

In contrast, max-norm constraints on the gradient amplitude and slew rate can be translated into linear inequality constraints

$$-\gamma G_{\max} \leqslant \mathbf{A}_1\mathbf{q}_\alpha \leqslant \gamma G_{\max}, \quad \alpha = x, y, z \tag{A.9}$$

$$-\gamma R_{\max} \leqslant \mathbf{A}_2\mathbf{q}_\alpha \leqslant \gamma R_{\max}, \quad \alpha = x, y, z. \tag{A.10}$$

Similarly, a constraint on the gradients being zero during an interval I_t can be written

$$\mathbf{A}_1 q_{\alpha,k} = 0 \quad \text{if } k\Delta t \in I_t, \quad \alpha = x, y, z. \tag{A.11}$$

The heat dissipation constraint, Eq. (11), can be approximated as

$$\int_0^\tau \left(\frac{dq_\alpha}{dt}\right)^2 dt \approx \Delta t \cdot \mathbf{q}_\alpha^T \mathbf{A}_1^T \mathbf{A}_1 \mathbf{q}_\alpha, \quad \alpha = x, y, z. \tag{A.12}$$

In conclusion, following the discretization scheme above, the explicit formulation of the constrained optimization problem in Eq. (12) is:

$$\begin{aligned} \underset{\mathbf{Q}, b}{\text{minimize}} \quad & -b \\ \text{subject to} \quad & \|\mathbf{Q}^T\Theta\mathbf{Q} - b\tilde{\mathbf{B}}\|_{\mathrm{F}}^2 \leqslant (b\epsilon)^2 \\ & \mathbf{A}_1 q_{\alpha,k} = 0 \quad \text{if } k\Delta t \in I_t \\ & q_{\alpha,1} = q_{\alpha,N} = 0 \\ & -\gamma G_{\max} \leqslant \mathbf{A}_1\mathbf{q}_\alpha \leqslant \gamma G_{\max} \\ & -\gamma R_{\max} \leqslant \mathbf{A}_2\mathbf{q}_\alpha \leqslant \gamma R_{\max} \\ & \mathbf{q}_\alpha^T \mathbf{A}_1^T \mathbf{A}_1 \mathbf{q}_\alpha \leqslant \eta G_{\max}^2 \tau / \Delta t, \end{aligned} \tag{A.13}$$

where the constraints are understood to apply to each coil separately ($\alpha = x, y, z$). If the Euclidean version of the gradient constraint is desired, one just has to replace the corresponding max-norm expression with that in Eq. (A.8). In addition to that nonlinear inequality, there are two more: the measurement tensor constraint, Eq. (A.4), and the heat dissipation constraint, Eq. (A.12). The cross-terms in the measurement tensor constraint make the problem non-convex. Nevertheless, Sequential Quadratic Programming (SQP) [32] seems to produce a good local optimum reasonably fast—typical computation times on a modern laptop are about 30 s for $N = 100$ and 15 min for $N = 200$.

Appendix B. Derivation of the ratio of SNRs

Here we will show how the assumptions in Section 2.4 lead to Eq. (16) for the ratio of the SNRs of pulse sequences A and B.

Requiring equal b-values and using the first assumption gives

$$\tau_B = \tau_A \left(\frac{\kappa(\eta_A)}{\kappa(\eta_B)}\right)^{1/3} \triangleq \tau_A \Psi, \tag{B.1}$$

where we for convenience have introduced the function $\Psi = (\kappa(\eta_A)/\kappa(\eta_B))^{1/3}$.

From the second assumption and Eq. (11) it follows that the maximum heat dissipation per unit time is

$$w = \frac{\eta_A \gamma^2 G_{\max}^2 \tau_A}{T_R^{(A)}}. \tag{B.2}$$

For gradient sequence B to have the same heat dissipation per unit time it must hold that

$$\frac{\eta_B \tau_B}{T_R^{(B)}} = \frac{\eta_A \tau_A}{T_R^{(A)}}. \tag{B.3}$$

Of course, $T_R^{(B)} \geqslant \tau_B$, which means that

$$\frac{\eta_B}{\eta_A} \geqslant \frac{\tau_A}{T_R^{(A)}}. \tag{B.4}$$

The number of repetitions n (neglecting round-off) is

$$n_A = \frac{T_{\text{total}}}{T_R^{(A)}}, \quad n_B = \frac{T_{\text{total}}}{T_R^{(B)}} = \frac{\eta_A \tau_A}{\eta_B \tau_B} \frac{T_{\text{total}}}{T_R^{(A)}}, \tag{B.5}$$

where we used Eq. (B.3) in the second expression. The ratio is

$$\frac{n_B}{n_A} = \frac{\eta_A \tau_A}{\eta_B \tau_B} = \frac{\eta_A}{\eta_B} \Psi^{-1}. \tag{B.6}$$

From Eq. (15) it follows that

$$\frac{\mathrm{SNR}_B}{\mathrm{SNR}_A} = \sqrt{\frac{n_B}{n_A}} \exp\left(-\frac{(\tau_B - \tau_A)}{T_2}\right) \frac{1 - \exp\left(\frac{\tau_B}{2T_1}\right) \exp\left(-\frac{T_R^{(B)}}{T_1}\right)}{1 - \exp\left(\frac{\tau_A}{2T_1}\right) \exp\left(-\frac{T_R^{(A)}}{T_1}\right)} \tag{B.7}$$

$$= \left(\frac{\eta_A}{\eta_B}\right)^{1/2} \Psi^{-1/2} \exp\left((1 - \Psi)\frac{\tau_A}{T_2}\right) \cdot \tag{B.8}$$

$$\frac{1 - \exp\left(\Psi \frac{\tau_A}{2T_1}\right) \exp\left(-\Psi \frac{\eta_B}{\eta_A} \frac{T_R^{(A)}}{T_1}\right)}{1 - \exp\left(\frac{\tau_A}{2T_1}\right) \exp\left(-\frac{T_R^{(A)}}{T_1}\right)}. \tag{B.9}$$

Appendix C. Experimental verification of isotropic encoding

To experimentally verify that the optimization produces a waveform that achieves isotropic diffusion encoding we prepared a sample consisting of a nonionic surfactant mixed with water, as in [33]. This sample is characterized by the formation of concentric cylindrical layers throughout the test tube, which in this case had an inner diameter of 4 mm. The mean diffusivity in each domain is expected to be the same, but the orientations different.

In Section 2 we saw that, under the assumption of Gaussian diffusion, the normalized echo amplitude $E(\mathbf{q}) = \mathrm{Tr}(\mathbf{BD})$. Consequently, an isotropically encoding pulse results in $\log(E_{\text{iso}}(b)) = -b\bar{\mathbf{D}}$, where $\bar{\mathbf{D}}$ is the mean diffusivity. A conventional SDE sequence applied in the direction $\hat{\mathbf{n}}$ corresponds to a measurement tensor $\mathbf{B}_{\hat{\mathbf{n}}} = b\hat{\mathbf{n}}\hat{\mathbf{n}}^T$. So, it gives rise to a normalized echo amplitude

$$\log(E_{\hat{\mathbf{n}}}(b)) = \mathrm{Tr}(b\hat{\mathbf{n}}\hat{\mathbf{n}}^T\mathbf{D}) = -b\mathrm{Tr}(\hat{\mathbf{n}}^T\mathbf{D}\hat{\mathbf{n}}) = -b\hat{\mathbf{n}}^T\mathbf{D}\hat{\mathbf{n}}. \tag{C.1}$$

For a system consisting of multiple non-interacting compartments, the total signal is the sum of the signals from each compartment. Assuming that the experimental conditions are such that the diffusion in each compartment can be approximated as Gaussian, the resulting echo amplitudes using SDE and an isotropically encoding pulse are,

$$E_{\hat{\mathbf{n}}}(b) = \sum_{i=1}^N p_i e^{-b\hat{\mathbf{n}}^T\mathbf{D}_i\hat{\mathbf{n}}}, \quad E_{\text{iso}} = \sum_{i=1}^N p_i e^{-b\bar{\mathbf{D}}_i}, \tag{C.2}$$

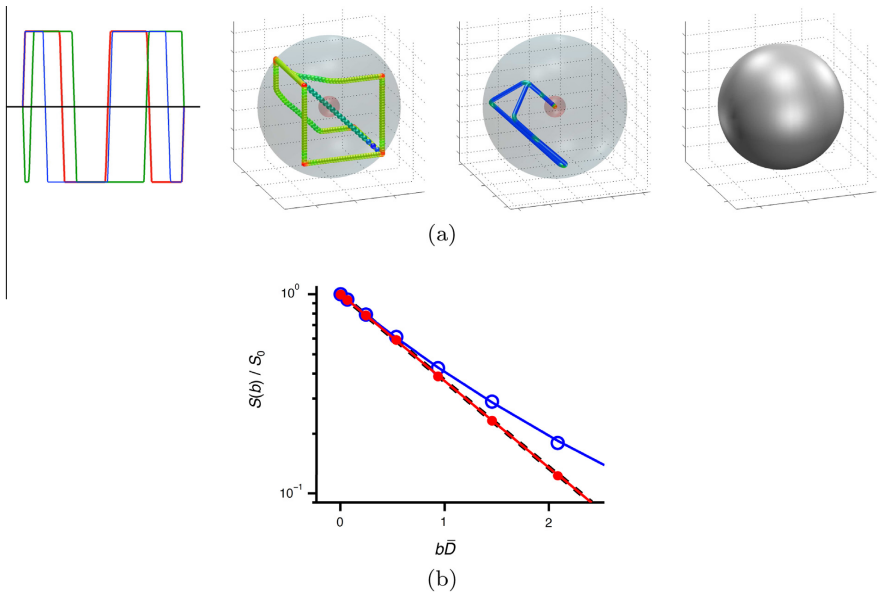

Fig. C.10. (a) Waveform optimized to achieve isotropic diffusion encoding for an NMR experiment. See caption of Fig. 4 for figure details. (b) Normalized signal $E(b) = S(b)/S_0$ vs. normalized diffusion weighting $b\bar{\mathbf{D}}$ for a representative pixel in an NMR experiment on a water/surfactant mixture. Powder-averaged measurements are shown with open blue circles, the measurements using the optimized waveform are shown with solid red circles. The blue and red lines show the corresponding fits of Eq. (C.3). The dashed black line is the single-exponential $E(b) = e^{-b\bar{\mathbf{D}}}$. The overlapping of the solid red and dashed black lines shows that the optimized waveform achieves the expected encoding. (For interpretation of the references to color in this figure legend, the reader is referred to the web version of this article.)

where p_i is the fraction of protons in compartment i. If the mean diffusivity in every compartment is the same, then $E_{\text{iso}} = e^{-b\bar{\mathbf{D}}\sum_{i=1}^{N} p_i} = e^{-b\bar{\mathbf{D}}}$. To derive a rotationally invariant quantity from SDE measurements one may average the signal over all directions. This is sometimes referred to as the powder average and can be approximated as [11]

$$\log E(b) = -\frac{3}{\bar{K}} \log\left(1 + \frac{\bar{K}}{3} b\bar{\mathbf{D}}\right) \tag{C.3}$$

$$\approx -b\bar{\mathbf{D}} + \frac{\bar{K}}{6}(b\bar{\mathbf{D}})^2 \tag{C.4}$$

where $\bar{K}$ is the kurtosis of the powder-averaged data [34]. The approximation (C.4), which coincides with the cumulant expansion [35], follows from a Taylor expansion of the logarithm.

Experiments were performed on a 11.74 T Bruker AVII-500 spectrometer equipped with a MIC-5 probe capable of delivering 3 T/m gradients in three orthogonal directions. We optimized an isotropically encoding waveform with $G_{\max} = 0.3$ T/m, $R_{\max} = 1000$ T/m/s, echo time $\tau = 20$ ms, no heating constraint ($\eta = 1$), max norm constraint on the gradients and used $N = 200$ discretization points. The pulse sequence was the same as in Fig. 4 of [11], i.e. spin-echo diffusion encoding with RARE image read-out, wherein the optimized gradient waveform was inserted before and after the first 180° RF pulse. The directional measurements were done with a waveform for which the magnitude of $\mathbf{q}(t)$ was the same as for the isotropic waveform [10]. The optimized waveform and resulting measurements, in a representative pixel, are shown in Fig. C.10 together with powder averaged measurements. The expected behavior is clearly visible: a straight line for the optimized isotropic waveform ($E_{\text{iso}} = e^{-b\bar{\mathbf{D}}}$) and a curved line for the powder average, corresponding to Eq. (C.3).

References

[1] P.T. Callaghan, Translational Dynamics and Magnetic Resonance: Principles of Pulsed Gradient Spin Echo NMR, Oxford University Press, 2011.
[2] M. Nilsson, D. van Westen, F. Ståhlberg, P.C. Sundgren, J. Lätt, The role of tissue microstructure and water exchange in biophysical modelling of diffusion in white matter, Magn. Reson. Mater. Phys., Biol. Med. 26 (4) (2013) 345–370.
[3] W.S. Price, NMR Studies of Translational Motion: Principles and Applications, Cambridge University Press, 2009.
[4] M.E. Moseley, J. Kucharczyk, H.S. Asgari, D. Norman, Anisotropy in diffusion-weighted MRI, Magn. Reson. Med. 19 (2) (1991) 321–326.
[5] P.J. Basser, J. Mattiello, D. LeBihan, MR diffusion tensor spectroscopy and imaging, Biophys. J. 66 (1) (1994) 259–267.
[6] P.J. Basser, C. Pierpaoli, Microstructural and physiological features of tissues elucidated by quantitative-diffusion-tensor MRI, J. Magn. Reson., Ser. B 111 (3) (1996) 209–219.
[7] L. Chen, M. Liu, J. Bao, Y. Xia, J. Zhang, L. Zhang, X. Huang, J. Wang, The correlation between apparent diffusion coefficient and tumor cellularity in patients: a meta-analysis, PloS one 8 (11) (2013) e79008.
[8] G. Schlaug, B. Siewert, A. Benfield, R. Edelman, S. Warach, Time course of the apparent diffusion coefficient (ADC) abnormality in human stroke, Neurology 49 (1) (1997) 113–119.
[9] S. Mori, P. Van Zijl, Diffusion weighting by the trace of the diffusion tensor within a single scan, Magn. Reson. Med. 33 (1) (1995) 41–52.
[10] S. Eriksson, S. Lasic, D. Topgaard, Isotropic diffusion weighting in PGSE NMR by magic-angle spinning of the q-vector, J. Magn. Reson. 226 (2013) 13–18.
[11] S. Lasič, F. Szczepankiewicz, S. Eriksson, M. Nilsson, D. Topgaard, Microanisotropy imaging: quantification of microscopic diffusion anisotropy and orientational order parameter by diffusion MRI with magic-angle spinning of the q-vector, Front. Phys. 2 (2014) 11.
[12] F. Szczepankiewicz, S. Lasič, D. van Westen, P.C. Sundgren, E. Englund, C.-F. Westin, F. Ståhlberg, J. Lätt, D. Topgaard, M. Nilsson, Quantification of microscopic diffusion anisotropy disentangles effects of orientation dispersion from microstructure: applications in healthy volunteers and in brain tumors, NeuroImage 104 (1) (2015) 241–252.

[13] S. Hidalgo-Tobon, Theory of gradient coil design methods for magnetic resonance imaging, Concepts Magn. Reson. Part A 36 (4) (2010) 223–242.
[14] K. Setsompop, R. Kimmlingen, E. Eberlein, T. Witzel, J. Cohen-Adad, J.A. McNab, B. Keil, M.D. Tisdall, P. Hoecht, P. Dietz, S.F. Cauley, V. Tountcheva, V. Matschl, V.H. Lenz, K. Heberlein, A. Potthast, H. Thein, J. Van Horn, A. Toga, F. Schmitt, D. Lehne, B.R. Rosen, V. Wedeen, L.L. Wald, Pushing the limits of in vivo diffusion MRI for the Human Connectome Project, Neuroimage 80 (2013) 220–233.
[15] D. Topgaard, Isotropic diffusion weighting in PGSE NMR: numerical optimization of the q-MAS PGSE sequence, Microporous Mesoporous Mater. 178 (2013) 60–63.
[16] E.C. Wong, R.W. Cox, A.W. Song, Optimized isotropic diffusion weighting, Magn. Reson. Med. 34 (2) (1995) 139–143.
[17] C.-F. Westin, F. Szczepankiewicz, O. Pasternak, E. Özarslan, D. Topgaard, H. Knutsson, M. Nilsson, Measurement tensors in diffusion MRI: generalizing the concept of diffusion encoding, in: P. Golland, N. Hata, C. Barillot, J. Hornegger, R. Howe (Eds.), Medical Image Computing and Computer-Assisted Intervention MICCAI 2014, Lecture Notes in Computer Science, vol. 8675, Springer International Publishing, 2014, pp. 209–216.
[18] I. Drobnjak, G. Cruz, D.C. Alexander, Optimising oscillating waveform-shape for pore size sensitivity in diffusion-weighted MR, Microporous Mesoporous Mater. 178 (2013) 11–14.
[19] I. Drobnjak, B. Siow, D.C. Alexander, Optimizing gradient waveforms for microstructure sensitivity in diffusion-weighted MR, J. Magn. Reson. 206 (1) (2010) 41–51.
[20] E. Stejskal, J. Tanner, Spin diffusion measurements: spin echoes in the presence of a time-dependent field gradient, J. Chem. Phys. 42 (1) (1965) 288–292.
[21] D. Le Bihan, Looking into the functional architecture of the brain with diffusion MRI, Nat. Rev. Neurosci. 4 (6) (2003) 469–480.
[22] D.S. Tuch, T.G. Reese, M.R. Wiegell, N. Makris, J.W. Belliveau, V.J. Wedeen, High angular resolution diffusion imaging reveals intravoxel white matter fiber heterogeneity, Magn. Reson. Med. 48 (4) (2002) 577–582.
[23] Y. Qiao, P. Galvosas, P.T. Callaghan, Diffusion correlation NMR spectroscopic study of anisotropic diffusion of water in plant tissues, Biophys. J. 89 (4) (2005) 2899–2905.
[24] P.P. Mitra, Multiple wave-vector extensions of the NMR pulsed-field-gradient spin-echo diffusion measurement, Phys. Rev. B 51 (21) (1995) 15074.
[25] H. Knutsson, C.-F. Westin, Tensor metrics and charged containers for 3D Q-space sample distribution, in: Medical Image Computing and Computer-Assisted Intervention–MICCAI 2013, Springer, 2013, pp. 679–686.
[26] J. Veraart, J. Rajan, R.R. Peeters, A. Leemans, S. Sunaert, J. Sijbers, Comprehensive framework for accurate diffusion MRI parameter estimation, Magn. Reson. Med. 70 (4) (2013) 972–984.
[27] S. Klein, M. Staring, K. Murphy, M. Viergever, J.P. Pluim, Elastix: a toolbox for intensity-based medical image registration, IEEE Trans. Med. Imaging 29 (1) (2010) 196–205.
[28] M. Nilsson, F. Szczepankiewicz, D. van Westen, O. Hansson, Extrapolation-based references improve motion and eddy-current correction of high B-value DWI data: application in Parkinson's disease dementia, PLoS ONE 10 (11) (2015) e0141825, http://dx.doi.org/10.1371/journal.pone.0141825.
[29] P.J. Basser, D.K. Jones, Diffusion-tensor MRI: theory, experimental design and data analysis–a technical review, NMR Biomed. 15 (7–8) (2002) 456–467.
[30] S. Eriksson, S. Lasič, M. Nilsson, C.-F. Westin, D. Topgaard, NMR diffusion-encoding with axial symmetry and variable anisotropy: distinguishing between prolate and oblate microscopic diffusion tensors with unknown orientation distribution, J. Chem. Phys. 142 (10) (2015) 104201.
[31] J.P. Wansapura, S.K. Holland, R.S. Dunn, W.S. Ball, NMR relaxation times in the human brain at 3.0 tesla, J. Magn. Reson. Imaging 9 (4) (1999) 531–538.
[32] J. Nocedal, S.J. Wright, Numerical Optimization, second ed., Springer Verlag, 2006.
[33] D. Bernin, V. Koch, M. Nydén, D. Topgaard, Multi-scale characterization of lyotropic liquid crystals using 2H and diffusion MRI with spatial resolution in three dimensions, PloS one 9 (6) (2014) e98752.
[34] J.H. Jensen, J.A. Helpern, MRI quantification of non-Gaussian water diffusion by kurtosis analysis, NMR Biomed. 23 (7) (2010) 698–710.
[35] V.G. Kiselev, Diffusion MRI: Theory, Methods, and Applications, Oxford University Press, 2011. pp. 152–168. (Ch. The cumulant expansion: an overarching mathematical framework for understanding diffusion NMR).

Paper V

ARTICLE IN PRESS

YNIMG-13334; No. of pages: 11; 4C: 3, 6

NeuroImage xxx (2016) xxx–xxx

Contents lists available at ScienceDirect

NeuroImage

journal homepage: www.elsevier.com/locate/ynimg

The link between diffusion MRI and tumor heterogeneity: Mapping cell eccentricity and density by diffusional variance decomposition (DIVIDE)

Filip Szczepankiewicz [a,*], Danielle van Westen [b,c], Elisabet Englund [d], Carl-Fredrik Westin [e], Freddy Ståhlberg [a,b], Jimmy Lätt [c], Pia C. Sundgren [b], Markus Nilsson [b,f]

[a] Lund University, Department of Clinical Sciences Lund, Medical Radiation Physics, Lund, Sweden
[b] Lund University, Skåne University Hospital, Department of Clinical Sciences Lund, Diagnostic Radiology, Lund, Sweden
[c] Skåne University Hospital, Department of Imaging and Function, Lund, Sweden
[d] Lund University, Skåne University Hospital, Department of Clinical Sciences Lund, Division of Oncology and Pathology, Lund, Sweden
[e] Harvard Medical School, Brigham and Women's Hospital, Department of Radiology, Boston, MA, USA
[f] Lund University, Lund University Bioimaging Center, Lund, Sweden

ARTICLE INFO

Article history:
Received 29 April 2016
Accepted 16 July 2016
Available online xxxx

Keywords:
Tumor heterogeneity
Microscopic anisotropy
Diffusional variance
Diffusional kurtosis
Diffusion tensor distribution
Quantitative microscopy

ABSTRACT

The structural heterogeneity of tumor tissue can be probed by diffusion MRI (dMRI) in terms of the variance of apparent diffusivities within a voxel. However, the link between the diffusional variance and the tissue heterogeneity is not well-established. To investigate this link we test the hypothesis that diffusional variance, caused by microscopic anisotropy and isotropic heterogeneity, is associated with variable cell eccentricity and cell density in brain tumors. We performed dMRI using a novel encoding scheme for diffusional variance decomposition (DIVIDE) in 7 meningiomas and 8 gliomas prior to surgery. The diffusional variance was quantified from dMRI in terms of the total mean kurtosis (MK_T), and DIVIDE was used to decompose MK_T into components caused by microscopic anisotropy (MK_A) and isotropic heterogeneity (MK_I). Diffusion anisotropy was evaluated in terms of the fractional anisotropy (FA) and microscopic fractional anisotropy (μFA). Quantitative microscopy was performed on the excised tumor tissue, where structural anisotropy and cell density were quantified by structure tensor analysis and cell nuclei segmentation, respectively. In order to validate the DIVIDE parameters they were correlated to the corresponding parameters derived from microscopy. We found an excellent agreement between the DIVIDE parameters and corresponding microscopy parameters; MK_A correlated with cell eccentricity ($r = 0.95$, $p < 10^{-7}$) and MK_I with the cell density variance ($r = 0.83$, $p < 10^{-3}$). The diffusion anisotropy correlated with structure tensor anisotropy on the voxel-scale (FA, $r = 0.80$, $p < 10^{-3}$) and microscopic scale (μFA, $r = 0.93$, $p < 10^{-6}$). A multiple regression analysis showed that the conventional MK_T parameter reflects both variable cell eccentricity and cell density, and therefore lacks specificity in terms of microstructure characteristics. However, specificity was obtained by decomposing the two contributions; MK_A was associated only to cell eccentricity, and MK_I only to cell density variance. The variance in meningiomas was caused primarily by microscopic anisotropy (mean ± s.d.) $MK_A = 1.11 \pm 0.33$ vs $MK_I = 0.44 \pm 0.20$ ($p < 10^{-3}$), whereas in the gliomas, it was mostly caused by isotropic heterogeneity $MK_I = 0.57 \pm 0.30$ vs $MK_A = 0.26 \pm 0.11$ ($p < 0.05$). In conclusion, DIVIDE allows non-invasive mapping of parameters that reflect variable cell eccentricity and density. These results constitute convincing evidence that a link exists between specific aspects of tissue heterogeneity and parameters from dMRI. Decomposing effects of microscopic anisotropy and isotropic heterogeneity facilitates an improved interpretation of tumor heterogeneity as well as diffusion anisotropy on both the microscopic and macroscopic scale.

Introduction

Tumors exhibit structural heterogeneity on the macroscopic and microscopic scale. The cell morphology and cytoarchitecture is determined by the tumor origin, and depends on factors such as local oxygen gradients, nutritional and growth factors, metabolites, genetically divergent clones, and interactions with other tissues (Marusyk and Polyak, 2010). Although histopathological examination of the excised tissue is

* Corresponding author at: Lund University, Dept. of Clinical Sciences, Medical Radiation Physics, Lund, Barnvägen 2A, 22185, Lund, Sweden.
E-mail addresses: filip.szczepankiewicz@med.lu.se, filip.szczepankiewicz@gmail.com (F. Szczepankiewicz).

http://dx.doi.org/10.1016/j.neuroimage.2016.07.038
1053-8119/

the gold standard for the clinical diagnosis, valuable information on the tissue microstructure and its heterogeneity can be probed non-invasively by diffusion MRI (dMRI) (Le Bihan, 2013; Padhani et al., 2009). For example, gross tumor heterogeneity can be estimated from the distribution of apparent diffusion coefficients (ADC) across the whole tumor (Ryu et al., 2014; Wang et al., 2012), where the ADC in each imaging voxel reflects characteristics such as the average tumor cellularity (Chenevert et al., 2000; Padhani et al., 2009), extent of infiltration (Sternberg et al., 2014), and treatment response (Moffat et al., 2005). However, the ADC is an average metric that does not capture heterogeneity within individual voxels. Hence, the ADC may be equal in homogeneous tissue and in tissue with densely packed cells interspersed with loose necrotic regions. In previous studies, heterogeneity has been probed by assigning a distribution of apparent diffusivities to each voxel and relating the variance of the distribution to the tissue heterogeneity. For example, diffusional kurtosis imaging (DKI) (Jensen et al., 2005) probes heterogeneity in terms of a normalized variance metric called the diffusional kurtosis. The kurtosis has been used to differentiate low and high grade gliomas, where increased heterogeneity was related to higher malignancy (Raab et al., 2010; Tietze et al., 2015; Van Cauter et al., 2012). However, the interpretation of diffusional variance parameters, such as the mean kurtosis, is challenging, and its link to relevant features of the underlying microstructure remain unclear (Jespersen et al., 2010; Le Bihan, 2013; Maier et al., 2010; Tietze et al., 2015; Wu and Cheung, 2010).

We argue that the link between dMRI parameters and tissue heterogeneity can be better understood by considering two separate components of the diffusional variance. The anisotropic variance component reflects the diffusion anisotropy on the microscopic scale, e.g., due to eccentric cells and cell structures (microscopic anisotropy), whereas the isotropic variance component reflects heterogeneous isotropic diffusivity, e.g., due to variable cell density or tissue mixtures (isotropic heterogeneity) (Szczepankiewicz et al., 2015; Westin et al., 2016). Although these two sources of diffusional variance originate from markedly different microstructural features, they cannot be separated by techniques based on conventional single diffusion encoding (SDE), i.e., encoding along a single direction for each signal acquisition, because such encoding conflates the effects of microscopic anisotropy and isotropic heterogeneity (Mitra, 1995). Instead, these features can be separated by performing experiments with varying 'shapes' of the diffusion encoding tensor (Westin et al., 2016). In this work, we exploit the contrast between conventional and isotropic diffusion encoding to separate the effects of microscopic anisotropy and isotropic heterogeneity, as recently proposed by Lasič et al. (2014). The conventional and isotropic encoding will be denoted 'linear' and 'spherical' tensor encoding (LTE and STE) to comply with the nomenclature proposed by Westin et al. (2016), and we will refer to methods aimed at separating the two sources of variance as 'diffusional variance decomposition' (DIVIDE).

Microscopic diffusion anisotropy has been previously estimated by employing double diffusion encoding (DDE) (Callaghan and Komlosh, 2002; Jensen et al., 2014; Jespersen et al., 2013; Lawrenz et al., 2010; Ozarslan and Basser, 2008; Shemesh et al., 2010), however, the isotropic component has so far only been reported in a limited number of studies (Lasič et al., 2014; Szczepankiewicz et al., 2015; Westin et al., 2016). The link between dMRI and the underlying tissue microstructure has been studied by comparing several dMRI parameters to corresponding features observed by qualitative and quantitative microscopy. Human studies are scarce due to the invasive nature of resection and biopsies but initial studies have shown a relation between diffusion anisotropy and tissue microstructure in brain (Ronen et al., 2014), tumor (Szczepankiewicz et al., 2015) and prostate tissue (Bourne et al., 2012). In animals, the investigated features range across structure eccentricity and orientation (Budde and Frank, 2012; Khan et al., 2015; Schilling et al., 2016), neurodegeneration (Jelescu et al., 2016; Jespersen et al., 2010; Kamagata et al., 2016), and axonal diameter (Barazany et al., 2009). However, the link between microscopic tissue heterogeneity and diffusional variance has not yet been studied.

The purpose of this study was therefore to investigate the link between diffusional variance and tissue heterogeneity in tumors. We use DIVIDE to assess the presence of microscopic anisotropy and isotropic heterogeneity, and we correlate these measures to cell eccentricity and density derived from quantitative microscopy. The study was performed in meningiomas and gliomas because these tumors exhibit a wide range of microstructural features that contribute to relevant aspects of the diffusional variance (Szczepankiewicz et al., 2015). We observed a strong correlation between microscopic anisotropy and cell eccentricity, as well as between isotropic heterogeneity and cell density variance.

Theory

The microscopic anisotropy and isotropic heterogeneity of tissue can be quantified by considering that each imaging voxel contains an ensemble of microenvironments. We model the diffusion within each microenvironment by a microscopic diffusion tensor, and the ensemble is therefore modelled by a distribution of microscopic diffusion tensors ($\mathbf{D}$) (Jespersen et al., 2013; Lasič et al., 2014; Topgaard, 2016; Westin et al., 2016). This representation assumes Gaussian diffusion in each microenvironment, which is accurate for moderate signal attenuation, i.e., for encoding strengths where at least 10% of the initial signal remains, for diffusion times that are long relative to the size of the restrictions (Topgaard and Söderman, 2003). Averaging across the distribution of microscopic tensors in a voxel yields a single voxel-scale tensor, $\langle\mathbf{D}\rangle$, equivalent to the tensor derived from diffusion tensor imaging (DTI) (Basser et al., 1994), where the averaging operation is denoted by $\langle\cdot\rangle$. Although the voxel scale diffusion tensor is useful in a plethora of applications (Alexander et al., 2007), it does not retain information on the heterogeneity of the underlying distribution of diffusion tensors. To retain such information, the distribution of diffusion tensors can be parameterized in terms of its mean diffusivity and two components of diffusional variance. The mean diffusivity (MD) is defined from the distribution of isotropic diffusivities ($D_\mathrm{I} = \mathrm{E}_\Lambda[\mathbf{D}]$) averaged across all microenvironments in a voxel, according to

$$\mathrm{MD} = \langle \mathrm{D_I} \rangle = \langle \mathrm{E}_\Lambda[\mathbf{D}] \rangle = \mathrm{E}_\Lambda[\langle \mathbf{D} \rangle], \tag{1}$$

where the average over tensor eigenvalues is denoted $\mathrm{E}_\Lambda[\cdot]$. We note that MD in Eq. 1 is not affected by the order in which the averaging is applied, i.e., across eigenvalues or microenvironment tensors first. Unlike DKI, where specific sources of diffusional variance are not considered (Jensen et al., 2005), diffusional variance decomposition is used to separate the diffusional variance into two components: the anisotropic and isotropic variance (V_A and V_I), where the total variance (V_T) is simply the sum of its components ($V_\mathrm{T} = V_\mathrm{I} + V_\mathrm{A}$) (Lasič et al., 2014; Szczepankiewicz et al., 2015). The isotropic heterogeneity is related to the isotropic variance, according to

$$V_\mathrm{I} = \mathrm{V}[D_\mathrm{I}] = \mathrm{V}[\mathrm{E}_\Lambda[\mathbf{D}]], \tag{2}$$

where $\mathrm{V}[\cdot]$ is the variance operator. We note that V_I is zero for tissues where all microenvironments exhibit identical isotropic diffusivity. The value of V_I for the voxel-scale tensor, $\langle\mathbf{D}\rangle$, is zero by definition since the isotropic diffusion of $\langle\mathbf{D}\rangle$ is defined by a scalar MD, and will therefore not be considered beyond this point. The anisotropic variance is related to the microscopic anisotropy, according to

$$V_\mathrm{A} = \frac{2}{5}\langle \mathrm{V}_\Lambda, [\mathbf{D}] \rangle, \tag{3}$$

where the factor 2/5 relates the eigenvalue population variance, denoted by the operator $\mathrm{V}_\Lambda[\cdot]$, to the variance of the distribution of diffusivities in the powder sample (Topgaard, 2016). We note that V_A is zero

Please cite this article as: Szczepankiewicz, F., et al., The link between diffusion MRI and tumor heterogeneity: Mapping cell eccentricity and density by diffusional variance decompositio..., NeuroImage (2016), http://dx.doi.org/10.1016/j.neuroimage.2016.07.038

for tissue that comprises only isotropic microenvironments, and that the voxel-scale counterpart is closely related to the voxel-scale anisotropy, as described below.

An inherent limitation of conventional dMRI, performed with so-called single diffusion encoding, here referred to as linear tensor encoding, is that it cannot be used to distinguish the two sources of variance (Mitra, 1995). To disentangle the two sources of variance, DIVIDE employs diffusion encoding tensors (**B**) with multiple shapes, namely linear and spherical encoding tensors, i.e., LTE and STE. Linear tensor encoding yields a 'stick' shape (**B** has one non-zero eigenvalue), for which the signal is sensitive to the total variance since both isotropic heterogeneity and microscopic anisotropy contribute to the variance of the underlying distribution of diffusivities. Spherical tensor encoding yields a 'sphere' shape (**B** has three equal eigenvalues), which removes the effects of microscopic anisotropy making the signal sensitive only to the variance due to isotropic heterogeneity (Eriksson et al., 2013; Lasič et al., 2014; Szczepankiewicz et al., 2015). The benefit of introducing multiple tensor shapes is visualized in Fig. 1, where three radically different microstructures are indistinguishable by LTE alone, but can be separated when both STE and LTE are employed. Notably, DIVIDE is compatible with arbitrary tensor shapes, enabled by techniques such as free gradient waveforms modulation or double diffusion encoding, as long as more than one shape is employed (Eriksson et al., 2015; Topgaard, 2016; Westin et al., 2016). In summary, LTE probes V_T, whereas STE probes V_I, as exemplified in Fig. 1, and V_A is recovered by simply subtracting the isotropic variance from the total variance ($V_A = V_T - V_I$) (Lasič et al., 2014; Szczepankiewicz et al., 2015).

We emphasize that the term 'diffusional variance' refers to the same phenomenon as intended by 'diffusional kurtosis' (from DKI), and in keeping with the formalism presented by Jensen et al. (2005), we normalize and scale the diffusional variance, according to

$$\mathrm{MK_x} = 3 \cdot \frac{V_\mathrm{x}}{\mathrm{MD}^2}, \tag{4}$$

where the subscript 'x' denotes the specific component that it reflects. For example, $\mathrm{MK_I}$ denotes the normalized variance due to isotropic heterogeneity.

The macroscopic and microscopic fractional anisotropy, i.e., FA (Basser et al., 1994; Basser and Pierpaoli, 1996) and μFA (Lasič et al., 2014; Westin et al., 2016), can also be written in terms of the eigenvalue expectance and variance, according to

$$\mathrm{FA}^2 = \frac{3}{2} \cdot \frac{\mathrm{V_\Lambda}[\langle \mathbf{D} \rangle]}{\mathrm{E_\Lambda}[\langle \mathbf{D} \rangle]^2 + \mathrm{V_\Lambda}[\langle \mathbf{D} \rangle]}, \tag{5}$$

$$\mu\mathrm{FA}^2 = \frac{3}{2} \cdot \frac{\langle \mathrm{V_\Lambda}[\mathbf{D}] \rangle}{\left\langle \mathrm{E_\Lambda}[\mathbf{D}]^2 \right\rangle + \langle \mathrm{V_\Lambda}[\mathbf{D}] \rangle}. \tag{6}$$

The distinction between macroscopic and microscopic anisotropy is defined by the stage at which the averaging operation is applied. Averaging over tensors first, as denoted by $\langle \mathbf{D} \rangle$, probes the macroscopic anisotropy, whereas averaging over variance and expectancy first, as denoted by $\langle \mathrm{V_\Lambda}[\mathbf{D}] \rangle$ and $\langle \mathrm{E_\Lambda}[\mathbf{D}]^2 \rangle$, probes the microscopic anisotropy. Note that the order of averaging across eigenvalues is no longer arbitrary since the expected value is squared, i.e., $\mathrm{E_\Lambda}[\langle \mathbf{D} \rangle]^2 \neq \langle \mathrm{E_\Lambda}[\mathbf{D}]^2 \rangle$ unless $V_I = 0$, since (Westin et al., 2016)

$$V_\mathrm{I} = \left\langle \mathrm{E_\Lambda}[\mathbf{D}]^2 \right\rangle - \mathrm{E_\Lambda}[\langle \mathbf{D} \rangle]^2. \tag{7}$$

The impact of averaging over microenvironment tensors is determined by the size of the averaging volume, i.e., the voxel size, where larger voxels tend to reduce the macroscopic anisotropy in tissues that are not perfectly coherent (De Santis et al., 2013; Szczepankiewicz et al., 2015; Vos et al., 2011). Assuming that a voxel contains only one type of tissue, i.e., that the microenvironments differ only in orientation, the μFA is independent of the voxel size and may be interpreted as the FA that would be observed if the tissue exhibited complete orientation coherence, i.e., that all anisotropic structures were parallel (Jespersen et al., 2013; Lasič et al., 2014; Szczepankiewicz et al., 2015).

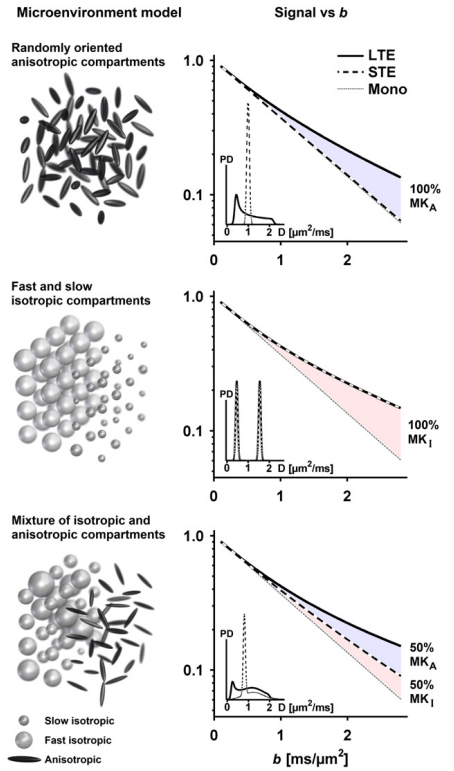

Fig. 1. Simulated tissue models that contain variable levels of microscopic anisotropy and isotropic heterogeneity. The first model contains randomly oriented anisotropic microenvironments, designed to mimic eccentric and disordered cells. The second model contains microenvironments with slow and fast isotropic diffusion, designed to mimic a mixture of high and low cell density. The third model is a mixture of the previous two. The right column shows the signal vs *b* curves in each case, where linear and spherical tensor encoding (LTE and STE) are shown as solid and broken lines, respectively. The dotted line shows mono-exponential signal decay for visual reference. The light blue and red fields accentuate the effect of microscopic anisotropy and isotropic heterogeneity, respectively. The inset plots show the distributions of apparent diffusion coefficients when using LTE (solid line) and STE (broken line), where the y-axis is the unitless probability density (PD). All three models have MD = 1.0 μm²/ms, and $\mathrm{MK_T} = 0.6$, and would thus be indistinguishable with LTE, i.e., conventional diffusion encoding. By adding isotropic encoding the three environments can be distinguished and the measured diffusional variance can be attributed to the appropriate microstructural feature.

Materials and methods

Patient population

Patients were recruited and scanned between October 2013 and October 2014. The study was approved by the Regional Ethical Review

Please cite this article as: Szczepankiewicz, F., et al., The link between diffusion MRI and tumor heterogeneity: Mapping cell eccentricity and density by diffusional variance decompositio..., NeuroImage (2016), http://dx.doi.org/10.1016/j.neuroimage.2016.07.038

Board at Lund University, and written consent was obtained from all patients prior to participation. Patients with suspected meningioma or glioma based on radiological findings, who were scheduled for surgical treatment, were considered for inclusion. The sample size was determined by the number of participating patients who were histologically confirmed to have a meningioma or glioma. In total, 14 patients were included. One patient had both a meningioma and a glioma and was therefore included in both groups. The meningioma group comprised 7 patients (6 women, 1 man; mean age ± s.d., 66 ± 11 years), and the glioma group 8 patients (5 women, 3 men; 54 ± 14 years). One patient from each group was analyzed and presented in a preliminary study (Szczepankiewicz et al., 2015), and several were also included in an independent study on water exchange (Lampinen et al., 2016). The tumors were graded according to the World Health Organization guidelines (Louis et al., 2007), resulting in 6 grade I, and 1 grade II meningiomas; and 1 grade II, 3 grade III, and 4 grade IV gliomas. Of the meningiomas, four were fibroblastic, two were transitional, and one was atypical (Riemenschneider et al., 2006). Due to the small number of subjects, associations between parameters and tumor grade were not investigated.

MRI data acquisition and analysis

MRI data was acquired using a Philips Achieva 3T system, equipped with 80 mT/m gradients with a maximum slew rate of 100 mT/m/ms, and an eight-channel receiver head-coil. The dMRI sequence was identical to that reported by Szczepankiewicz et al. (2015). Briefly, we used linear and spherical tensor encoding at ten equidistant b-values between 100 and 2800 s/mm^2. The LTE was performed in 15 directions, distributed on the half-sphere using electrostatic repulsion (Jones et al., 1999). The STE was achieved by magic angle spinning of the q-vector (qMAS) (Eriksson et al., 2013), and was repeated 15 times per b-value without rotation since it is assumed to be independent of rotation. The sequence had an echo time of 160 ms where the diffusion encoding lasted 62.5 ms before and after the refocusing pulse, and were separated by approximately 9 ms. The b-value was adjusted by modulating the gradient amplitude. We note that significantly shorter encoding and echo times are possible by using optimized waveforms, rather than repeating the qMAS waveform before and after the refocusing pulse (Sjölund et al., 2015). All images were acquired using a repetition time of 2000 ms, 96 × 96 acquisition matrix, spatial resolution of 3 × 3 × 3 mm^3, partial Fourier factor of 0.8, and a SENSE factor of 2. The image volume contained five axial slices centered on the tumor. In the patient with both meningioma and glioma, the slices were placed slightly off the axial plane to include both tumors. Total scan time for LTE and STE was approximately 10 min. All data was corrected for motion and eddy-currents in ElastiX (Klein et al., 2010) using extrapolated reference images (Nilsson et al., 2015). Whole-brain morphological T1-weighted, and T2-weighted fluid-attenuated inversion recovery (FLAIR) sequences were acquired, as well as gadolinium-enhanced T1-weighted images as part of clinical routine.

Diffusional variance decomposition was used to estimate MD, V_T, V_A and V_I (Lasič et al., 2014). In this method the inverse Laplace transform of the gamma distribution function (Röding et al., 2012) is fitted to the powder average of the diffusion weighted signal (S), according to

$$S(b) = S_0\left(1 + b\frac{V}{\mathrm{MD}}\right)^{-\frac{\mathrm{MD}^2}{V}}, \tag{8}$$

where S_0 is the signal at $b = 0$ s/mm^2, and V is the observed variance. The powder average is used to remove the effects of orientation coherence, and is calculated by averaging the signal across all diffusion directions at each b-value (Edén, 2003; Lasič et al., 2014; Szczepankiewicz et al., 2016b). As described in the theory, the observed variance in Eq. 8 depends on the shape of the encoding tensor, according to

$$V = V_\mathrm{I} + f \cdot V_\mathrm{A}\,, \tag{9}$$

where f is the encoding shape factor; for linear and spherical tensor encoding, $f = 1$ and 0, respectively (Topgaard, 2016). Other encoding shapes can also be used, for example, DDE that renders axially symmetric prolate encoding tensors, i.e., planar tensor encoding (PTE), where $f = 1/4$ (Topgaard, 2016). The fitting was weighted to suppress the effect of signal attenuated below 10% of its initial value in order to alleviate effects of non-Gaussian phase distribution (Topgaard and Söderman, 2003) and the noise floor (Gudbjartsson and Patz, 1995). The fitting software is available online at https://github.com/markus-nilsson/md-dmri. The normalized variance was calculated according to Eq. 4, and we note that $\mathrm{MK_T}$ and the mean kurtosis, derived from conventional DKI, are representations of the same phenomenon although their numerical values are expected to differ due to differences in signal parameterization (Lätt et al., 2007). To elucidate the connection between diffusional anisotropy on the voxel- and microscopic scale, we also interpret the diffusional variance in terms of the fractional anisotropy, i.e., FA and μFA, respectively. The FA was calculated from Eq. 5, where the voxel scale tensor $\langle \mathbf{D} \rangle$ was estimated through conventional DTI analysis (Basser et al., 1994) based on LTE at $b \leq 1000$ s/mm^2. The μFA was calculated from Eq. 6 by substituting the eigenvalue mean and variance for the expressions in Eqs. 1, 3 and 7, according to

$$\mu\mathrm{FA} = \sqrt{\frac{3}{2}}\left(1 + \frac{\mathrm{MD}^2 + V_\mathrm{I}}{\frac{5}{2}V_\mathrm{A}}\right)^{-\frac{1}{2}}. \tag{10}$$

Note that the μFA in Eq. 10 is defined according to Westin et al. (2016), and differs slightly from the definition used by Lasič et al. (2014) and Szczepankiewicz et al. (2015).

The solid part of each tumor was manually defined in a region of interest (ROI) by an experienced neuroradiologist using anatomical, contrast-enhanced, and diffusion-weighted images for guidance. The operator was instructed to avoid including edema, confluent necroses, corticospinal fluid, and brain tissue that appeared healthy. The parameter mean across all included voxels was calculated for each tumor.

Histological preparation and quantitative microscopy

All tumors were resected 1 day after the MRI procedure and the preparation of tissue was performed according to clinical routine. Each tumor was fixed in 4% buffered formaldehyde solution and embedded in paraffin. The tissue specimens were sectioned at 4 μm through the bulk of the tumor, and stained with hematoxylin and eosin (H&E). Automated microscopy was performed on an Aperio ScanScope AT Turbo. All samples were scanned at ×20 magnification at a spatial resolution of 1.0 μm/pixel and a complete image was stitched together by vendor software. Tumor specimens ranged in size between 8 and 28 mm across, resulting in at most 780 megapixels per image.

The presence of anisotropic tissue structures was quantified with structure tensor analysis of histological images (Bigun, 1987; Budde and Annese, 2013; Budde and Frank, 2012; Khan et al., 2015). Briefly, the two-dimensional structure tensors ($\mathbf{S}$) were calculated for each pixel from the spatial derivative of the image in a given neighborhood defined by the size of a discrete Gaussian derivative filter (Bigun, 1987). We assume that the structure tensors reflect the local diffusion anisotropy and orientation, in accordance with similar studies of neural tissue (Budde and Frank, 2012; Khan et al., 2015). Thus, analogues to $\mathrm{MK_A}$, μFA and FA can be calculated from the structure tensors. The standard deviation of the Gaussian derivative filter was set to 1 μm. To visualize coherent structures spanning the distance of diffusing water

Please cite this article as: Szczepankiewicz, F., et al., The link between diffusion MRI and tumor heterogeneity: Mapping cell eccentricity and density by diffusional variance decompositio..., NeuroImage (2016), http://dx.doi.org/10.1016/j.neuroimage.2016.07.038

during one imaging experiment, the structure tensor field was convolved with another Gaussian kernel with a standard deviation of 20 μm. This is adjusted to approximately match the root mean square displacement of water molecules in the tissue assuming a diffusivity of 2 μm^2/ms and diffusion time of 100 ms. The normalized variance of structure tensor eigenvalues (H_A) was calculated from Eq. 3 and Eq. 4, where we hypothesize that H_A across an appropriate length scale is proportional to MK_A, according to

$$H_A = 3 \cdot \frac{\langle V_\lambda[\mathbf{S}]\rangle}{\langle E_\lambda[\mathbf{S}]\rangle^2} \propto MK_A. \quad (11)$$

The structure tensor analogues to FA and μFA (FA_{ST} and μFA_{ST}) were calculated by inserting **S** into Eq. 5 and Eq. 6, respectively, where the factor 3/2 was replaced by 2 to scale the parameters to the interval 0 to 1. We note that the relation between parameters derived from 2D and 3D tensors are not straight forward (see Kingsley (2006) for a comprehensive review), however, we may assume that **D** and **S** are both sensitive to tissue anisotropy and should therefore be correlated (Budde and Frank, 2012). Note that in contrast to dMRI, we can access the structure tensor field at the resolution of a single microenvironment, and must therefore construct the macroscopic structure tensor **S** by averaging the tensor field across an appropriate area in order to allow comparison with **D** and its parameters. Unless stated otherwise, all structure tensor anisotropy parameters were calculated from an averaged structure tensor field with spatial resolution 3 × 3 mm^2, to mimic the resolution of the dMRI data.

The analogue to MK_I was calculated by assuming that the isotropic diffusivity of a microenvironment is related to the local cell density. This assumption is based on previous observations where cell density has been negatively correlated to the apparent diffusivity (Chenevert et al., 2000; Kinoshita et al., 2008; Padhani et al., 2009; Sugahara et al., 1999). Thus, we hypothesize that the distribution of isotropic diffusivities within a voxel is determined by the cell density distribution (ρ_c), and that the normalized variance of cell densities from microscopy (H_I) across an appropriate length scale, is proportional to MK_I, according to

$$H_I = 3 \cdot \frac{V[\rho_c]}{\langle \rho_c \rangle^2} \propto MK_I. \quad (12)$$

The local density of cells was calculated as the number of cell nuclei per unit area. The cell nuclei were automatically segmented and counted in tissue sub-sections of 300 × 300 μm^2, as described by Al-Kofahi et al. (2010). The detection of red blood cells was suppressed by using only the red channel of the original H&E stained image, and the detection of psammoma grains was suppressed by removing features with areas above 900 μm^2. Clustered nuclei were separated using the watershed algorithm (Malpica et al., 1997). Maps of H_I were calculated from the distribution of cell densities across 10 × 10 subsections, which yielded a spatial resolution of 3 × 3 mm^2.

The mean parameter values in each tumor were calculated across all tumor tissue in each section. To avoid the inclusion of empty space, and artefacts due to edge effects, hemorrhage, knife scoring, and folding, the parameter maps were masked based on manually adjusted image intensity thresholding.

Statistical analysis

The associations between parameters derived from dMRI and their corresponding variants derived from microscopy, i.e., MK_A vs H_A, MK_I vs H_I, FA vs FA_{ST}, and μFA vs μFA_{ST}, were estimated using linear correlation. Pearson's correlation coefficient (r) was used to describe the strength of the correlation and the threshold for significance was set to $\alpha = 0.05$. For simplicity, the measurement uncertainty in the independent variables (from microscopy) was assumed to be negligible. We note that MK_A and μFA are closely related and are expected to render similar correlations. Nevertheless, the μFA is presented in addition to the MK_A to provide a straightforward microscopic analogue to the FA. A multiple linear regression analysis was used to investigate which histological features were significant predictors for the outcome of the variance detected through dMRI. The analysis was performed separately for MK_T, MK_A and MK_I where the regression model was defined according to $MK_x = m + \beta_A H_A + \beta_I H_I$. The threshold for considering H_A and/or H_I to be significant predictors was set to $\alpha = 0.05$. The intercept, m, was not interpreted.

The diffusional variance, and its components, were explored between and within tumor groups. The dominant source of variance was established by comparing MK_A and MK_I within each group. The variance parameter that best distinguished between tumor types was established by estimating the 95% confidence interval of the absolute effect ($CI_{95\%}$), and Cohen's d (d, normalized by the pooled standard deviation). Thus, a total of five t-tests were performed (two tails, independent samples, not assuming equal variance, significance threshold $\alpha = 0.05$). The fact that one patient appeared in both tumor groups was assumed to have a negligible effect on the statistical analysis. Thus, samples taken from this patient were considered to be independent throughout the analysis. All statistical analysis was performed in MATLAB (R2013b, The Mathworks, Natick, MA).

Results

We performed dMRI in vivo in 7 meningiomas and 8 gliomas, and DIVIDE was used to probe the microscopic anisotropy and isotropic heterogeneity of the tumor tissue. Fig. 2 shows DIVIDE parameter maps (MK_T, MK_A and MK_I) in a meningioma and a glioma. Both tumors exhibited elevated MK_T, which indicated that both tumors are heterogeneous, although the specific source of heterogeneity cannot be established from MK_T. By contrast, the source of tumor heterogeneity was distinguishable based on the MK_A and MK_I, where the diffusional variance in the meningioma was dominated by the anisotropic component, and primarily due to isotropic heterogeneity in the glioma. The difference between tumors was also clearly discernible from the signal vs b curves in the two tumor ROIs. In the meningioma, the signal from linear and spherical encoding diverges, which indicates microscopic anisotropy (compare to first model in Fig. 1); whereas both types of encoding exhibit similar divergence from mono-exponential decay in the glioma, which indicates isotropic heterogeneity (compare to second model in Fig. 1). Overall, the DIVIDE parameters showed that the meningiomas comprised a microstructure that yielded prominent microscopic diffusion anisotropy, whereas the gliomas did not. The estimated mean [min, max] signal-to-noise ratio of the STE signal across all tumor ROIs was 39 [19, 75] at $b = 0$ s/mm^2, and 5.5 [3.0, 10] at the highest b-value where at least 10% signal remained, indicating that the data quality was sufficient for the analysis (Gudbjartsson and Patz, 1995). Furthermore, using 15 diffusion encoding directions was sufficient to render a rotationally invariant powder average since all tumors exhibited a relatively low voxel scale anisotropy (all tumors had a mean FA below 0.5) (Szczepankiewicz et al., 2016b).

All tumors were resected, and quantitative microscopy was used to measure the cell eccentricity and cell density in sections through the bulk of the tumor tissue. Fig. 3 shows quantitative microscopy parameter maps derived from structure tensor analysis and cell nuclei segmentation at the nominal resolution (1 × 1 μm^2) in a meningioma and a glioma. Fig. 3 also presents the structure tensors, orientation field, and cell nuclei outlines in magnified subsections of each tumor. Overall, the meningiomas comprised prominently eccentric cells and cell structures, while gliomas contained few, or no, such structures. The meningiomas exhibited variable anisotropy within and between tumors, where patches of coherent fascicles were mixed with highly disordered tissue (Fig. 3). By contrast, the gliomas exhibited low and relatively homogeneous structural anisotropy throughout the section, as well as regions

Please cite this article as: Szczepankiewicz, F., et al., The link between diffusion MRI and tumor heterogeneity: Mapping cell eccentricity and density by diffusional variance decompositio..., NeuroImage (2016), http://dx.doi.org/10.1016/j.neuroimage.2016.07.038

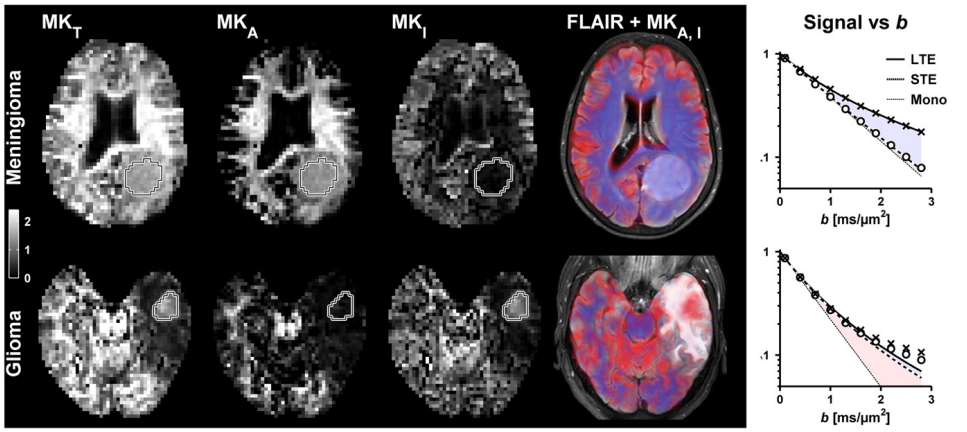

Fig. 2. Examples of DIVIDE parameter maps in a meningioma and a glioma. MK_T is elevated in both tumors but cannot distinguish between the isotropic and anisotropic components. By contrast, MK_A and MK_I are markedly different in the two tumors. These parameter maps were superimposed on a high resolution morphological image (FLAIR + $MK_{A,I}$), where MK_A and MK_I are coded in blue and red, respectively. The meningioma exhibited high MK_A and low MK_I (blue), whereas the opposite is true in the glioma (red). In the white matter the diffusional variance is mostly due to microscopic anisotropy, whereas the isotropic heterogeneity dominates in gray matter and voxels that contain both tissue and cerebrospinal fluid. The powder averaged signal vs *b* curves are shown in the rightmost column. The white-black outline shows the ROIs used for analysis. Note that the signal characteristics in the meningioma and glioma resemble the first and second models in Fig. 1, respectively.

of heterogeneous cell density, especially in necrotic regions (Fig. 3). The spatial heterogeneity of cell eccentricity and density within each tumor in Fig. 3 visualizes the need to analyze large tissue sections because small sub-sections may inadvertently sample regions of tissue that are not representative, leading to a large sampling error.

The parameters derived from dMRI were validated by correlating them to corresponding parameters from quantitative microscopy. All tests showed strong positive correlations, which indicates that the two components of diffusional variance indeed reflect specific features of the underlying microstructure. Fig. 4 shows scatterplots of the variance parameters where the strength of the correlation was $r = 0.95$ for MK_A ($p < 10^{-7}$) and $r = 0.83$ for MK_I ($p < 10^{-3}$). Similarly, Fig. 5 shows that both voxel-scale and microscopic parameters were correlated, where $r = 0.80$ for FA ($p < 10^{-3}$) and $r = 0.93$ for μFA ($p < 10^{-6}$). Furthermore, the regression analysis showed that both H_A and H_I were significant predictors for MK_T, where the estimated coefficients ± s.d. were $\beta_A =$

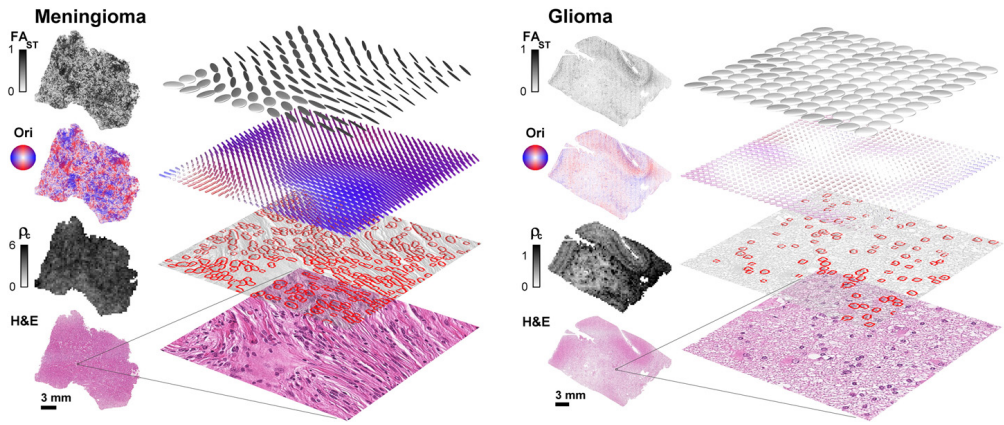

Fig. 3. Quantitative microscopy in a meningioma and a glioma. The full-section images show the structure tensor fractional anisotropy (FA_{ST}), orientation (Ori), cell density (ρ_c, $10^3/mm^2$), and the hematoxylin and eosin stain (H&E) in a meningioma and a glioma. Along with each map we visualize the tensor field, orientation field, cell outlines and H&E stain in a magnified sub-section ($300 \times 300\ \mu m^2$) of the tissue. The meningioma is grade I, fibroblastic subtype, with abundant anisotropic structures organized in large fascicles that render anisotropic diffusion. It has a high cell density and low density variance, i.e., the cell density map is uniform. The glioma is grade IV glioblastoma with few structures that are anisotropic, however, weakly coherent regions are observed in the normal-appearing cortex. The tumor tissue has a relatively low cell density and comprises large necrotic regions which exhibit highly variable cell density, i.e., the cell density map is non-uniform. The glioma is surrounded by cortical gray matter wherein the cortical layers can be partially distinguished in the cell-density map. Note that the anisotropy and orientation maps are calculated at $1 \times 1\ \mu m^2$ resolution, whereas the cell density is calculated at $300 \times 300\ \mu m^2$. Furthermore, the orientation map and orientation field are color coded to indicate local direction and anisotropy (color shows direction, saturation shows local FA_{ST}).

Please cite this article as: Szczepankiewicz, F., et al., The link between diffusion MRI and tumor heterogeneity: Mapping cell eccentricity and density by diffusional variance decompositio..., NeuroImage (2016), http://dx.doi.org/10.1016/j.neuroimage.2016.07.038

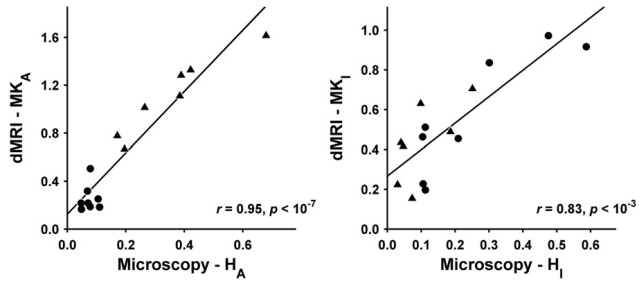

Fig. 4. Correlation between variance parameters derived from dMRI and microscopy in meningiomas (triangles) and gliomas (circles). The anisotropic and isotropic components of diffusional variance (MK_A and MK_I) exhibit strong positive correlations to structural anisotropy and cell density variance (H_A and H_I), respectively. Note that H_A and H_I are derived from structure tensor analysis and cell nuclei segmentation, respectively.

2.7 ± 0.4 ($p < 10^{-4}$) and $\beta_I = 1.4 \pm 0.4$ ($p < 10^{-2}$), respectively. This supports the notion that MK_T is not specific to either type of heterogeneity because it composes them into a single value. A more specific link between parameters was achieved by DIVIDE, where each variance component was significantly predicted by the corresponding microstructural features; the only significant predictor for MK_A was H_A, where $\beta_A = 2.5 \pm 0.3$ ($p < 10^{-6}$) and $\beta_I = 0.0 \pm 0.3$ ($p = 0.9$); the only significant predictor for MK_I was H_I, where $\beta_I = 1.4 \pm 0.3$ ($p < 10^{-3}$) and $\beta_A = 0.1 \pm 0.3$ ($p = 0.6$).

The comparison of diffusional variance within and between tumor groups is shown in Fig. 6 and Table 1. The microscopic anisotropy dominated in the meningiomas ($MK_A = 1.11 \pm 0.33$ vs $MK_I = 0.44 \pm 0.20$, $p < 10^{-3}$), whereas isotropic heterogeneity dominated in the gliomas ($MK_I = 0.57 \pm 0.30$ vs $MK_A = 0.26 \pm 0.11$, $p = 0.02$). Between tumor groups, MK_T and MK_A were found to be significantly higher in meningiomas (both $p < 10^{-3}$), while MK_I was not significantly different ($p = 0.3$). The largest effect size was found for MK_A where $d = 3.6$, compared to $d = 2.2$ for MK_T (see Table 1 for details). These findings suggest that the most prominent difference between the meningioma and glioma groups is driven by the presence or absence of microscopic anisotropy. To facilitate future comparisons we also report remaining parameters derived from dMRI and microscopy in Table 2.

Discussion

In this study, we used DIVIDE to decompose the anisotropic and isotropic components of the diffusional variance in meningioma and glioma tumors, and we pinpointed the source of these components through an independent analysis of the underlying microstructure. The MK_A parameter was shown to capture the structural anisotropy on the microscopic scale, where the diffusion anisotropy in the meningiomas was likely caused by an abundance of eccentric cells and cell structures. In agreement with preliminary results reported by Szczepankiewicz et al. (2015), such structures were absent in the gliomas. The MK_I parameter was shown to capture heterogeneous cell density which was caused by local patches of high and low cell density due to aggressive cell growth or necrosis. The strong correlations between parameters derived from dMRI and microscopy provide compelling evidence that MK_A, μFA and MK_I can be interpreted in terms of specific and intuitive features of tissue microstructure (Fig. 4). Furthermore, the regression analysis confirmed that MK_T conflates the effects of cell eccentricity and variable density (Mitra, 1995), and therefore lacks specificity, whereas MK_A and MK_I were specific to either of the two. Thus, the lack of specificity exhibited by MK_T can be recovered by decomposing MK_T into MK_A and MK_I. The FA and μFA also exhibited strong correlations

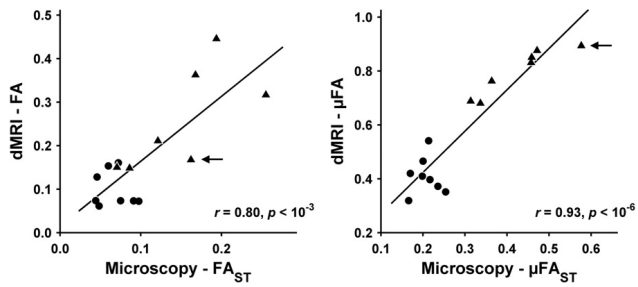

Fig. 5. Correlation between anisotropy parameters derived from dMRI and microscopy in meningiomas (triangles) and gliomas (circles). The diffusion anisotropy exhibits strong positive correlations with structure tensor anisotropy on the voxel (FA) and microscopic scale (μFA). Gliomas exhibit low FA and μFA, in agreement with the structure tensor analysis. By contrast, meningiomas exhibit a wide range of FA values, and relatively high μFA values. This suggests that the FA observed in meningiomas is strongly dependent on the orientation coherence of the tissue. The FA in meningiomas and gliomas may therefore overlap, impeding the ability of FA to differentiate the two tumor types despite their obvious difference in microscopic anisotropy. By contrast, the μFA clearly distinguishes the two tumor types. Moreover, the μFA stratified the fibroblastic meningiomas from the other subtypes, i.e., the fibroblastic tumors had the four highest μFA values, whereas the same stratification was not observed for FA. It may therefore be possible to use μFA for pre-surgical toughness estimation in meningiomas (Kashimura et al., 2007; Tropine et al., 2007). We emphasize that the tissue with the highest μFA is not necessarily mapped to the highest FA due to variable orientation coherence (black arrows point to the same tumor sample).

Please cite this article as: Szczepankiewicz, F., et al., The link between diffusion MRI and tumor heterogeneity: Mapping cell eccentricity and density by diffusional variance decompositio..., NeuroImage (2016), http://dx.doi.org/10.1016/j.neuroimage.2016.07.038

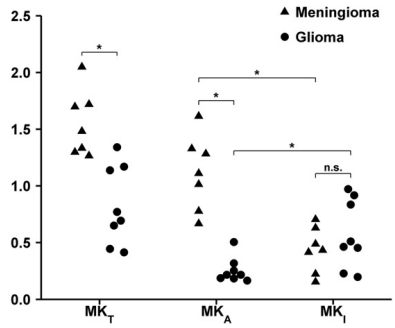

Fig. 6. Diffusional variance parameter distributions in the meningioma and glioma groups. Each data point shows the mean parameter value across all voxels in the tumor ROI. In the comparison between tumor groups, MK_T and MK_A were significantly different, whereas MK_I was not (* indicates statistical significance, n.s. indicates no significance; see Table 1 for details). Most notably, MK_A exhibits a distinct separation between the meningioma and glioma groups, indicating that the presence of anisotropic microstructures can be used to effectively differentiate the tumors. The comparison of MK_A and MK_I within tumor groups revealed that MK_A is dominant in the meningiomas, and MK_I is dominant in the gliomas.

with their structure tensor analogues (Fig. 5). This result is in accordance with similar studies performed in animals where voxel-scale diffusion anisotropy parameters, at high resolution, correlate with structure tensor anisotropy (Budde and Frank, 2012; Khan et al., 2015). However, here we show that the correlation also extends to measures of microscopic anisotropy and isotropic heterogeneity, which to our knowledge, have not been investigated previously.

The difference between the FA and μFA in the meningiomas is likely explained by the interaction between orientation coherence and voxel size (Oouchi et al., 2007). Fig. 7 utilizes the high-resolution microscopy images to demonstrate how larger voxels cause the FA in complex tissue to decrease due to a decreasing orientation coherence. It also highlights that this limitation can be mitigated by methods, such as DIVIDE, that recover the microscopic anisotropy (Jespersen et al., 2013; Lasič et al., 2014; Lawrenz and Finsterbusch, 2015; Westin et al., 2016). Thus, when interpreting voxel-scale anisotropy parameters such as the FA, the orientation coherence of the tissue is a potential confounder (De Santis et al., 2013).

Probing MK_A and MK_I separately revealed that the variance in meningioma tumors arises mainly due to the presence of anisotropic cell structures, whereas it was mainly due to isotropic heterogeneity in the gliomas (Fig. 6 and Table 1). Furthermore, MK_A exhibited the largest

Table 1
DIVIDE parameters in meningiomas and gliomas. Values are presented as group mean ± one standard deviation. For t-tests performed within and between groups we present the corresponding Cohen's d (d), 95% confidence interval ($CI_{95\%}$), and p-value (p). For meningiomas the dominant component was MK_A, whereas in gliomas the MK_I was dominant. Between tumor groups MK_T and MK_A differed significantly, where the MK_A exhibited the largest effect size. No significant difference between tumor types was found for MK_I.

		Meningioma	Glioma	Meningioma vs Glioma		
		($n = 7$)	($n = 8$)	$CI_{95\%}$	d	p
	MK_T	1.55 ± 0.29	0.83 ± 0.35	[0.37 1.08]	2.2	$<10^{-3}$
	MK_A	1.11 ± 0.33	0.26 ± 0.11	[0.55 1.16]	3.6	$<10^{-3}$
	MK_I	0.44 ± 0.20	0.57 ± 0.30	[−0.42 0.15]	−0.5	0.3
MK_A vs MK_I	$CI_{95\%}$	[0.35 1.00]	[−0.57 −0.06]			
	d	2.5	−1.4			
	p	$<10^{-3}$	0.02			

MK_T, total mean kurtosis; MK_A, anisotropic kurtosis; MK_I, isotropic kurtosis.

Table 2
Parameters derived from DTI, DIVIDE and quantitative microscopy in meningiomas and gliomas. Values are presented as group mean ± one standard deviation. The MD is in $\mu m^2/ms$, the ρ_c is in $10^3/mm^2$, remaining parameters are unitless.

	Meningioma	Glioma
	($n = 7$)	($n = 8$)
MD	1.08 ± 0.13	1.60 ± 0.22
FA	0.26 ± 0.12	0.10 ± 0.04
μFA	0.80 ± 0.09	0.41 ± 0.07
$<\rho_c>$	3.4 ± 1.8	2.2 ± 2.4
H_A	0.36 ± 0.17	0.08 ± 0.02
H_I	0.14 ± 0.09	0.11 ± 0.11
FA_{ST}	0.15 ± 0.06	0.07 ± 0.02
μFA_{ST}	0.43 ± 0.09	0.21 ± 0.03

MD, mean diffusivity; FA, fractional anisotropy; μFA, microscopic FA; $<\rho_c>$, cell density; H_A, normalized variance of structure tensor eigenvalues; H_I, normalized variance of cell density; subscript 'ST' denotes parameters derived from structure tensor analysis.

effect size between meningioma and glioma groups. This indicates that the primary difference between meningiomas and gliomas is the presence of structures that yield anisotropic diffusion at the microscopic scale, while the difference in isotropic heterogeneity is secondary (Table 1). In a statistical sense, MK_A should therefore be a superior biomarker compared to MK_T whenever the difference between tissues is predominately due to microscopic anisotropy. In such circumstances the MK_I may be considered a nuisance parameter; removing it increases the separation between groups resulting in a higher statistical power (Szczepankiewicz et al., 2013). Although removing one component of variance may improve the statistical power of studies aimed to find a specific effect, we stress that this is contextual. For example, a similar analysis applied to the white matter in schizophrenia patients considered the isotropic variance as the relevant component (Westin et al., 2016).

We expect that the improved specificity gained from decomposing the two sources of diffusional variance may be used to infer additional information about the underlying tissue microstructure, and may facilitate an improved interpretation of parameters that reflect diffusional

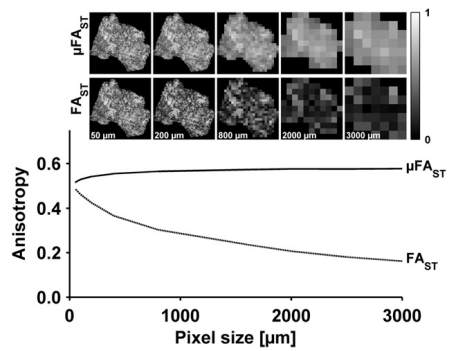

Fig. 7. Effect of spatial resolution and orientation coherence on anisotropy. The image array shows FA_{ST} and μFA_{ST} maps in a fibroblastic meningioma derived from the structure tensor field at spatial resolutions between 50 × 50 and 3000 × 3000 μm^2. The plotted lines show the average parameter values across the tumor section for the same interval of spatial resolutions. This showcases the interaction between the spatial resolution and the orientation coherence, where conventional anisotropy parameters, such as the FA from DTI, are reduced as the resolution decreases, in accordance with similar effects shown by Budde and Annese (2013). By contrast, the microscopic anisotropy, i.e., the μFA, remains stable and is independent of the spatial resolution. This demonstrates the inherent limitation of FA, and the advantage of μFA, when estimating anisotropy in complex tissue.

Please cite this article as: Szczepankiewicz, F., et al., The link between diffusion MRI and tumor heterogeneity: Mapping cell eccentricity and density by diffusional variance decompositio..., NeuroImage (2016), http://dx.doi.org/10.1016/j.neuroimage.2016.07.038

variance and kurtosis, as well as diffusion anisotropy. The method presented here is applicable to a wide variety of inquiries as it requires few assumptions about the investigated tissue and is implemented as a straight-forward modification to the conventional diffusion encoding sequence (Lasič et al., 2014; Szczepankiewicz et al., 2015). This is especially true if diffusion anisotropy parameters are intended to differentiate tumor subtypes (Jolapara et al., 2010; Sanverdi et al., 2012; Wang et al., 2012), preoperative estimation of tumor consistency (Kashimura et al., 2007; Tropine et al., 2007), delineation for biopsies (Kinoshita et al., 2008), and tumor proliferation (Beppu et al., 2005). Such cases warrant the use of MK_A or μFA, since conventional measures of anisotropy ignore the interaction between orientation coherence and voxel size, and may therefore be strongly biased (Fig. 7). This also extends to tissues outside of the central nervous system, such as the prostate where the stromal tissue is anisotropic and highly disordered on the sub-voxel scale (Bourne et al., 2012). Moreover, the ability to isolate the effects of isotropic heterogeneity may improve the characterization of tissue. For example, tumor infiltration in white matter may be better detected and delineated by removing the dominant effects of white matter anisotropy and instead characterizing the subtle changes in the isotropic heterogeneity (Sternberg et al., 2014).

We stress that the use of multiple encoding tensor shapes is required to probe the microscopic anisotropy and isotropic heterogeneity separately. As illustrated in Fig. 1, conventional encoding (LTE, solid lines) is theoretically incapable of distinguishing the three environments since all signal curves are virtually identical regardless of their anisotropic content (Mitra, 1995). Therefore, the microscopic anisotropy cannot be isolated by conventional encoding alone. This stands in contrast to Kaden et al. (2016) who claim that microscopic diffusion coefficients can be probed using only conventional SDE. Methods that attempt to estimate microscopic anisotropy and microscopic diffusion coefficients based only on SDE must either ignore the presence of isotropic diffusional variance, or assign values to it based on prior assumptions, e.g., assume that the system is composed of a mixture of specific microenvironments. However, since the isotropic variance exhibits considerable variation within individual subjects as well as between patients and controls (Szczepankiewicz et al., 2015), ignoring it will likely render an unpredictable bias that erroneously interprets isotropic heterogeneity as the presence of anisotropic structures, which impairs the interpretation of parameters such as the microscopic diffusion coefficients (Kaden et al., 2016).

We have identified three limiting aspects of the current study, pertaining to the generalization of the findings, the accuracy of the quantitative microscopy, and the clinical feasibility of the method. The generalization is limited because the present study comprises only two tumor types and a small number of tumors. Furthermore, the DIVIDE parameters may depend on features that are not included in the current models. For example, intra-voxel incoherent motion of blood may affect the diffusion weighted signal (Le Bihan et al., 1986). This may become relevant in well vascularized tumors, particularly since each waveform may contribute different levels of flow compensation (Ahlgren et al., 2016). The effects of water exchange across microenvironments could also affect the parameterization (Nilsson et al., 2013b). However, a preliminary study of the apparent exchange rate (Nilsson et al., 2013a) in meningiomas and gliomas reported residence times that were markedly longer than the diffusion times used in the current study (Lampinen et al., 2016), which suggests that the effects are negligible in these tumors. Restricted diffusion may yield an interaction between the diffusion time and the size distribution of restrictions (Gore et al., 2010). This may be especially relevant in diseased tissue where such features are unpredictable, and for non-conventional waveform shapes where the effective diffusion time is not well-defined (Nilsson et al., 2016). Although variable diffusion times normally have a limited influence in neural tissues (Nilsson et al., 2013b), integrating a model of restricted diffusion and DIVIDE may improve parameter accuracy (Ianus et al., 2016).

Several limitations pertain specifically to the quantitative microscopy. In the current implementation structural information is investigated in a two dimensional plane, whereas the diffusion takes place in three dimensions. This likely introduces a negative bias in structure anisotropy since through-plane anisotropy cannot be captured (Khan et al., 2015). Furthermore, 2D structure tensors cannot distinguish between structures that render oblate and prolate diffusion tensors which may impede the correlation between diffusion and structure tensors (Kingsley, 2006). More elaborate techniques based on confocal microscopy are able to reconstruct microscopic images in thin three dimensional slabs (Khan et al., 2015), however, these techniques were outside the scope of the present work. Although these limitations may impact the parameter accuracy, they may be partially mitigated by designing the microscopy-based metrics to be mathematically proportional to their dMRI analogues, and quantifying their association based on the strength of the correlation rather than the correspondence of absolute values.

The dMRI acquisition protocol reported in the present study was designed to oversample the directions and b-values for validation purposes (Szczepankiewicz et al., 2015) and therefore featured a relatively low spatial resolution and a long acquisition time at a limited slice coverage. A clinically feasible protocols can be achieved by reducing the number of b-values and by tailoring their distribution to the tissue of interest (Alexander, 2008; Knutsson and Westin, 2013; Szczepankiewicz et al., 2016b). For example, whole brain acquisition is possible at a resolution of $2 \times 2 \times 3$ mm^3 in less than 8 min by using only two non-zero b-values and optimized asymmetric waveforms (Sjölund et al., 2015), which can reduce the TE from 160 ms (presented herein) to below 100 ms (Szczepankiewicz et al., 2016a). Simultaneous multi-slice acquisitions could potentially reduce it below 4 min (Setsompop et al., 2012). The design of clinical protocols with respect to tissue characteristics and hardware capabilities will be addressed in future works.

Conclusions

We found an excellent agreement between DIVIDE parameters and tissue microstructure in meningiomas and gliomas. This constitutes compelling evidence that a link exists between diffusional variance and structural heterogeneity. The diffusional variance due to microscopic anisotropy and isotropic heterogeneity could be disentangled and linked specifically to cell eccentricity and cell density variance, where MK_A and μFA reflect cell eccentricity independent of orientation coherence, and MK_I reflects variable cell density. The separation of cell eccentricity from variable cell density relies on diffusion encoding tensors with multiple shapes and is therefore not accessible by methods based on conventional diffusion encoding, such as DKI. Thus, DIVIDE provides a more comprehensive and specific description of the tissue microstructure and heterogeneity, which can be used to improve the interpretation of diffusional variance and diffusional anisotropy.

Author contributions

All authors conceived and designed the study. MRI pulse sequence programming was done by FSz and MN. Patients were recruited by DvW and PS. Histological evaluation and quantitative microscopy was performed by FSz and EE. dMRI data was acquired and analyzed by FSz, DvW, JL and MN. Statistical evaluation was done by FSz and MN. All authors contributed to the writing of the manuscript.

Funding information

This research was supported by the Swedish Cancer Society (grant nos. CAN 2012/597 and CAN 2013/321), the Swedish Research Council (grant no. K2011-52X-21737-01-3), the Swedish Foundation for Strategic Research (grant no. AM13-0090), the National Institutes of Health

Please cite this article as: Szczepankiewicz, F., et al., The link between diffusion MRI and tumor heterogeneity: Mapping cell eccentricity and density by diffusional variance decompositio..., NeuroImage (2016), http://dx.doi.org/10.1016/j.neuroimage.2016.07.038

(grant nos. R01MH074794 and P41EB015902), the Swedish Brain Foundation (grant no. FO2014-0133), and CR Development AB (grant no. MN15).

Conflict of interest statement

MN declares research support from Colloidal Resource, and patent applications in Sweden (1250453-6 and 1250452-8), USA (61/642 594 and 61/642 589), and PCT (SE2013/050492 and SE2013/050493). Remaining authors declare no conflict of interest.

References

Ahlgren, A., Knutsson, L., Wirestam, R., Nilsson, M., Ståhlberg, F., Topgaard, D., Lasič, S., 2016. Quantification of microcirculatory parameters by joint analysis of flow-compensated and non-flow-compensated intravoxel incoherent motion (ivim) data. NMR Biomed. 29, 640–649.

Alexander, D.C., 2008. A general framework for experiment design in diffusion MRI and its application in measuring direct tissue-microstructure features. Magn. Reson. Med. 60, 439–448.

Alexander, A.L., Lee, J.E., Lazar, M., Field, A.S., 2007. Diffusion tensor imaging of the brain. Neurotherapeutics 4, 316–329.

Al-Kofahi, Y., Lassoued, W., Lee, W., Roysam, B., 2010. Improved automatic detection and segmentation of cell nuclei in histopathology images. IEEE Trans. Biomed. Eng. 57, 841–852.

Barazany, D., Basser, P.J., Assaf, Y., 2009. In vivo measurement of axon diameter distribution in the corpus callosum of rat brain. Brain 132, 1210–1220.

Basser, P.J., Pierpaoli, C., 1996. Microstructural and physiological features of tissues elucidated by quantitative-diffusion-tensor MRI. J. Magn. Reson. 209–2019.

Basser, P.J., Mattiello, J., Le Bihan, D., 1994. MR diffusion tensor spectroscopy and imaging. Biophys. J. 66, 259–267.

Beppu, T., Inoue, T., Shibata, Y., Yamada, N., Kurose, A., Ogasawara, K., Ogawa, A., Kabasawa, H., 2005. Fractional anisotropy value by diffusion tensor magnetic resonance imaging as a predictor of cell density and proliferation activity of glioblastomas. Surg. Neurol. 63, 56–61 (discussion 61).

Bigun, J., 1987. Optimal Orientation Detection of Linear Symmetry. Proc. of the IEEE First International Conference on Computer Vision, London. pp. 433–438.

Bourne, R.M., Kurniawan, N., Cowin, G., Sved, P., Watson, G., 2012. Microscopic diffusion anisotropy in formalin fixed prostate tissue: preliminary findings. Magn. Reson. Med. 68, 1943–1948.

Budde, M.D., Annese, J., 2013. Quantification of anisotropy and fiber orientation in human brain histological sections. Front. Integr. Neurosci. 7, 3.

Budde, M.D., Frank, J.A., 2012. Examining brain microstructure using structure tensor analysis of histological sections. NeuroImage 63, 1–10.

Callaghan, P.T., Komlosh, M.E., 2002. Locally anisotropic motion in a macroscopically isotropic system: displacement correlations measured using double pulsed gradient spin-echo nmr. Magn. Reson. Chem. 40, S15–S19.

Chenevert, T.L., Stegman, L.D., Taylor, J.M., Robertson, P.L., Greenberg, H.S., Rehemtulla, A., Ross, B.D., 2000. Diffusion magnetic resonance imaging: an early surrogate marker of therapeutic efficacy in brain tumors. J. Natl. Cancer Inst. 92, 2029–2036.

De Santis, S., Drakesmith, M., Bells, S., Assaf, Y., Jones, D.K., 2013. Why diffusion tensor MRI does well only some of the time: variance and covariance of white matter tissue microstructure attributes in the living human brain. NeuroImage 89C, 35–44.

Edén, M., 2003. Computer simulations in solid-state nmr. Iii. Powder averaging. Concepts in Magnetic Resonance Part A 18A, 24–55.

Eriksson, S., Lasič, S., Topgaard, D., 2013. Isotropic diffusion weighting in PGSE nmr by magic-angle spinning of the q-vector. J. Magn. Reson. 226, 13–18.

Eriksson, S., Lasič, S., Nilsson, M., Westin, C.F., Topgaard, D., 2015. Nmr diffusion-encoding with axial symmetry and variable anisotropy: distinguishing between prolate and oblate microscopic diffusion tensors with unknown orientation distribution. J. Chem. Phys. 142, 104201.

Gore, J.C., Xu, J., Colvin, D.C., Yankeelov, T.E., Parsons, E.C., Does, M.D., 2010. Characterization of tissue structure at varying length scales using temporal diffusion spectroscopy. NMR Biomed. 23, 745–756.

Gudbjartsson, H., Patz, S., 1995. The rician distribution of noisy MRI data. Magn. Reson. Imaging 910–914.

Ianus, A., Drobnjak, I., Alexander, D.C., 2016. Model-based estimation of microscopic anisotropy using diffusion MRI: a simulation study. NMR Biomed. 29, 672–685.

Jelescu, I.O., Zurek, M., Winters, K.V., Veraart, J., Rajaratnam, A., Kim, N.S., Babb, J.S., Shepherd, T.M., Novikov, D.S., Kim, S.G., Fieremans, E., 2016. In vivo quantification of demyelination and recovery using compartment-specific diffusion MRI metrics validated by electron microscopy. NeuroImage 132, 104–114.

Jensen, J.H., Helpern, J.A., Ramani, A., Lu, H., Kaczynski, K., 2005. Diffusional kurtosis imaging: the quantification of non-Gaussian water diffusion by means of magnetic resonance imaging. Magn. Reson. Med. 53, 1432–1440.

Jensen, J.H., Hui, E.S., Helpern, J.A., 2014. Double-pulsed diffusional kurtosis imaging. NMR Biomed. 27, 363–370.

Jespersen, S.N., Bjarkam, C.R., Nyengaard, J.R., Chakravarty, M.M., Hansen, B., Vosegaard, T., Østergaard, L., Yablonskiy, D., Nielsen, N.C., Vestergaard-Poulsen, P., 2010. Neurite density from magnetic resonance diffusion measurements at ultrahigh field: comparison with light microscopy and electron microscopy. NeuroImage 49, 205–216.

Jespersen, S.N., Lundell, H., Sønderby, C.K., Dyrby, T.B., 2013. Orientationally invariant metrics of apparent compartment eccentricity from double pulsed field gradient diffusion experiments. NMR Biomed. 26, 1647–1662.

Jolapara, M., Kesavadas, C., Radhakrishnan, V.V., Thomas, B., Gupta, A.K., Bodhey, N., Patro, S., Saini, J., George, U., Sarma, P.S., 2010. Role of diffusion tensor imaging in differentiating subtypes of meningiomas. J. Neuroradiol. 37, 277–283.

Jones, D.K., Horsfield, M.A., Simmons, A., 1999. Optimal strategies for measuring diffusion in anisotropic systems by magnetic resonance imaging. Magn. Reson. Med. 42, 515–525.

Kaden, E., Kruggel, F., Alexander, D.C., 2016. Quantitative mapping of the per-axon diffusion coefficients in brain white matter. Magn. Reson. Med. 75, 1752–1763.

Kamagata, K., Kerever, A., Yokosawa, S., Otake, Y., Ochi, H., Hori, M., Kamiya, K., Tsuruta, K., Tagawa, K., Okazawa, H., Aoki, S., Arikawa-Hirasawa, E., 2016. Quantitative histological validation of diffusion tensor MRI with two-photon microscopy of cleared mouse brain. Magn. Reson. Med. Sci.

Kashimura, H., Inoue, T., Ogasawara, K., Arai, H., Otawara, Y., Kanbara, Y., Ogawa, A., 2007. Prediction of meningioma consistency using fractional anisotropy value measured by magnetic resonance imaging. J. Neurosurg. 107, 784–787.

Khan, A.R., Cornea, A., Leigland, L.A., Kohama, S.G., Jespersen, S.N., Kroenke, C.D., 2015. 3d structure tensor analysis of light microscopy data for validating diffusion MRI. NeuroImage 111, 192–203.

Kingsley, P.B., 2006. Introduction to diffusion tensor imaging mathematics: part ii. Anisotropy, diffusion-weighting factors, and gradient encoding schemes. Concepts in Magnetic Resonance Part A 28A, 123–154.

Kinoshita, M., Hashimoto, N., Goto, T., Kagawa, N., Kishima, H., Izumoto, S., Tanaka, H., Fujita, N., Yoshimine, T., 2008. Fractional anisotropy and tumor cell density of the tumor core show positive correlation in diffusion tensor magnetic resonance imaging of malignant brain tumors. NeuroImage 43, 29–35.

Klein, S., Staring, M., Murphy, K., Viergever, M.A., Pluim, J.P., 2010. Elastix: a toolbox for intensity-based medical image registration. IEEE Trans. Med. Imaging 29, 196–205.

Knutsson, H., Westin, C.F., 2013. Tensor metrics and charged containers for 3d q-space sample distribution. Med. Image Comput. Comput. Assist. Interv. 16, 679–686.

Lampinen, B., Szczepankiewicz, F., van Westen, D., Englund, E., Sundgren, P., Lätt, J., Ståhlberg, F., Nilsson, M., 2016. Optimal experimental design for filter exchange imaging: apparent exchange rate measurements in the healthy brain and in intracraniale tumors. Magn. Reson. Med.

Lasič, S., Szczepankiewicz, F., Eriksson, S., Nilsson, M., Topgaard, D., 2014. Microanisotropy imaging: quantification of microscopic diffusion anisotropy and orientational order parameter by diffusion MRI with magic-angle spinning of the q-vector. Front. Phys. 2, 11.

Lätt, J., Nilsson, M., Malmborg, C., Rosquist, H., Wirestam, R., Ståhlberg, F., Topgaard, D., Brockstedt, S., 2007. Accuracy of q-space related parameters in MRI: simulations and phantom measurements. IEEE Trans. Med. Imaging 26, 1437–1447.

Lawrenz, M., Finsterbusch, J., 2015. Mapping measures of microscopic diffusion anisotropy in human brain white matter in vivo with double-wave-vector diffusion-weighted imaging. Magn. Reson. Med. 73, 773–783.

Lawrenz, M., Koch, M.A., Finsterbusch, J., 2010. A tensor model and measures of microscopic anisotropy for double-wave-vector diffusion-weighting experiments with long mixing times. J. Magn. Reson. 202, 43–56.

Le Bihan, D., 2013. Apparent diffusion coefficient and beyond: what diffusion MR imaging can tell us about tissue structure. Radiology 268, 318–322.

Le Bihan, D., Breton, E., Lallemand, D., Grenier, P., Cabanis, E., Laval-Jeantet, M., 1986. MR imaging of intravoxel incoherent motions: application to diffusion and perfusion in neurologic disorders. Radiology 161, 401–407.

Louis, D.N., Ohgaki, H., Wiestler, O.D., Cavenee, W.K., Burger, P.C., Jouvet, A., Scheithauer, B.W., Kleihues, P., 2007. The 2007 who classification of tumours of the central nervous system. Acta Neuropathol. 114, 97–109.

Maier, S.E., Sun, Y., Mulkern, R.V., 2010. Diffusion imaging of brain tumors. NMR Biomed. 23, 849–864.

Malpica, N., de Solorzano, C.O., Vaquero, J.J., Santos, A., Vallcorba, I., Garcia-Sagredo, J.M., del Pozo, F., 1997. Applying watershed algorithms to the segmentation of clustered nuclei. Cytometry 28, 289–297.

Marusyk, A., Polyak, K., 2010. Tumor heterogeneity: causes and consequences. Biochimica et Biophysica Acta (BBA) - Reviews on Cancer 1805, 105–117.

Mitra, P., 1995. Multiple wave-vector extensions of the nmr pulsed-field-gradient spin-echo diffusion measurement. Phys. Rev. B 51, 15074–15078.

Moffat, B.A., Chenevert, T.L., Lawrence, T.S., Meyer, C.R., Johnson, T.D., Dong, Q., Tsien, C., Mukherji, S., Quint, D.J., Gebarski, S.S., Robertson, P.L., Junck, L.R., Rehemtulla, A., Ross, B.D., 2005. Functional diffusion map: a noninvasive MRI biomarker for early stratification of clinical brain tumor response. Proc. Natl. Acad. Sci. U. S. A. 102, 5524–5529.

Nilsson, M., Lätt, J., van Westen, D., Brockstedt, S., Lasič, S., Ståhlberg, F., Topgaard, D., 2013a. Noninvasive mapping of water diffusional exchange in the human brain using filter-exchange imaging. Magn. Reson. Med. 69, 1573–1581.

Nilsson, M., van Westen, D., Ståhlberg, F., Sundgren, P.C., Lätt, J., 2013b. The role of tissue microstructure and water exchange in biophysical modelling of diffusion in white matter. MAGMA 26, 345–370.

Nilsson, M., Szczepankiewicz, F., van Westen, D., Hansson, O., 2015. Extrapolation-based references improve motion and eddy-current correction of high b-value dwi data: application in Parkinson's disease dementia. PLoS One 10, e0141825.

Nilsson, M., Lasič, S., Topgaard, D., Westin, C.F., 2016. Estimating the axon diameter from intra-axonal water diffusion with arbitrary gradient waveforms: resolution limit in parallel and dispersed fibers. Proc. Int. Soc. Magn. Reson. Med. 24, 0663 (Singapore).

Oouchi, H., Yamada, K., Sakai, K., Kizu, O., Kubota, T., Ito, H., Nishimura, T., 2007. Diffusion anisotropy measurement of brain white matter is affected by voxel size: underestimation occurs in areas with crossing fibers. AJNR Am. J. Neuroradiol. 28, 1102–1106.

Please cite this article as: Szczepankiewicz, F., et al., The link between diffusion MRI and tumor heterogeneity: Mapping cell eccentricity and density by diffusional variance decompositio..., NeuroImage (2016), http://dx.doi.org/10.1016/j.neuroimage.2016.07.038

Ozarslan, E., Basser, P.J., 2008. Microscopic anisotropy revealed by nmr double pulsed field gradient experiments with arbitrary timing parameters. J. Chem. Phys. 128, 154511.
Padhani, A.R., Liu, G., Mu-Koh, D., Chenevert, T.L., Thoeny, H.C., Takahara, T., Dzik-Jurasz, A., Ross, B.D., Van Cauteren, M., Collins, D., Hammoud, D.A., Rustin, G.J.S., Taouli, B., Choyke, P.L., 2009. Diffusion-weighted magnetic resonance imaging as a cancer biomarker: consensus and recommendations. Neoplasia 11, 102–125.
Raab, P., Hattingen, E., Franz, K., Zanella, F.E., Lanfermann, H., 2010. Cerebral gliomas: diffusional kurtosis imaging analysis of microstructural differences. Radiology 254, 876–881.
Riemenschneider, M.J., Perry, A., Reifenberger, G., 2006. Histological classification and molecular genetics of meningiomas. The Lancet Neurology 5, 1045–1054.
Röding, M., Bernin, D., Jonasson, J., Sarkka, A., Topgaard, D., Rudemo, M., Nyden, M., 2012. The gamma distribution model for pulsed-field gradient nmr studies of molecular-weight distributions of polymers. J. Magn. Reson. 222, 105–111.
Ronen, I., Budde, M., Ercan, E., Annese, J., Techawiboonwong, A., Webb, A., 2014. Microstructural organization of axons in the human corpus callosum quantified by diffusion-weighted magnetic resonance spectroscopy of n-acetylaspartate and post-mortem histology. Brain Struct. Funct. 219, 1773–1785.
Ryu, Y.J., Choi, S.H., Park, S.J., Yun, T.J., Kim, J.H., Sohn, C.H., 2014. Glioma: application of whole-tumor texture analysis of diffusion-weighted imaging for the evaluation of tumor heterogeneity. PLoS One 9, e108335.
Sanverdi, S.E., Ozgen, B., Oguz, K.K., Mut, M., Dolgun, A., Soylemezoglu, F., Cila, A., 2012. Is diffusion-weighted imaging useful in grading and differentiating histopathological subtypes of meningiomas? Eur. J. Radiol. 81, 2389–2395.
Schilling, K., Janve, V., Gao, Y., Stepniewska, I., Landman, B.A., Anderson, A.W., 2016. Comparison of 3d orientation distribution functions measured with confocal microscopy and diffusion MRI. NeuroImage 129, 185–197.
Setsompop, K., Cohen-Adad, J., Gagoski, B.A., Raij, T., Yendiki, A., Keil, B., Wedeen, V.J., Wald, L.L., 2012. Improving diffusion MRI using simultaneous multi-slice echo planar imaging. NeuroImage 63, 569–580.
Shemesh, N., Ozarslan, E., Adiri, T., Basser, P.J., Cohen, Y., 2010. Noninvasive bipolar double-pulsed-field-gradient nmr reveals signatures for pore size and shape in polydisperse, randomly oriented, inhomogeneous porous media. J. Chem. Phys. 133, 044705.
Sjölund, J., Szczepankiewicz, F., Nilsson, M., Topgaard, D., Westin, C.F., Knutsson, H., 2015. Constrained optimization of gradient waveforms for generalized diffusion encoding. J. Magn. Reson. 261, 157–168.
Sternberg, E.J., Lipton, M.L., Burns, J., 2014. Utility of diffusion tensor imaging in evaluation of the peritumoral region in patients with primary and metastatic brain tumors. AJNR Am. J. Neuroradiol. 35, 439–444.
Sugahara, T., Korogi, Y., Kochi, M., Ikushima, I., Shigematu, Y., Hirai, T., Okuda, T., Liang, L.X., Ge, Y.L., Komohara, Y., Ushio, Y., Takahashi, M., 1999. Usefulness of diffusion-weighted MRI with echo-planar technique in the evaluation of cellularity in gliomas. Jmri-Journal of Magnetic Resonance Imaging 9, 53–60.
Szczepankiewicz, F., Lätt, J., Wirestam, R., Leemans, A., Sundgren, P., van Westen, D., Ståhlberg, F., Nilsson, M., 2013. Variability in diffusion kurtosis imaging: impact on study design, statistical power and interpretation. NeuroImage 76, 145–154.
Szczepankiewicz, F., Lasič, S., van Westen, D., Sundgren, P.C., Englund, E., Westin, C.F., Ståhlberg, F., Lätt, J., Topgaard, D., Nilsson, M., 2015. Quantification of microscopic diffusion anisotropy disentangles effects of orientation dispersion from microstructure: applications in healthy volunteers and in brain tumors. NeuroImage 104, 241–252.
Szczepankiewicz, F., Westin, C.F., Ståhlberg, F., Lätt, J., Nilsson, M., 2016a. Microscopic anisotropy imaging at 7 t using asymmetrical gradient waveform encoding. Proc. Int. Soc. Magn. Reson. Med. 24, 1081 (Singapore).
Szczepankiewicz, F., Westin, C.F., Ståhlberg, F., Lätt, J., Nilsson, M., 2016b. Minimum number of diffusion encoding directions required to yield a rotationally invariant powder average signal in single and double diffusion encoding. Proc. Int. Soc. Magn. Reson. Med. 24, 2065 (Singapore).
Tietze, A., Hansen, M.B., Ostergaard, L., Jespersen, S.N., Sangill, R., Lund, T.E., Geneser, M., Hjelm, M., Hansen, B., 2015. Mean diffusional kurtosis in patients with glioma: initial results with a fast imaging method in a clinical setting. AJNR Am. J. Neuroradiol. 36, 1472–1478.
Topgaard, D., 2016. Nmr methods for studying microscopic diffusion anisotropy. In: Valiullin, R. (Ed.), Diffusion NMR in Confined Systems: Fluid Transport in Porous Solids and Heterogeneous Materials. Royal Society of Chemistry, Cambridge, UK.
Topgaard, D., Söderman, O., 2003. Experimental determination of pore shape and size using q-space nmr microscopy in the long diffusion-time limit. Magn. Reson. Imaging 21, 69–76.
Tropine, A., Dellani, P.D., Glaser, M., Bohl, J., Ploner, T., Vucurevic, G., Perneczky, A., Stoeter, P., 2007. Differentiation of fibroblastic meningiomas from other benign subtypes using diffusion tensor imaging. J. Magn. Reson. Imaging 25, 703–708.
Van Cauter, S., Veraart, J., Sijbers, J., Peeters, R.R., Himmelreich, U., De Keyzer, F., Van Gool, S.W., Van Calenbergh, F., De Vleeschouwer, S., Van Hecke, W., Sunaert, S., 2012. Gliomas: diffusion kurtosis MR imaging in grading. Radiology 263, 492–501.
Vos, S.B., Jones, D.K., Viergever, M.A., Leemans, A., 2011. Partial volume effect as a hidden covariate in DTI analyses. NeuroImage 55, 1566–1576.
Wang, S., Kim, S., Zhang, Y., Wang, L., Lee, E.B., Syre, P., Poptani, H., Melhem, E.R., Lee, J.Y., 2012. Determination of grade and subtype of meningiomas by using histogram analysis of diffusion-tensor imaging metrics. Radiology 262, 584–592.
Westin, C.F., Knutsson, H., Pasternak, O., Szczepankiewicz, F., Özarslan, E., van Westen, D., Mattisson, C., Bogren, M., O'Donnell, L.J., Kubicki, M., Topgaard, D., Nilsson, M., 2016. Q-space trajectory imaging for multidimensional diffusion MRI of the human brain. NeuroImage 135, 345–362.
Wu, E.X., Cheung, M.M., 2010. MR diffusion kurtosis imaging for neural tissue characterization. NMR Biomed. 23, 836–848.

Please cite this article as: Szczepankiewicz, F., et al., The link between diffusion MRI and tumor heterogeneity: Mapping cell eccentricity and density by diffusional variance decompositio..., NeuroImage (2016), http://dx.doi.org/10.1016/j.neuroimage.2016.07.038

Paper VI

The manuscript "*Whole-brain diffusional variance decomposition (DIVIDE): Demonstration of technical feasibility at clinical MRI systems*" by Szczepankiewicz et al., is not available in this version of the thesis document to avoid a potential copyright infringement at the time of publication.

Printed by Media-Tryck, Lund University 2016
Nordic Ecolabel 3041 0903

LUND UNIVERSITY

Lund University
Department of Medical Radiation Physics
Faculty of Science
ISBN: 978-91-7753-034-3 (print)
ISBN: 978-91-7753-035-0 (pdf)